APPROVAL SHEET

Title of Dissertation: SIGNAL PROCESSING, PERFORMANCE METRICS, AND LIFETIME OF A ^{6}LiF:ZnS(Ag) NEUTRON DETECTOR WITH WLS FIBERS AND SIPM PHOTODETECTOR

Name of Candidate: KEVIN M. PRITCHARD
DOCTOR OF SCIENCE, 2020

Dissertation and Abstract Approved: _____

FOW-SEN CHOA
PROFESSOR
Department of Computer Science and Electrical Engineering

_____

RYAN ROBUCCI
ASSISTANT PROFESSOR
Department of Computer Science and Electrical Engineering

Date Approved: _____

ABSTRACT

Title of Document: SIGNAL PROCESSING, PERFORMANCE METRICS, AND LIFETIME OF A ^{6}LiF:ZnS(Ag) NEUTRON DETECTOR WITH WLS FIBERS AND SIPM PHOTODETECTOR

KEVIN M. PRITCHARD,
DOCTOR OF SCIENCE, 2020

Directed By: RYAN ROBUCCI
ASSOCIATE PROFESSOR
Department of Computer Science and Electrical Engineering

FOW-SEN CHOA
PROFESSOR
Department of Computer Science and Electrical Engineering

ABSTRACT:

The NIST Center for Neutron Research studies the molecular and molecular-magnetic structure of materials using neutrons as a probing radiation. To further the speed of neutron scattering instrumentation, the NCNR has commissioned the Chromatic Analysis Neutron Diffractometer or Reflectometer (CANDOR) instrument. The CANDOR instrument has the potential to increase measurement speed by a factor of 1000. Detectors for neutron scattering instruments need to have high detection efficiency (90%), very high gamma rejection (10E-7), and operate at high count rates (10 kHz). Additionally for the CANDOR instrument, a neutron detector must be extremely thin (< 2mm) and use an alternative to the scarce helium-3 absorber isotope. The CANDOR neutron detector uses ^{6}LiF:ZnS(Ag) neutron scintillator to generate light pulses which are

transported to a silicon photomultiplier (SiPM) via wavelength shifting (WLS) fibers. An optimized detector design yields approximately 100 photons per neutron capture.

Specially designed signal processing schemes were developed to meet the neutron scattering requirements in spite of the large noise background produced by the SiPM photodetector and low light neutron signals. The signal processing algorithms use pulse shape discrimination (PSD), noise rejection filters, and maintain high count rates by compensating for the slow fluorescence decay of ZnS(Ag) neutron scintillator.

The Receiver Operator Characteristic (ROC) curve was used as a metric for gauging detection efficiency and gamma rejection, while arrival time statistics were used for gauging detector deadtime and doublecount fraction. Two detectors were characterized in detail; one detector very dim, one very bright. These two end cases encompass the performance of all detectors used in the CANDOR instrument. At a 10E-7 detection ratio for 662keV ^{137}Cs gammas and a negligible doublecount fraction, the absolute efficiency ranged from 87% to 91%, and deadtime from 2μs to 4μs for the dim and bright end cases respectively.

The photopeak, neutron transmission, and detection efficiency were measured for more than 1000 CANDOR detectors as a fitness test before installation in the CANDOR instrument. Most detectors passed, but there are manufacturing variations that still need to be eliminated for high manufacturing yields.

The CANDOR detectors can withstand approximately 10E+12 neutrons per cm^2 irradiation before their performance degrades to an unacceptable level. This translates to more than 20 years of expected service life.

SIGNAL PROCESSING, PERFORMANCE METRICS, AND LIFETIME OF A ^{6}LiF:ZnS(Ag) NEUTRON DETECTOR WITH WLS FIBERS AND SIPM PHOTODETECTOR

by

KEVIN M. PRITCHARD

Dissertation submitted to the Faculty of the Graduate School of the
University of Maryland, Baltimore County, in partial fulfillment
of the requirements for the degree of
Doctor of Science
2020

Preface

I am a member of a research and development team at the NIST (National Institute of Standards and Technology) Center for Neutron Research. Over the last eight years, our team has developed a new instrument for neutron scattering called CANDOR (Chromatic Analysis Neutron Diffractometer or Reflectometer). This instrument is a research and development project all its own, but within it is a newly developed neutron detector utilizing ^{6}LiF:ZnS(Ag) scintillator. This dissertation is all about the CANDOR neutron detector; it's component parts; how it works; design challenges; optimizations; its performance metrics; and its expected lifetime.

The R&D of the CANDOR instrument and its detector have been group efforts. This is clear from the Acknowledgements which I recommend you read first. Chapter 3 gives an overview of much of the research that was done during CANDOR detector development. Although I helped with much of the testing, this research was mostly performed by Dr. Alon Osovizky or under his guidance. Chapters 2, 4, and 5 are a combination of introductory information, literature reviews, and descriptions of the CANDOR detector. Chapters 6, 7, and 8 are where I have begun to be the primary investigator, and though all of this research has been a group effort, this is where most of my contributions are demonstrated.

Dedication

For my parents and grandparents who have always shown me

unconditional love and support

Acknowledgements

Professor Ryan Robucci and Professor Fow-Sen Choa – Thank you to my Ph.D. advisors who have been willing and open supporters of the non-traditional path that I've taken through my graduate school career. Neutron detectors may be a topic outside of their comfort zone, but my advisors have shown great curiosity for learning about neutron detectors, the they have found ways in which their unique expertise has been able to improve my research, and most of all they have been very helpful in showing me how to explain my research to scientists and engineers outside of the neutron scattering field.

Dr. Nicholas Maliszewskyj and Dr. Charles Majkrzak – Thank you for serving on my Ph.D. committee, and advocating for the CANDOR instrument and the CANDOR neutron detector development. If it weren't for these R&D projects, I wouldn't have a research avenue! Also thank you both for your long-term guidance and collaboration throughout the CANDOR neutron detector development.

Professor Carlos Romero-Talamas, Professor Narsingh Singh, and Professor Seung Jun Kim – Thank you for serving on my Ph.D. committee, for pushing me to explore other areas of radiation science & engineering, and to explore wavelet analysis techniques.

The UMBC CSEE Department – Thank you for showing great flexibility in allowing me to pursue research interests outside of the UMBC laboratories, and for allowing me to continue research on a part-time basis and an extended schedule.

Dr. Alon Osovizky – Thank you for teaching me about radiation detectors as I shadowed you through the process of testing scintillators with all manner of test equipment… from optical transmission, electron microscopes, radiation sources, pulse height analyzers, photomultipliers, and computer simulations. Alon's contribution to improving the brightness of our scintillator is the main reason why our CANDOR detector has been so successful.

Charles Hurlbut and Matt Jackson from Eljen Technology – Thank you for your willingness to spend time and effort creating a variety of scintillator mixtures for testing, and for manufacturing our CANDOR detectors which are rather unique and labor intensive to construct.

NIST Center for Neutron Reasearch (NCNR) Management including George Baltic, Dr. Richard Ibberson, Dr. Dan Neumann, and Dr. Rob Dimeo – Thank you for your faithful funding of the CANDOR project over its many years, even at the expense of other worthwhile research projects at our facility.

Edward Binkley – Thank you for your many mechanical designs and iterations of the CANDOR detector frame, fiber block, CAD models, and the very complex CANDOR

analyzer array. Thank you for the mechanical design and construction of several detector test stations.

Nancy Hadad – Thank you for steadfast project management of the CANDOR project, and for the many mechanical designs in the CANDOR instrument including the main detector arm and electronics carriages.

Jean-Philip Chabot – Thank you for creating the CANDOR_DAQ printed circuit assembly, firmware, and software. This is an incredible platform for doing detector signal processing and it works really, really well!

Jeffrey Ziegler – Thank you for the CANDOR preamplifier designs which are incredibly low noise and packed full of features. Your scintillator expertise and critical thinking have also been a great help throughout the project.

Peter Tsai – Thank you for the analog PSD discriminator designs and discriminator power supply designs. Also thank you for leading the search and elimination of switching power supply noise in our system.

Andrew Malone and Thaun Thai – Thank you for constructing the many electronics assemblies used in the CANDOR project and CANDOR instrument.

William “Bud” Dickerson – Thank you for trying to run me over in your car.

Yaacov Yehuda-Zada – Thank you for performing essential GEANT 4 computer simulations, which were essential in optimizing our detector geometry.

Stephen Phieffer – Thank you for your help in integrating the CANDOR test fixtures with facility software.

Dr. Eamon Anderson and Dr. Maynard Scott Dewey – Thank you for performing efficiency measurements with the Alpha-Gamma technique of our Helium-3 reference detector and CANDOR detector. Without these, we would not know the absolute efficiency of our detectors.

Dr. Daniel Hussy – Thank you for helping perform several rounds of neutron exposure measurements for detector lifetime predictions.

Timothy Barvitskie – Thank you for performing gamma spectroscopy analysis of our neutron-exposed detectors.

Table of Contents

List of Tables

List of Figures

Chapter 1: Introduction

Most technological changes in our society stem from an underlying advancement in materials science. Computing, healthcare devices, metallurgy, transportation, are just several examples of technologies which have been revolutionized by exploiting of the physical and chemical properties of materials for a particular purpose. Many historical advances in science and technology, and many more today even, begin with understanding the microscopic and submicroscopic nature of chemicals and lifeforms. Antonie van Leeuwenhoek used an early optical microscope to image cells, never before seen building blocks of organisms on the micro scale. It would be centuries later before scientific advancement reached a point where much smaller nanostructures could be understood. The fundamental reason why smaller structures could not be probed or imaged is due to the relatively long wavelength of optical light. Below 1um, light begins to diffract around tiny structures, due to the 300nm - 700nm optical wavelengths washing out features of smaller size. But measurement techniques improved.

Nowadays, much smaller chemical structures can be mapped using X-ray scattering and neutron scattering techniques. One of the most famous X-ray diffraction patterns is the double helix pattern of DNA taken by Franklin and Gosling in 1952 (***Figure 1***).

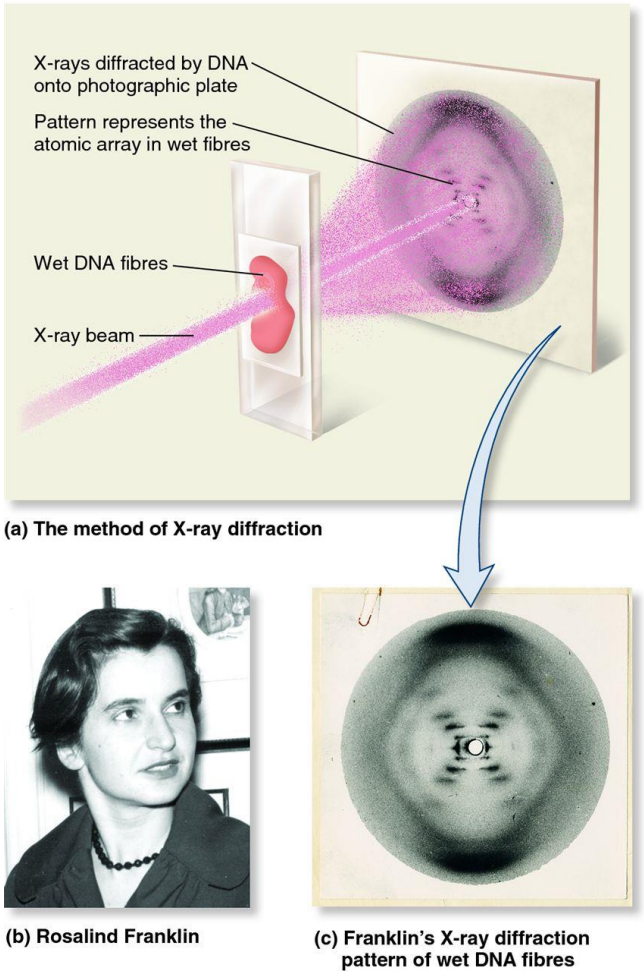

Figure 1: X-ray diffraction and neutron diffraction go beyond the limits of optical microscopy [1].

Rather than a direct image of chemical bonds and structures, scatter patterns contain features which can be interpreted to infer nanoscale structure. The field of crystallography has developed extensive models toward this purpose.

Slow neutron scattering and X-ray scattering are much the same in technique, but there are some significant differences. Slow neutrons are non-ionizing so they do not disturb the chemical bonds in the process of scattering. They also have tendencies to scatter from complementary elements from the periodic table, meaning neutrons are

better for studying structures composed of certain elements. Lastly, neutrons have a magnetic moment, and they are uniquely able to probe magnetic nanostructures.

The economics of neutron scattering experiments are also quite unique. A typical light bulb produces 10E+20 photons per second, whereas the core of a nuclear reactor has neutron flux densities of 10E+14 neutrons/cm^2/s. The neutron source is 1 million times weaker than a light bulb in terms of particles produced per second. By the time neutron optics have been built to guide a neutron beam onto a sample, the neutron flux drops to 10E+7 neutrons/cm^2/s. These tiny fluxes are akin to performing pinhole photography in the 1860s! The subject would need to be still in the frame while an image is exposed over many seconds.

The very expensive, but very dim nature of neutron sources sets the requirements for neutron detectors used in neutron scattering. A neutron detector must be:

1. High Neutron Detection Efficiency. <70% is unacceptable. >90% is preferred.

2. Very High noise & gamma rejection. >10E-7 gamma rejection ratio. Signal to noise must be very high or else small diffraction pattern features will be washed out.

3. High count rate. Able to process up to 10k events per second with minimal deadtime.

Toward the mission of effectively using as many neutrons as possible in neutron scattering experiments, a new Chromatic Analysis Neutron Diffractometer or Reflectometer (CANDoR) has been developed at the NIST Center for Neutron Research (NIST). This instrument uses a spectrum of neutron wavelengths between 4-6 angstroms, and it is able to analyze both the energy and direction of scattered neutrons at a very high rate by using multiple detector banks (*Figure 2*). If these detector banks are closely spaced sufficiently close to one another, then the solid angle for specular scattering from a layered thin film system sample will be optimized.

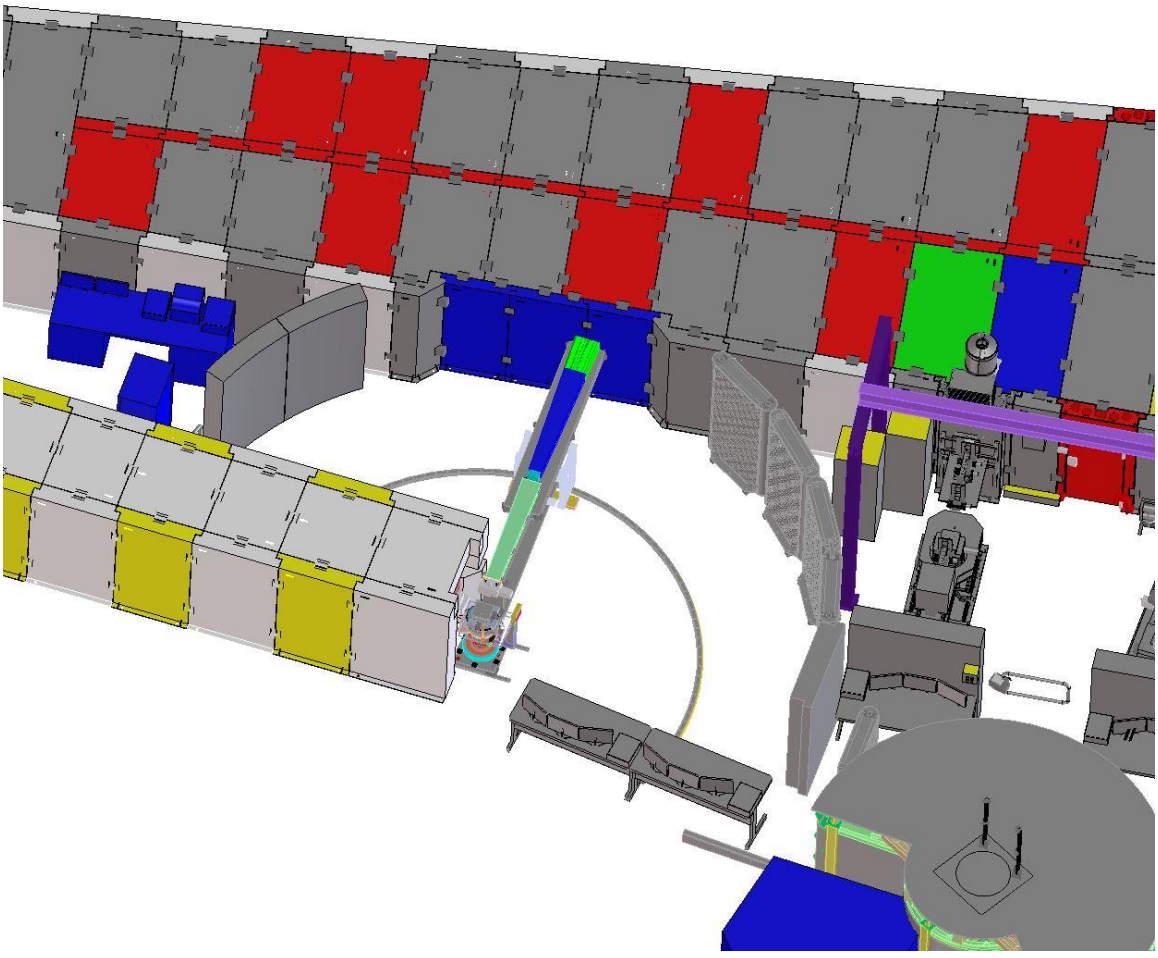

Figure 2: A CAD model of the CANDOR instrument.

The CANDOR prototype instrument can perform measurements at a rate 100x faster than a traditional reflectometer, with the potential to make measurements 1000x faster if the instrument is expanded by adding additional detector banks. There is a fourth requirement for the detectors used in the CANDOR instrument:

4. The detector must be very thin, < 2mm. This allows for closer spacing of detector banks and more solid angle coverage.

Finally, a fifth goal for the CANDOR detector has more to do with the long term strategy of the NCNR for finding alternatives to a rare and expensive neutron detection isotope, Helium-3, which is a strategically rationed resource globally.

5. Use an alternative detection isotope instead of Helium-3

The objective of the CANDOR detector project is to create a neutron detector which meets the 5 stated goals above, even though no currently existing detector technology meets all of these goals. Additionally, at the end of the CANDOR detector project, a neutron detector device must be designed, constructed, and replicated hundreds if not thousands of times. These detectors will be used in large quantities in a working neutron reflectometer. The goal of this work is to research and implement signal processing for the CANDOR detector, and to evaluate the performance of the CANDOR detector.

As mentioned, no detector technology currently exists which meets all 5 goals of the CANDOR reflectometer, but ultimately there must be a reliable, reproducible product. To increase the odds of success, an existing neutron technology was selected for further development. LiF:ZnS(Ag) scintillator technology was selected, and improvements were made ranging from maximizing the physical signals produced by captured neutrons, to optimizing the detection efficiency, gamma rejection ratio, and deadtime of the detector via signal processing. A number of innovations were developed to evaluate the CANDOR detector's key performance metrics.

Chapter 2 covers a review of neutron detector technologies, and why a LiF:ZnS(Ag) scintillator based detector was chosen as our focus for improvement. Chapter 3 describes the design of the scintillator detector, and how the light signal was increased and optimized for CANDOR. Chapter 4 discusses sources of signal and noise in the CANDOR detector. Chapter 5 reviews Pulse Shape Discrimination (PSD) and pattern recognition tools which are used in CANDOR signal processing for meeting the requirements of a neutron scattering detector. Chapter 6 will show an in-depth look at some real-world examples of CANDOR detector signals and the statistics of these signals. CANDOR signal processing algorithms are described. The trade-off between neutron identification and noise rejection is quantified, and the trade-off between detector count rate and double-count errors is also quantified. Chapter 7 will look at the performance metrics for a large number of manufactured detectors. Finally, Chapter 8 will look at the longevity of the CANDOR neutron detector, and planning for its complete lifecycle. Chapters 3, 4, 6, 7, and 8 may contain data and analysis similar to that contained in journal papers, as this work is based on the same research.

The CANDOR project has been in development for the better part of a decade, and the prototype instrument is now being commissioned. The project has been a large group effort involving dozens of scientists and engineers. The acknowledgements should be reviewed to realize just how complex the CANDOR instrument is in scope and how many systems and sub-systems were developed to create a working high-speed neutron reflectometer. I hope you enjoy reading this paper, and I hope you learn something as well!

Chapter 2: Review of Neutron Detector Technologies

2.1. Fundamental Properties of Neutrons

There are four fundamental forces of nature listed in order of ascending strength: gravity, weak nuclear force, electromagnetism, and the strong nuclear force. Most nuclear physics applications deal with the interaction of the two strongest forces: electromagnetism and the strong nuclear force. Most technical readers are familiar with electricity, magnetism, and have heard of the strong nuclear force that binds subatomic particles within the nucleus of an atom and is dominant at very small distances on the order of femtometers ($1fm = 10^{-15}m$).

Neutrons are subatomic particles which reside in the nucleus of an atom. They have no net charge. However, neutrons are made of charged quarks, and they have a magnetic dipole as well as a very weak electric dipole. In free space, neutrons will decay into a proton and an electron with an exponential decay time of 881 seconds [2], but this is still plenty of time to use neutrons in scientific experiments. The neutron's unique combination of no net charge, magnetic dipole moment, and adequate lifetime make it very useful for probing the molecular and magnetic structure of materials.

Neutrons interact with the nuclei of atoms via the strong nuclear force. They can be scattered (change in momentum and/or energy) as they travel in close proximity to an atomic nucleus. Different isotopes (nuclei with varying numbers of protons and neutrons) have different interaction strengths with passing neutrons. The likelihood that an isotopic nucleus will scatter a neutron is given by the scattering cross section in units of *barns*. 1 barn = 100 fm^2. An isotope with a large scattering cross section will have a stronger

interaction with a passing neutron than an isotope with a small scattering cross section [3].

In addition to being scattered by a nucleus, neutrons can also be absorbed by a nucleus. The probability of a nucleus absorbing a neutron is given by the absorption cross section and it is also measured in barns. After absorbing a neutron, the absorbing nucleus may: 1. be transformed into another isotope with one additional neutron; 2. it may enter an energized state and promptly decay back to its ground energy state giving off a high energy gamma photon (known as a prompt gamma); or 3. the nucleus may become unstable and fission into smaller fragments releasing a large amount of energy in the process.

The likelihood of a neutron interacting with a nucleus is also a function of the amount of time the neutron spends in close proximity to the nucleus. The time spent near a nucleus is inversely proportionally to the velocity of the interacting neutron. So, the neutron scattering cross section is inversely proportional to neutron velocity. This is known as the "1/*v* rule". There are also energy resonances of specific isotopes with a neutron moving at a specific speed/energy, but these will not be discussed in detail and they do not play a role in "slow" neutron scattering applications [4].

2.2. Slow Neutrons vs. Fast Neutrons

It is helpful to understand the difference between "slow" neutrons and "fast" neutrons. "Slow" is a relative term referring to neutrons which have been moderated down to room temperature or even cryogenic temperatures. In contrast, "Fast" or "Hot"

neutrons are neutrons which are ejected during a nuclear reaction, and these particles may even be moving at relativistic speeds and mega-electronvolt (MeV) energies. Fast neutrons can be scattered by any material, but most commonly by hydrogen and hydrogen containing water, waxes, and plastics. Graphite is sometimes used as a moderator also [5], [6]. As neutrons scatter inside of a moderator such as water, the fast neutrons transfer their kinetic energy to the moderator via the scattering mechanism until they are in thermal equilibrium with the moderator or until they exit the moderator material. “Thermal” neutrons have been moderated to room temperature (293ºK) where their velocity is ~2200 meters per second and their kinetic energy is 25.3 milli-electronvolts. “Cold” neutrons are moderated to cryogenic temperatures and have energies less than 10 meV. There is a class of neutron detectors which have been developed to measure the energy (and sometimes direction) of high energy “fast” neutrons directly from scattering interactions via the proton recoil ionization mechanism [7], but the focus of this work is on slow neutron detectors which use the neutron absorption mechanism rather than the neutron scattering mechanism.

2.3. Slow Neutron Detection

Detecting a thermal or cold neutron is a simple two-step process.

Step 1: Absorb the neutron (creates a nuclear fission)

Step 2: Use the nuclear fission to generate a signal

As mentioned earlier, the probability of neutron absorption by a nucleus is inversely proportional to the velocity of the neutron and directly proportional to the amount of time the neutron spends in close proximity to an absorbing nucleus. *Figure 3* shows that the neutron absorption cross section of select isotopes dramatically increases with decreasing neutron energy.

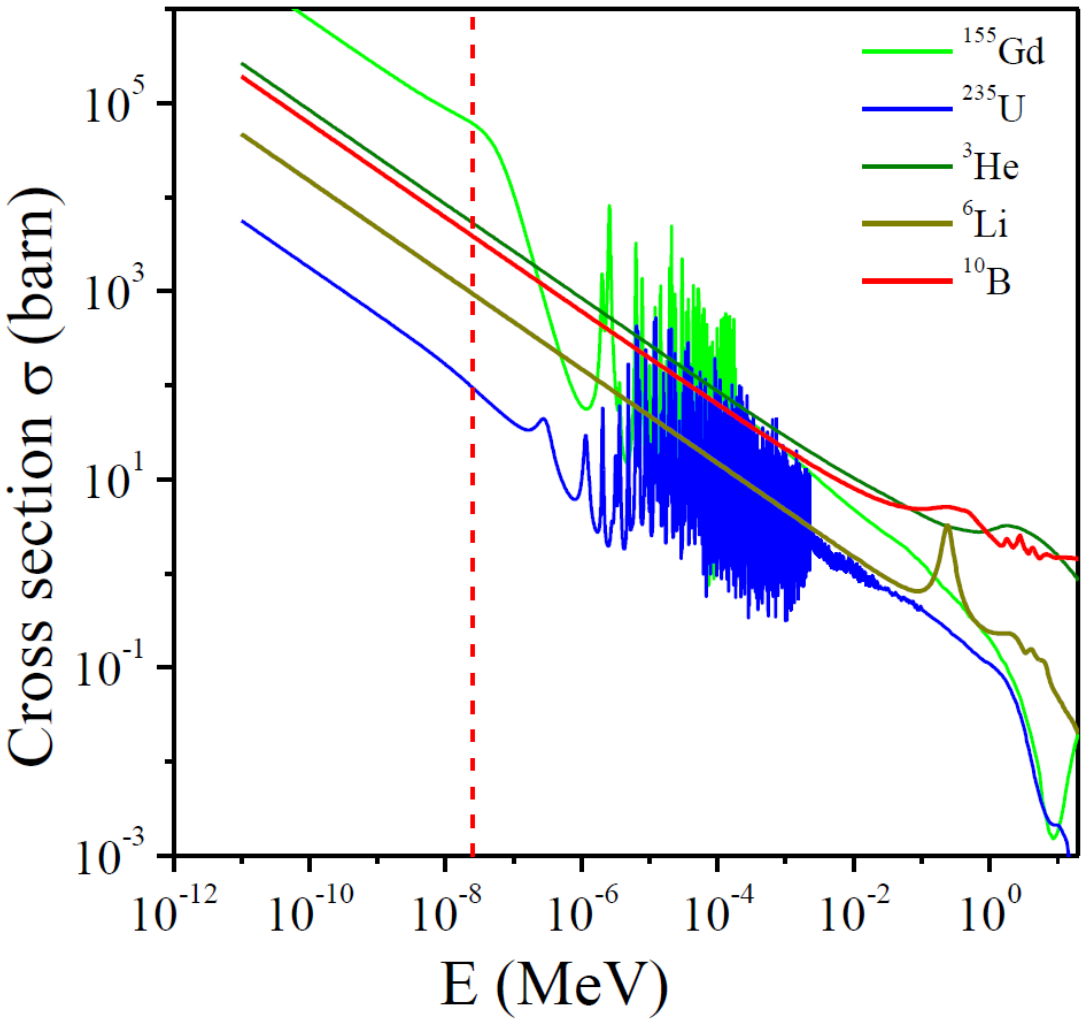

Figure 3: Neutron cross section as a function of neutron energy **[8]** *. The vertical dashed line (red) is placed at 25meV, or thermal neutron energy.*

There are many isotopes with large thermal neutron absorption cross sections. But, only a subset of these isotopes is useful for neutron detection. As mentioned earlier, after absorbing a neutron, a nucleus will enter a high energy state. Usually the energized nucleus will promptly decay to ground state and emit a gamma ray (high energy photon) in the process. However, this is not so helpful, because gamma rays do not deposit much energy in the immediate vicinity of the neutron capture. Gamma rays pass through most materials much like an X-ray passes through soft tissue in a medical scan. A good detection isotope undergoes nuclear fission after absorbing a neutron, rather than prompt gamma decay. The energy from these fissions is released as high energy ions (alphas, betas, less massive nuclei). These high energy ions will cause a powerful disturbance in the immediate vicinity via electric force (negatively charged electrons / positively charged nuclei) interactions, depositing their energy within several micrometers up to tens of micrometers from the capture site. Prevalent isotopes for neutron detection include Helium-3, Lithium-6, Boron-10, Gadolinium-157, and Uranium-235. Here are reaction equations for selected isotopes. Basic nuclear chemistry is described in [9] , and "Q" is the amount of released energy from the nuclear reaction.

Helium-3:

$$ {}^{3}_{2}He + {}^{1}_{0}n \rightarrow {}^{3}_{1}H + {}^{1}_{1}p + Q \tag{2.1} $$

$$ Q = 0.765\ MeV $$

Lithium-6:

$$ {}^{6}_{3}Li + {}^{1}_{0}n \rightarrow {}^{3}_{1}H + {}^{4}_{2}\alpha + Q \tag{2.2} $$

$$ Q = 4.78\ MeV $$

Boron-10:

$$ {}^{10}_{5}B + {}^{1}_{0}n \rightarrow \begin{cases} {}^{7}_{3}Li + {}^{4}_{2}\alpha + Q, & excited\ state\ \ Q = 2.310\ MeV\ \ (94\%) \\ {}^{7}_{3}Li + {}^{4}_{2}\alpha + Q, & ground\ state\ \ Q = 2.792\ MeV\ \ (6\%) \end{cases} \quad (2.3) $$

Uranium-235:

$$ {}^{235}_{92}U + {}^{1}_{0}n \rightarrow [{}^{236}_{92}U] \xrightarrow{85\%} {}^{139}_{56}Ba + {}^{94}_{36}Kr + 3\,{}^{1}_{0}n + Q \quad (2.4) $$

$$ Q = 202.5\ MeV $$

Q-value is how much energy is released in the fission reaction. A higher Q-value reaction will release more energy in the form of fast moving ions. Neutron detectors use a variety of methods to convert these high Q ions into an electrical signal for readout. In general, higher Q means a larger, more robust readout signal and improved signal-to-noise ratio for electronics, which makes it easier to identify a particular fission event.

Summarizing, slow neutron detectors use nuclear fission initiated by neutron capture to create high energy ions. The energy in these ions is converted into an electrical signal for identifying the neutron capture event. The probability of capturing a passing neutron is a function of the neutron absorption cross-section (larger cross sections are more likely to absorb, measured in barn) and the density of capture atoms in a volume of space. Higher Q fission reactions produce larger electrical signals which make identifying the neutron capture event easier. *Table 1* summarizes the important physical properties of 5 commonly used fission reactions which produce high Q ion products, as opposed to gamma radiation which is difficult to extract an electrical signal from. These are not the

only isotopes that readily absorb neutrons, but these are some of the isotopes that create ion radiation from those interactions!

Table 1: Useful properties of fission isotopes [3], [8], [10]

Isotope Reaction	Cross section @ 25.3 meV (barn)	Q-value	Abundance in Nature (%)
^{3}He	5316	0.77 MeV	0.01
^{6}Li	938.5	4.78 MeV	7.60
^{10}B	3842.6	2.31MeV (94%), 2.79 MeV (6%)	19.90
^{157}Gd	255000.0	0.072 MeV (39%)	15.70
^{235}U	584.3	202.5 MeV	0.75
^{239}Pu	750.0	211.5 MeV	0.00

Of the six tabulated isotopes, both Helium-3 and Plutonium-239 are not readily found in nature but are derived from manmade processes.

The physical mechanisms for extracting electrical signals from the high Q-value ions varies depending on the style of detector. Several types of detectors: ion chambers, scintillators, and solid-state devices will be discussed in the next sections.

2.4. Ionization Chambers

An ionization chamber is a sealed volume filled usually with a noble gas. The volume is surrounded by two electrodes as shown in *Figure 4*.

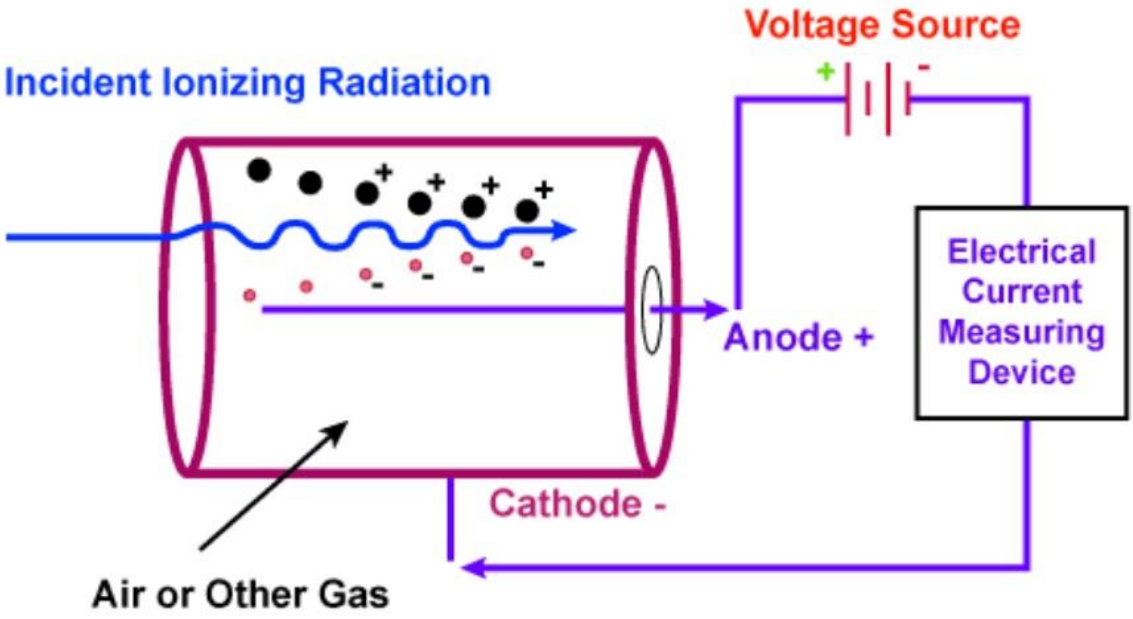

Figure 4: Diagram of an ionization chamber **[11]**

A high energy particle travels through the ionization chamber ionizing the fill gas along its path. Freed electrons drift toward the center anode. Heavy positive ions travel toward the cathode. This results in a charge pulse that is read by electronics. The number of ion pairs created by the fission particles depends on the "W-value" of the gas and the energy deposited by the fission products. The W-value is the average energy dissipated in a gas per ion-pair and it is always greater than the gas's ionization energy. Some common gases and their W-values are listed in *Table* 2 [12].

Table 2: energy dissipation per ion pair **[12]**

W-value in eV / Ion Pair

Gas	Fast Electrons (betas)	Alphas
Ar	27.00	25.90
He	32.50	31.70
H_2	38.00	37.00
N_2	35.80	36.00
Air	35.00	35.20
O_2	32.20	32.20
CH_4	30.20	29.00

For rough estimates, a 1 MeV particle dissipating all of its energy in the fill gas will create 30000 ion pairs. The number of ion pairs generated is proportional to the particle energy.

The voltage applied to the electrodes is also important, affecting how the device behaves. There are four regions of behavior: recombination region, ionization chamber region, proportional region, and Geiger-Mueller region.

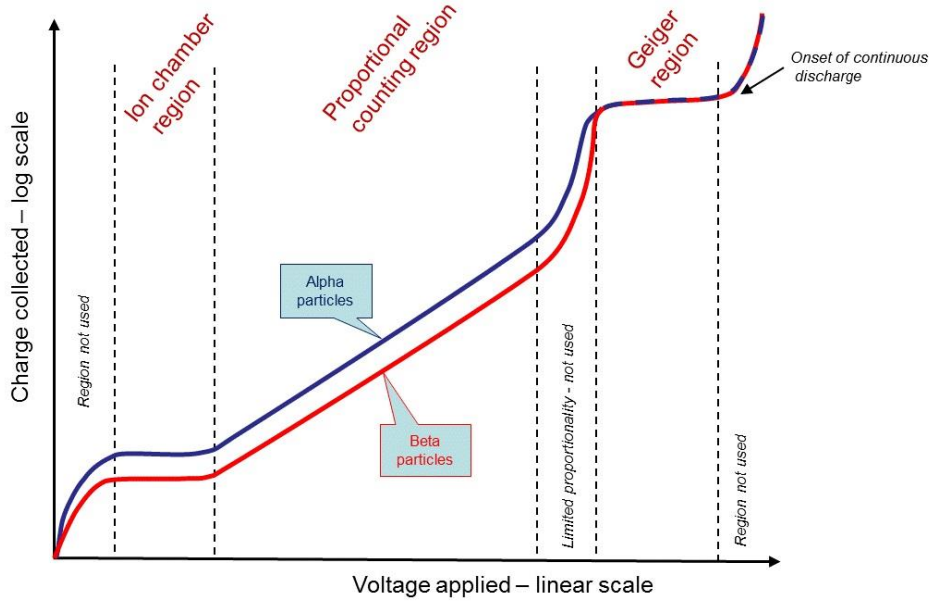

Figure 5: Practical Gaseous Ionization Detection Regions **[13]**

The *recombination region* is found at the lowest applied voltage. In this region, the electric field between the anode and cathode is so small that the positive and negative ions will recombine before reaching the electrodes.

In the *ionization chamber region*, almost all the ions produced by the high-Q particle reach the collection electrodes, and the readout charge is roughly equal to the charge produced.

The *proportional counting region* is used most often for slow neutron detectors. In this region, the electric field between the anode and cathode will accelerate the ionized electrons to a high speed. The electrons reach a high enough energy near the anode to create additional ion pairs. Essentially, each electron creates an "avalanche" that has a charge multiplication effect. Charge multiplication factors are on the order of 100 to 10000. The avalanches are self-terminating, as the local electric field is reduced by positive ions created during said avalanche. The output pulse magnitude is proportional to the initial number of ion pairs created. But, the charge is multiplied by a factor which depends on the chamber geometry, the properties of the fill gas, and the applied voltage. This means that proportional counters can be used for radiation energy spectroscopy, and charge multiplication enhances signal-to-noise ratio in electronic readouts [12].

The *Geiger-Mueller* region is the region using the highest applied voltage before continuous discharge between the electrodes begins. In this region, avalanches spread across the entire length the anode wire, due to UV light emitted near the primary avalanche from excited molecules. The UV photons create additional ion pairs throughout the volume of the chamber, and these ions in turn cause secondary avalanches. An illustration of this concept is shown in *Figure 6*.

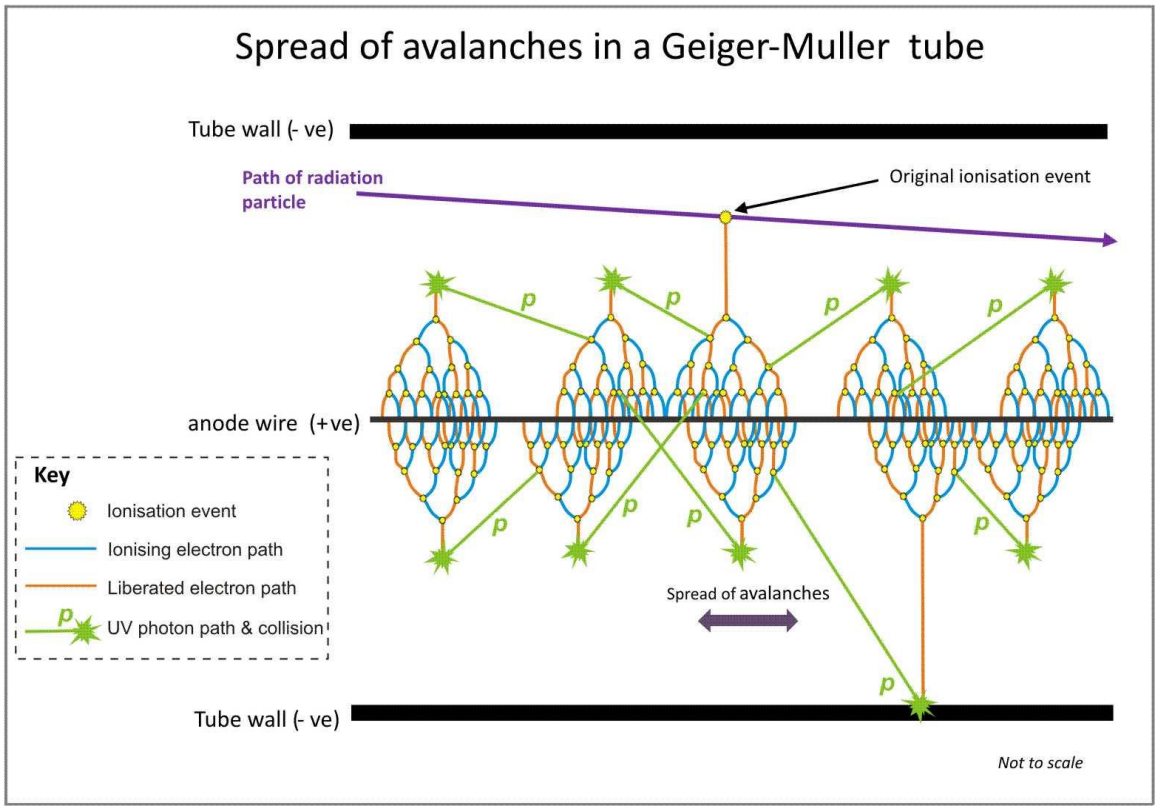

Figure 6: Spread of Avalanches in a Geiger-Mueller Tube **[14]**

2.4.1. BF_3 Tubes

For slow neutron detection, it is common to use an ionization chamber filled with a neutron-absorbing gas for neutron absorbtion, ionization, and charge multiplication all-in-one. Boron-Triflouride is one of the earliest gases to be used in this way. The first reference to a BF_3 gas filled ionization chamber was in 1939 [15]. Although this detector did not use enriched ^{10}B, natural boron is routinely enriched to >96% ^{10}B for neutron detection. Boron-Triflouride proportional counters were at one time widely used for neutron detection, but they have some important limitations and they were superseded by Helium-3 gas filled detectors once stockpiles of manmade Helium-3 were available.

BF_3 gas is not ideal for proportional counting. BF_3 is an electronegative molecule, which has a number of implications. Pulse amplitudes vary with the distance between the absorption site and the anode wire. BF_3 gas strongly quenches charge avalanches, and so the gas cannot be used at concentrations/pressures greater than 200 kPa which limits maximum neutron absorption. For the same reason, the anode voltage in BF_3 gas detectors must be very high to create avalanches with the desired charge multiplication. The performance of BF_3 gas is degraded greatly by impurities in the production process and a large variety of build materials readily react with fluorine including glass and sealing grease. Lastly, BF_3 gas is highly toxic and safety requirements include expensive airflow systems and monitoring in a laboratory environment [16], [17].

2.4.2. Helium-3 Tubes

Helium-3 gas filled detectors are the most widely used slow neutron detectors today, and for good reason. Helium-3 gas detectors are relatively simple to manufacture, and Helium-3 gas has very desirable physical properties for neutron detector systems.

^{3}He has a large thermal neutron cross section, 5316 barns (*Table 1*). This is about 35% higher than the Boron-10 cross section. Helium-3 is a noble gas, so it is safe to work with (no chemical hazards) and it is not corrosive or toxic like boron tri-fluoride. Helium-3 also remains proportional at high fill pressure (1500kPa) as opposed to a 200kPa limitation with Boron Trifluoride [16]. This means that pressurized Helium-3 proportional counters can be made far more absorbing than Boron Trifluoride.

One drawback of Helium-3 gas is the relatively low Q-value of the fission reaction. Helium-3 fission following neutron capture only releases 0.77MeV of energy,

which is several times less than other neutron capture isotopes. This makes discriminating neutron fission from ionization events caused by other radiation sources (such as gamma radiation) more challenging [18]. A second drawback of Helium-3 is its low electron density. Helium is a light gas, with only two electrons. Therefore, the ionization path of the proton and triton fission products is rather long. There simply is not enough charged material in the path of these high energy particles to bring them to a stop within a short distance. To reduce fission product path lengths, quench UV emissions, and avoid electrical breakdown of the fill gas, secondary gases are added to the Helium-3 gas. These gases often include propane (C_3H_8), isobutane (iC_4H_{10}), and others [19], [20]. The addition of secondary fill gases in helium-3 tubes increases the scattering-to-absorption cross section ratio of these types of detectors. Even so, Helium-3 gas filled detectors remain the gold standard for slow neutron detection.

2.5. Helium-3 Shortage

Helium-3 has been used for its unique physical properties in a variety of applications including radiation portal monitors (RPMs) for port and border security of special nuclear material, magnetic cryogenics, low temperature physics, lasers, quantum computing, oil and gas well logging, gyroscopes, magnetically polarized He3 for magnetic resonance imaging (MRI), and neutron scattering science for characterizing the molecular structure of materials [8], [21].

Dwindling stockpiles of tritium (a isotope of hydrogen containing one proton and two neutrons) decay into Helium-3 via the beta decay process, where one of the neutrons in the tritium nucleus decays into a proton and an electron. The electron is ejected from

the tritium nucleus releasing 14keV of energy. Tritium decays into Helium-3 with a half-life of 12.3 years [22], [23]. Stockpiles of both tritium and helium-3 remain in the United States and Russia, the result of nuclear weapons programs. Nuclear non-proliferation and reduction policies have restricted new production of tritium, which in turn restricts future supplies of helium-3 gas. From a high of 235,000 liter-atmospheres in 2001, the helium-3 stockpile was depleted to just 50,000 liter-atmospheres by 2010, most of which went to Radiation Portal Monitor (RPM) installations for border and port security.

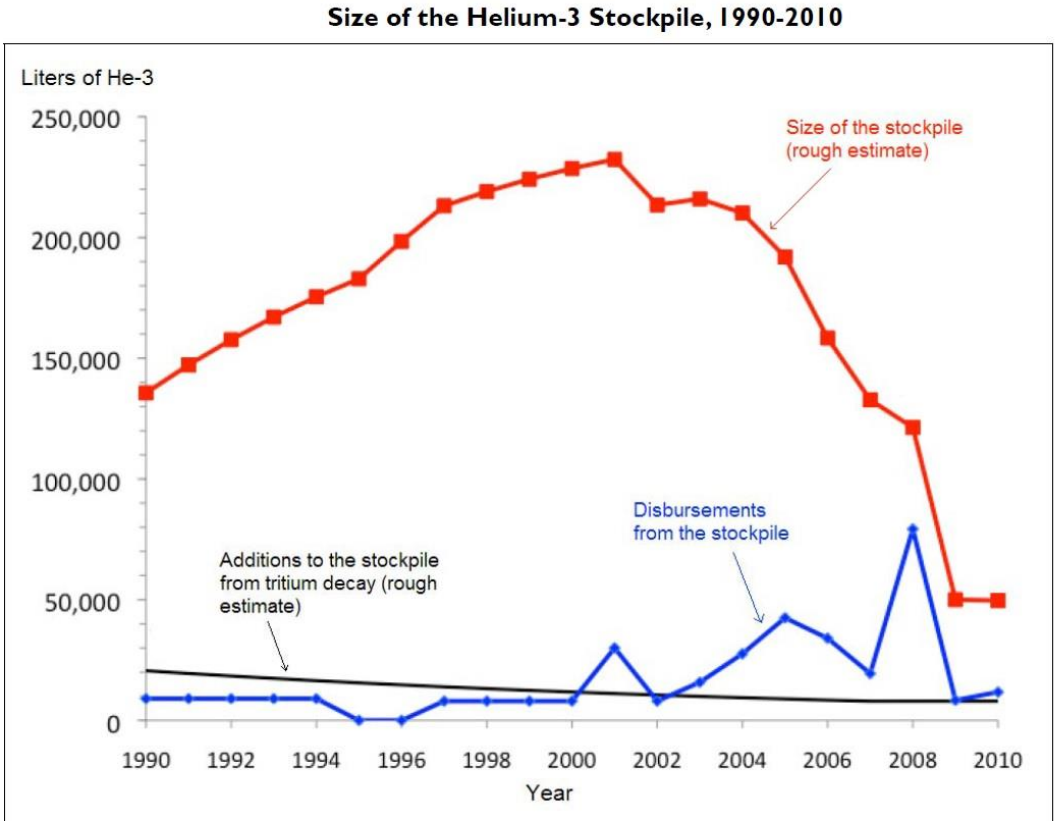

Figure 7 **[24]**.

Figure 7 charts the pace of the U.S. helium-3 stockpile depletion from 1990 until 2010 [24]. In response to the helium-3 shortage, the U.S. government began a rationing program and the price of helium-3 gas rose as high as 3000€ per liter-atmosphere [22],

[24], [25]. The cost of producing new tritium is roughly $15,000 USD per liter-atm [24]. All industries which rely on helium-3 gas have been scrambling to reduce their usage, and if possible, to find alternatives. The neutron scattering community, which historically has used thousands of liters of helium-3 in a single instrument suite has been developing alternative technologies which use lithium-6 and boron-10 absorption isotopes. These efforts have been ongoing over the last decade, and large-area neutron detection systems are beginning to be proven. The next sections discuss helium-3 replacement technologies for thermal and cold neutron detection.

2.6. Ionization/Fission Chambers with Neutron Absorbing Surfaces

Up until this point, ionization chambers with a neutron absorbing fill gas have been discussed. However, ionization chambers are also used with neutron absorbing thin films deposited onto the inner walls of the cathode or using thin films and foils within the interior of the gas filled volume. Boron-10 containing thin films have been explored extensively, and several neutron scattering facilities have pursued this technology for helium-3 replacement [26]–[29]. The primary drawback of this technology is that boron-10 fission products do not travel very far in the solid thin-film material, only about 3μm - 5μm. To recover a usable signal from the fission products, the films must be kept very thin, only about 1μm thick. This means that the total number of boron-10 atoms for neutron absorption is relatively low, and therefore to obtain satisfactory absorption from the entire system, as many as 34 thin film layers must be used. This results in a large, cumbersome, and complicated system overall. The other drawback is that the fission

products spread out isotropically from the neutron capture site. Generally, only one of the two fission products (lithium nucleus and alpha particle) travels through the proportional counting gas while the other wastes its energy in the thin film substrate. This means that less than half of the fission energy is recovered for a usable signal.

2.7. Scintillation Detectors

Ionization chambers operated in the proportional counting region are one of the two primary neutron detector technologies in widespread use. The other class of radiation detectors preeminent in neutron detection are called “scintillation detectors”, and there are many kinds. Organic scintillators (crystallized, liquid, and plastic) and inorganic scintillators (halide crystal, elpasolite crystal, and glass) are the main subclasses of scintillators [12]. The overall concept of a scintillation detector is shown in *Figure 8*.

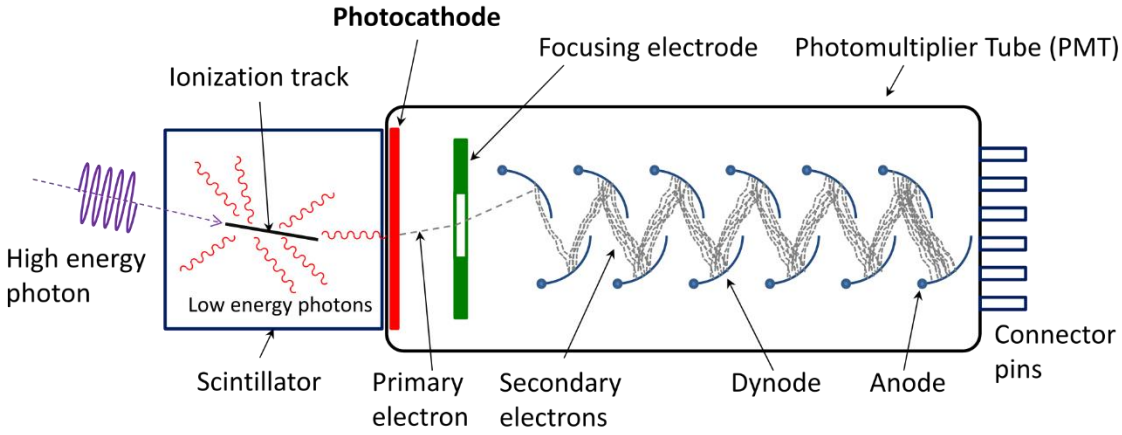

Figure 8: Concept of a scintillation detector **[30]**

In this conceptual drawing, a high energy photon enters the scintillator material on the left. In response, the scintillator becomes energized via electromagnetic

interactions. Subsequently, the energized medium emits low energy photons (often in the visible blue light spectrum). The photons are emitted isotropically along the flight path of the high energy radiation. Some of the photons will make their way to a photomultiplier where the faint optical signal is amplified into a much larger charge signal for readout electronics. Typical photomultiplier gains are on the order of 10^6 electrons per photon.

2.7.1. Scintillation Fundamentals

The physical processes for scintillation light emission include fluorescence, phosphorescence, and sometimes delayed fluorescence. Florescence is the prompt emission of visible light from a material following its excitation (by radiation). Phosphorescence is the emission of a longer wavelength photon with a longer excitation decay time. *Organic* scintillators fluoresce from transitions in the energy level structure of a single molecule (*Figure 9*). In a parallel fashion, most *inorganic* crystal scintillators fluoresce from activator sites created from dopant atoms that disrupt the energy band structure of the crystal (*Figure 10*). A high energy particle will excite many activation sites resulting in tens of thousands of photon emissions, similar to the number of ion pairs generated in an ion chamber.

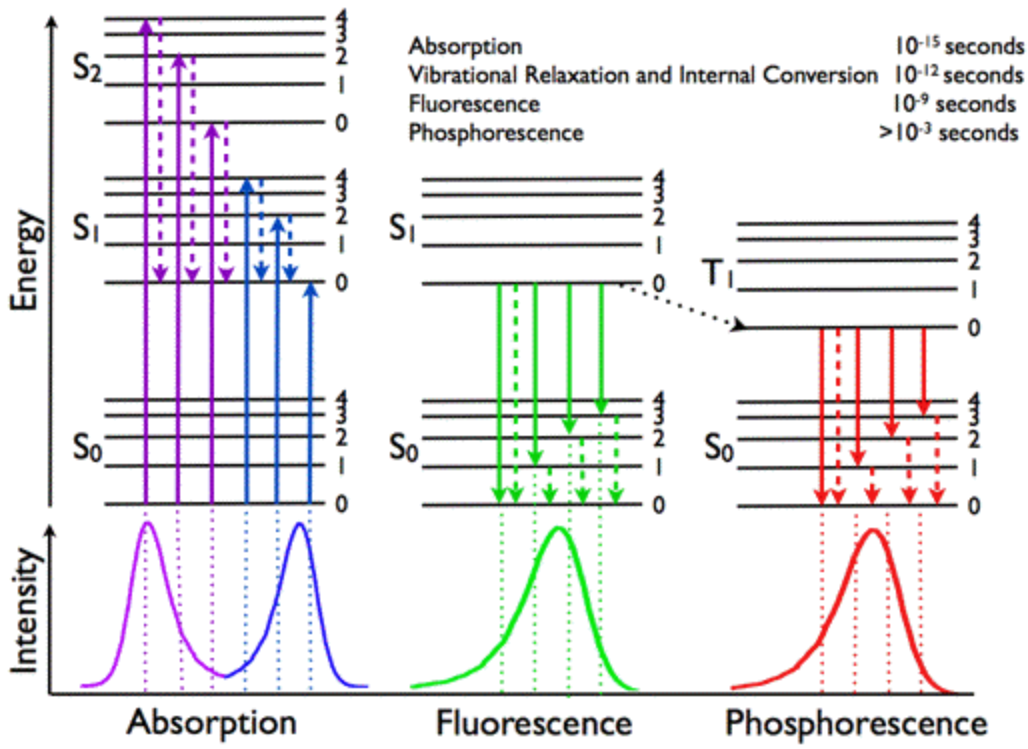

Figure 9: Jablonski Diagram **[31]**

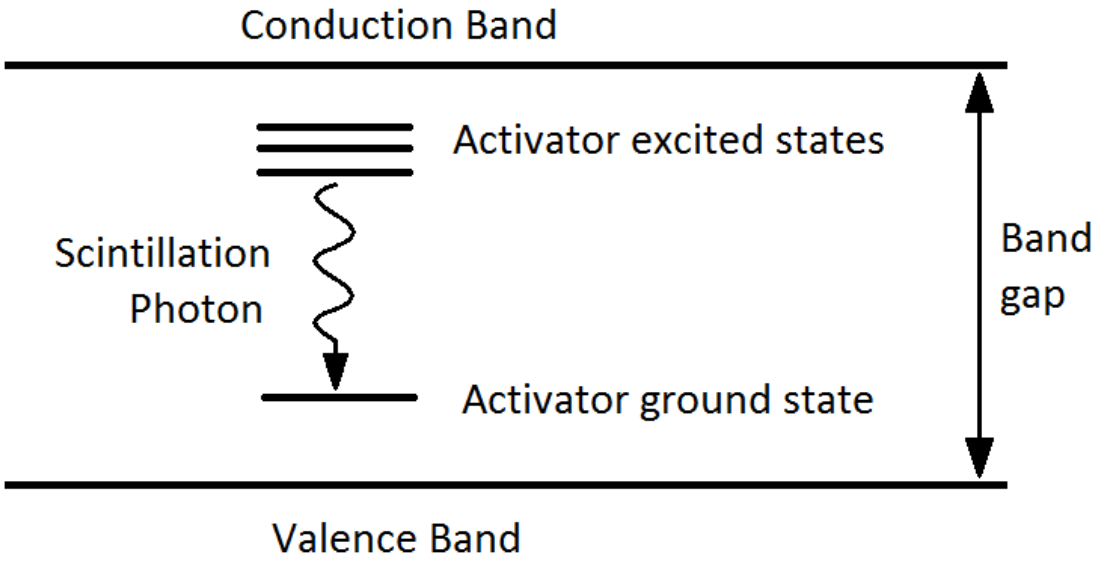

Figure 10: Crystal Scintillator Mechanism

An ideal scintillator material possesses the following properties:

1. It converts the kinetic energy of high energy particles into detectable light with a high scintillation efficiency.
2. The conversion should be linear… the light yield should be proportional to the deposited energy.
3. The medium should be transparent to the wavelength of its own emission for good light transport… minimal self-absorption.
4. The decay time of the induced luminescence should be short so that a high count rate can be achieved.
5. The optical index of refraction should match that of the photodetector for good optical transmission. Most glass/silicate windows have an index of 1.5 [32].

Sodium Iodide doped with 10^{-3} mole fraction of Thallium, NaI(Tl), is the most widely used scintillator material since its discovery in 1948 [32], [33]. NaI(Tl) yields 38000 photons per MeV of energy deposition by beta radiation (high energy electrons) and gamma radiation (high energy photons). Its emission photopeak is at 415nm (in the blue spectrum), it has a refractive index of 1.85, and a scintillation decay time of 230ns. Like most inorganic scintillator crystals, sodium iodide is hygroscopic, meaning that it absorbs moisture. Most crystal scintillators must be hermetically sealed to prevent their degradation from water absorption. NaI(Tl) is often the standard to which other scintillator materials are compared. A comprehensive list of scintillator materials and

their properties can be found online at http://scintillator.lbl.gov/ [34]. NaI(Tl) does not readily absorb neutrons.

2.7.2. Pulse Height Spectrum

Before moving on to neutron detecting scintillators, there are two more concepts that are important for gauging the performance of scintillator materials. The first concept is the Pulse Height Spectrum. It was mentioned before that good scintillator materials have linear energy conversion; the number of photons generated is proportional to the energy deposited. Since radioactive isotopes undergo radioactive decay in a characteristic fashion, the energy and type of radiation released is signature of that specific isotope. For instance, when undergoing beta decay, ^{137}Cs emits a gamma photon with an energy of 662keV. When analyzing this radiation, readout electronics measure the signal strength for each event. A large number of events are histogramed by their pulse height. This is called a pulse height spectrum (*Figure 11*).

The most prominent peak in this pulse height spectrum corresponds to the 662keV emission peak of ^{137}Cs. Lower energy features are also labeled. A good scintillator has a very good energy resolution, and energy peaks have a crisp FWHM (full width half maximum) so that many features can be discerned. A good energy resolution for a scintillator detector displays features with FWHM less than 4%.

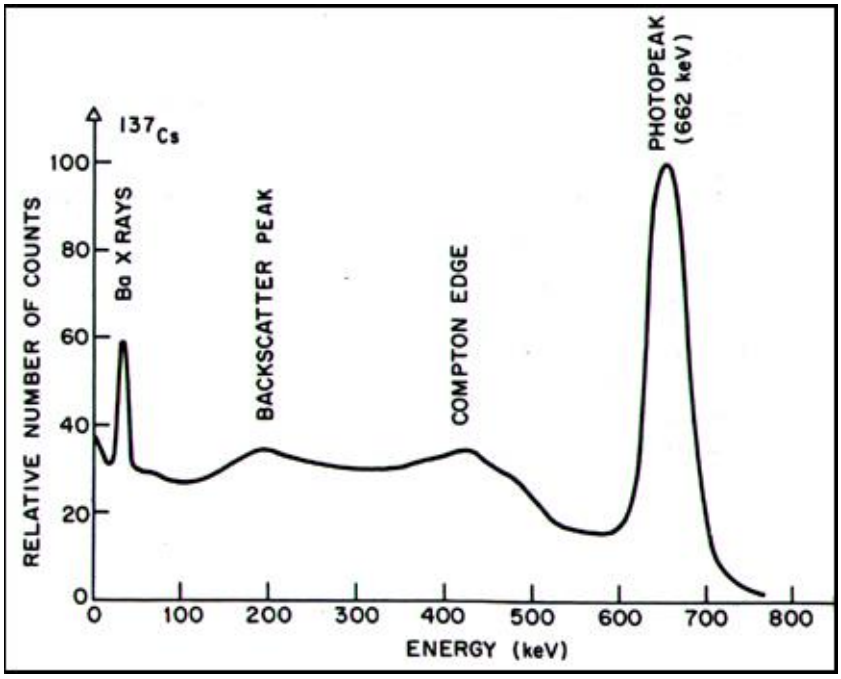

Figure 11: ^{137}Cs pulse height spectrum **[35]**

2.7.3. Pulse Shape Discrimination

Some inorganic crystal scintillators respond differently to different classes of radiation. Gamma radiation, beta radiation (electrons), and alpha radiation (helium-4 nucleus) deposit energy in some scintillators with different efficiency, and the electronic structure of the scintillator relaxes to ground state with different decay times. It has been observed that there are two relaxation decay times for fluorescence transitions in some scintillator materials. Many excited electrons return to ground state in a relatively short period of time (10ns – 200ns). However, for heavy charged particles which deposit their energy within a very short distance, there is a pronounced and much slower decay component. The slow decay component can last from several hundred nanoseconds, to tens of microseconds depending on the material. The slow component of fluorescence

decay appears to depend on dE/dx, or the spatial concentration of energy deposition by the high energy particle [32], [36]. The slower relaxation may be due to a high density of excited electrons, but a limited number of relaxation pathways through which to decay to ground state. Regardless of the physical processes the behavior is apparent, and the decay profile of a scintillation signal can be used to infer the type of radiation… gamma ray, electron, or heavy charged particle [36]–[39].

Scintillators have been doped with lithium-6 and sometimes boron-10 for slow neutron absorption. Because the fission products of a neutron absorption event are heavy charged particles, the resulting scintillation signals have significant slow decay components, and they can be distinguished from gamma signals [40]–[42]. There are a number of signal processing techniques which have been used for discriminating between radiation types. These will be discussed in-depth at a later point.

2.8. Solid State Neutron Detectors

Aside from ionization chambers and scintillators, there are a variety of solid state neutron detectors. Because of their limited size, they are not used for large area detector suites. But, they have found uses in high resolution neutron imaging of small objects.

Crystalline silicon diodes doped with neutron absorbers have been devised in many varieties. These types of diode detectors are operated in reverse bias. The depletion region, which has no free charge carriers, is doped with neutron absorber atoms. Alternatively, thin film neutron absorbing layers can be deposited onto the diode such that fission products can reach the depletion region. After a neutron absorption event, fission products produce a large number of electron-hole pairs in the depletion region.

These charge carriers are swept to the anode and cathode of the diode to provide an electrical signal for readout. There is no charge multiplication like there is in photomultiplier tubes and proportional counters, but there is very little noise, so the signal-to-noise ratio is acceptable [43]–[46]. Other semiconductor materials such as hexagonal boron-nitride [47], have been used as well as silicon. the basic concept is similar. A new lithiated semiconductor material, $6LiInP_2Se_6$, has been discovered recently and shows potential as an effective material for neutron detection [48].

Microchannel plates (MCPs) are a completely different concept for solid state detectors. MCPs are comprised of an array of tiny holes etched into a processed glass wafer. Electrodes are attached to the faces of the highly resistive glass wafer to produce an electric field in the cylindrical microchannels from end-to-end. Individual microchannels have a diameter of approximately 10µm. When an operating voltage is applied to the electrode faces, each microchannel becomes a continuous dynode, which amplifies charge like a photomultiplier tube. Amplification factors vary from $10^4 – 10^7$.

MCPs are used to detect high energy photons and charged particles at a high spatial resolution (15µm - 50µm) and time resolution (~100ns) [49]. They are used in mass spectrometers, astronomy, night vision goggles, and nuclear science (*Figure 12*).

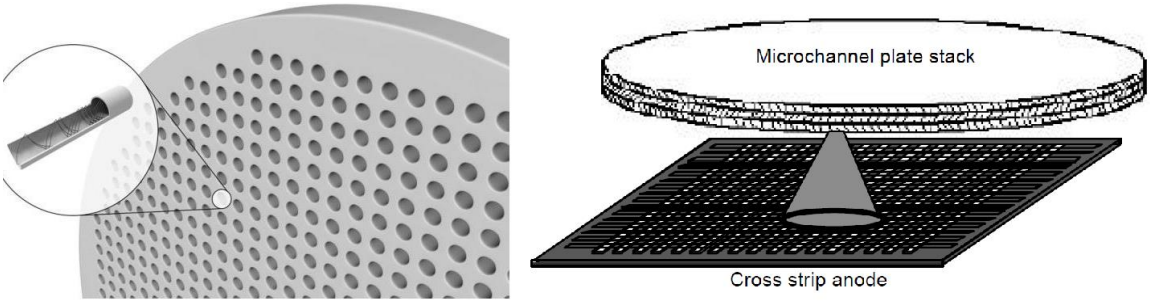

Figure 12: Illustrations of microchannel plate (MCP) concept **[50], [51]**

Microchannel plates are the result of a very complex glass drawing process. “Billets” of etchable glass rods with non-etchable leaded glass cladding are heated and drawn to a 0.8mm diameter. The drawn rods are cut, and thousands of these rods are stacked into a hexagonal rod. They are heated and drawn again. The drawn hexagonal rods are then cut, restacked together, and fused into a boule. The boule is cut into wafers, etched, and the wafers are heated in a hydrogen atmosphere to chemically reduce the exposed microchannel surfaces. Finally, electrodes are deposited on the MCP faces (*Figure 13*) [52].

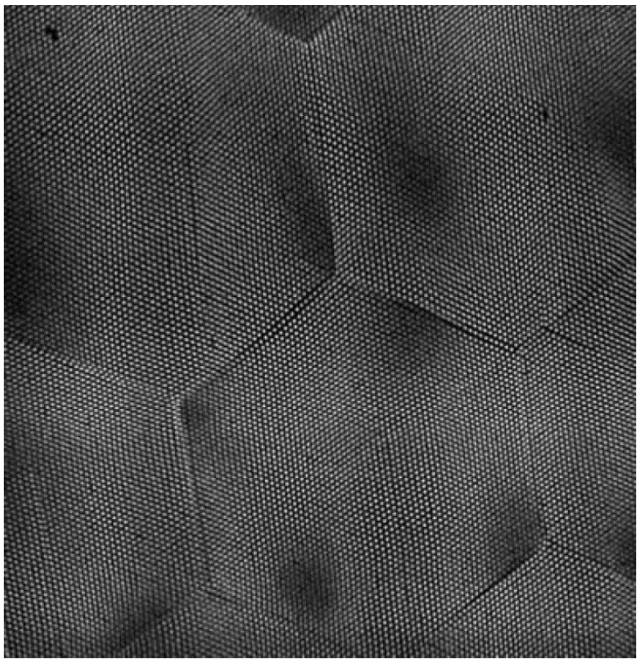

Figure 13: 2mm x 2mm image of a microchannel plate **[50]**.

Microchannel plates doped with ^{6}Li or ^{10}B show high neutron absorption, high spatial resolution, and high count rate ability [53]–[56]. Their drawbacks are inferior gamma rejection and high complexity/cost per unit area.

2.9. Detector Requirements for Neutron Scattering

The field of neutron scattering science has unique requirements for neutron detectors. Neutron reflectometry and diffractometry are frequently used techniques for studying materials at molecular length scales. Performing neutron experiments quickly and with high precision is a real challenge. First off, neutron sources are very, very weak compared to light sources used in photograph. A 100-Watt light bulb radiates between 10^{19} - 10^{20} photons per second. Flash bulbs used in photography radiate light at a much higher intensity for brief moments to enable crisp pictures at fast shutter speeds. In comparison, a neutron beam tube may only illuminate the sample position of a neutron reflectometer with 10^{7} - 10^{8} neutrons per second [57]. Neutron experiments are conducted with exceedingly dim sources. The exposure time for developing a reflectomogram can be hours or days. If experiment conditions change within the exposure time period, the resulting data will not be reliable. High neutron detection efficiency is very important for reducing the time it takes to conduct neutron scattering measurements. If detection efficiency is halved, then exposure time must double to obtain the same fidelity.

Signal-to-noise ratio is also very important. The dynamic range needed for reflectometry experiments is up to eight orders of magnitude [58]. *Figure 14* shows data from one neutron reflectometry experiment with very faint features that are eight orders of magnitude smaller than the incident neutron flux on sample.

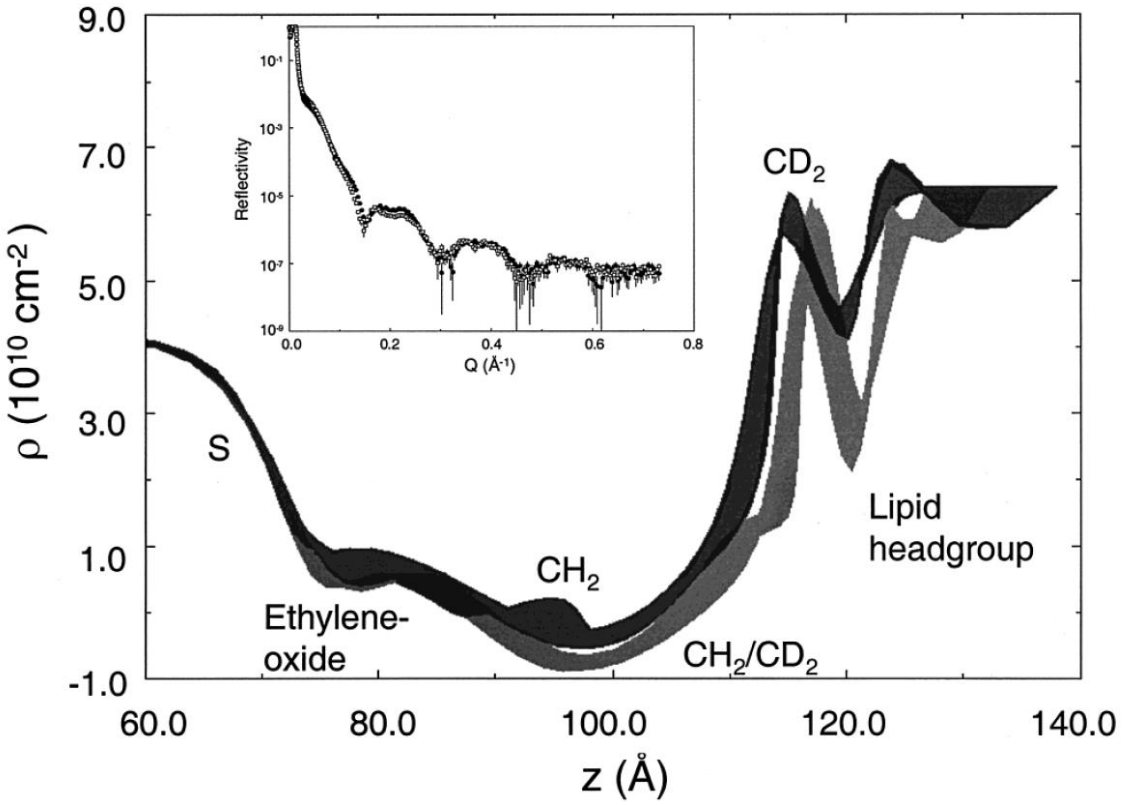

Figure 14: Thin film reflectometry data and its Fourier transform reveals scattering length density, which can be interpreted for chemical structures. The inlayed raw reflectometry data shows features with 10^{-8} dynamic range [35].

Background radiation can obscure faint features that have low counting statistics to begin with. Neutron cross-scattering must be kept to a minimum, i.e. only neutrons originating from the sample under test should have access to the detector suite. This is accomplished using heavy collimation, shielding, and detectors with a very low neutron scattering cross section to minimize neutron backscattering. Also, gamma radiation must never be counted as a neutron. Neutron scattering facilities inherently are mixed radiation environments with both neutron and gamma radiation present. The sensitivity of neutron detectors to gamma radiation must be less than one detection per 10^7 incident gamma photons.

Finally, a neutron detector must have durable construction and operation. The service life of a neutron detector is more than 15-years. During its operating life, a detector will be exposed to chronic low-level radiation as well as brief periods of high intensity neutron radiation which can cause acute failure of some detector systems. There have been cases at the NIST Center for Neutron Research when Helium-3 position sensitive detectors have been damaged/rendered unusable from high intensity radiation as well as from high voltage arcing between anode and cathode. Damage in Helium-3 ionization chamber variants usually results from degradation of the anode wire(s). A successful neutron detector should meet or even exceed the durability of ^{3}He systems.

2.10. Neutron Detector Technology Comparison

Table 3 is a compilation of neutron detector technologies. For detector technologies presented in this chart, the overall detector efficiency is closely related to neutron absorption. For the purposes of neutron scattering science, neutron absorption (detector efficiency) and low gamma sensitivity are the most important aspects. Signal decay time is a third aspect of importance as this will define the maximum count rate of the detector. Short signal decay time translates to a high potential count rate. Table entries which are highlighted in **bold print** have excellent performance in their category compared to other technologies.

Table 3: Neutron Detector Comparison Chart

Neutron Detector Comparison Chart

Detector Technology	Thermal Neutron Absorption (1.47 Å)	Cold Neutron Absorption (5 Å)	Absorber Layer Thickness	Q-Value	Signal Yield per neutron	Amplification Mechanism	Neutron/ Gamma Discrimination
Ion Chamber							
Helium-3 Tube	**68% (25mm)**	**98% (25mm)**	7mm - 25mm	0.77 MeV	~23k ion pairs	charge avalanche	Pulse Height
Helium-3 cross-wire array	38%	80%	7mm - 25mm	0.77 MeV	~23k ion pairs	charge avalanche	Pulse Height
Fission Chamber	0.1% - 1.0%	0.4% - 4.0%	1µm - 5µm	**~200 MeV**	**~5M ion pairs**	charge avalanche	Pulse Height
Boron Trifluoride	15%	42%	20mm	2.31 MeV	~70k ion pairs	charge avalanche	Pulse Height
Boron-lined Multigrid (34-layer)	30%	70%	1µm	2.31 MeV	~70k ion pairs	charge avalanche	Pulse Height
Boron thin-film GEM Detectors (6-layer)	21%	45%	0.8µm - 1.5µm	2.31 MeV	~70k ion pairs	charge avalanche	Pulse Height
Inorganic Scintillator							
6LiF:ZnS w/ WLS (NCNR)	**65%**	**97%**	400µm	4.78 MeV	~160k photons	photomultiplier	**Pulse Shape**
6LiF:ZnS w/ WLS (ISIS)	**55%**	**94%**	N/A	4.78 MeV	~160k photons	photomultiplier	**Pulse Shape**
6LiF:ZnS screen	5%	16%	100µm - 200µm	4.78 MeV	~160k photons	none, intensifier	**Pulse Shape**
Gd Scintillator Screen	5%	16%	100µm	72 keV	~1k photons	none, intensifier	**Pulse Shape**
GS20 glass (Li glass:Ce)	**75%**	**99%**	1.0 mm	4.78 MeV	~6k photons	photomultiplier	Pulse Height
Elpasolite crystals (CLYC,CLYB,etc.)	**90%**	**99%**	12.5mm	4.78 MeV	~80k photons	photomultiplier	**Pulse Shape**
Solid State							
Boron µChannel Plate	45%	60%	1mm	2.31 MeV	electrons	continuous dynode	Pulse Height
Seminconductor	1% - 25%	3% - 50%	1µm - 10µm	various	electron-hole pairs	none	Pulse Height

Neutron Detector Comparison Chart (continued)

Detector Technology	Gamma Sensitivity	Position Sensitive Mechanism	Fission product pathlength	Spatial Resolution	Signal Decay Time	References
Ion Chamber						
Helium-3 Tube	10^{-6} - 10^{-7}	RC delay line	1mm - 5mm	N/A	1µs	[18]–[20], [59]–[61]
Helium-3 cross-wire array	10^{-6} - 10^{-7}	cross-wire readout	1mm - 5mm	1 - 2 mm	1µs	[62]–[64]
Fission Chamber	**< 10^{-9}**	N/A	N/A	N/A	N/A	[65]–[68]
Boron Trifluoride	10^{-6} - 10^{-7}	RC delay line	1mm - 5mm	N/A	1µs	[15], [16], [69]
Boron-lined Multigrid (34-layer)	10^{-6} - 10^{-7}	cross-pattern readout	1µm - 3µm (B_4C), 10mm ($Ar:CO_2$)	0.6 mm	4µs	[26]–[28]
Boron thin-film GEM Detectors (6-layer)	10^{-6} - 10^{-7}	cross-pattern readout	1µm - 3µm (B_4C), 10mm ($Ar:CO_2$)	1.45 mm	**100ns**	[70]–[73]
Inorganic Scintillator						
6LiF:ZnS w/ WLS (NCNR)	< 10^{-7}	N/A	20µm - 30µm	various	2µs	[74], [75]
6LiF:ZnS w/ WLS (ISIS)	10^{-6} - 10^{-7}	cross-pattern readout	20µm - 30µm	various	2µs	[76]–[78]
6LiF:ZnS screen	~ 10^{-2}	Anger, optical camera	20µm - 30µm	100µm - 200µm	2µs	[78]–[80]
Gd Scintillator Screen	~ 10^{-2}	Anger, optical camera	< 20 µm	100µm	**80 ns**	
GS20 glass (Li glass:Ce)	10^{-5} - 10^{-6}	Anger camera	20µm - 30µm	various	**100ns**	[78], [81], [82]
Elpasolite crystals (CLYC,CLYB,etc.)	10^{-6} - 10^{-7}	various	< 20 µm	N/A, < 50µm	1µs	[78], [83]–[87]
Solid State						
Boron µChannel Plate	~ 10^{-2}	ASIC readout	4µm	**15µm - 55µm**	**100ns**	[49], [52]–[56]
Semiconductor	10^{-5} - 10^{-6}	various	1µm - 30µm	**1µm - 50µm**		[43]–[47]

Summarizing *Table 3*, some of the more compelling alternatives to helium-3 for neutron scattering applications come from the inorganic scintillator category. Boron-lined ionization chambers are large and complicated due to the large number of boron-10 thin films that must be incorporated to achieve appreciable neutron absorption. As mentioned before, solid state devices are too small to be economical for large area detectors. Glass scintillators which contain lithium-6 for neutron absorption seem to have good properties for neutron detection, however they also contain trace amounts of naturally radioactive thorium and potassium and have background alpha count rates of 100-200 disintegrations per minute per 100g of material. Special glass processed to minimize background radioactivity still has about 20 disintegrations per minute per 100g of material [32]. This is too high a background for many neutron scattering experiments.

Elpasolite crystal scintillators, chief among them Cs_2LiYCl_6 (CLYC), seem to have all of the desirable properties for neutron scattering instrumentation. Their only drawback is size, cost, and manufacturability. Elpasolite crystals are grown as ingots using the bridgeman growth method [85], but defects are still an issue for high yield manufacturing of large pieces. They are gamma sensitive, but pulse shape discrimination can be used to differentiate gammas from neutrons. Elpasolite crystals will show more and more promise as manufacturing prowess improves. And, synthesizing larger volumes and areas using smaller CLYC crystal pieces in a composite PVT plastic has been attempted [88].

This leaves LiF:ZnS(Ag) scintillator as the remaining detector technology with the potential for both high neutron absorption and very low gamma sensitivity. Although

LiF:ZnS(Ag) has excellent neutron absorption and very high photon yield from fission products, it also has a fundamental flaw. Lithium Fluoride Zinc-Sulfide mixtures are opaque to their own light emissions. Therefore, absorber sheets must be limited in thickness (0.1mm – 0.5mm) in order to recover a fission signal. This thickness is still hundreds of times thicker than the boron-10 thin films discussed earlier, and so these detectors will have a higher potential for neutron detection. The CANDOR neutron detector is based on LiF:ZnS(Ag) scintillator technology. Hereafter, a number of innovations are detailed which show how the CANDOR detector was developed as an alternative to helium-3 gas filled detectors for the purposes of neutron scattering science.

Chapter 3: The CANDOR detector overview

3.1. Basic Neutron Detector Processes

First, it is important to understand what qualities make an ideal neutron detector for neutron scattering. The basic neutron detector processes are illustrated in *Figure 15*.

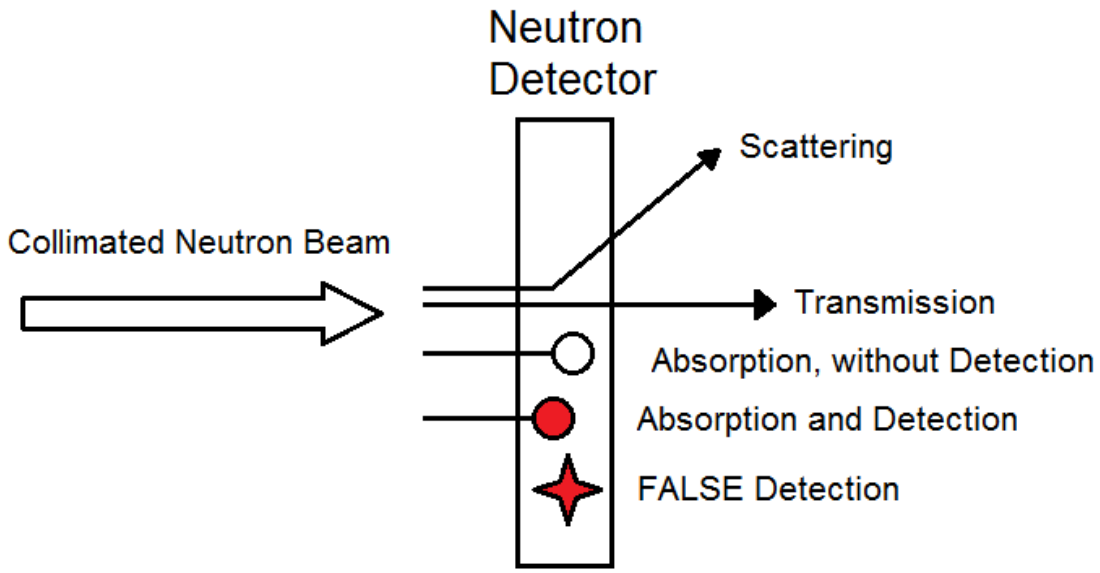

Figure 15: Neutron Detector Processes

Transmission occurs when a neutron passes through the detector without any interaction, maintaining its speed and direction. Scattering is when a neutron interacts with a neutron detector, changing the neutron's speed and/or direction, but the neutron still exits the detector. Absorption occurs when the neutron is captured by the nucleus of an absorber atom. When a neutron is absorbed in a detector, the neutron may or may not be detected depending on the size and quality of the signal produced by the absorption/fission. Finally, it is possible for a detector to produce a signal that can be misconstrued as a

neutron, even though this signal was not generated by a neutron absorption. These four qualities: Absorption Efficiency, Detection Efficiency, Scattering Profile, and Noise Rejection, are each valued differently depending on the application.

For particle physics applications, such as neutron scattering experiments done at the National Institute of Standards and Technology, our goal is to make use of as many neutrons as possible. The cost of creating neutrons in a nuclear reactor, moderating them (sometimes cryogenically 4meV - 6meV), and then guiding and/or collimating the neutrons onto a sample under test is very expensive. Wasting neutrons is a shame! For this reason, neutron absorption and detection efficiency are both highly valued. Additionally, as mentioned in *Section 2.9*, very high noise rejection is needed to distinguish very faint features seen in neutron scatter patterns. Noise rejection (ANYTHING other than a neutron) is of upmost importance, because the number of neutrons being measured in some cases is very, very small (0.001 - 0.01 neutrons square centimeter per second). So for neutron scattering, the ideal neutron detector has 100% neutron absorption, 100% neutron detection, and 0% of the other four processes: scattering, transmission, absorption without detection, and false detection.

3.2. Photon Production by ZnS(Ag)

The CANDOR detector's active material consists of a ^{6}LiF salt for neutron absorption mixed with ZnS(Ag) material for producing photons from fission products. The two materials are ground to a fine powder with grain sizes averaging 8μm and mixed together with a binding agent. An SEM micrograph is shown in *Figure 16*.

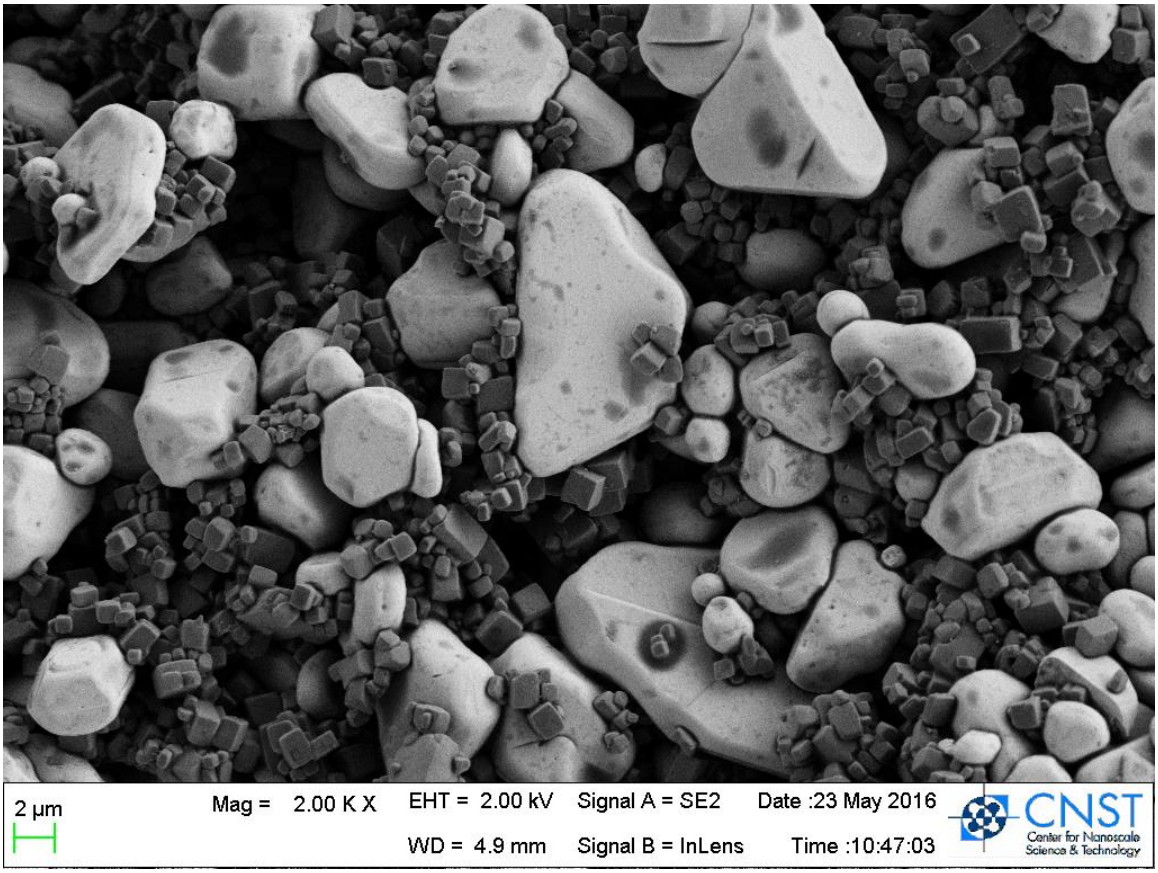

Figure 16: An SEM micrograph of the CANDOR scintillator material. The darker shaded cubes are LiF salt for neutron absorption. The lighter shaded, rounded particles are ZnS(Ag) scintillator.

Extensive work was done to optimize the scintillator mixture for neutron absorption, photon production, and photon transport [74], [89].

ZnS(Ag) produces photons in the blue visible light spectrum, with peak emission at 450nm as shown in the emission spectrum of EJ-426-HD2 manufactured by Eljen Technology. EJ-426-HD2 is the ^{6}LiF:ZnS(Ag) thermal neutron scintillator material which was chosen for CANDOR detector production (*Figure 17*) [90].

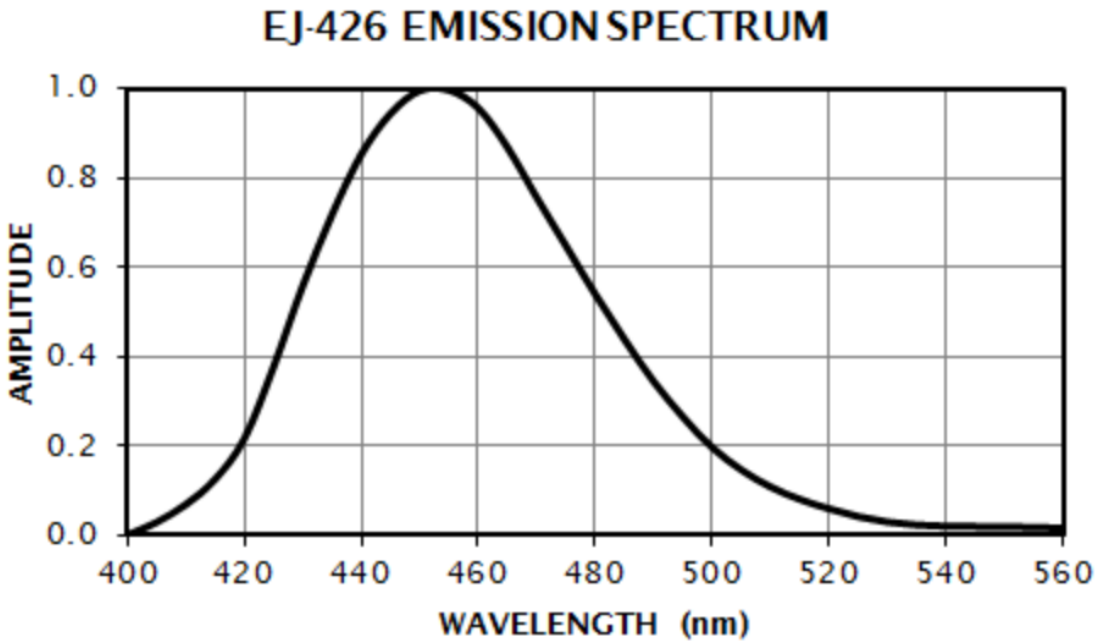

Figure 17: Emission spectrum of EJ-426 courtesy of Eljen Technology, a ^{6}LiF:ZnS(Ag) compound for neutron detection **[90]**

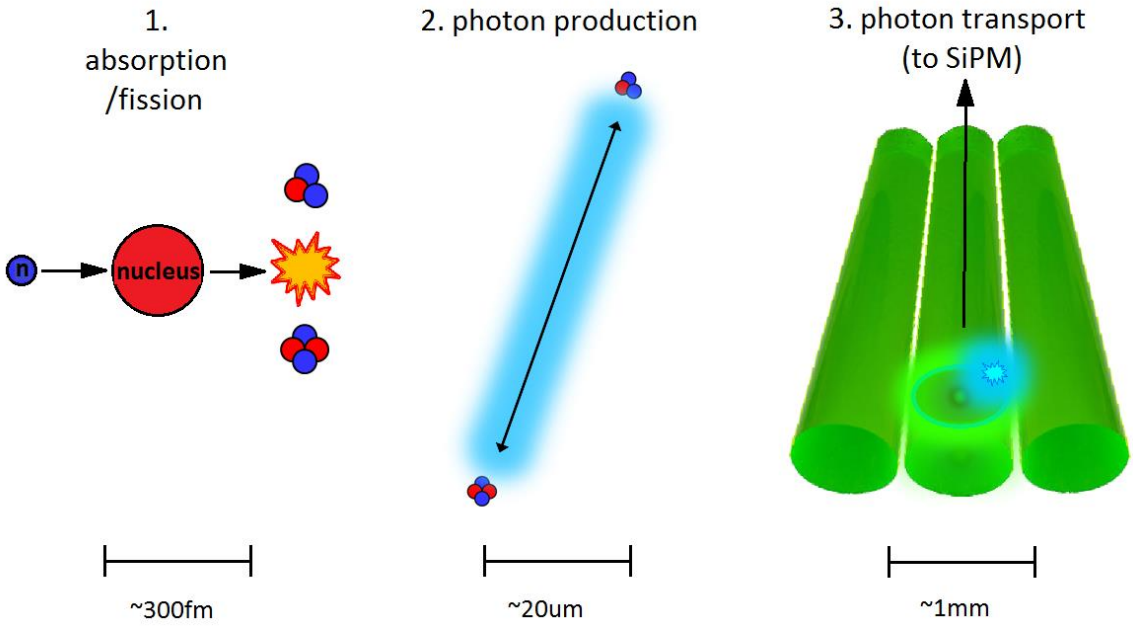

Figure 18: An illustration of neutron absorption, photon production, and photon transport. Approximate length scales are included below each step.

The photons that are generated by ZnS(Ag), and which also escape this highly opaque material, must next be routed to a photodetector. Wavelength Shifting (WLS) fibers are used to accomplish the task of routing light to an isolated photodetector located several inches from the neutron absorbing region. The overall concept is illustrated in *Figure 18*.

3.3. Wavelength Shifting (WLS) Fibers

Wavelength shifting fibers are optical waveguides containing fluorescent dye. They can be formed from optical grade glasses and plastics. WLS fibers serve a dual purpose. First, WLS fibers absorb light from the emission spectrum of the zinc-sulfide scintillator, and then they re-emit this light at a longer wavelength which matches the absorption spectrum of the photodetector. This can improve the quantum efficiency of scintillation light coupling onto the photodetector. There are a number of different fluorescent dyes with a variety of absorption and emission spectra. The absorption band of the dye should be chosen to match the emission band of the scintillator, the and emission band of the dye should be chosen to match the absorption band of the photodetector.

WLS fibers manufactured by Kuraray Co. Ltd. were chosen for the CANDOR detector. The WLS fibers have an outer diameter of 0.5mm and contain Y-11 fluorescent dye. Y-11's absorption spectrum (*Figure 19*) closely matches the emission spectrum of EJ-426 (*Figure 17*) with the most intense emissions between 440nm – 460nm. The emission wavelength of Y-11 dye (460nm – 530nm) is slightly longer than the peak

absorption wavelength (350nm – 500nm) of the chosen photodetector, MicroFJ-30035 by SensL Co. Ltd (*Figure 20*) [91].

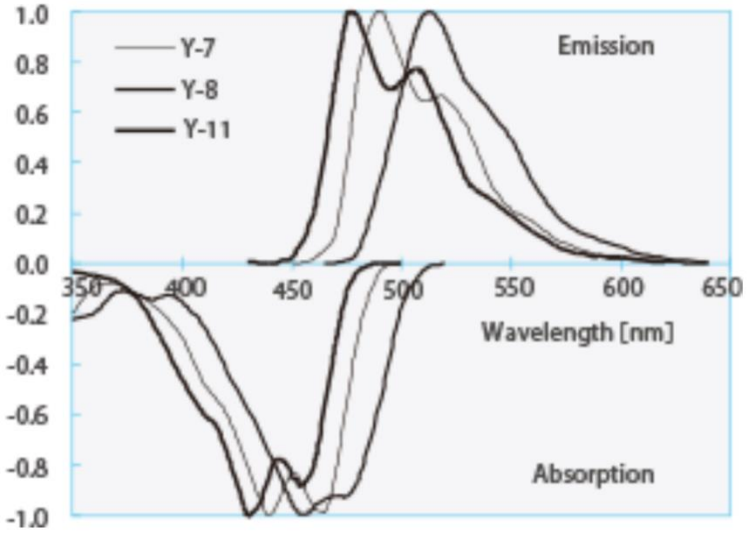

Figure 19: Absorption and emission spectra for selected WLS fiber dyes **[92]**

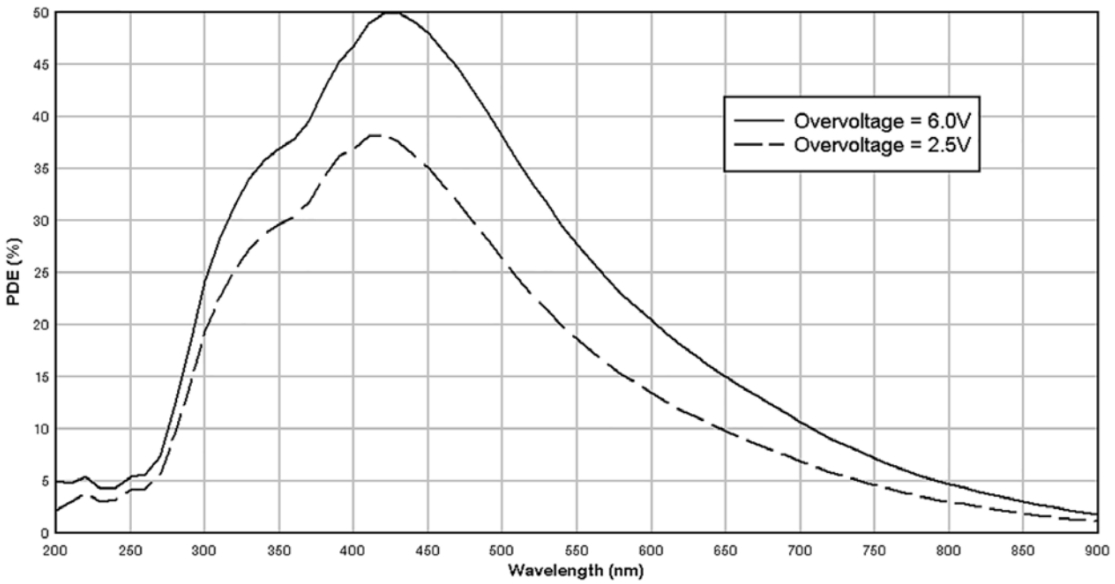

Figure 1. Photon Detection Efficiency (PDE)
(MicroFJ–60035–TSV)

Figure 20: Detection spectrum of SensL J-Series silicon photomultipliers **[91]**

Looking at the emission spectrum of EJ-426 scintillator (430nm – 480nm, *Figure 17*) and the absorption spectrum of the photodetector (350nm – 550nm, *Figure 20*), it doesn't appear that a wavelength shift is required at all and that these two spectra are well matched as is. The reason why WLS fibers are needed in the CANDOR detector is for photon transport. The optical depth of LiF:ZnS(Ag) is quite shallow, between 0.1mm – 0.2mm from optical transmission measurements**.** But, the photodetector is located more than 5 centimeters from the active area of the CANDOR detector. A waveguide is required to transport the scintillation photons from the active detector volume to the photodetector.

Wavelength shifting dyes are used for a variety of purposes, but when the dyes are incorporated within an optical waveguide, the fluorescent emissions can be transported long distances to a photodetector without significant losses. This allows for radiation shielding to be placed between the active area of the neutron detector and the photodetector/preamplifier to mitigate radiation damage to these components.

The CANDOR detector uses WLS fibers with a cylindrical waveguide geometry. The WLS fibers are manufactured by Kuraray Co. Ltd. They have an outer diameter of 0.5mm, multi-cladding layers for a broader angular acceptance of the waveguide, and a Y-11 dye concentration of 650ppm (98.5% photon absorption at 430nm). A cross sectional diagram of the waveguide is shown in *Figure 21*.

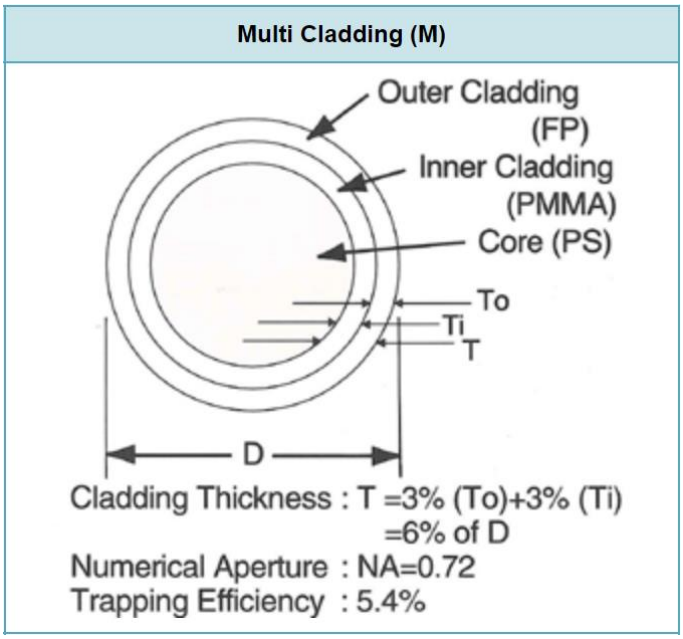

Figure 21: a cross sectional diagram of a cylindrical waveguide with a polystyrene core, manufactured by Kuraray Co. Ltd. **[93]**

The multi-clad waveguide has an acceptance cone of 26.7º from the waveguide axis (*Figure 22*). This translates into 5.4% of the hemisphere 2π solid angle, or 10.8% of the total 4π solid angle. Scintillation light that is wavelength shifted by the Y-11 dye is re-emitted isotropically. This means only a maximum of 10.8% of this light can be transported. 89.2% of the wavelength shifted photons will be refracted out of the waveguide. A small percentage of the transported photons will be reabsorbed by the Y-11 dye as they travel to the photodetector, but these losses are relatively small. The attenuation length of the WLS fibers with a 650ppm Y-11 dye concentration is >0.6m, which is about 10 times the distance from the detector's active area to the photodetector.

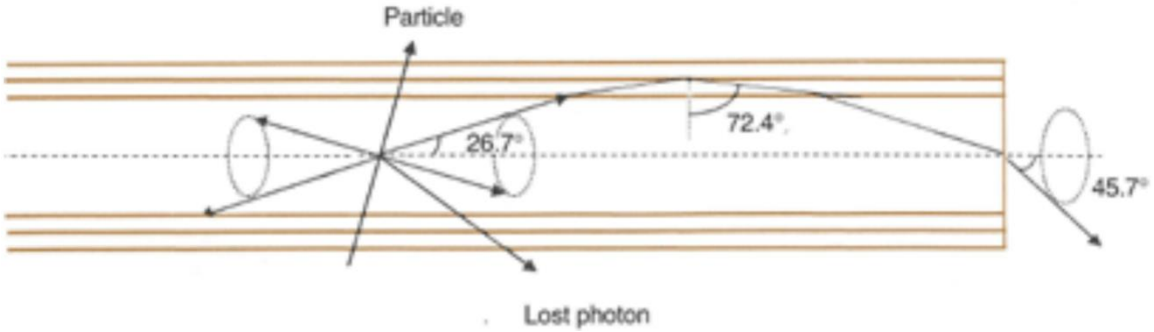

Figure 22: An axial diagram of a cylindrical waveguide illustrates the acceptance cone for photon transport **[93]**.

3.4. Silicon Photomultipliers (SiPM)

Photons are transported from the active ^{6}LiF:ZnS(Ag) volume by WLS fibers to a photodetector. The photodetector which was chosen for the CANDOR detector comes from a family of devices called “silicon photomultipliers” (SiPM). SiPMs are similar in concept to photomultiplier tubes in that they have the ability to detect individual photons by amplifying upwards of 10^{6} charge carriers from a single photon [94]–[97].

3.4.1. SiPM Mechanics

The mechanics of an SiPM, or its predecessor the avalanche photodiode (APD), are very similar. The structure is a bit more complicated than a simple PN junction. A highly doped N-type silicon rests at the cathode, while P-type silicon layers of various doping concentrations are sandwiched between the N+ later and the anode. A diagram is shown in *Figure 23*.

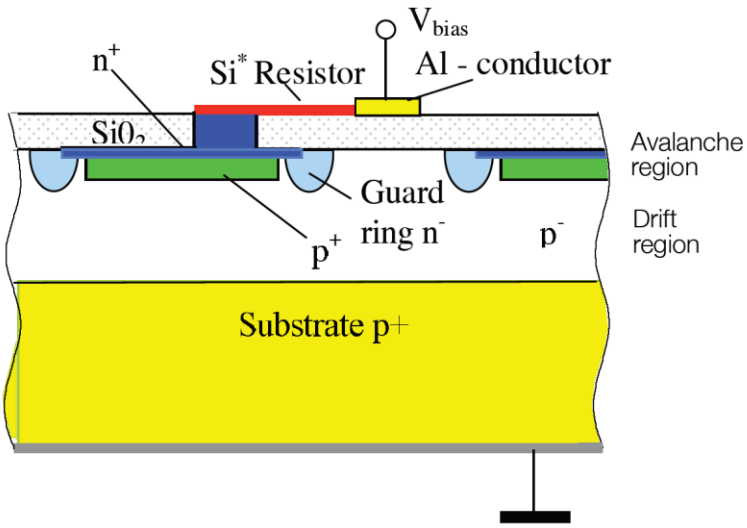

Figure 23: Structure of a SiPM microcell **[98]**

The goal in SiPM diode design is to create a region with very high electric fields so that a photoelectron will be accelerated to a very high velocity, where it can ionize additional electrons and create an avalanche. This is achieved with highly doped PN regions placed adjacent to each other in the diode. When under reverse bias, these regions are depleted of charge carriers leaving a dense space charge region of immobile doping ions. Opposing positive and negative ion layers in close proximity to one another result in a very large internal electric field as seen in *Figure 24*.

Most photons are absorbed in the lightly P-doped π-region of the diode, which extends several micrometers in depth. Electron-hole pairs created in the π-region drift toward the anode and cathode. When the electron passes into the highly doped Geiger/avalanche region (typically much less than 1µm in depth) it accelerates and causes a charge avalanche. *Figure 25* shows the absorption length of 500nm photons in silicon is about 1µm. The plot showing internal electric field of an SiPM as a function of depth is more typical of a device with sensitivity in the red visible spectrum [98], [99].

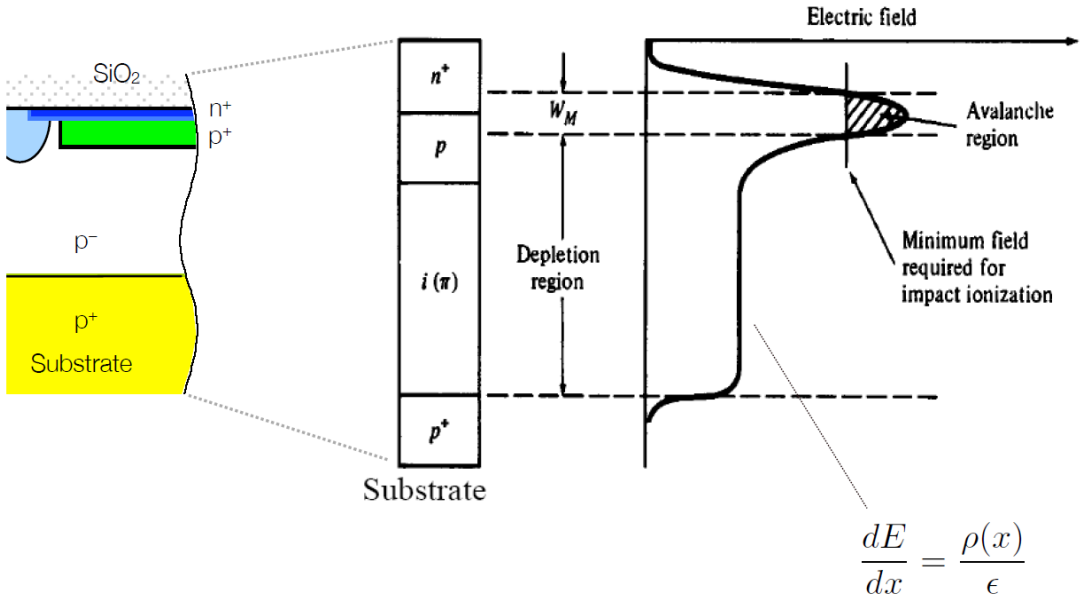

Figure 24: Silicon doping is structured for high electric field **[98]**.

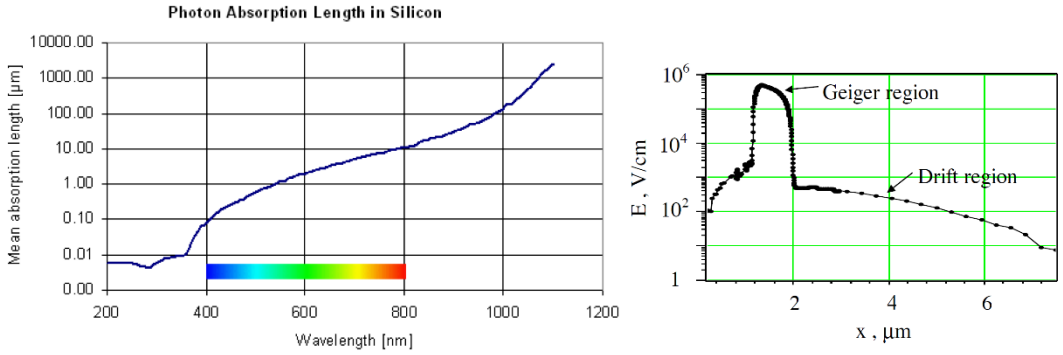

Figure 25: (left) 500nm photon absorption length in silicon is about 1µm. (right) a realistic model of electric fields in an SiPM diode **[98], [99]**

A high-resolution photograph of an SiPM shows a grid of microcells. The grid of microcells are connected in parallel with internal resistors. The resistors quench the charge avalanches by reducing the voltage/electric field following a microcell discharge *Figure 26* [98].

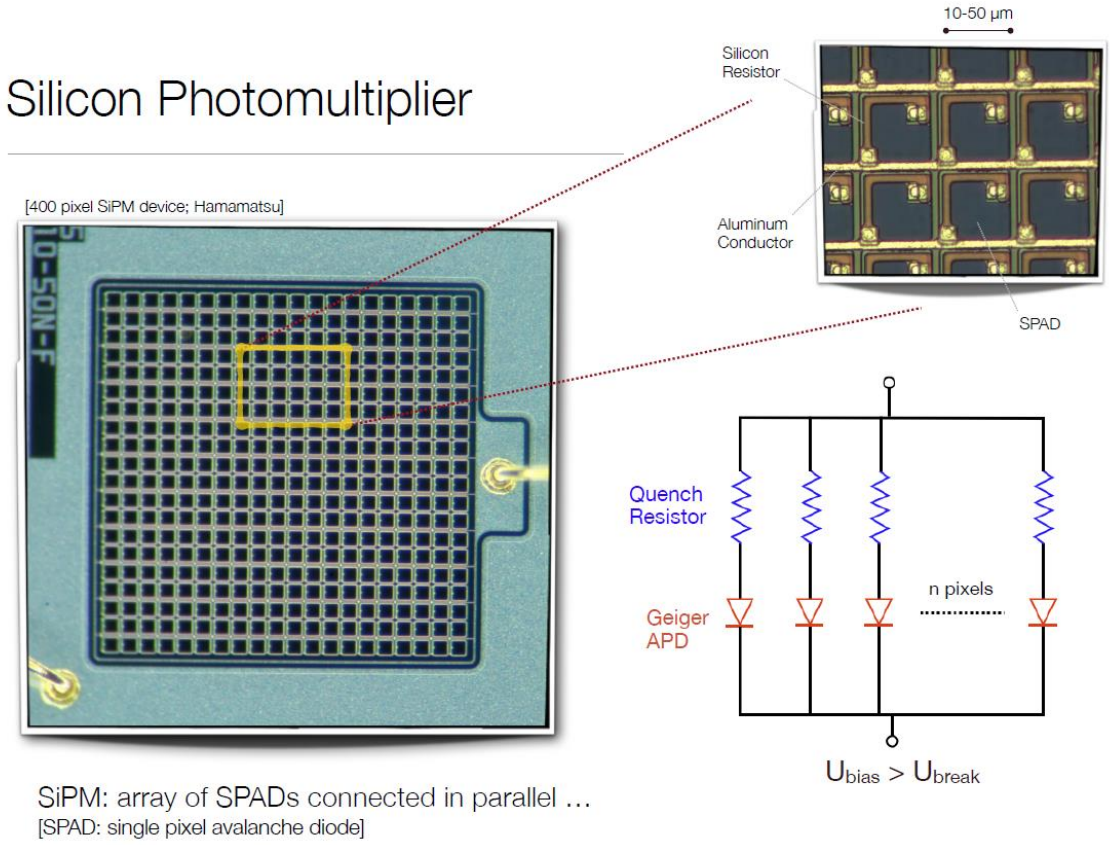

Figure 26: Close-up photograph of a SiPM **[98]**

SiPMs must have a high voltage applied in reverse bias to enable avalanche inducing electric fields. The minimum voltage required for avalanche breakdown is known as the "breakdown voltage" also referred to as V_{BD}. The breakdown voltage depends on the specifics of an SiPM device, but values generally range from 25V – 100V. The electrical discharge of an avalanche scales linearly with the amount of excess voltage applied above breakdown ($V_{applied}$ - V_{BD}). This is because a microcell can be electrically modelled as a capacitor and the linear relationship of charge and voltage ($q = CV$). Each microcell has a capacitance associated with it, and the amount of charge released in an avalanche is approximated as $q_{discharge} = C_{photocell}$ x $(V_{bias} - V_{BD})$.

SiPMs are attractive low-light sensors because of their high gain, compact size, insensitivity to magnetic fields, low cost, and low operating voltage (< 100V compared to > 1000V for a photomultiplier tube or ion chamber). Unfortunately, they also have a non-linear signal response and they show some temperature dependence as well.

3.4.2. Non-linearities: dark counts, cross-talk, and afterpulsing

"Dark counts" are one type of non-linearity displayed by SiPMs. Dark counts are when pixels spontaneously discharge without photon absorption. The signal generated from this type of pixel discharge is indistinguishable from a discharge caused by a photon. There are a couple of processes which cause dark counts. One process is thermal excitation of electron-hole pairs in the π-region. Thermal excitation follows Boltzmann statistics of intrinsic semiconductors. The second process is electron tunneling from the valence band to the conduction band induced by the very high electric fields located in the avalanche region. Both processes are illustrated in *Figure 27*.

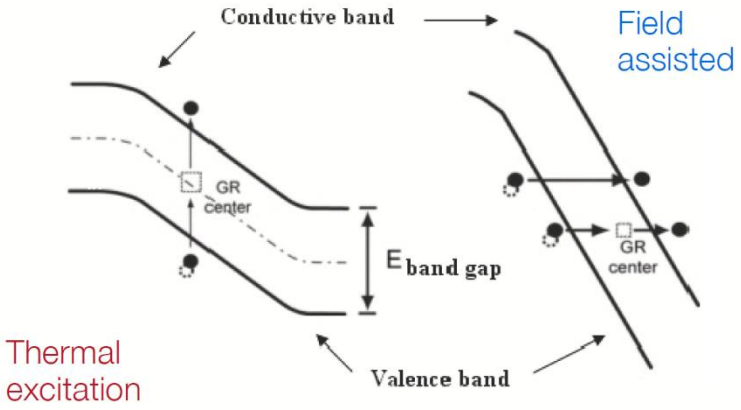

Figure 27: Dark count processes; (1) thermal excitation and (2) tunneling **[98]**

Thermal excitation is the dominant process at temperatures above 150ºK. Below this temperature, thermal excitations are exceedingly rare and the tunneling process dominates [100], [101].

Other non-linearities include “cross-talk” and “afterpulsing”. Cross-talk is when a secondary photon produced in the primary microcell avalanche creates a free charge carrier in a neighboring microcell which subsequently creates an avalanche in that adjacent microcell [102]–[104]. Optical trenches are used in recent SiPM devices to reduce the probability of crosstalk. Optical trenches are etched between microcells and filled with aluminum to absorb photons moving in the lateral direction [105].

Afterpulsing results from a charge carrier becoming trapped within the avalanche region, and then re-emerging at a later time to induce a second avalanche. Both crosstalk and afterpulse processes are illustrated in *Figure 28*.

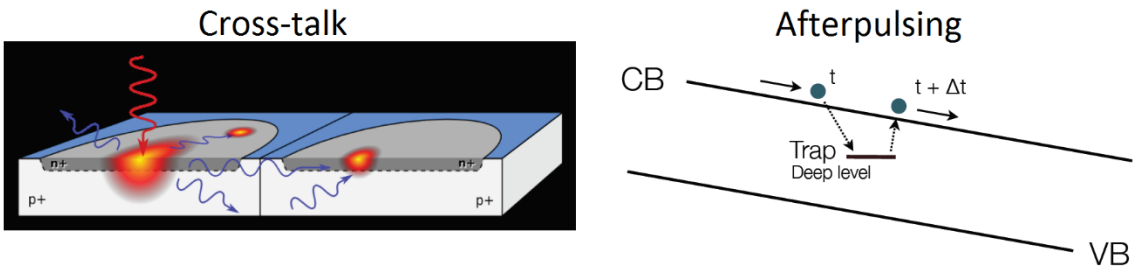

Figure 28: illustrations of cross-talk and afterpulsing non-linearities **[98]**

Models and simulations of SiPMs have shown that if the probabilities of cross-talk and afterpulsing are low (maximum 20%, preferably below 10%), then the nonlinearities may be acceptable for some applications, including the radiation spectroscopy [103], [105], [106]. Recent devices which are offered commercially have

crosstalk probabilities ranging from 1% - 25%, and afterpulsing probabilities ranging from 1% - 5% [91], [107].

3.4.3. Temperature dependence

Several properties of SiPMs change with temperature. Breakdown voltage rises with temperature, because decreased charge carrier mobility from lattice vibrations inhibits Geiger avalanches. This has the effect of decreasing gain of a photocell discharge ($q_{discharge} = C_{photocell}$ x $(V_{bias} - V_{BD})$). V_{BD} increases at a rate of approximately 40mV/ºK [100].

The dark count rate also increases with temperature, as there are more thermally excited electron-hole pairs. Dark counts can be reduced dramatically by cooling a SiPM device down to about 130ºK. Below this temperature, carrier freeze out affects the photo detection efficiency of SiPM devices. Additionally, afterpulsing becomes a major issue at cryogenic temperatures below 130ºK, because more trapping centers become active [101].

3.4.4. Radiation tolerance

SiPMs appear to possess adequate radiation tolerance for most applications. They can withstand up to 1kRad of x-ray and gamma radiation [108], which is many orders of magnitude higher than the lifetime expected dose at the CANDOR instrument. They also can withstand neutron fluxes of approximately 10^8 n/cm^2 (at 1MeV) before significant degradation of SiPM device performance is seen [108]–[110]. Although instrument suites

at the NCNR have a non-trivial neutron radiation background, these neutrons are at thermal and cold energies (< 25meV), and so they do not pose a risk for lattice displacement defects in silicon which require upwards of 25meV to form. In addition, the SiPM detectors will be located away from any neutron beam and scatter pathways, so their exposure to neutrons will be minimal.

3.4.5. SiPM for the CANDOR detector

Many SiPM devices were explored as candidates for the CANDOR detector's photosensor. Other single-photon detector technologies, such as photomultiplier tubes, were not seriously considered due to their relatively large size, cost, and susceptibility to magnetic fields which are prevalent in neutron scattering experiments. The photon yield from the CANDOR absorber/scintillator is high enough that neutron signals can be discerned above the parasitic noise and non-linearities introduced by SiPM devices, especially after using digital signal processing and pattern recognition techniques.

Devices manufactured by SensL, Hamamatsu, Ketek, Excelitas, and Advansid were tested [111]. In the end, the SensL MicroFJ-30035-TSV device was selected. It has an active area of 3mm x 3mm with 5676 individual microcells, a breakdown voltage of 24.5V ± 0.25V, and a temperature dependence of 21.5mV/ºC. When biased to V_{BR} + 5V it has a photo-detection efficiency (PDE) of 40% at 476nm, dark count rate less than 1MHz, cross-talk probability of 20%, and an afterpulsing probability of 4% [91].

One of the factors for choosing the SensL MicroFJ-30035-TSV is the consistency of its breakdown voltage. With many SiPM products, the specified breakdown voltage has a large range, up to ± 3V between individual devices. In contrast, the SensL

breakdown voltage is specified to within ± 0.25V. Since the gain is linearly dependent on ($V_{applied}$ - V_{BD}), variations in V_{BD} will radically change the electrical gain between detectors, unless the applied bias voltage is controlled separately for each detector. Separate voltage control of each SiPM device is complex design challenge to be avoided if possible. Temperature dependence of SiPMs is not a concern because the internal temperature of the CANDOR analyzer and detectors is stable and can even be regulated. Radiation fields in the SiPM and preamplier chamber will be below harmful levels, so this is not a concern either.

Figure 29 shows a photograph of SiPMs mounted on printed circuit boards. These assemblies are mounted to the face of the WLS fiber blocks.

Figure 29: a photograph of SiPMs mounted on PCBs for mounting to face of the WLS fiber block

3.5. Optical Enhancements

Every effort was made to maximize the light signal recovered by the SiPM photodetector. Out of a possible ~100000 photons generated by ^{6}Li fission products in the ZnS(Ag), the actual number of photons detected by the SiPM per neutron event is estimated to be between 30 photons and 3000 photons, with a photopeak of about 100 photons (***Figure 30***).

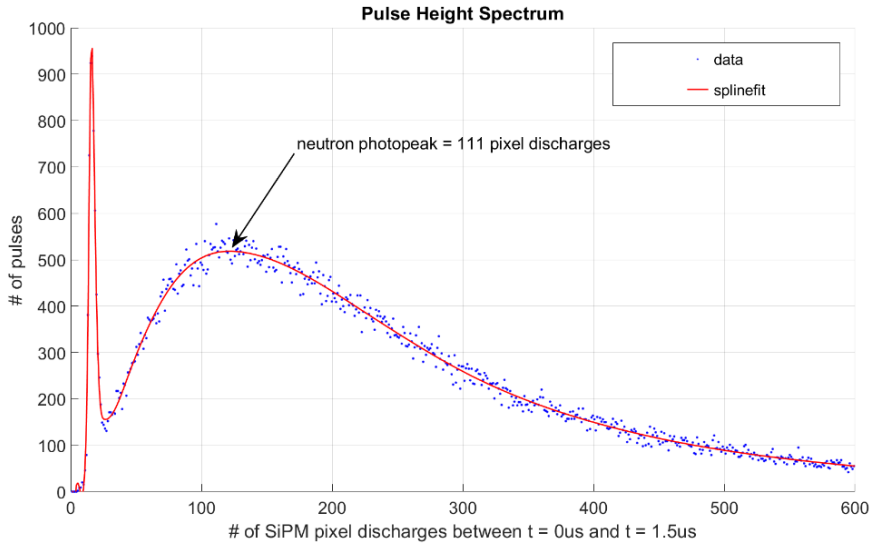

Figure 30: A pulse height spectrun from a CANDOR detector, with a photpeak of 111 SiPM pixel discharges

3.5.1. Removal of air voids in the scintillator mixture

Several innovations were used to maximize optical transport. One innovation came from the discovery that microscopic air voids were present in the ^{6}LiF:ZnS(Ag) absorber/scintillator mixture. This was realized by Yehuda-Zada and Osovizky, when simulations showed that experimental measurements of neutron absorption were lower

than those predicted by simulations [74], [89]. Subsequent SEM images showed the existence of voids in the mixture. Working with the scintillator manufacturer, Eljen Technology, we devised a method for mechanically pressing the scintillator mixture firmly over the WLS fibers, squeezing out the microscopic air pockets. As a result, the scintillator volume was reduced by 25% on average. Photon transport was boosted as well, because optical scattering within the material was reduced (*Figure 31*).

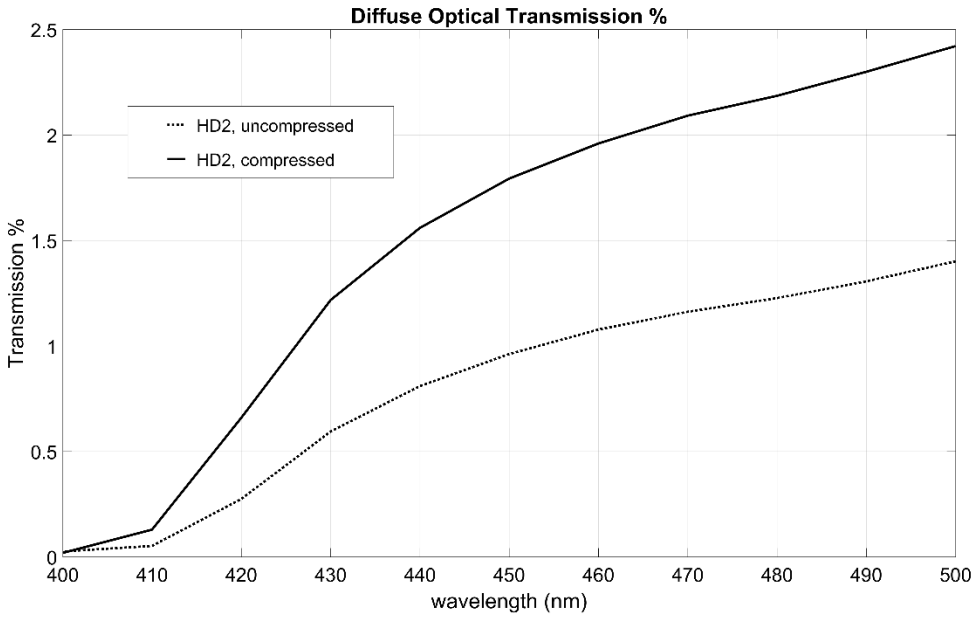

Figure 31: Pressing the scintillator around the WLS fibers significantly enhances optical transmission of the scintillator.

3.5.2. Reflectors covering the scintillator volume

The scintillator volume is sandwiched between reflective surfaces to reflect photons back toward the WLS fibers. The front reflector is MIRO-SILVER® primarily made of finished aluminum with a thickness of 0.2mm [112]. Since aluminum has very small neutron scattering and absorption cross sections, neutrons are unaffected prior to reaching the scintillator. The rear reflector is Vikuiti™ Enhanced Specular Reflector

which is constructed of special plastics and is very, very thin (50μm) [113]. Plastics contain light elements including carbon and hydrogen, and these materials are heavy neutron scatterers. We found that approximately 2% of incident neutrons were back-scattered off of the Vikuiti reflector, and so this material could not be used on the front face of the CANDOR detector even though this was the most reflective material we tested (***Figure 32***).

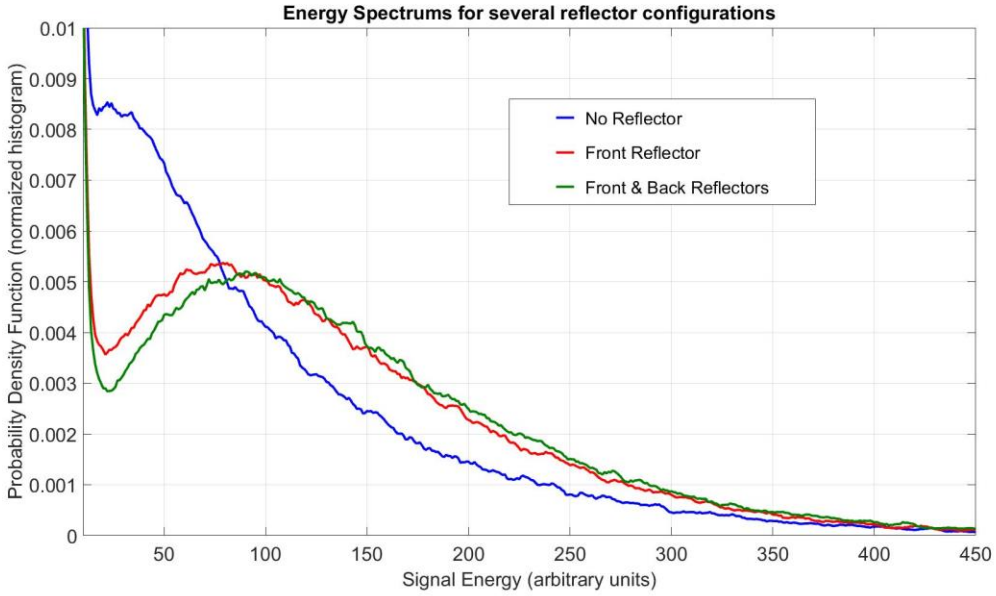

Figure 32: Reflectors provide a great enhancement to optical yield

3.5.3. WLS fiber to SiPM optical coupling

The optical coupling between the WLS fibers and the SiPM is achieved using a machined "fiber block." The WLS fibers are bundled into an area smaller than the active area of the SiPM and epoxied in place. The fibers are cut with a hot knife just above the plane of the block and the remaining material is ground/polished down using successively finer grits of sandpaper until they are flush with the metal. Mechanical shearing can cause

splintering and fractures in the WLS fibers which degrade the optical properties of the waveguide. SiPMs are located on a printed circuit board which aligns them with the WLS fiber bundles. A thin layer of optical grease is applied between the SiPM and fibers to make the optical connection between them (by matching the refractive index of both materials).

3.5.4. Loops and reflectors for efficient transport through WLS fibers

Efficient transport of photons through the WLS fiber waveguides to the SiPM was also an important detail. Photons that are reemitted toward the SiPM through the WLS fibers will reach the SiPM with very high transport efficiency. However, just as many photons are reemitted through the WLS fibers in the opposite direction.

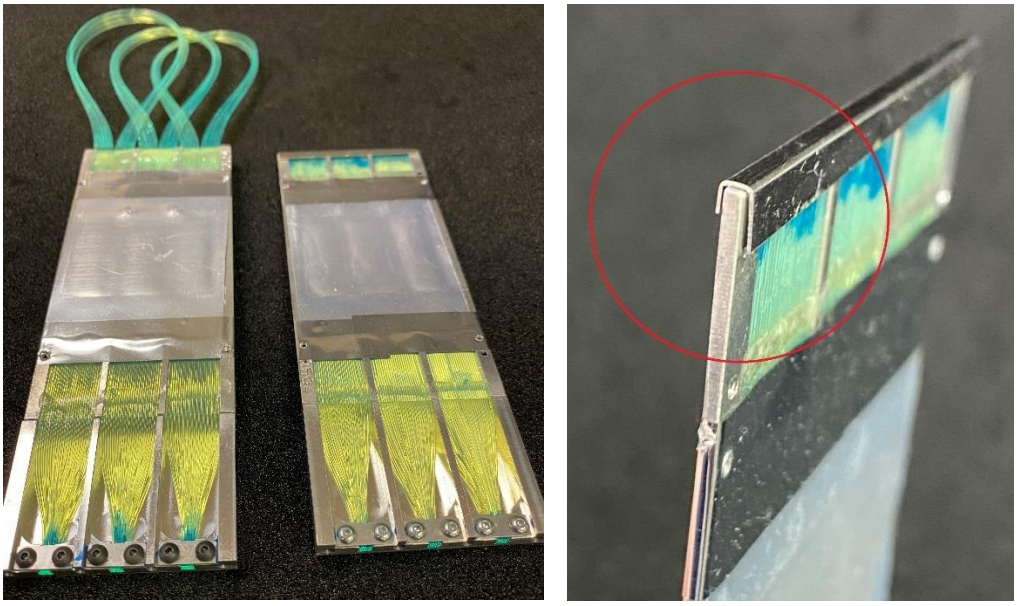

Figure 33: (left) a detector with a WLS fiber loop and a detector with the end reflector termination. (right) close-up of the end reflector termination

The most efficient way to transport these photons is to bend the WLS fiber waveguide back toward the SiPM, making sure not to violate the minimum bend radius of the waveguide and maintain total internal reflection. Although this solution is the most efficient, it almost doubles the size of the detector since the loop diameter is >5cm. We found that with careful craftsmanship, is it possible to manufacturer and attach an end-reflector that is almost as effective as the WLS fiber loop. Both the loop and end reflector terminations are shown in *Figure 33*. We used Alanod MIRO-SILVER® because it had good adhesion using optical cement (model EJ-500 by Eljen Technology). Eljen Technology also developed a tool for bending the aluminum reflector so that it forms a flat-bottom trough that fits the thin profile of the CANDOR detector. The WLS fibers are polished before cementing this reflector over top, making sure to maintain pressure while the epoxy cures for a tight fit. Pulse height spectra show that the photon transport can be just as good as with the WLS fiber loops, if the craftsmanship of the reflector termination is flawless.

3.6. CANDOR detector CAD Model

A diagram of the final detector design is shown in *Figure 34*. Item A in the CAD model is a white beveled square, which represents a very thin ~25μm primer layer of scintillator material which is painted directly onto both sides of the wavelength shifting fibers. The primer aids adhesion of the main scintillator slab, B, represented by a pink beveled square, which is about 450μm thick on each side. The scintillator is enclosed between two thin reflective sheets. Sheet C represented by a blue square is Vikuiti, a very

highly reflective plastic material on the rear face of the detector. Sheet D, also represented by a blue square, is Alanod, a slightly less reflective material made primarily from Aluminum. Alanod is used on the front face, because Aluminum is transparent to neutrons, where as plastic is a very strong scatterer of neutrons. It is best not to scatter neutrons away from the detector before they have had a chance to pass through the scintillator. The WLS fibers are polished at both ends of the detector. On the end opposite the SiPM photodetectors, a bent strip of Alanod (E) is formed around the end of the detector to reflect light back toward the SiPMs.

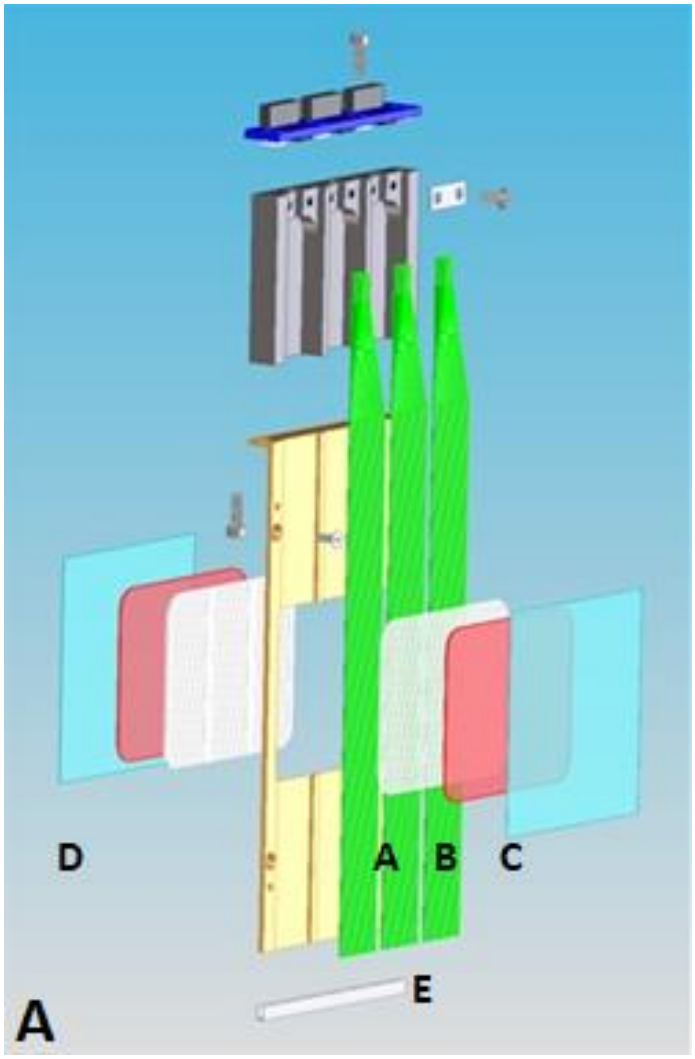

Figure 34: A CAD model of the CANDOR detector.

3.7. Preamplifier

A preamplifier array was specially designed for the CANDOR instrument (*Figure 35*). This preamplifier PCB contains circuitry for 18 individual neutron detectors (6 triple-detector units). The gain of the preamplifier is 10V/mA and it includes an 50Ω output termination resistor. Aside from the basic function of providing high signal-to-noise ratio amplification to drive 50-Ohm loads, this preamplifier contains circuitry and logic for switching between “Geiger mode” and “current mode”, so that the system can be used in both high neutron flux and low neutron flux radiation environments. Three of these preamplifier arrays will be used in each 54-channel energy analyzing blade.

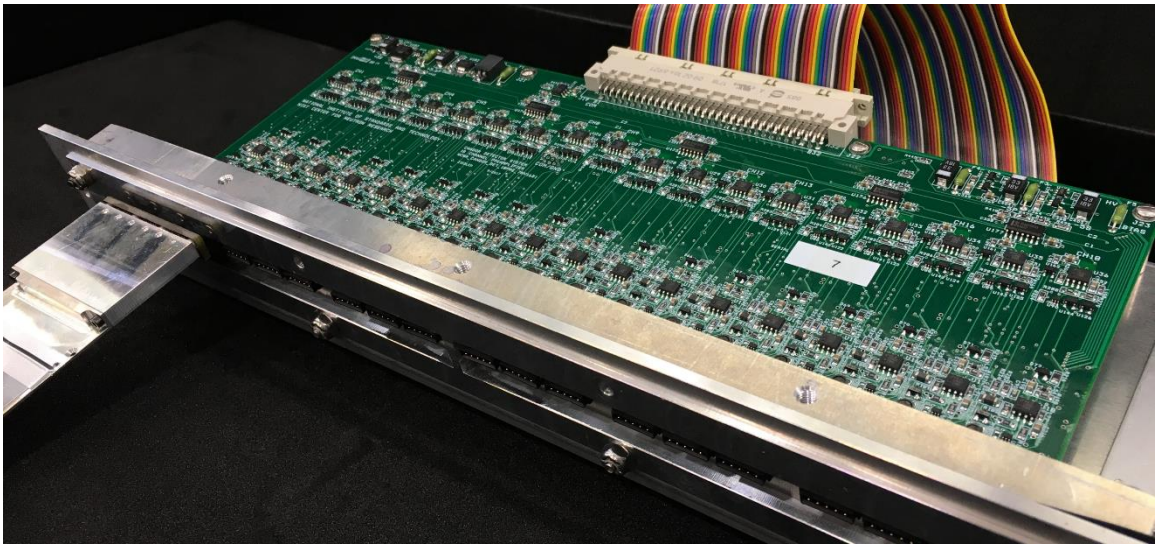

Figure 35: a photograph of the CANDOR preamplifier

3.8. Pulse Shape Discriminator

A digital pulse shape discriminator (PSD) is used to interpret signals sent from the preamplifier. It was discussed in section 2.7.3 that many scintillator materials have a delayed fluorescence component when high concentrations of energy are deposited in a

small volume of material. Scintillation of fission products in ^{6}LiF:ZnS(Ag) is a prime example of delayed fluorescence. A significant portion of photons are emitted from ZnS(Ag) many hundreds and even thousands of nanoseconds after a neutron absorption. This is in stark contrast to the emission decay time by gamma radiation in ^{6}LiF:ZnS(Ag) which is only about 200 nanoseconds after neutron absorption. The decay profile a neutron signal can be discerned from that of SiPM noise and gamma signals even if the magnitude of noise and gamma signals is higher than the neutron signal (*Figure 36*).

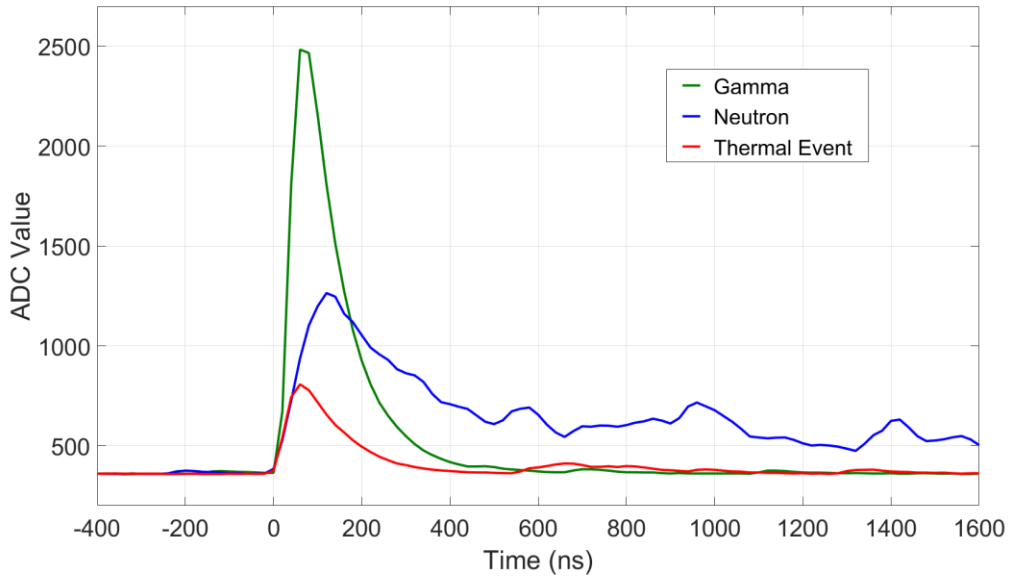

Figure 36: Signals recovered from the preamplifier output for neutron, gamma, and SiPM noise events

Two separate signal processing schemes were developed for CANDOR. (1) An analog solution uses an analog Pulse Shape Discriminator (PSD), which outputs a TTL logic level pulse in response to an event. (2) A digital PSD uses an A/D converter to digitize the preamplifier signal at a sample rate of 50MHz followed by an FPGA for

digital signal processing (*Figure 37*). The dynamic range of the A/D converter on the digital PSD is between 0V -2V.

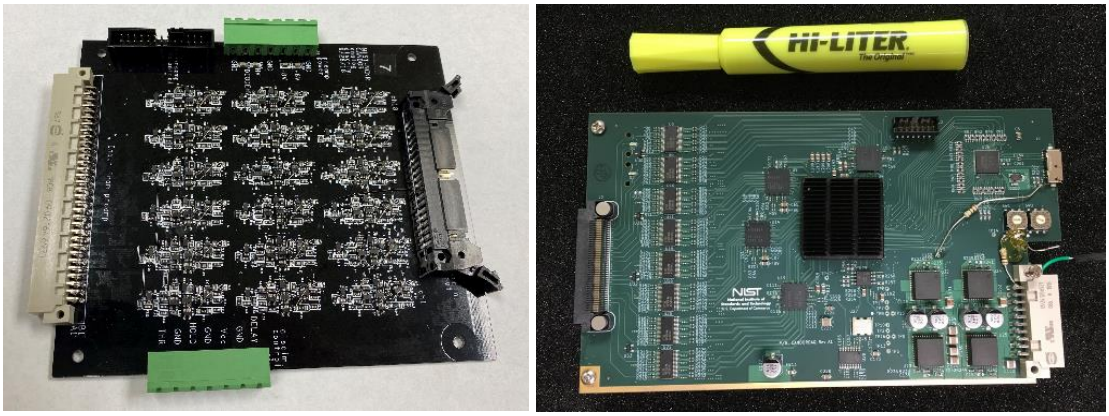

Figure 37: (left) analog PSD. (right) CANDOR_DAQ for digital PSD

The digital PSD circuit board is named the "CANDOR_DAQ", for CANDOR data acquisitions. CANDOR_DAQ has several data export options. With the detection of each event, an event word is generated and sent to a PC. The event word contains a timestamp marking the event's arrival time with a precision of 100ns, compatible with a PTP timing protocol. It can also send information about the size of the pulse. And, the digital PSD can record and send a complete waveform trace, like an oscilloscope but with an elaborate triggering algorithm. The PSD schemes for both analog and digital discriminators will be discussed in detail later.

Chapter 4: Signal Processing Challenges

4.1. Signal Flow Diagram

The signal flow diagram in *Figure 38* represents the cascade of processes between absorption/fission of a ^{6}Li nucleus and signal readout by a pulse shape discriminator (PSD). All ^{6}Li fissions induced by slow neutron absorption are identical, but from here the signal strength of events diverges based on the location and geometry of where the event took place. Along the way, there are several points where noise can be injected to corrupt a neutron signal.

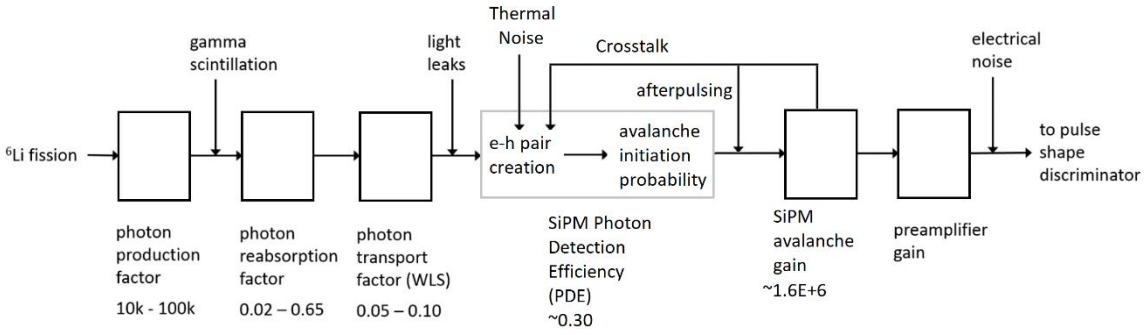

Figure 38: Process flow diagram

4.1.1. Photon Production

The signal chain begins with photon production. Photons are only produced by ZnS(Ag) particles within the LiF:ZnS(Ag):binder mixture. Not all of the energy from the fission products is converted into photons, and the amount of light produced depends on the local geometry of the grains and the flight path of the fission products. If the absorption takes place near the outside face of the scintillator volume, only one of the two

fission products may interact with the scintillator because the second fission product may travel out of the detector. The distribution of photons produced in the CANDOR detector scintillator was simulated by Yehuda-Zada [89]. *Figure 39* shows that the number of photons produced ranges from 7000 – 70000 photons.

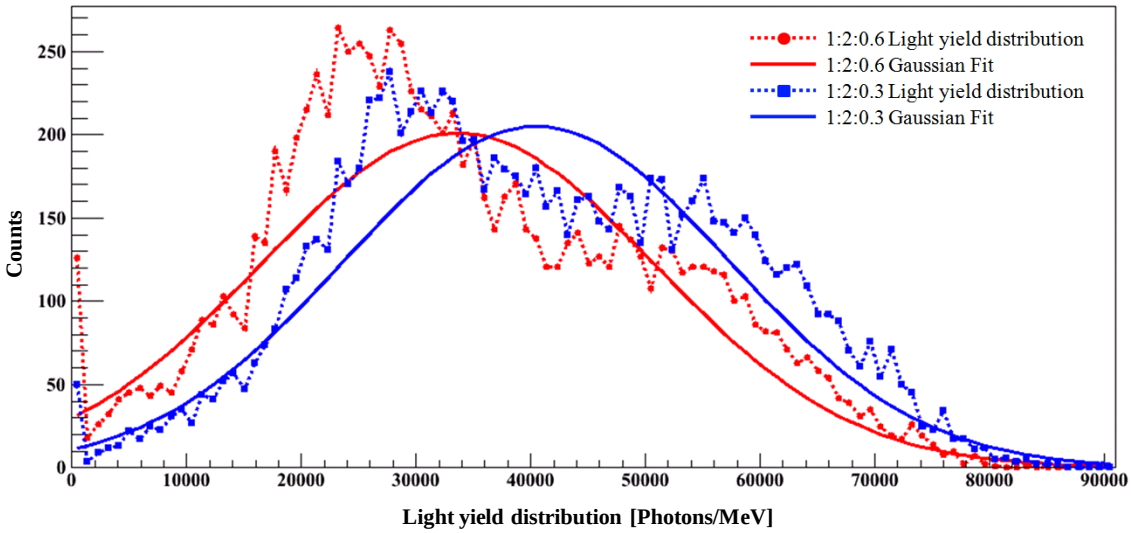

Figure 39: Photon production distributions based on GEANT4 simulations **[89]**

4.1.2. Photon reabsorption

Most of the generated photons are reabsorbed again by the scintillator. Diffuse optical transmission measurements were performed on a 0.4mm thick slab of compressed EJ-426-HD2. The results show 1.85% diffuse light transmission at 450nm. This is a very good representation of the scintillator material and thickness used for the actual CANDOR detector. As a worst case, less than 2% of generated photons will reach the WLS fibers when neutron absorption takes place near the outside surface of the detector.

If neutron absorption takes place just 50μm from the WLS fibers, then nearly 65% of the generated photons will reach the WLS fibers.

4.1.3. Photon Transport

It was discussed in Chapter 3.3 that about 98.5% of photons that reach the WLS fibers are absorbed and re-emitted by the Y-11 fluorescent dye, and this photon re-emission is isotropic such that only about 5% of photons are transported by the WLS fiber cylindrical waveguide in each direction (10% in both directions). Overall, between 5%-10% of photons will be transported into the SiPM device depending on the quality of the optical couplings: scintillator/WLS fiber, WLS fiber/end-reflector, WLS fiber/SiPM.

4.1.4. SiPM photo-detection efficiency (PDE) & SiPM Gain

The photodetection efficiency of the SensL MicroFJ-30035-TSV device is about 30% for 476nm photons when the device is biased to V_{BR} + 5V (which is the operating voltage for the CANDOR detector). The overall PDE depends on a number of variables including the quantum efficiency and the microcell fill factor.

The SiPM is the point in the signal chain where the leap is made from an optical signal to and electrical signal. Since the SiPM is detecting single photons, a very high optoelectrical gain is needed for signal readout. After a photon detection, a MicroFJ-30035-TSV microcell discharges of 5.0×10^6 electrons at $V_{bias} = V_{BR} + 5V$. Since the breakdown voltage is specified to ± 0.25V, the opto-electric gain will vary by ± 5% from between devices.

4.1.5. Preamplifier gain

The gain of the preamplifier is 10V/mA and it includes an 50Ω output termination resistor. The circuitry shows very high fidelity with a very low white noise level. The preamplifier will not introduce significant electrical noise, but the cabling between the preamplifier and the pulse shape discriminator is more susceptible to picking up electrical noise as well as creating opportunity for ground loops.

4.2. Sources of Noise

The signal flow diagram (*Figure 38*) also shows several noise sources which are injected at different stages.

4.2.1. Gamma scintillation noise

The first source of noise is scintillation light produced by gamma radiation. ZnS(Ag) is also energized by high energy photons (X-rays, gamma rays). The properties of zinc-sulfide phosphors have been studied in depth in the past, so some of these characterizations can offer insights into how many photons are produced by gamma radiation in the CANDOR detector.

In one study, a 107µm thick screen was illuminated with 50keV x-rays, and was found to absorb 55% of the x-ray energy [114]. The absorption depth of ZnS increases linearly with photon energy, but with the CANDOR scintillator thickness of about 900µm, about 50% of photon energy will be absorbed by the detector at an energy of

500keV. Not all of the energy will be deposited in the ZnS phosphor, because the scintillator is a mixture of several materials. As a very rough estimate, about ~50% of gamma energy is deposited in the ZnS(Ag) phosphor. Combining these very rough estimates, about 25% of gamma energy is deposited in the CANDOR detector's ZnS phosphors.

ZnS(Ag) has a photon energy conversion efficiency of about 23% [114]. This efficiency is used to estimate the number of 430nm photons produced per gamma photon. *Table 4* shows estimates of photon production by the CANDOR detector in response to several gamma sources. Cesium-137 and cobalt-60 isotopes are commonly used in radiation spectroscopy for calibration. Boron-10 gamma resulting from neutron absorption is the predominant gamma radiation at the NIST Center for Neutron Research, because boron is used in neutron shielding materials.

Table 4: Photon production estimates by ZnS(Ag) from gamma absorption

Gamma source	**Photon Energy**	**# of 430nm photons (η_c = 0.23)**	**# of photons @ 25% ZnS energy absorption**
B-10 fission	480 keV	38069	9517
Cs-137 source	662 keV	52503	13126
Co-60 source	1.33MeV	105483	26371

Photons generated by gamma radiation are subject to all of the same photon transport losses described earlier. The only difference is that production of 430nm photons are distributed along the flight path of the gamma photon which often extends over the entire depth of the CANDOR detector, whereas neutron generation of photons is very localized.

4.2.2. Light leaks

The CANDOR detector measures very faint light pulses… so faint that the CANDOR detector must be housed in a box that is perfectly dark to outside light. One issue that has come up while implementing the CANDOR detector has been ambient light leaking into the detector chamber. This generally results in the SiPM signal being very noisy, as if the dark count rate was exceedingly high with frequent and random microcell discharges. Light which leaks into the dark chamber can be conducted through the WLS fibers to the SiPM, or strike the SiPM directly. Light leaks have been eliminated in our designs through the use of optical gaskets and proper mechanical design. The signal processing work in this paper assumes that there are no external light leaks.

4.2.3. SiPM dark counts, cross-talk, and afterpulsing

SiPM nonlinearities including dark counts, cross-talk, and afterpulsing (see chapter 3.4.2) are perhaps the most troublesome source of noise from a signal processing perspective. Dark counts are frequent and when combined with cross-talk and afterpulsing they will produce large (albeit infrequent) pulses when these effects superimpose over one another, or “pile-up”. Sometimes, these effects can pile-up in such a way as to resemble a very faint neutron signal. SiPM nonlinearities superimpose themselves overtop gamma noise as well, which raises the risk of falsely interpreting signals. Examples of noise signals will be illustrated later.

4.2.4. Electrical noise

Electrical noise can couple onto signal cables. Several common sources of noise include ground loops, RF noise, and crosstalk from adjacent cables. RF noise has not been observed during our circuit development.

Ground loops have been a design concern. Switching DC power supply noise has been observed by Tsai and Pritchard, and this noise was determined to have coupled into the signal lines through ground loops. The effects have been eliminated by isolating the DC power-supplies and grounding the entire system at a single point.

Capacitive cross-talk from adjacent signal lines in a ribbon cable has been observed by Ziegler and Chabot, but the effect is about 1% crosstalk for a 1 nanosecond rise time (50mV peak amplitude observed from a 5V square wave with 1 nanosecond rise time). Our preamplifier rise times are 40ns, so we do not expect capacitive crosstalk to pose a serious issue.

White noise is also evident on our signal traces, but the amplitude of this noise is very low in comparison to the dark-noise amplitude and it can be neglected. Electrical noise issues have been addressed through proper circuit design. As with “light leaks”, electrical noise will be neglected in the proceeding analysis and discussion.

4.3. Objectives of Signal Processing

There are three main objectives for signal processing:

1. High Neutron Identification >70% minimum, >90% preferred

2. Very High Noise Rejection ($< 10^{-7}$ detections per gamma, < 1 noise count per 10000 seconds)
3. High Count Rate (> 10000 neutrons per second with minimal deadtime)

It was discussed previously that overall detection efficiency is one of the most important criteria for neutron detectors used for neutron scattering. Neutron sources are very costly to build, maintain, and operate. Despite this, the neutron fluence usable for experiments is still very low and exposure times are very long. Detecting every neutron possible is most important. Overall detection efficiency is calculated as follows:

Equation 1:

$$Detection\ Efficiency\ =\ (Absorption) \times (Neutron\ ID\ Rate)$$

Signal processing's role in improving detection efficiency is to identify neutron signals from noise with very high efficiency and nearly zero false positives. In Chapter 2.9 it was discussed that neutron scattering experiments require very high noise rejection so that very faint scattering features can be resolved over a 10^8 dynamic range of neutron intensities.

Given that a detector and signal processing scheme meets the noise rejection requirements, the neutron ID rate should be very high (~95% - 99%). If the neutron ID rate is lower than this, it is likely that the detector is not designed well, because it does not produce a strong enough signal from fission products. If this is the case, the neutron absorber layer can be thinned to allow fission products to escape and deposit more energy in the signal creating medium (34-layer boron thin-film detectors for instance). If the

detector has an extremely high neutron ID rate (>99%), it is likely that the absorber layers can be made thicker to absorb more neutrons, because the signals produced by the fission products are more than strong enough. The optimum trade-off between absorption strength and signal strength will be application specific.

The maximum count rate stems from the physical limits of the CANDOR scintillator. In ***Table 3***, the signal decay time of the CANDOR detector is about 2μs. If a second neutron pulse arrives before the first neutron signal has decayed, the second pulse may not be resolved from the first, and only one event will be counted. This concept is known as "dead-time", or the amount of time following an event before a second event can be reliably identified. The CANDOR detector has a non-paralyzable deadtime, which means that if a second event arrives within the deadtime window of the first event, then one event will be counted. For paralyzable systems, if a second event arrives within the deadtime window, neither the first nor second events are identified. For the non-paralyzable case, the actual number of events (N_{actual}) can be calculated from the measured number of events ($N_{measured}$) at high count rates using the following equation:

Equation 2:

$$N_{actual} = \frac{N_{measured}}{1 - N_{measured}\left(\frac{\tau}{T}\right)}$$

where τ is the deadtime of the system and T is the average time interval between events. The arrival time of neutrons is assumed to be random.

The deadtime of a system can be computed from the measured count rate vs. actual count rate if the actual count rate is known. The actual count rate can be inferred by using a low efficiency fluence monitor with minimal deadtime in the same neutron

beam as the detector under test. Or, a progression of attenuators with a known attenuation factor can be inserted into the beam to create a progression of count rates. ***Figure 40*** shows how non-paralyzable systems with various deadtimes behave as the event rate increases. At high count rates, the measured rate plateaus and the actual count rate becomes uncertain.

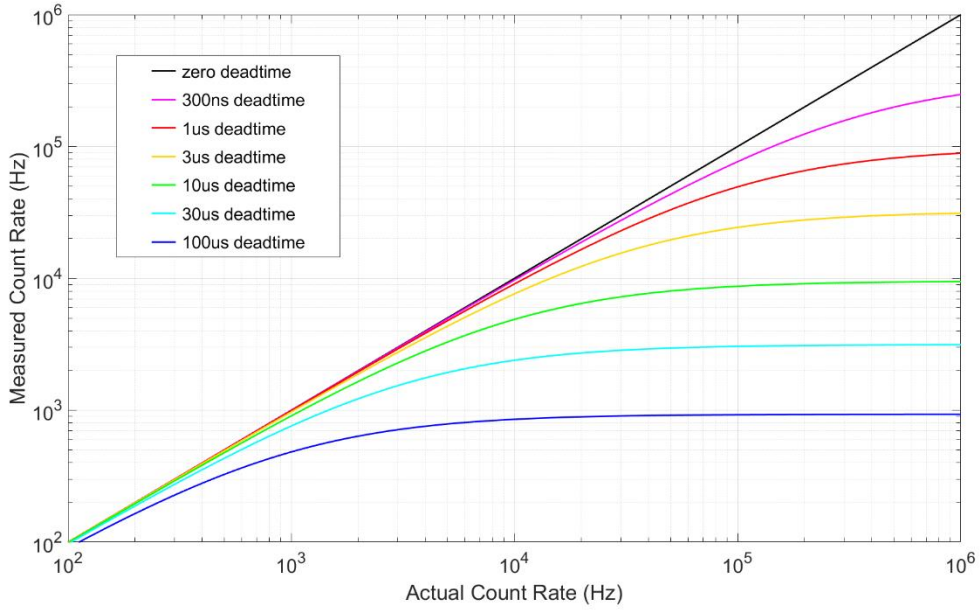

Figure 40: The count rate behavior of detector systems with a progression of deadtimes

The deadtime of the CANDOR detector should be as short as possible. As a benchmark, many 1cm diameter Helium-3 tube detectors have a deadtime of 1μs.

Chapter 5. Pulse Shape Discrimination (PSD) and Pattern Recognition Review

High neutron ID percentage, extremely high gamma and noise rejection, and high count rate are achieved using pulse shape discrimination (PSD) techniques. There are many, many PSD schemes that have been developed over time, and the signal processing schemes grow more and more complicated as computing power increases. Some of the original PSD algorithms were realized using analog electronics. More modern PSD systems perform some of the same PSD algorithms using analog-to-digital converters (ADCs) to first digitize a signal, and then algorithms are performed in real-time using field programmable gate arrays (FPGAs) or digital signal processors (DSPs). Some of the newest PSD algorithms use Fourier analysis, wavelet analysis, and artificial neural networks which require modern digital electronics [115], [116].

5.1. Pulse Height Discrimination

Signal energy is the most basic feature used discriminate between signal classes., when the energy spectra of the two classes overlap, then perfect discrimination is not possible. For better signal differentiation, Pulse Shape Discrimination (PSD) is used. There are a number of signal features which are exploited in order to discriminate between radiation types. The first pulse shape discrimination algorithms were realized using analog electronics.

5.2. Zero Crossing Algorithm

The zero-crossing algorithm passes the incoming signal through a tuned AC bandpass filter (RC-CR). The time between the rising edge trigger and subsequent zero crossing is measured using a Time-to-Analog Converter (TAC) via the Op-Amp ramp function. The signal and measurement are illustrated in *Figure 41*.

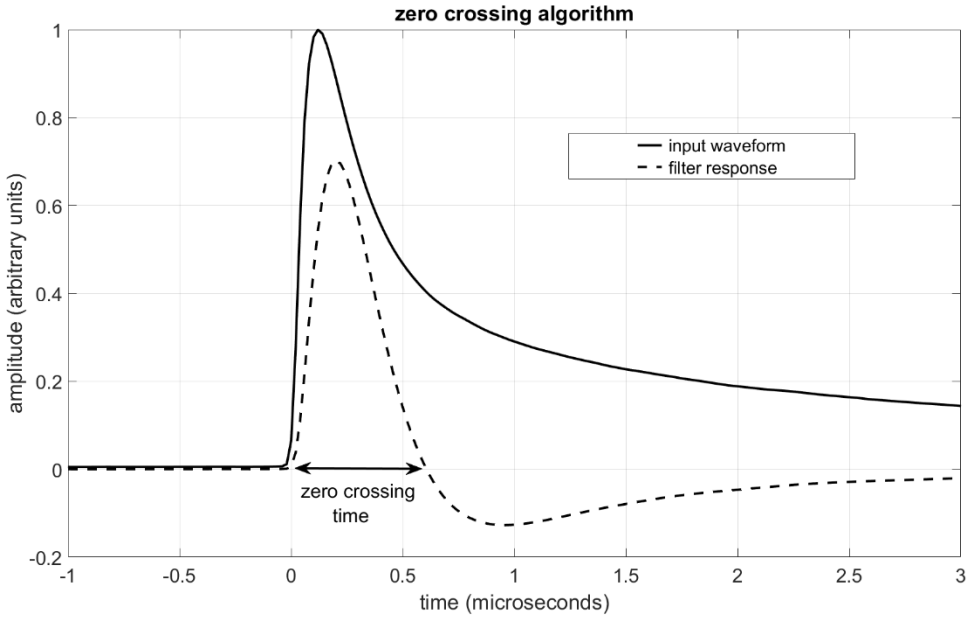

Figure 41: zero crossing algorithm

5.3. Rise Time Algorithm

In some scintillators such as Ce:$LiCaAlF_6$, the rise time of gamma signals is faster than the rise time of neutron signals. The rising edge trigger to waveform maximum time is used as a feature discriminate between signal classes (*Figure 42*) [117].

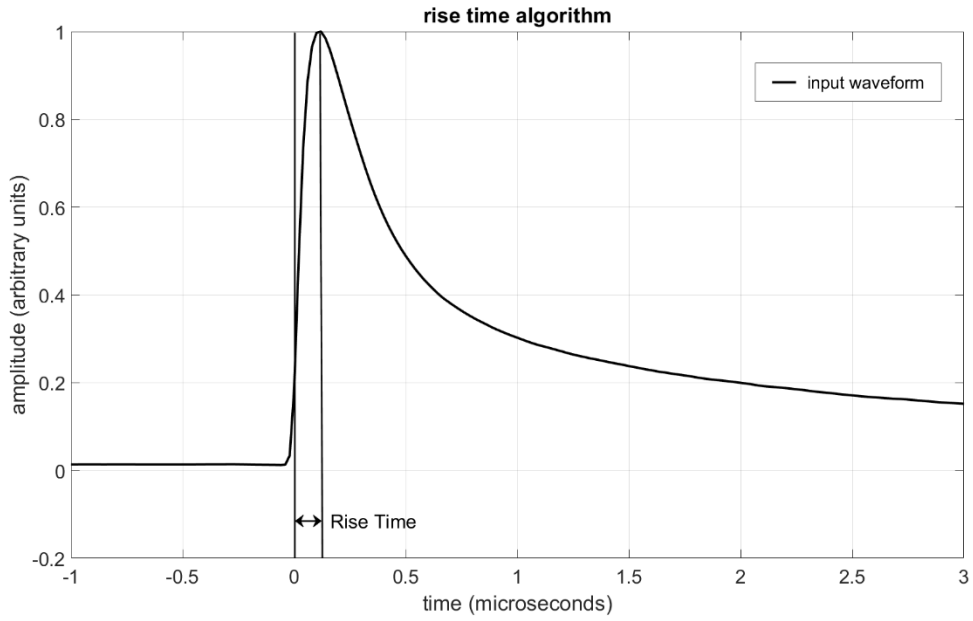

Figure 42: rise time algorithm

5.4. Charge Comparison Algorithm

Another commonly used PSD algorithm is the Charge Comparison (CC) method. After triggering, the incoming signal is integrated during two separate time intervals. The ratio of the two integrals is a discriminating feature between signal classes (see *Figure 43*).

The charge comparison algorithm has been used in both fast neutron detectors as well as slow neutron detectors. Fast neutron detectors are usually composed of hydrogenous compounds, including water and plastics, with a fluorescent dye for scintillation. High energy neutrons, usually > 1MeV, transfer momentum and energy to hydrogen nuclei which in turn ionize the scintillator medium. In the case of fast neutrons, the decay time of the scintillation is only slightly longer than for gamma photons, perhaps only 10's or 100's of nanoseconds longer. The differences are subtle. Still, the charge

comparison algorithm is able to discern these differences, especially at higher energies (>1MeV) where the signal-to-noise ratio is higher [38], [118]. In the case of fast neutron detectors, photomultiplier tubes (PMTs) are used almost exclusively as the photodetector, because SiPM non-linearities foul the signal so that the small differences between neutron and gamma decay times are no longer discernable. The charge comparison algorithm has also been used in GS20 glass scintillator, which is a slow neutron detector but does not have a strikingly different response to neutron and gamma radiation [119].

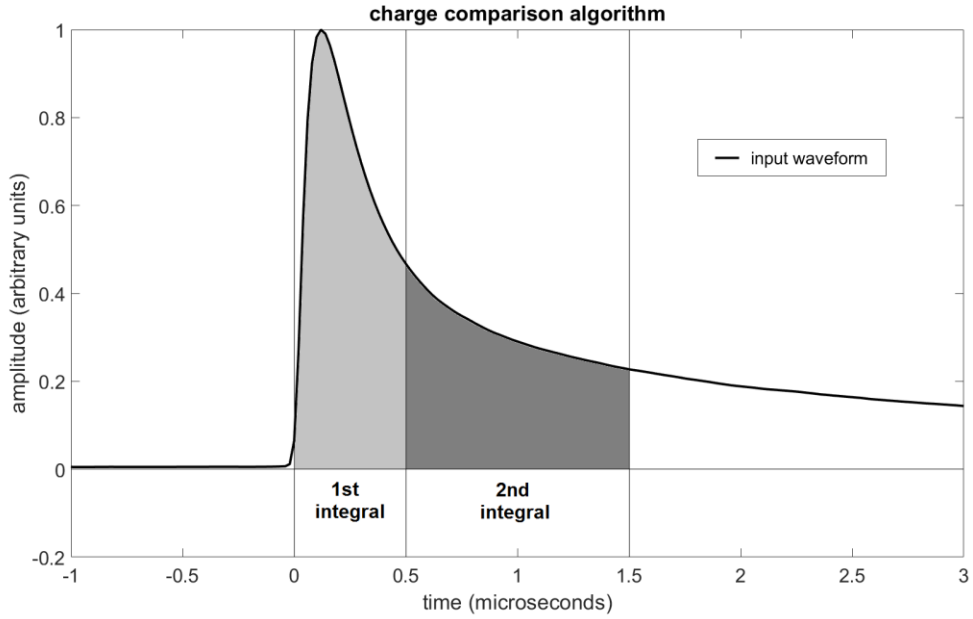

Figure 43: charge comparison algorithm

A variation of the charge comparison algorithm uses individual photon counting. In this case, the scintillation signal exceedingly small, averaging only 20 – 30 photons per event. Instead of integrating the area under the curve, individual photons are counted during delineated time intervals and compared [120] [121] [122] [123].

5.5. Customized Digital Filters

After digitizing input waveforms with an analog-to-digital converter (ADC), many types of digital filters can be applied to the input waveform. Trapezoidal filters are one of the simplest types of filters to apply, and can reveal subtle differences in pulse shape. By correlating the filtered output with a reference waveform, the result can be scored (*Figure 44*) [124].

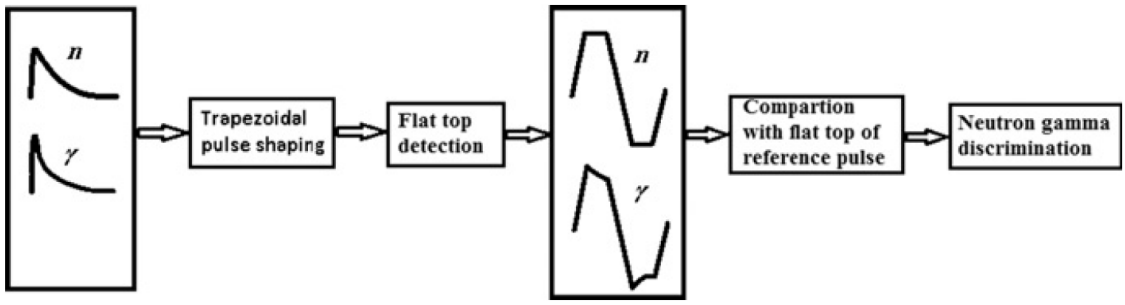

Figure 44: Trapezoidal filter & correlation **[124]**

Triangular filters have been used in a similar fashion for pulse shape discrimination, and have been shown to perform better than the charge comparison algorithm [125] [37]. A moving sum filter after signal differentiation has also been used successfully [126].

A customized filter was proposed in 1962 by Gatti and de Martini which maximizes the theoretical difference between pulse shapes of different radiation classes [127]. The scalar product of the incoming waveform and the customized weighting vector is evaluated. The resulting score is used as a discriminating feature. The weighting vector, *P*, is determined using *Equation 3*:

Equation 3:

$$P_i = \frac{n_i - \gamma_i}{n_i + \gamma_i}$$

where P_i is an element of vector P, n_i is the averaged normalized neutron amplitude at time i, and γ_i is the averaged normalized gamma amplitude at time i. The scalar product of the weighting vector, P, and the incoming waveform is evaluated with *Equation 4*:

Equation 4:

$$S = \sum_i P_i x_i$$

Where x_i is the input waveform and S is the pulse shape score. An illustration of two averaged and normalized waveforms as well as a customized weighting vector are shown in *Figure 45*.

Gatti's customized filter and similar variations have been used in many instances [128] [129] [130] [131] [132]. The technique has gained popularity as waveform digitizers and digital signal processing have made the algorithm easy to implement. The most popular electronics architecture for implementing these sorts of customized filters uses an analog-to-digital converter to digitize incoming waveforms and a field programmable gate array (FPGA) to evaluate the scalar product.

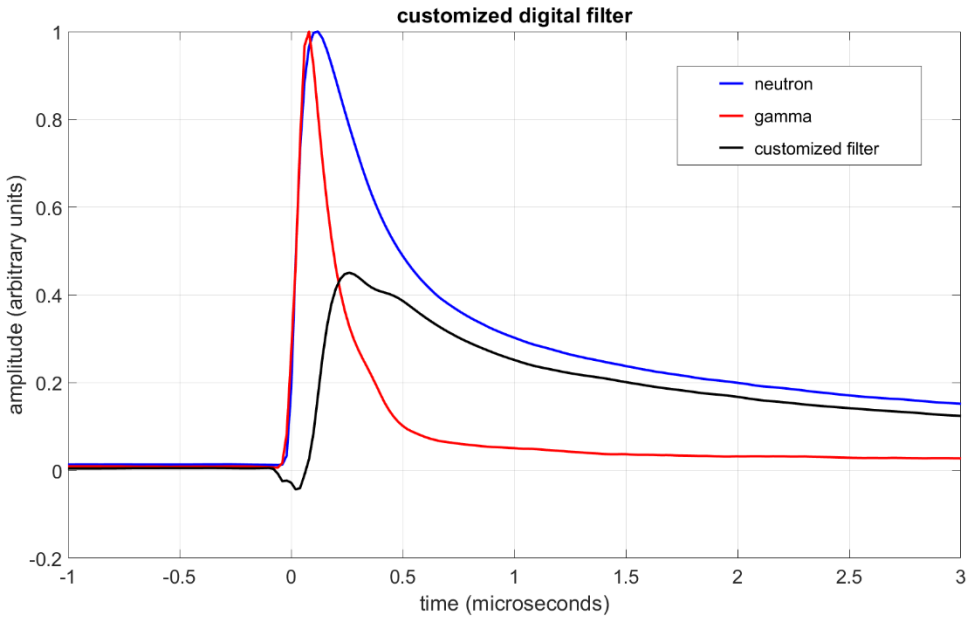

Figure 45: example of a customized digital filter

5.6. Pulse Gradient Analysis

Pulse gradient analysis (PGA) is similar to the charge comparison algorithm except that instead of comparing the accumulated charge over specific time windows, the waveform amplitude is compared at two discrete points in time: first at the waveform maximum, second at a set time after the maximum. The ratio of the two values is the pulse shape feature (*Figure 46*). A couple of examples show that PGA outperforms the charge comparison algorithm in specific instances [133] [134].

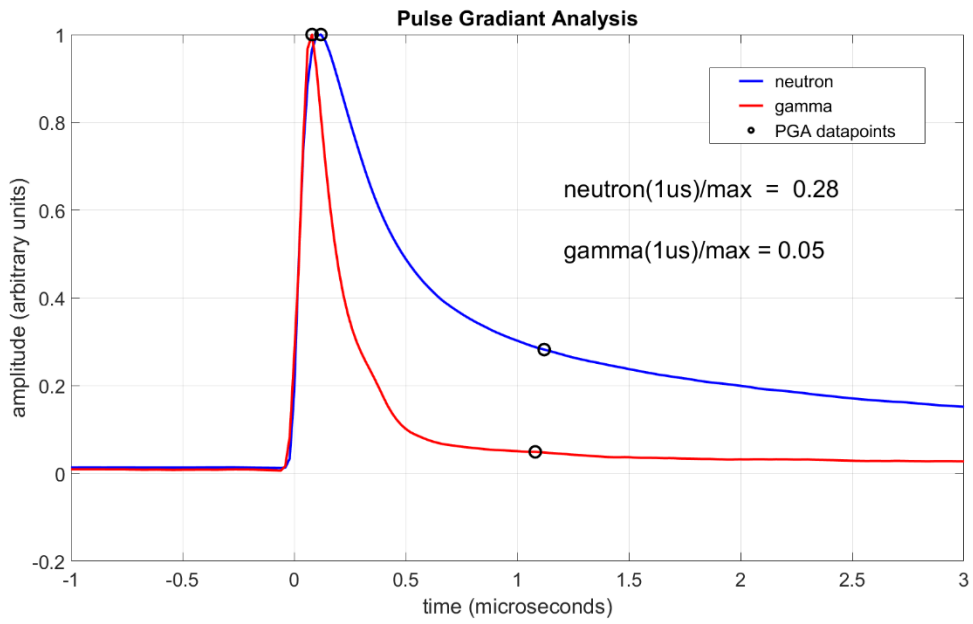

Figure 46: pulse gradient analysis

5.7. Frequency Gradient Analysis

Frequency gradient analysis (FGA) is similar to PGA in that the ratio of two discrete values is used as the shape feature. The difference between FGA and PGA is that PGA is a time domain technique. FGA is a frequency domain technique. A fast fourier transform (FFT) is computed from the input waveform, and then the energy content at two discrete frequencies are compared (*Figure 47*). FGA has been used in several instances, and the results were favorable when compared with the charge comparison algorithm, PGA, and digital filters [37] [135] [136]. The FFT computation works best when the waveform length is 2^n samples.

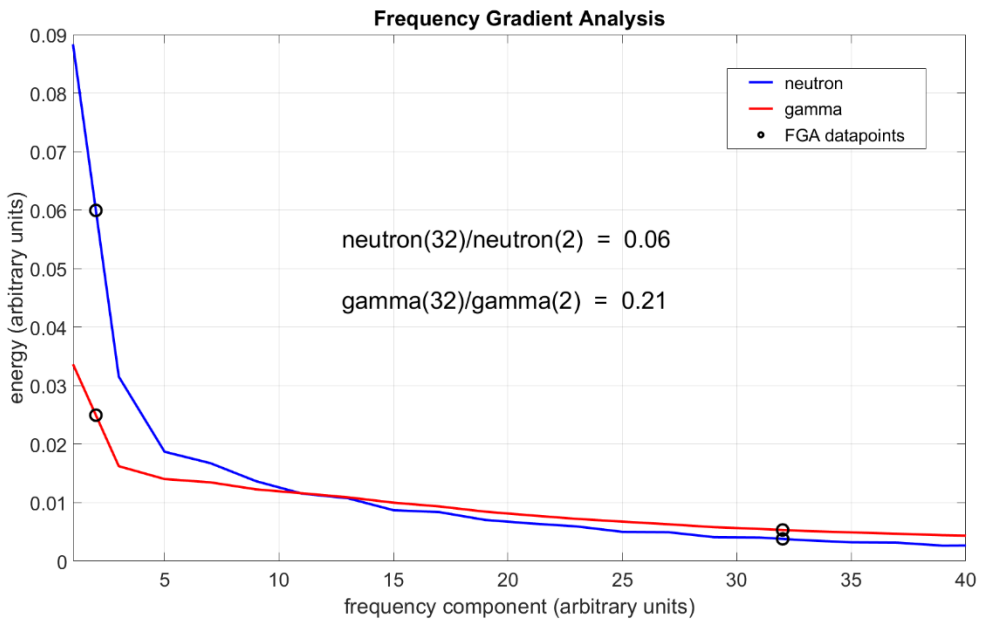

Figure 47: frequency gradient analysis

5.8. Wavelet Analysis

Wavelet analysis is a technique which examines both the time domain and frequency domain of a signal [137]–[139]. They have been a useful tool in a variety of fields from image compression, denoising, cardiology, encephalography, seismology, and audio deconstruction to name a few. Wavelets have also been used in the field of pulse shape discrimination for radiation detectors.

An appropriate wavelet shape depends on the characteristic shape of the underlying waveform. Haar wavelets [140], Daubechies wavelets [141], and Marr wavelets (Mexican hat wavelet) [142] are a few of the shapes that have been used in pulse shape discrimination. Wavelet analysis is excellent at detecting pile-up events and can identify features with minimal time length [143] [142]. The discrete wavelet

transform can be computed in real time, but it is computationally expensive and requires substantial processing resources [144] [145] [146].

5.9. Phoswich detectors

Phosphor sandwich detectors or “phoswich” detectors mix the signals from several different detection layers to classify radiation type. Radiation which interacts with different layers of a detector will have different mixtures of fast decaying components and slowly decaying components . Phoswich signal mixing requires a specialized physical design [147].

5.10. Feature self-discovery using artificial neural networks

Artificial neural networks (ANNs) are just recently being used to explore the field of pulse shape discrimination for radiation detectors. Most research has focused on identifying pulse pile-up and separating pulses which are super-imposed overtop one another, particularly in fast neutron detectors coupled to photomultiplier tubes [135], [147]–[151]. ANNs for pulse shape discrimination are currently an active field of study, and there has been limited use of ANNs in LiF:ZnS(Ag) detectors coupled to SiPMs.

5.11. Figure of Merit (FOM) for feature separation

A number of pulse shape features have been described in this section: zero-crossing time, charge comparison, rise time, response to digital filtering, pulse gradient,

frequency gradient, wavelet gradient, phoswich response, and ANN response. The effectiveness of each feature for separating neutron and gamma events is typically referred to as the Figure of Merit (FOM). For one dimensional features, the FOM is calculated as the distance between class peaks, divided by the combined full width half maximum of both class distributions, illustrated in *Figure 48*.

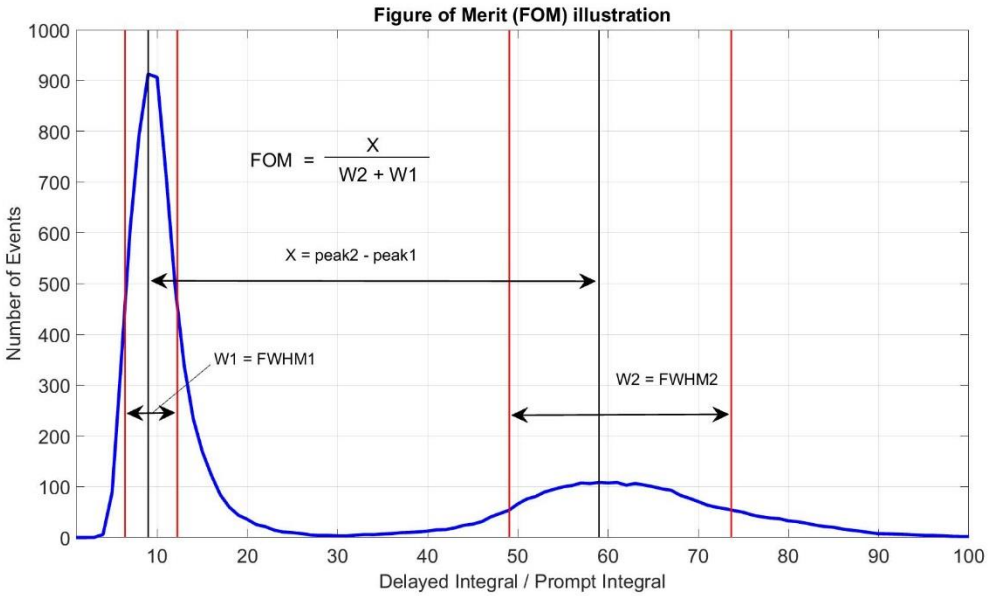

Figure 48: 1-Dimensional Figure of Merit (FOM) illustration

In multiple dimensions, the FOM is calculated as the distance between centroids divided by the total variance of the centroids.

Equation 5:

$$Gaussian\ FOM = \frac{\left(\mu_{neutron} - \mu_{gamma}\right)^2}{\sigma_{neutron}^2 + \sigma_{gamma}^2}$$

In both the 1-dimensional and multi-dimensional cases, a larger FOM indicates better separation between radiation types. So, the FOM can gauge the effectiveness of a pulse shape discrimination scheme.

5.12. Base Truth

Definitively knowing the class of a signal pulse (base truth) prior to classification by a PSD algorithm is important for gauging the algorithm's performance. Correct classification percentage and the false positive percentage are important metrics. There are several ways that the base truth of radiation signals can be ascertained.

Time of Flight has been used in mixed signal environments such as pulsed particle accelerators. When a pulsed particle beam hits a target, producing neutrons and gamma photons, gamma photons will travel from the target to the detector at the speed of light. In comparison, neutrons which have mass will arrive at the detector some time later. The time elapsed between the target strike and detection is used to determine the base truth of the detected signal [148], [152].

In the case of a noisy SiPM photodetector, a photomultiplier tube was coupled separately to the same scintillator crystal. PMT signal pulses were classified and used as the base truth for the much noisier SiPM signals [149].

Radiation source purity is another way to ensure the base truth of event signals. If gammas can be perfectly shielded from the detector while recording neutron waveforms, and conversely if neutrons can be perfectly shielded from the detector while recording gamma waveforms, then the base truth of both gamma and neutron datasets is established.

5.13. Pattern Recognition and Classification

Features (length, weight, energy, color, shape, etc.) are used by pattern recognition algorithms to classify objects. Principal component analysis (PCA) can identify which features are most important for classification [153].

If several features are correlated, they are not independent from one another. If this is the case, Independent Component Analysis can be used to reduce the number of features required for classification and in doing so will reduce the complexity of the classification algorithm [154].

After an appropriate number of features are identified for classification, there are several classification algorithms to choose from. Linear Discriminant Analysis (LDA) will find a line (2-dimensions), plane (3-dimensions), or hyperplane (4+ dimensions) that maximizes the Gaussian separation between two classes (*Figure 49*) [155].

A support vector machine (SVM) also tries to maximize the separation between to event classes. But, instead of maximizing the Gaussian separation, SVM maximizes the separation between the edges of the two datasets. If the datasets overlap (they are not perfectly separable), a “soft margin” is used minimize the overlap (*Figure 49*) [156]. SVM has been used in a gadolinium doped liquid scintillator coupled to a PMT to both classify a feature vector and give a confidence value [157].

Both LDA and SVM find linear boundaries between classes. In the case that the boundary between the classes is not linear, a “kernel” can be used to project the data onto a higher dimensional surface where a separating linear boundary does exist.

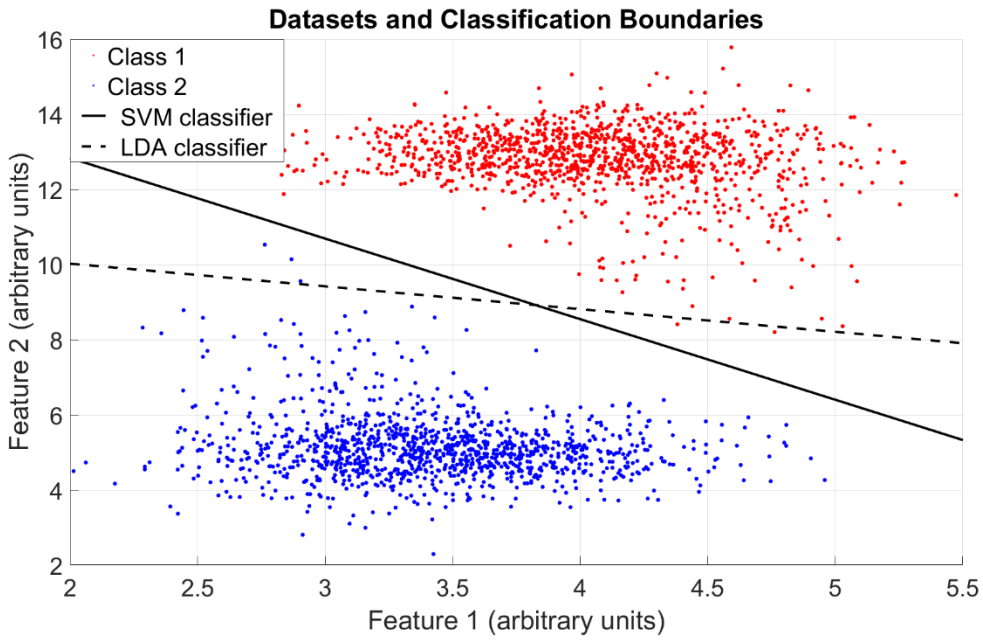

Figure 49: SVM maximizes the separation between edges of the two classes, while LDA maximizes the total Gaussian separation between the classes.

An Artificial Neural Network (ANN) is a nonlinear classification scheme where features are fed into the input later. Weighted combinations of the inputs can be fed into subsequent "hidden layers", and finally an output layer performs classification. A more complete description of ANNs can be found in [158]. Artificial neural networks have been used for classification of neutron events [147], [149], [151] as well as identifying pile-up events which require additional processing [135], [148], [150].

5.14. Pulse Pile-up and Reconstruction

In Chapter 4.3, it was mentioned that if a second neutron arrives during the classification period of a preceding neutron, the second neutron is discarded. This concept is known as discriminator dead-time, or a period of time following an event pulse

when the discriminator loses sensitivity. Secondary pulses which arrive during the classification period can also cause the discriminator to mis-label the event in some cases. At high event rates, pulse pile-up becomes a significant problem, and some researchers have turned to pulse fitting, wavelets, and ANNs to mitigate the issue.

In one case, an organic scintillator coupled to a PMT has very consistent and predictable signals, and pulse fitting has allowed for subtraction of the primary pulse from the incoming signal following event classification [159]. In [142], the use of Marr (Mexican hat) wavelets for feature extraction creates a classification scheme with a very short deadtime. And, several researchers have used ANNs to separately classify pile-up events as a third class separate from neutrons and gammas, and then use a separately trained ANN to classify pile-up cases [135] [148] [150], sometimes with pulse reconstruction. These methods are complex and difficult to achieve in a low-cost design and require substantial processing power for each detector. As computing power improves, these techniques may become more prevalent. The concept of pulse subtraction is used for the CANDOR detector, but the pulse subtraction is purely predictive, rather than using a curve fit after acquiring a complete waveform, and so this approach is done affordably in real-time.

5.15. Difficulties of Processing SiPM Signals

SiPM non-linearities such as dark noise, crosstalk, and afterpulsing cause major difficulties for pulse shape discrimination algorithms when photon yield is low as is the case with most LiF:ZnS(Ag) scintillators. Some publications demonstrate that the

average photon yield from neutron events in LiF:ZnS(Ag) can be as low as 22 individual photons with a standard deviation of 11 photons [121], [160]. In [161], the maximum observed photon yield from a neutron event was just 200 photons. The signal-to-noise ratio is a problem for sparce photon signals.

SiPMs superimpose their non-linearities overtop of these small signals. Modern SiPM devices have the lowest likelihood for dark noise, but the dark count rate still ranges from 50k – 200k counts per second per mm^2 of device area. Statistically for a 3mm x 3mm SiPM device ($9mm^2$), there will be a spontaneous pixel discharge every microsecond, and the probability of multiple discharges during a 2μs classification period is all too high. Spontaneous discharge combines with crosstalk and afterpulsing to create large signal artifacts on occasion. Very high gamma rejection (1 detection per 10^7 ^{60}Co incident gamma photons) has been reported to be the most challenging requirement in a LiF:ZnS(Ag) / SiPM neutron detector due to the high signal-to-noise ratio [162]. When the performance of SiPMs has been benchmarked against PMT photodetectors, the results always indicate better overall performance for PMT systems (detection efficiency, accuracy) [149] [163].

In terms of pulse shape discrimination, low signal-to-noise ratio manifests itself as greater signal variance, greater feature variance, and lower Figure of Merit (FOM) which is based on the Gaussian separation between classes.

Chapter 6: CANDOR Signal Processing and Performance Metrics

6.1. Hardware

Two separate signal processing schemes were developed for CANDOR. (1) An analog solution uses an analog Pulse Shape Discriminator (PSD), which outputs a TTL logic level pulse in response to an event. (2) A digital PSD uses an A/D converter to digitize the preamplified signal at a sample rate of 50MHz followed by an FPGA for signal processing (*Figure 37*). The dynamic range of the A/D converter on the digital PSD is between 0V -2V.

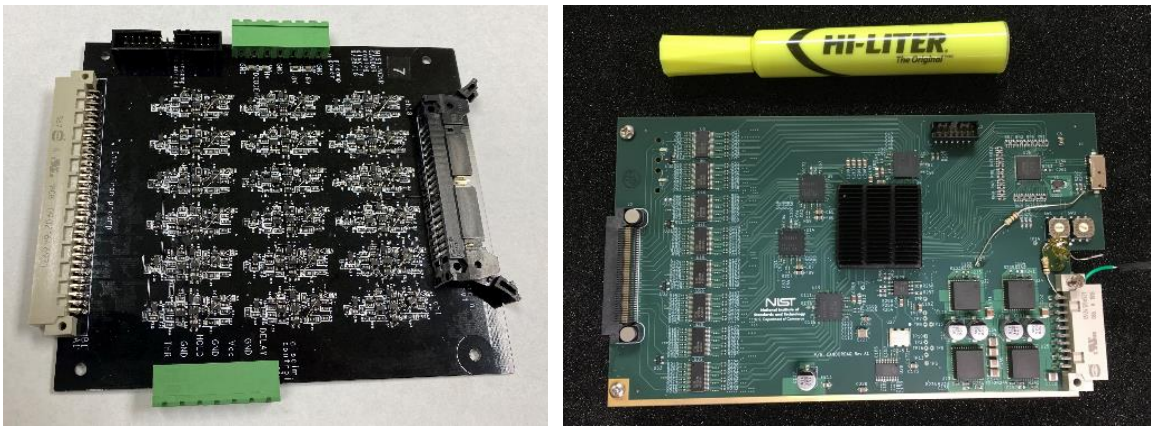

Figure 50: (left) analog PSD. (right) digital PSD

The digital PSD circuit board is named the "CANDOR_DAQ", for CANDOR data acquisitions. CANDOR_DAQ has several data export options. With the detection of each event, an event word is generated and sent to a PC. The event word contains a timestamp marking the event's arrival time with a precision of 100ns, compatible with a PTP timing protocol. It can also send information about the size of the pulse. And, the

digital PSD can record and send a complete waveform trace, like an oscilloscope but with an elaborate triggering algorithm. The PSD schemes for both analog and digital discriminators will be discussed in detail later.

6.2. Experiment Test Station

We used the PHADES (Polarized ^{3}He and Detector Experiment Station) test station at the NIST Center for Neutron Research to conduct our testing. PHADES uses a highly oriented pyrolytic graphite monochromator set at a fixed angle to steer a 4.87 meV (4.1 Å) neutron beam into a shielded cavity formed of borated polyethylene. Post-collimation, a rectangular beam has a width of 5 mm, a height of 20 mm, and the beam current can be varied using borated glass attenuators. Most detector measurements use a beam current of approximately 250 neutrons per second. A diagram illustrates the setup in *Figure 51*.

We recorded neutron waveforms while the reactor was on, expecting that some of the waveforms captured could include boron-10 capture gammas. To assess whether or not a boron-10 gamma field would foul the neutron dataset, the neutron beam was blocked completely with a 6.35mm thick plate of borated-aluminum, which totally absorbs the collimated neutron beam and isotropically emits 0.48MeV gamma photons in response to neutron absorption. Only background neutrons and multiply scattered neutrons occasionally struck the CANDOR detector. Under this configuration, the trigger rate for event detection dropped to 0.19Hz and most of these waveform recordings displayed as neutrons rather than the characteristic gamma response. This low boron-10 gamma trigger rate would account for less than 0.1% of the trigger rate when the detector is in a 250Hz neutron beam. The 0.48MeV photon rate on detector is calculated to be

2.3KHz by approximating the borated-aluminum beamstop as an isotropic point source emitting gamma photons at a rate of 200KHz and a distance of 5cm.

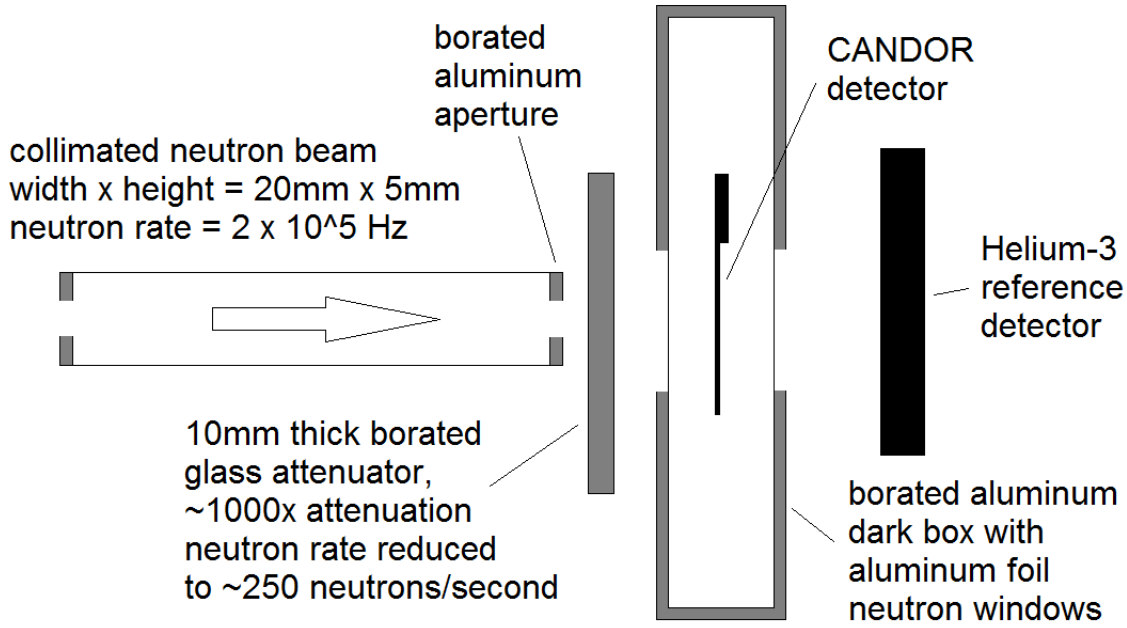

Figure 51: PHADES experiment test station diagram

We tested gamma rejection using two different isotopic sources: A ^{137}Cs source with an activity of 293kBq and a ^{60}Co source with an activity of 82.7kBq. The gamma rejection measurements were taken while the reactor was off to minimize the number of neutron capture events in the dataset. The number of gamma photons incident on the detector was calculated from the exposure time, source activity, photon yield per decay, and geometry factor (the source was placed directly on the detector so that the detector occupies nearly half of the solid angle). An example calculation (***Equation 6***) for the ^{60}Co photon exposure uses a geometry factor of 0.4:

Equation 6:

$$^{60}Co\ incident\ photons = (54000\ seconds) \times \left(82700\ \frac{disintegrations}{second}\right) \times \left(2\ \frac{photons}{disintegration}\right) \times (0.4)$$

$$^{60}Co\ incident\ photons = \ 1.85\ \times 10^{9}\ photons$$

6.3. Waveforms

The rationale behind the CANDOR pulse shape discriminators is better understood after viewing a series of pulse waveforms, some of neutrons, and others containing various mixtures of noise. First of all, there is a constant and random background of thermal noise generated by the SiPM illustrated in *Figure 52*.

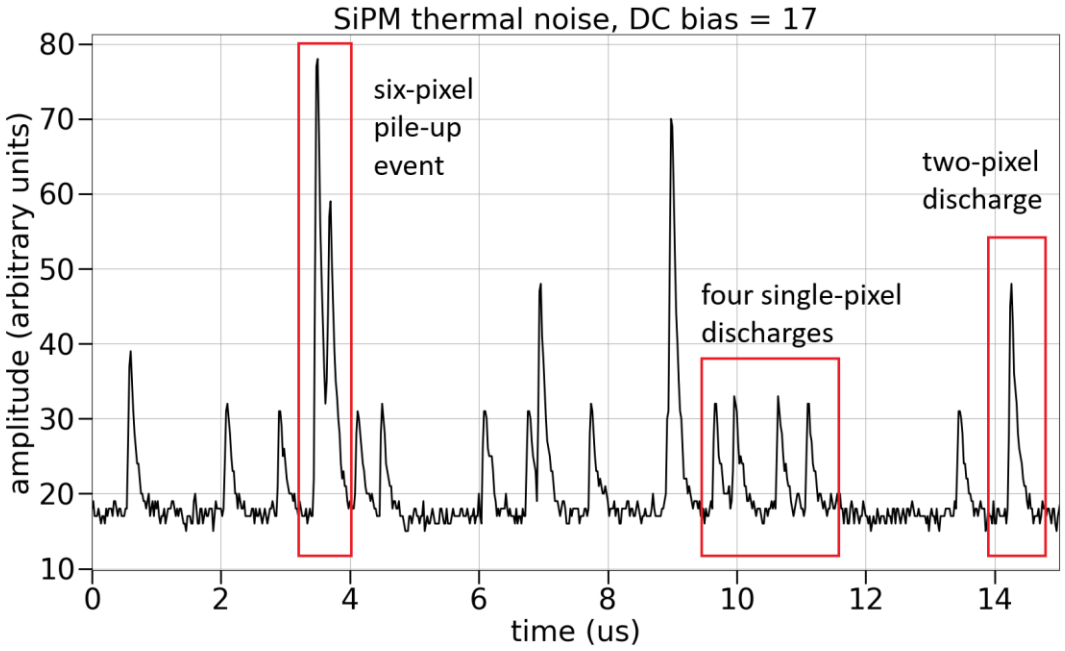

Figure 52: SiPM thermal noise

The smallest pulses are the result of a single pixel, or microcell discharge. The discharge is caused by a thermally created electron-hole pair in the avalanche region of the SiPM as opposed to e-h pair creation via the photoelectric effect. The thermal noise can be reduced by cooling the SiPM to a lower temperature. But, for practical reasons the CANDOR detector is kept at room temperature. Occasionally, two or more pixels discharge simultaneously (usually the second pixel is stimulated by the first via crosstalk) creating a larger pulse. Larger discharges are also possible with ten or more pixels firing

in close succession. These larger events will be referred to as “noise pile-up” events. A six-pixel pile-up event is seen in *Figure 52*.

Thermal noise is quantized. It comes in discrete numbers of pixel discharges. And, the total electrical gain in the signal chain can be found by analyzing the thermal noise events.

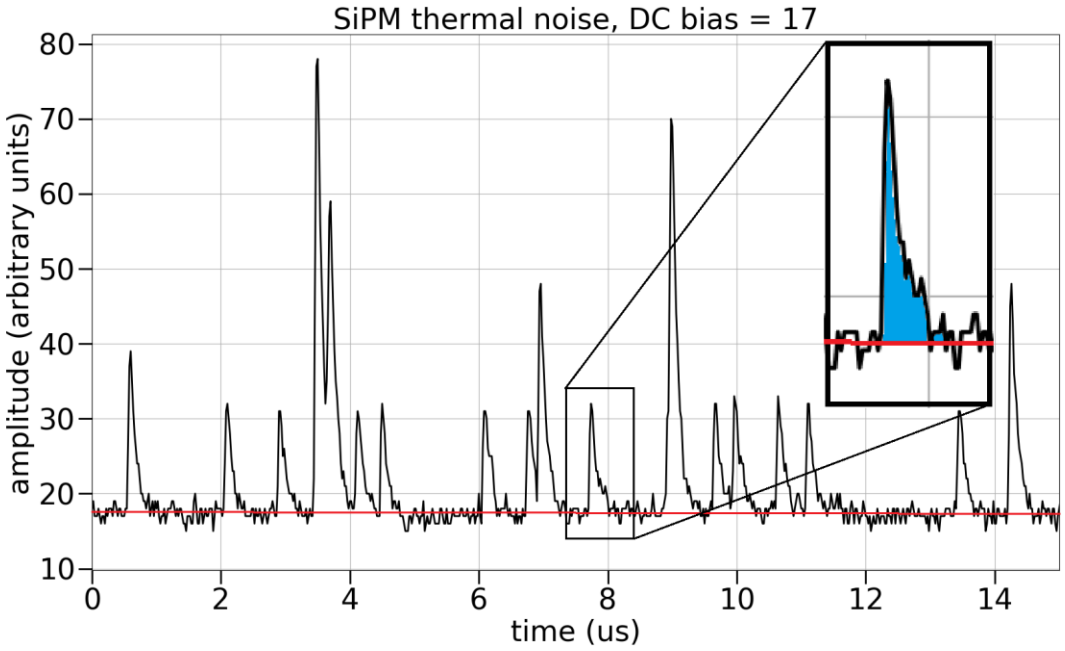

Figure 53: The area under the curve is highlighted for a thermal noise event

Figure 53 illustrates how the area under the curve of a single pixel discharge is calculated. A large number of thermal noise events can be integrated in this way, and the results are histogrammed.

Figure 54 shows a histogram of a large number of thermal events. You can see the quantized behavior of one, two, three, or more pixels discharging. The “single pixel discharge” can be calculated by subtracting the one-pixel value from the two-pixel value. This way, the DC bias does not affect the calculation of the pixel discharge. In *Figure 54*,

the single pixel discharge is calculated to be 100. Later, larger pulses will be normalized by the single pixel discharge to give the size of the pulse in pixel discharges, which follows the number of photons observed by the SiPM. This normalization also removes the electrical gain as a factor in system performance, which varies by ±10% (*Figure 113*).

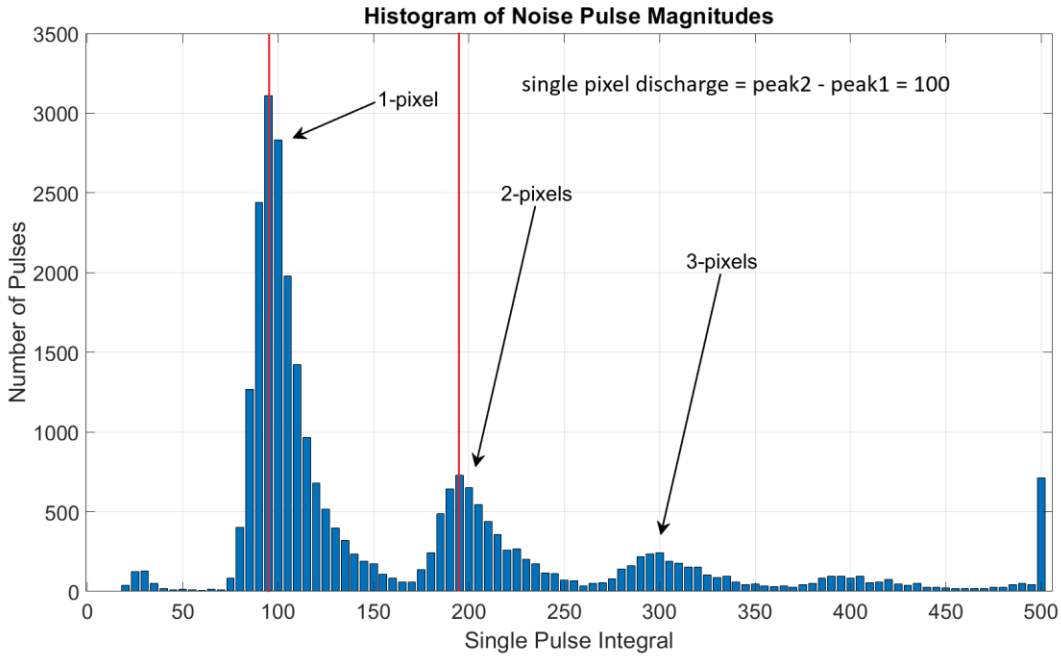

Figure 54: Histogram of thermal noise shows quantized behavior

Figure 55 shows archetypal waveforms of a thermal event, a gamma event, and a neutron. Gamma events and thermally generated SiPM events are short lived (~ 300 ns) compared to neutron capture events, which can last for tens of microseconds (due to delayed fluorescence of ZnS(Ag) following concentrated energy dissipation of the ^{6}Li fission products (Knoll, 2010). Also, the amplitudes of these signals can vary widely, because the ^{6}LiF:ZnS(Ag) scintillator is largely opaque to its scintillation light. Neutron capture events occurring far away from the WLS fibers will result in a tiny trickle of

photons reaching the photosensor. Of the hundreds of thousands of photons produced in a neutron capture event, only between 30 and 3000 photons are detected by the SiPM.

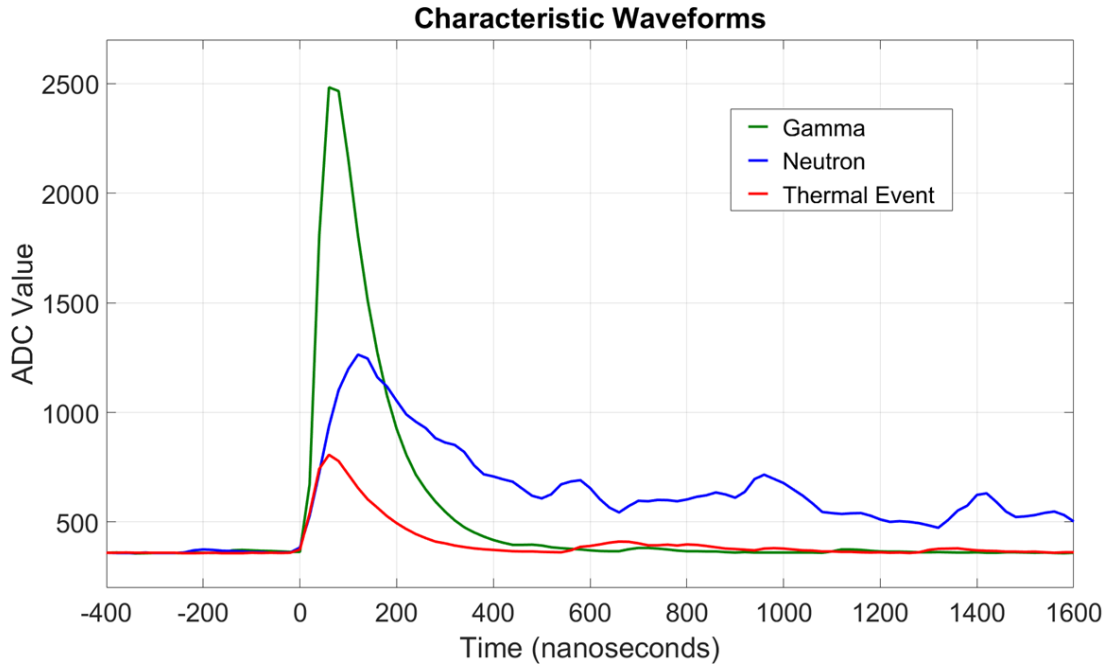

Figure 55: Characteristic waveforms

Neutron signals can vary by as much as 100 times in amplitude, depending on the photon production and transport to the SiPM from the scintillator. The shapes of neutron pulses are also jagged and irregular. Several example waveforms show the variations between neutron events in *Figure 56*.

The differences between neutrons and gammas appear to be very obvious. And, for the most part this is so. However, the neutron scattering requirements demand high detection rates even for small neutron pulses, and extremely high gamma rejection. There are a problematic number of noise/gamma pile-up events which eclipse small neutrons in size, and which have shapes that are not so easy to discern from neutrons. *Figure 57* shows two such waveforms.

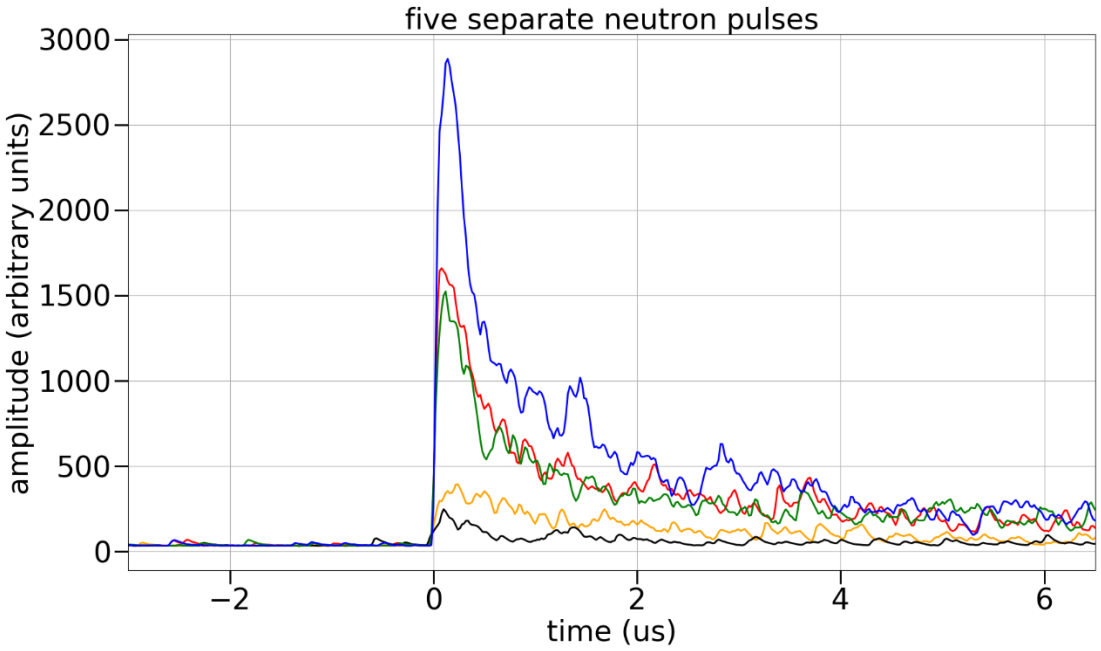

Figure 56: five neutron pulses show large variation in amplitude and shape

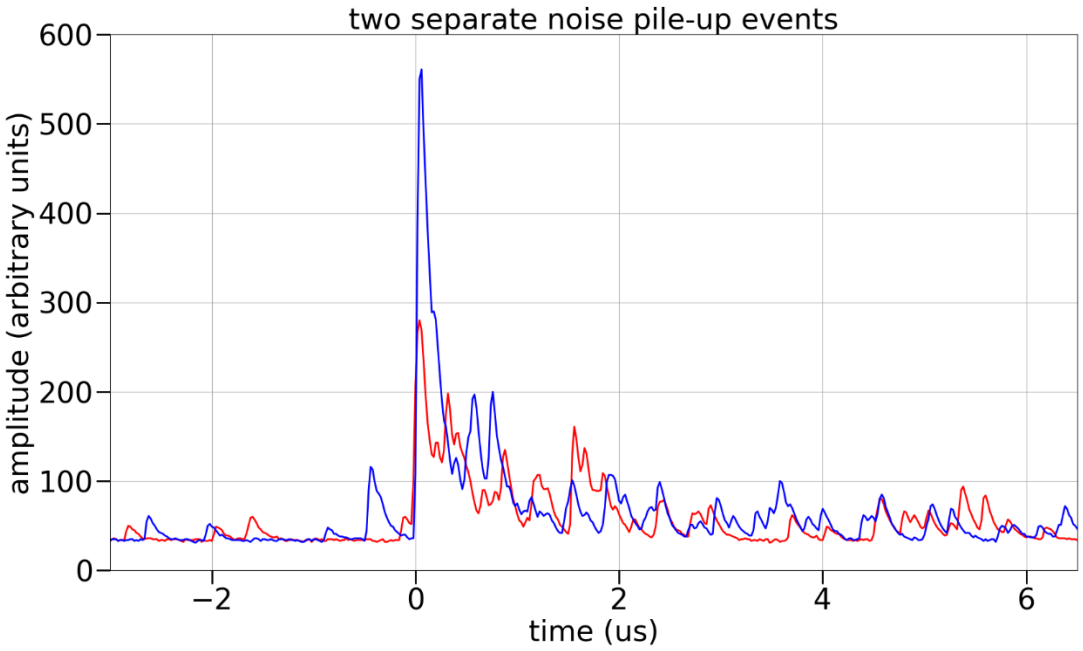

Figure 57: Two gamma/noise pile-up events

6.4. Pulse Energy Histogram (Pulse Height Distribution)

The shapes and sizes of noise, gammas, and neutrons have been discussed. Now it's time to look at some of the statistical distributions. First, the concept of an energy histogram is introduced. *Figure 58* and *Figure 59* show normalized energy histograms for two different detectors. These two detectors are actually the two boundary cases for all CANDOR detectors that will be used in the CANDOR instrument. Detector #558C is among the dimmest and poorest performing, and detector #418C is among the brightest and best performing.

Every neutron pulse generated by the CANDOR detector is integrated for a period of 1.28μs. The number of pixel discharges during the integration period is calculated from the integral and the single pixel discharge (*Figure 54*). The pulse is histogrammed by the number of pixel discharges (photons). The photopeak of the detector is the most common sized pulse in terms of number of photons. When interpreting these energy histograms, it is clear that detector #418C of *Figure 59* is almost twice as bright as detector #558C of *Figure 58*, yielding about twice as many photons per neutron event. However, the cobalt-60 energy spectrum does not scale by the same amount. In fact, the energy spectra of cobalt-60 gammas nearly identical for both detectors, with a slightly higher photon yield for detector #418C. A high trigger threshold (~50 photons) was used to reject most gammas, so only the highest yielding gamma events are seen in the histogram. The number of high yielding gammas is the most important feature for neutron/gamma discrimination.

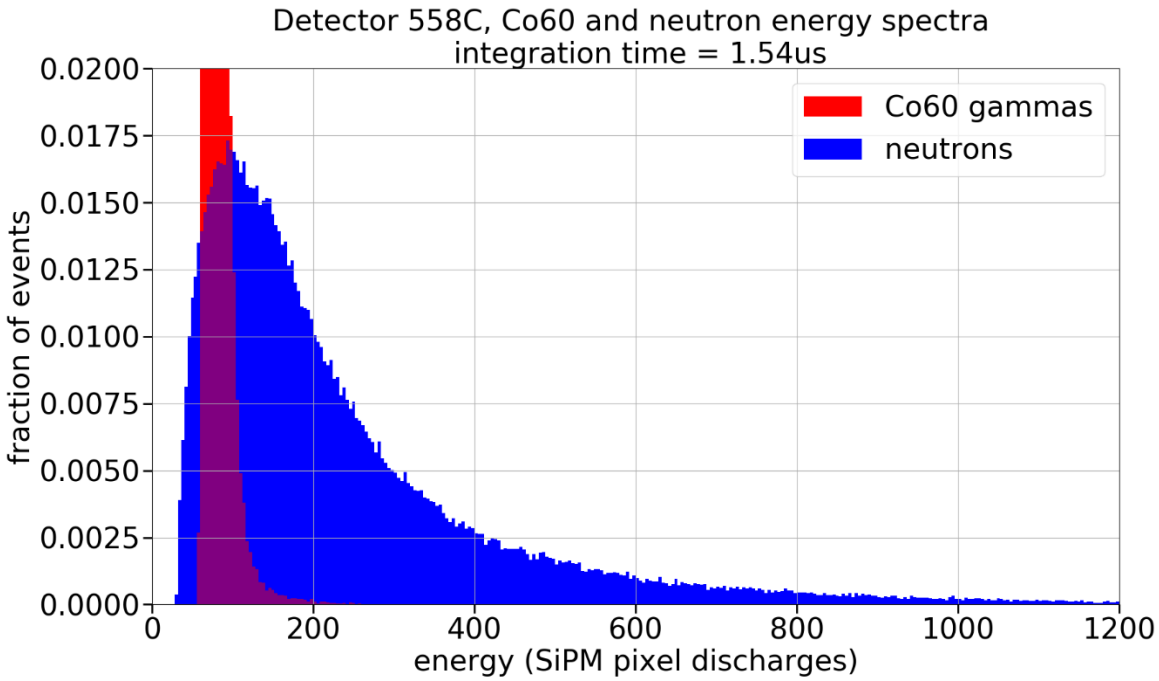

Figure 58: Energy Histogram for a detector with a neutron photopeak of 106 photons

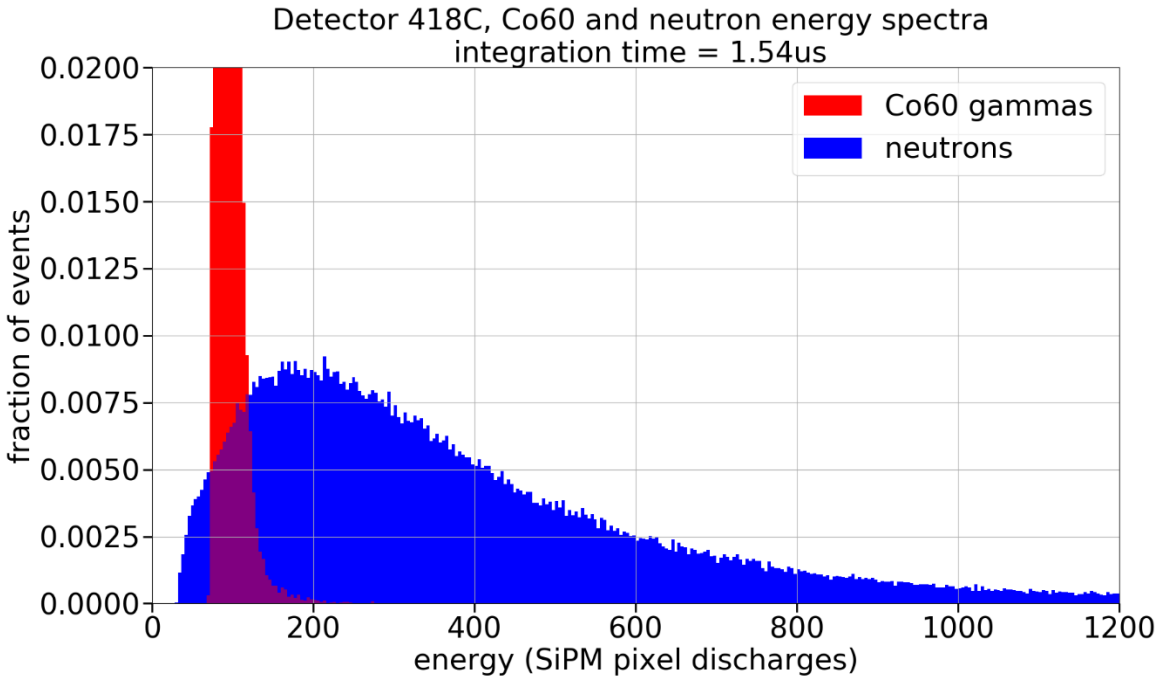

Figure 59: Energy Histogram for a detector with a neutron photopeak of 204 photons

Cobalt-60 and cesium-137 were both used as gamma sources for characterizing detector #418C and #558C. Cobalt-60 gammas are more energetic, with photon energies of 1.17MeV and 1.33MeV. Cesium-137 gammas have an energy of 662keV, about half the energy as a cobalt-60 gamma. Energy spectra using the ^{137}Cs source were also obtained. The ^{137}Cs spectrum follows a similar trend to the ^{60}Co energy spectrum but shifted to the right with lower photon yield.

6.5. Receiver Operating Characteristic (ROC) curves from energy spectrum

A receiver operating characteristic curve illustrates the ability of a binary classifier (neutron or not neutron) to identify events as a classification threshold is increased. The ROC curve compares the rate of true positives vs. false positives; in this case, neutron events being classified as neutrons vs. gamma events being classified as neutrons. This is the appropriate gauge for detector performance, because it simultaneously compares first two neutron detector requirements:

1. High Neutron Detection Efficiency. <70% is unacceptable. >90% is preferred.
2. Very High noise & gamma rejection. Fewer than one detection per 10E+7 gammas

In the case of a 1-dimensional histogram, such as the energy spectrum, a detection threshold is set as the number of pixel discharges. The threshold can be raised to reduce the number of gamma events (false positives) or lowered it to include more neutron

events (true positives). Because the gamma fluence rate is known, the recording duration of the gamma dataset was known, and the same trigger settings were used for the neutron dataset, we can calculate the neutron ID rate and gamma rejection as functions of the discriminator threshold. The neutron ID rate is calculated as:

Equation 7: $$Neutron\ ID\ Rate = \frac{\#\ neutron\ events\ above\ threshold}{Total\ \#\ of\ neutron\ events}$$

The gamma rejection ratio is calculated as:

Equation 8: $$\text{Gamma Rejection} = \frac{\text{\# of gamma events above threshold}}{\text{Total \# of incident gammas}}$$

The calculation for total number of incident gammas is shown in *Equation 6*.

These calculations are straightforward, and these two quantities can be calculated for hundreds of different threshold levels to yield curves for the both neutron ID rate and the gamma rejection (*Figure 60*). Next, the neutron ID rate and gamma rejection are compared directly using a receiver operating characteristic (ROC) curve (*Figure 61*).

Notice that for a false positive rate of 10E-7 detections per gamma photon, the neutron ID rate is about 35% and 53% for ^{60}Co and ^{137}Cs respectively. This is way below the minimum neutron detection efficiency of 70% and desired efficiency of 90%. Energy discrimination is clearly not adequate, and a couple of pulse shape discrimination systems were developed at the NCNR for use with the CANDOR detector.

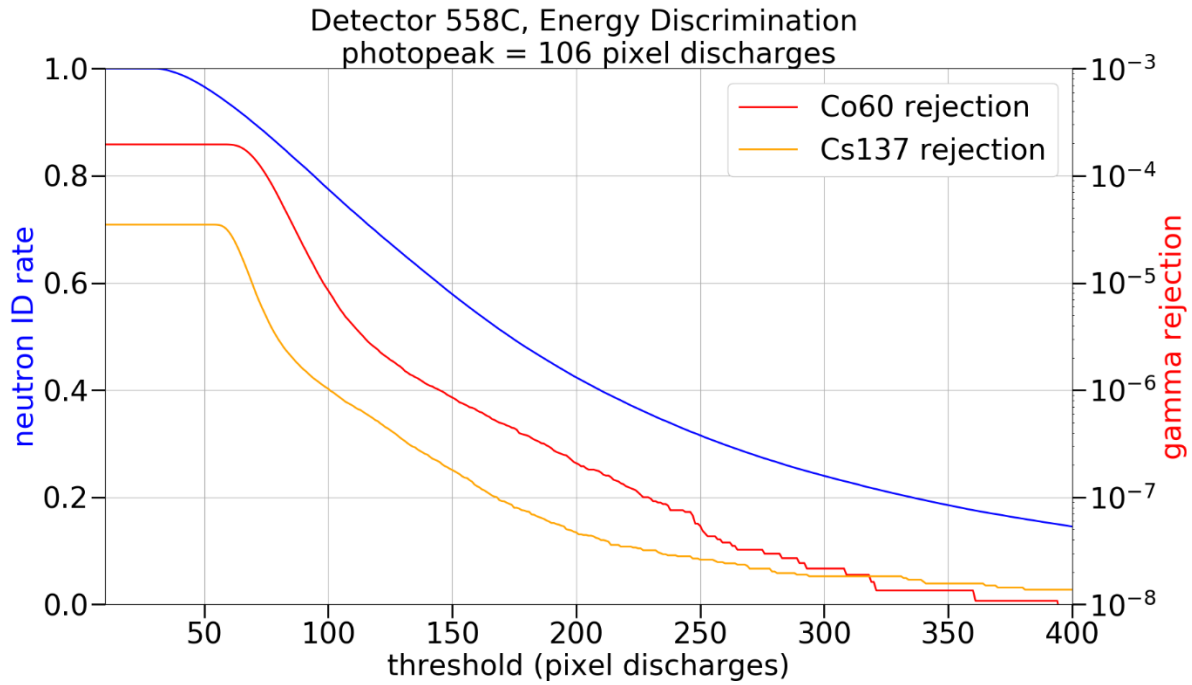

Figure 60: gamma rejection and Neutron ID rate as a function of threshold

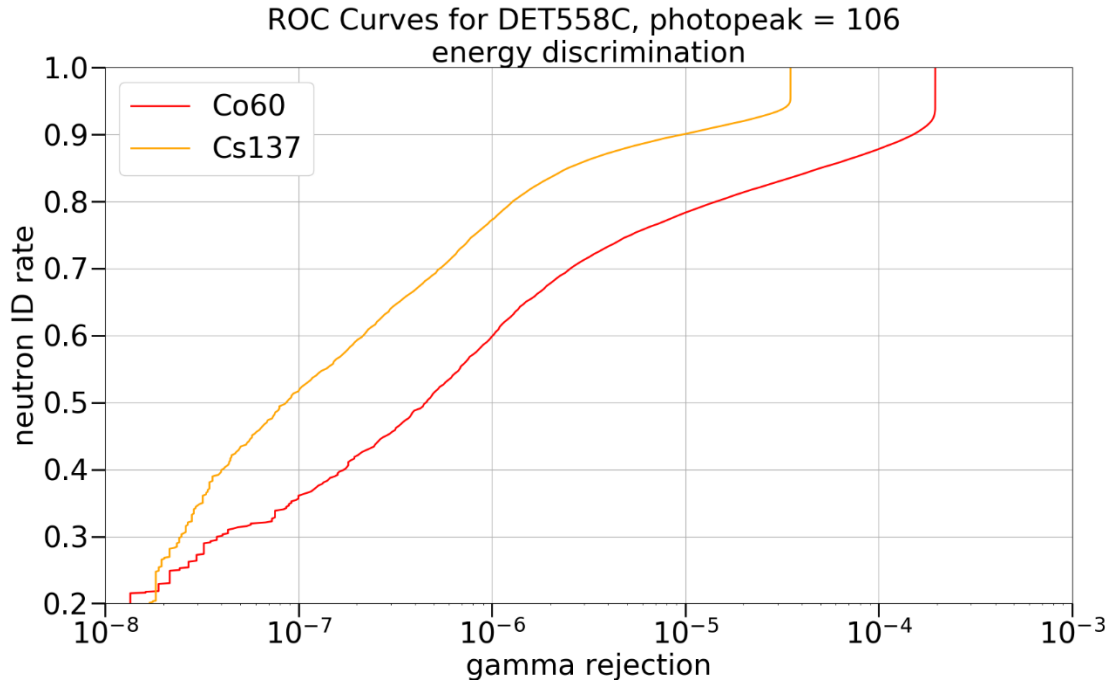

Figure 61: ROC curves for DET558C energy discriminator

6.6. Analog PSD Algorithm

A couple of pulse shape discrimination schemes were devised and tested at the NCNR. The first is a PSD based on analog circuitry. The analog discriminator uses the concept of "time over threshold". After crossing a trigger threshold the signal must remain above threshold for a specified period of time, or else the pulse is rejected and the circuit resets to look for the next pulse. Both the trigger threshold and the analog timer are controlled via separate DC voltages. A third control voltage is used to adjust the sensitivity of the analog discriminator following event detection. *Figure 62* shows the circuit schematic followed by a circuit description.

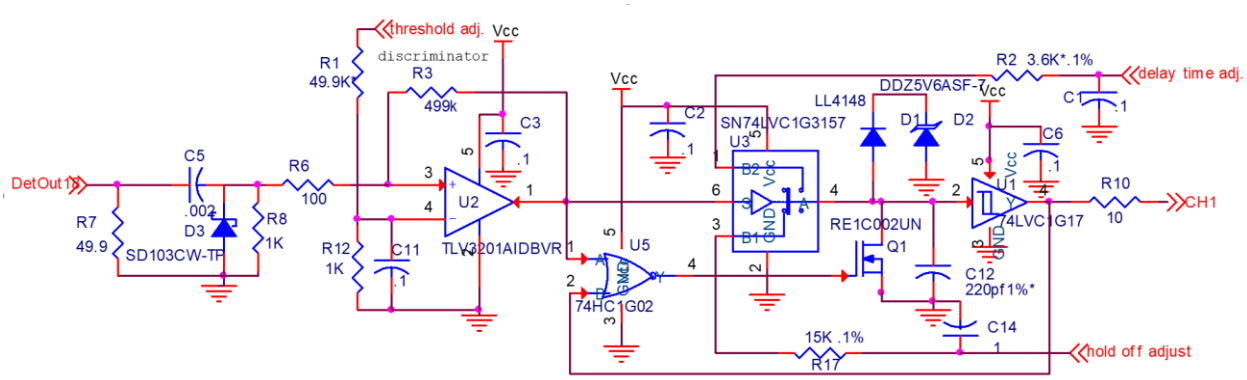

Figure 62: Schematic of the analog discriminator

6.6.1. Circuit Description:

First, the preamplifier signal is DC decoupled (high pass filter C5 and R8). This filter is designed to reduce the effects of the long neutron decay. D3 is the DC restoration diode for high level signals. U3 is an analog switch used to charge or discharge C12. U2 is a comparator which determines when a signal has risen past the trigger threshold. The threshold is controlled by voltage from the "threshold adj." power supply voltage.

The range of adjustment is from 0 – 5V DC. R6 and R3 form a Schmitt trigger to minimize oscillations and provide more stable output from the comparator.

The integrating capacitor is C12. Current flows into this capacitor after U2 determines that a signal has reached above threshold, whether it is gamma or neutron. Should the signal be short, U2 will switch back to the no signal state before the integrating capacitor, C12, reaches a high enough voltage to cause U1 to switch. Q1 and U5 will then discharge C12 so that the next signal will start integration at a repeatable voltage level. On short pulses, U1 never switches. On long pulses U1 switches, indicating a neutron detected at its output. The speed/time of this integration is controlled by the "delay time adj." power supply voltage. This power supply should be adjusted between 4 volts to 15 volts DC. The higher the voltage, the shorter the time interval (pulse width) between when U2 detects a signal to when U1 switches to signal neutron detection. When U1 switches to indicate neutron detection, it also inhibits the discharge of C12 integration capacitor by the threshold detector. This is to prevent voltage ripples in the tail of a neutron pulse from triggering extra neutron counts. The length of time where this is held off (making discriminator "blind" aka cool-off time) is controlled by the "hold off adj." power supply voltage. The power supply voltage is adjustable between 7V to 28V. The more negative the voltage, the shorter the hold-off time.

6.6.2. Tuning and Performance

Several different time over threshold adjustments were tested (*Figure 63*). These results indicate that the best performance for this discrimination scheme uses a time over

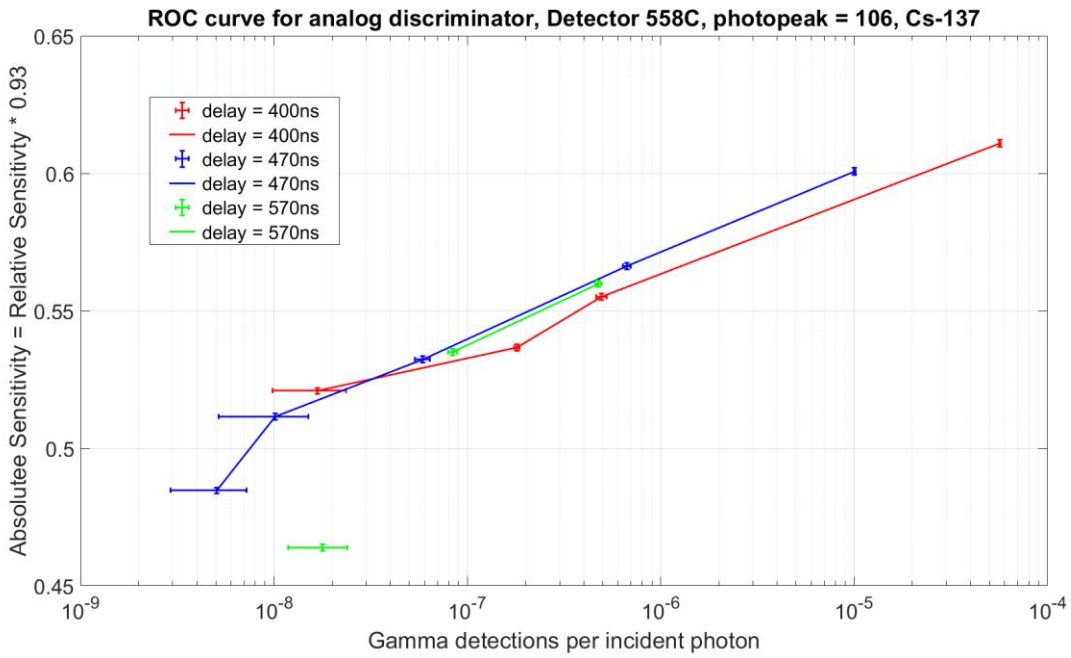

Figure 63: Detector #558C was tested with several time over threshold settings

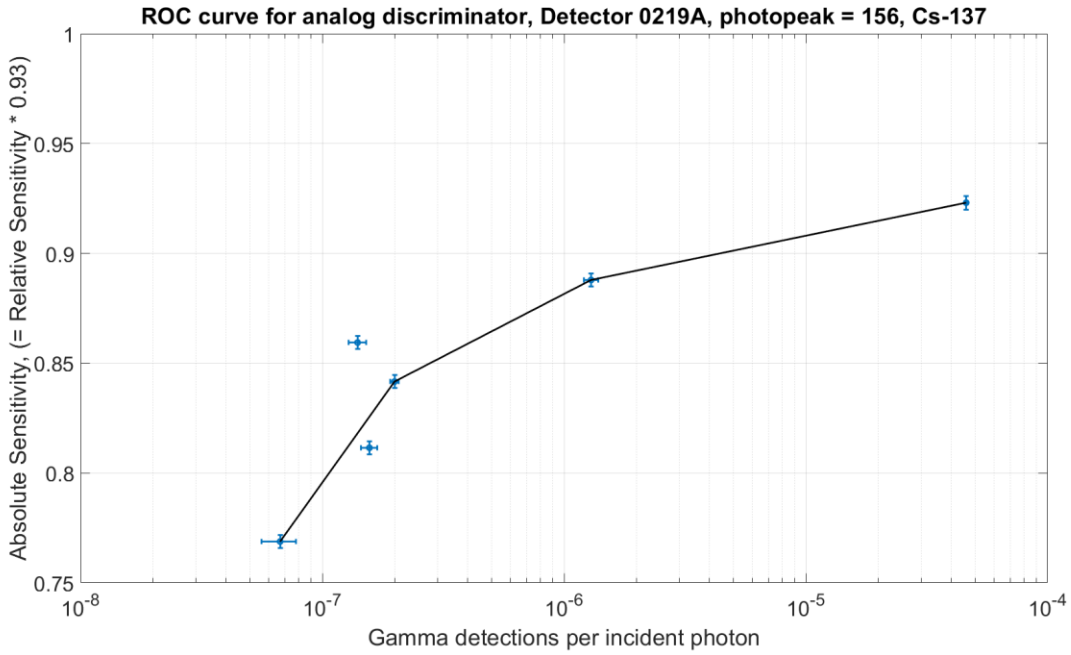

Figure 64: ROC curve for detector #219A

threshold of approximately 470ns. ROC curves for the analog discriminator were very time consuming to perform, because each point requires many hours of ^{137}Cs exposure time to acquire large enough counting statistics.

Using the same time over threshold setting, a single ROC curve was gathered for a better performing detector, #219A with a photopeak of 156 pixel discharges (*Figure 64*). When adjusted for 10E-7 detections per ^{137}Cs gamma, the absolute efficiency of detector #558C is 54% and the absolute efficiency of detector #219A is 80%.

6.7. Digital PSD Algorithm:

A second discrimination algorithm uses the CANDOR_DAQ to digitize and process waveforms on an FPGA. The digital PSD algorithm is much more complicated. First, there is some signal conditioning. The DC bias is subtracted from the incoming data stream. Next, a 320ns (16-sample) moving average filter is used to smooth the jagged data stream. The unsmoothed, dc-bias subtracted data stream is delayed by 340ns (17-samples). A trigger threshold is set. After the moving average triggers, the PSD algorithm is armed to begin computations as soon as the delayed data crosses the same threshold. A flow diagram of the algorithm is shown in *Figure 65*.

There are three separate criteria that a pulse must pass in order to be identified as a neutron:

1. Charge comparison algorithm
2. Noise rejection filter
3. Pile-up rejection filter

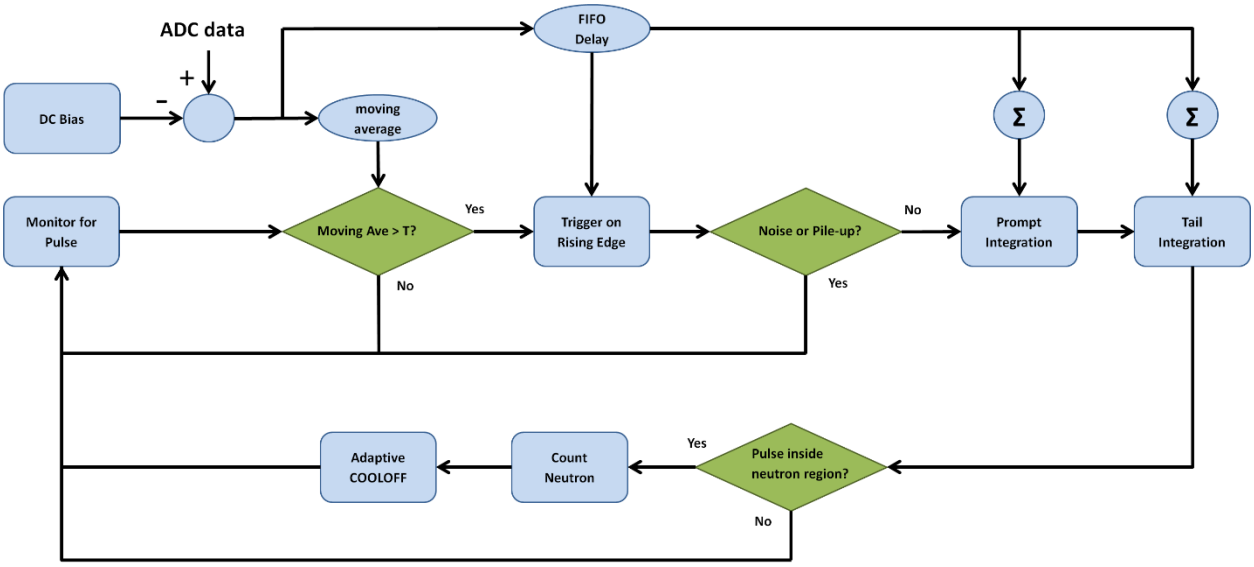

Figure 65: Digital PSD algorithm flow diagram

6.7.1. Charge Comparison Algorithm

The charge comparison algorithm is the main form of pulse shape discrimination used on the CANDOR_DAQ. The noise rejection filter and the pile-up filter are added to handle exceptions that pass the charge comparison algorithm, but that are obviously not neutrons.

We used a two-window charge comparison algorithm (*Figure 66*) to analyze the data in the waveforms. In this method, the signal is integrated over two intervals, a prompt interval beginning immediately following the trigger, and a delayed interval immediately following the prompt interval. Most of the signal contained in a gamma or thermal event is deposited into the first interval, while for a neutron, the signal is more evenly distributed between the 1st and 2nd intervals. A scatter plot using the sums over the

two intervals as coordinates is shown in *Figure 67*. The 1st and 2nd intervals used for these figures are 0ns – 240ns and 240ns – 2240ns respectively.

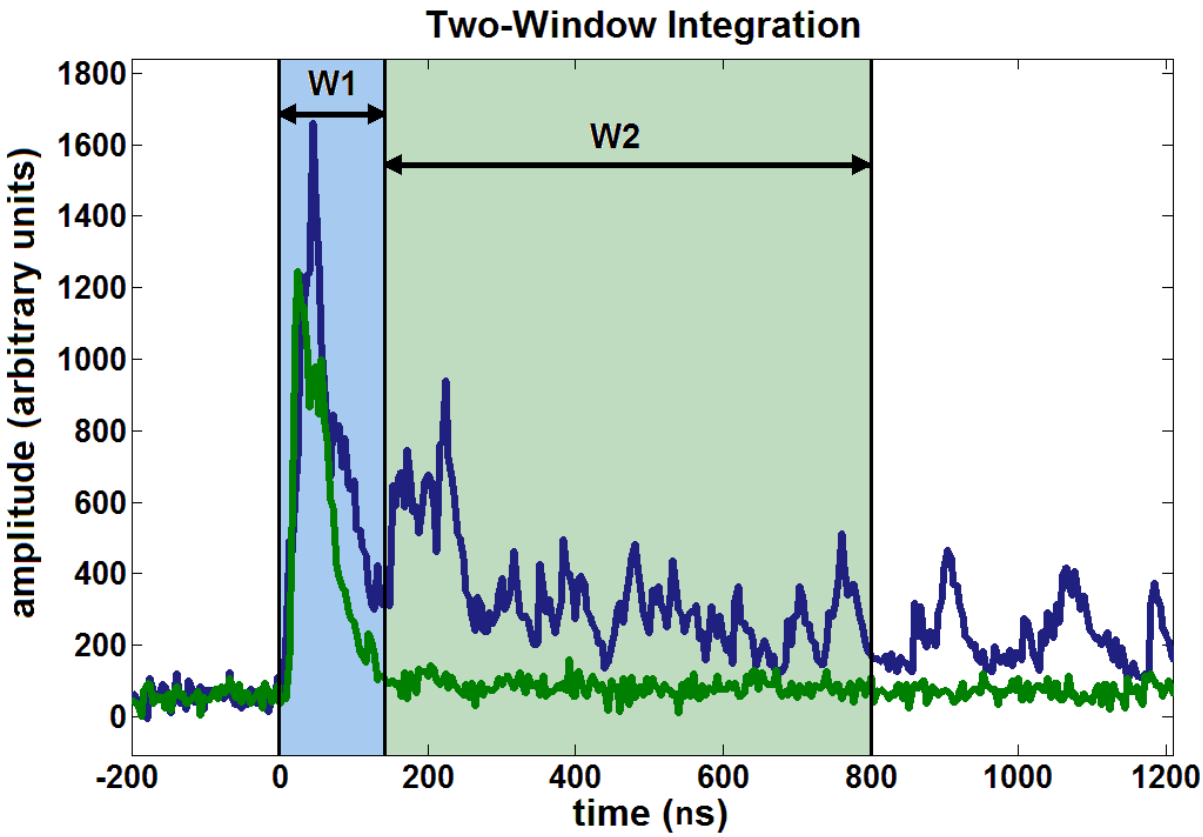

Figure 66: This is a diagram of to the Two-Window Charge Comparison algorithm. The green waveform is a gamma event. The blue waveform is a neutron event.

Typically, the output of the two-window charge comparison algorithm is represented as a scatter plot with the total energy (sum over both intervals) as the independent axis and a "shape score" (ratio of the delayed interval sum to the total sum) as the dependent axis. These same neutron and gamma datasets are represented this way in *Figure 68*. For the CANDOR detector however, the total pulse energy is not a differentiating feature of neutron pulses given the large range of amplitudes. And since

fewer computations are needed when using the integrals directly, the data rendering in *Figure 67* is used.

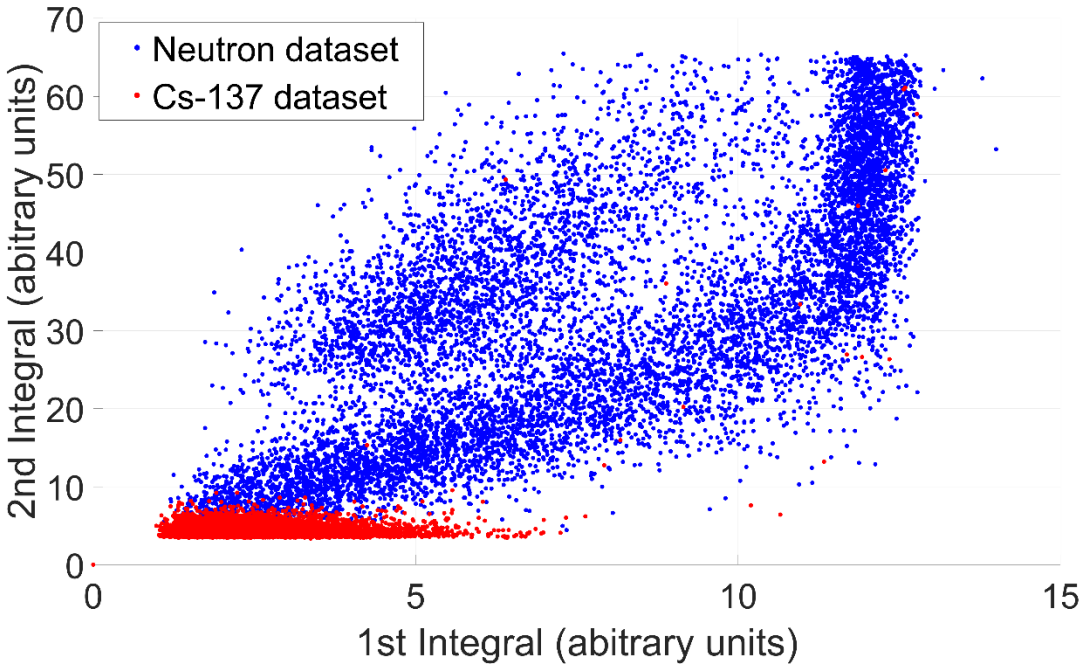

Figure 67: A scatter plot of the neutron and gamma datasets using the 2-window charge comparison algorithm. Preamplifier saturation "chops off" the peaks of large neutron waveforms. This distortion is seen in the scatter plot as the 1st Integral approaches a value of 12. Saturation at high energy does not affect neutron identification.

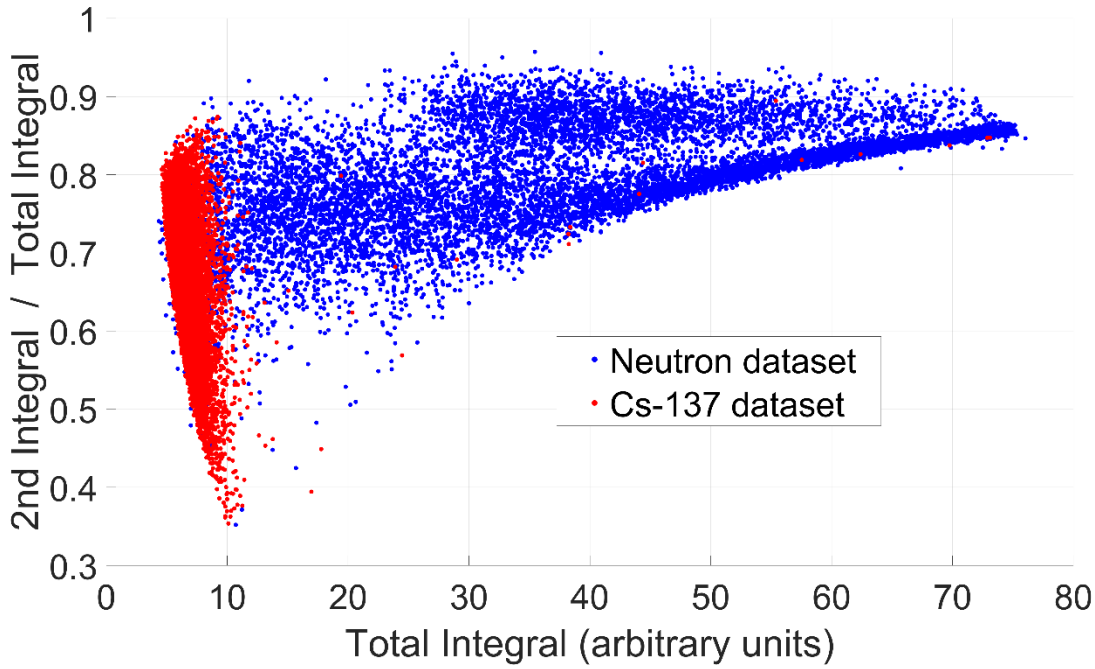

Figure 68: The scatter plot in Figure 4 is transformed to Energy vs. Shape Score coordinates. Again, preamplifier saturation can be seen in the neutron scatter plot at high energies.

6.7.2. Optimizing the CC Algorithm

The overall performance of the Charge Comparison algorithm depends largely on the integration intervals. The durations of the integration windows must be carefully chosen so that the separation between neutron and gamma populations in the scatter plot is maximized. This is explored by focusing on the region of interest (ROI) in which the neutron and gamma populations overlap (Figure *69*).

Gaussian statistics can be used as a metric to gauge the separation between these two populations. We define a Gaussian Separation Figure of Merit (FOM) in ***Equation 9***:

Equation 9: $Gaussian\ FOM = \frac{(\mu_{neutron} - \mu_{gamma})^2}{\sigma^2_{neutron} + \sigma^2_{gamma}}$

where $\mu_{neutron}$ is the centroid of the neutron ROI subset, μ_{gamma} is the centroid of the gamma ROI subset, $\sigma^2_{neutron}$ is the variance of the neutron ROI subset, and σ^2_{gamma} is the variance of the gamma ROI subset. The Gaussian FOM is calculated for an array of 1st and 2nd integral durations. Maximizing the Gaussian FOM maximizes the separation between the two datasets.

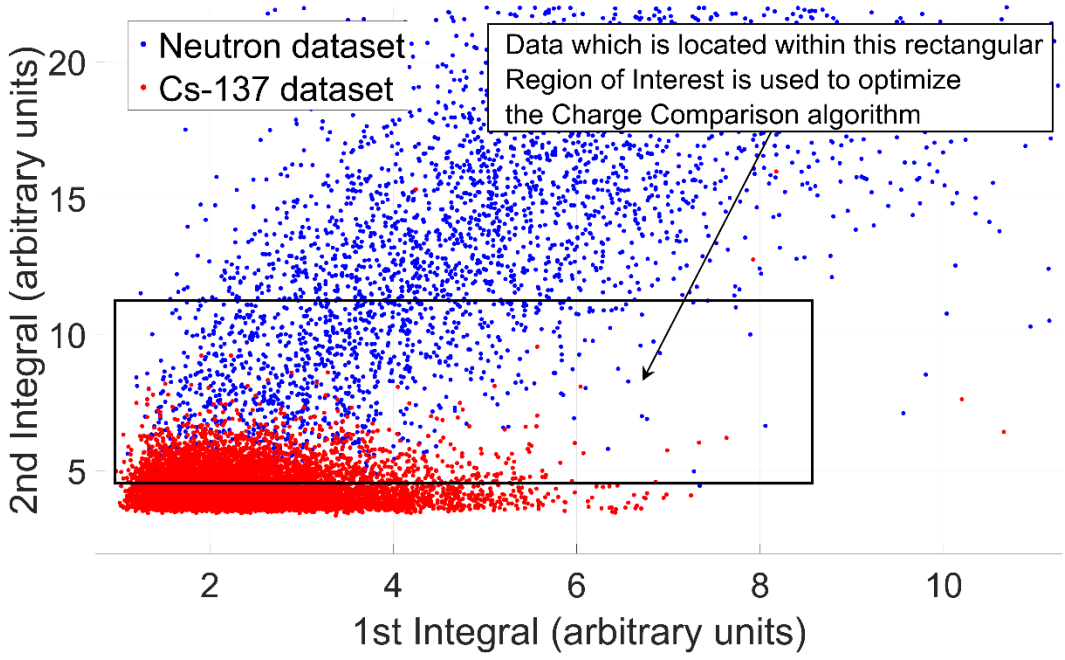

Figure 69: Neutron and Gamma data overlaps in the Region of Interest (ROI). Increasing separation in the ROI will enhance classification performance.

The contour plot in Figure *70* indicates that the best separation between neutron and gamma populations in our system is achieved if the 1st interval is from 0 ns to 100 ns following the trigger and the 2nd interval is from 100 ns to 2700 ns.

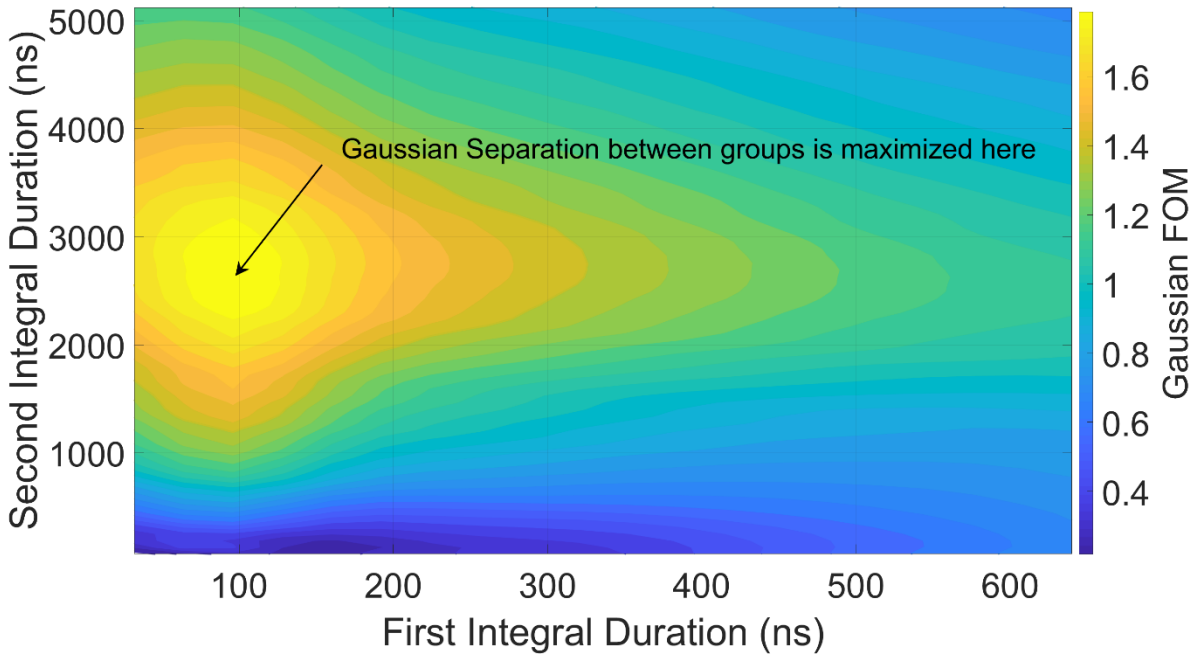

Figure 70: A contour map shows the separation between neutrons and gammas as a function of the first and second window lengths. Separation is gauged by the Gaussian FOM.

The optimal 1st and 2nd integration intervals also can be determined from an array of ROC curves. Neutron and gamma datasets which were recorded at a SiPM bias voltage of 28.5V were used for this analysis. A classifier threshold was set such that the Gamma Rejection Ratio was one count per 6 x 10^7 incident ^{137}Cs gammas. Then, the Neutron ID Rate is calculated using the same threshold. Holding the gamma rejection ratio constant, the Neutron ID Rate was calculated for an array of 1st and 2nd integral periods (Figure 71).

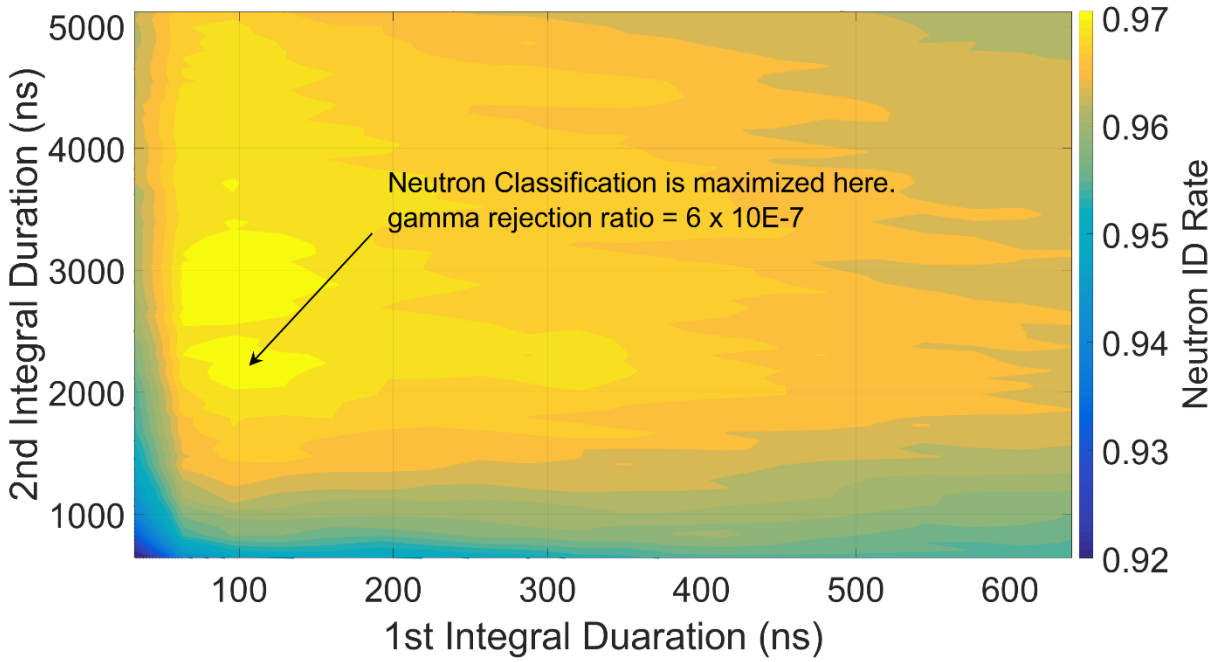

Figure 71: A contour map shows the performance of the 2-window charge comparison algorithm as a function of the first and second window lengths. The conclusions drawn from this contour map are very similar to those made from the Gaussian FOM

The analysis shown in Figure 71 yields similar conclusions as the Gaussian FOM in terms of the optimized integration windows. According to the "neutron ID rate FOM", the 1st integral is still optimized from 0 ns to 100 ns following the trigger, but the 2nd integral is optimized at a slightly shorter period from 100 ns to 2300 ns following the trigger. Shorter integration times are preferred in our application because they reduce the dead-time of the discriminator and increase the count rate capability. In fact, to increase the speed of the PSD algorithm, the 2nd integration duration was reduced even further to 1.28μs, knowing that this could reduce the sensitivity of the detector by about 1.0% but nearly double its speed. Additionally, the 1st integration duration was increased from an optimum of 100ns up to 240ns. The reason for this was to simplify classification

computation. Gamma and noise events deposit significant fractions of their energy after the first 100ns. An appropriate classifier would require a multiplication of the first and second integrals with a weighted vector. By increasing the 1st integration duration to 240ns (as shown in Figure 67), the gamma distribution is largely horizonal, and the 2nd integral alone can be used to accurately classify events. Additionally, an additional criterion that the 2nd integral be greater than 0.5 x 1st integral effectively eliminates high energy gammas with substantial energy deposited after 240ns (*Figure 72*).

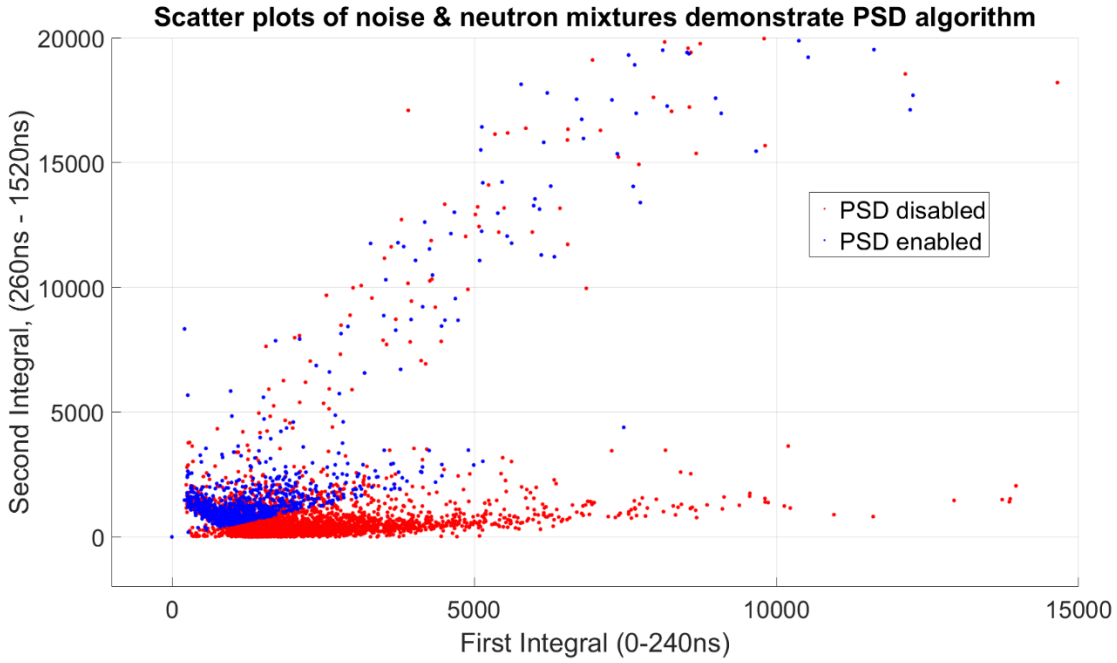

*Figure 72: The digital PSD algorithm includes the criteria: 2nd Integral > 0.5*1st Integral*

The primary PSD algorithm (the charge comparison algorithm) and its optimization have been discussed. On top of the charge comparison algorithm, there are some filters to handle exceptions created by the SiPM noise and non-linearities.

6.7.3. Noise Rejection Filter

The noise rejection filter eliminates pulses which decay quickly. The algorithm finds the first maximum after the rising edge trigger. If the pulse falls below 50% of the maximum within 80ns (4 samples), the pulse is rejected. Additionally, if the pulse falls below 25% of the maximum within 200ns (10 samples) the pulse is also rejected. Pass/Fail examples are illustrated in *Figure 73* and *Figure 74*.

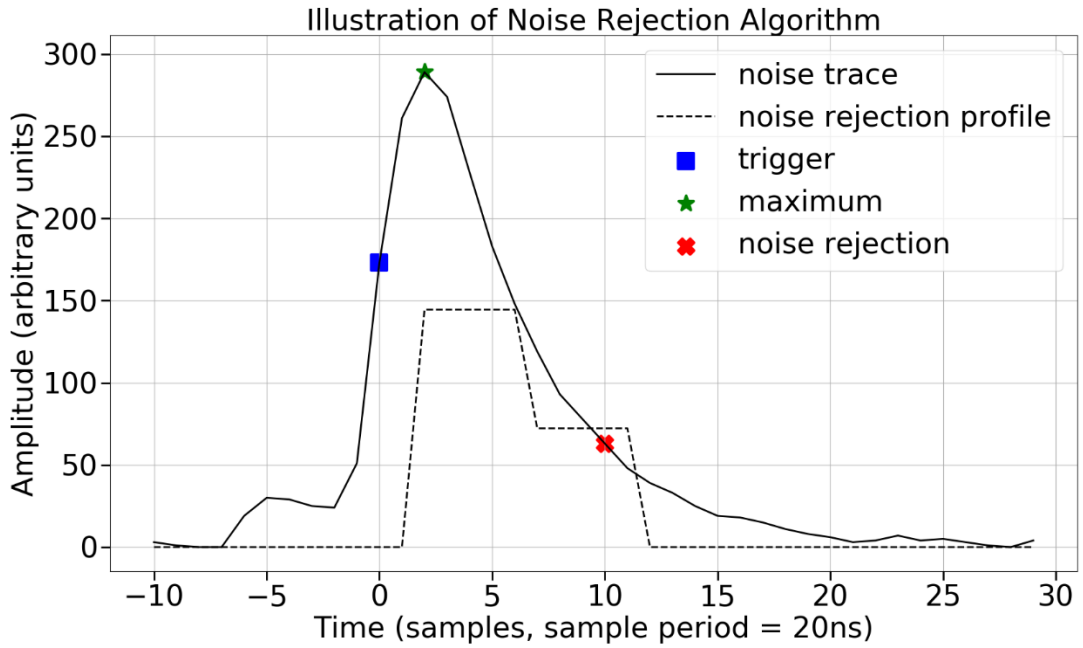

Figure 73: Noise is rejected by the Noise Rejection Filter

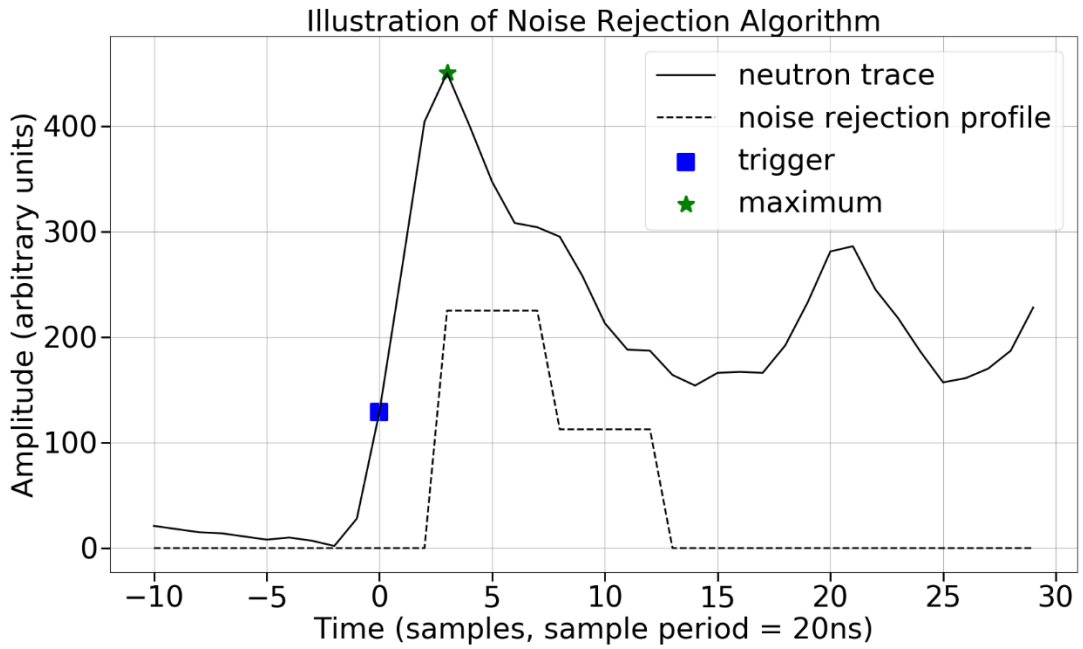

Figure 74: A neutron passes the noise rejection filter

The noise rejection filter rejects approximately 70% of pulses which are large enough to trigger the PSD algorithm (*Figure 75*). The number of neutrons rejected by the noise rejection filter is difficult to compute, because the dataset in *Figure 76* is a mixture of noise and neutrons. But, the neutron rejection rate is estimated to be less than 2%. The trigger threshold was tuned so that between 10 and 100 thermal noise events pass the noise rejection filter per second, so as to reduce the deadtime for examining noise events with the charge comparison algorithm, but still being sensitive to low amplitude neutrons. A pulse may re-trigger the PSD algorithm after initial rejection and be identified as a neutron.

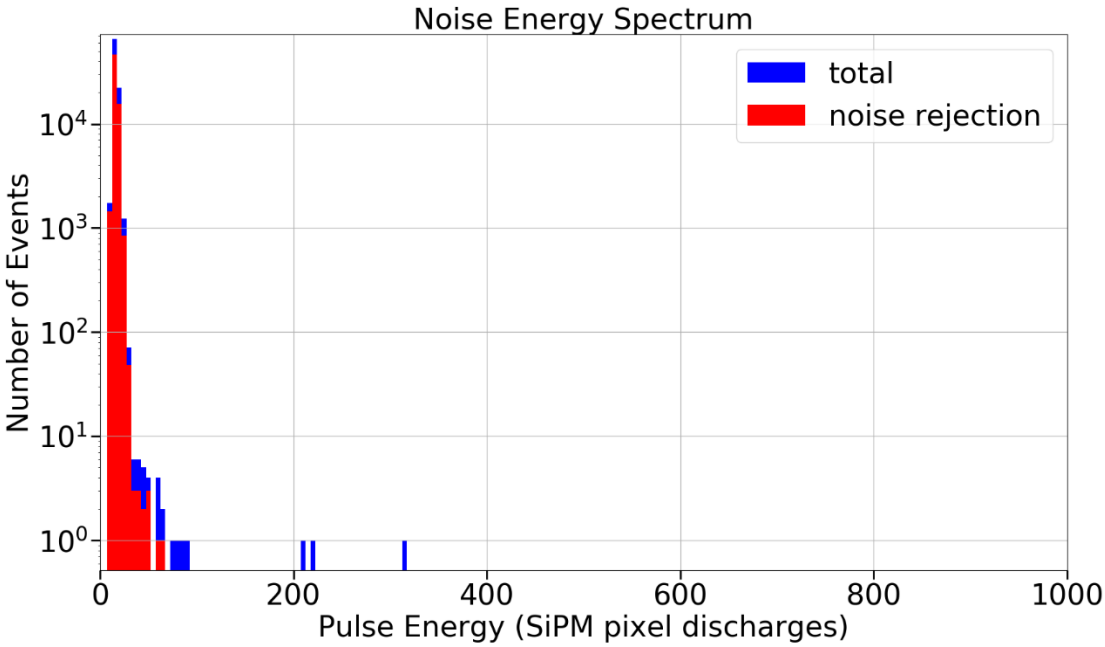

Figure 75: Energy spectrum of noise and rejected pulses

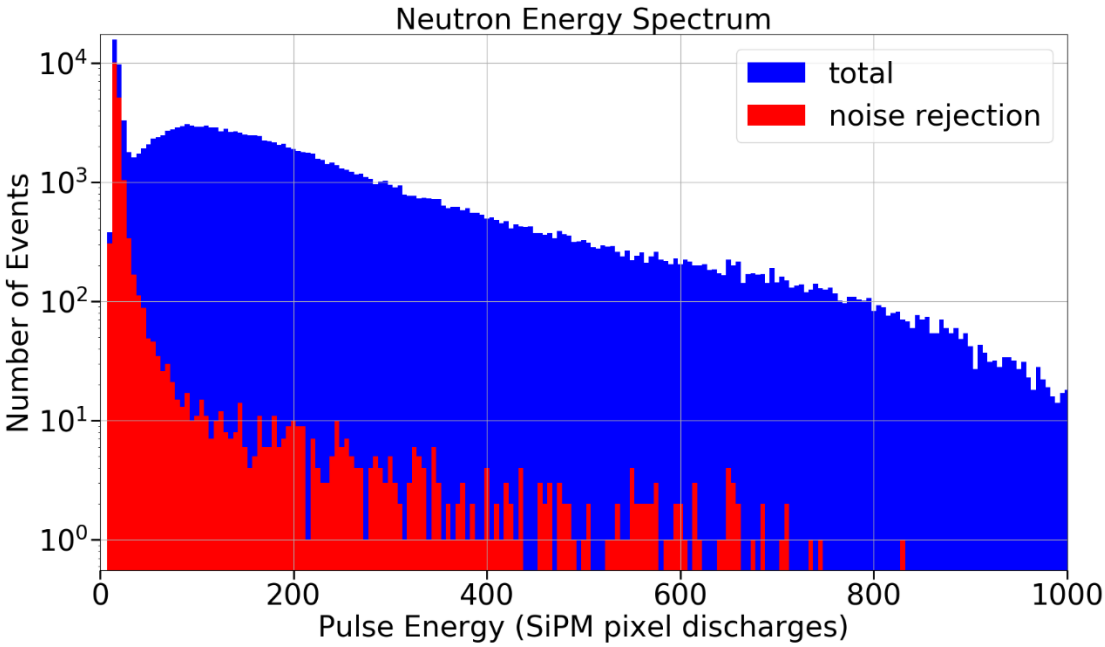

Figure 76: Energy spectrum of neutrons and rejected pulses

6.7.4. Pile-up Filter

The pile-up filter rejects pile-up events of a conspicuous shape. The waveform in *Figure 77* is an archetypal example of a pile-up of two pulses which together can pass both the noise rejection filter and the charge comparison algorithm. These pulses were found to be non-trivial in frequency and tend to accumulate in the left-most region of the charge comparison scatter plot (*Figure 78*). Pile-up pulses were originally extracted using wavelet analysis. However, a much simpler way of identifying pile-ups was devised rather than computing wavelet transforms.

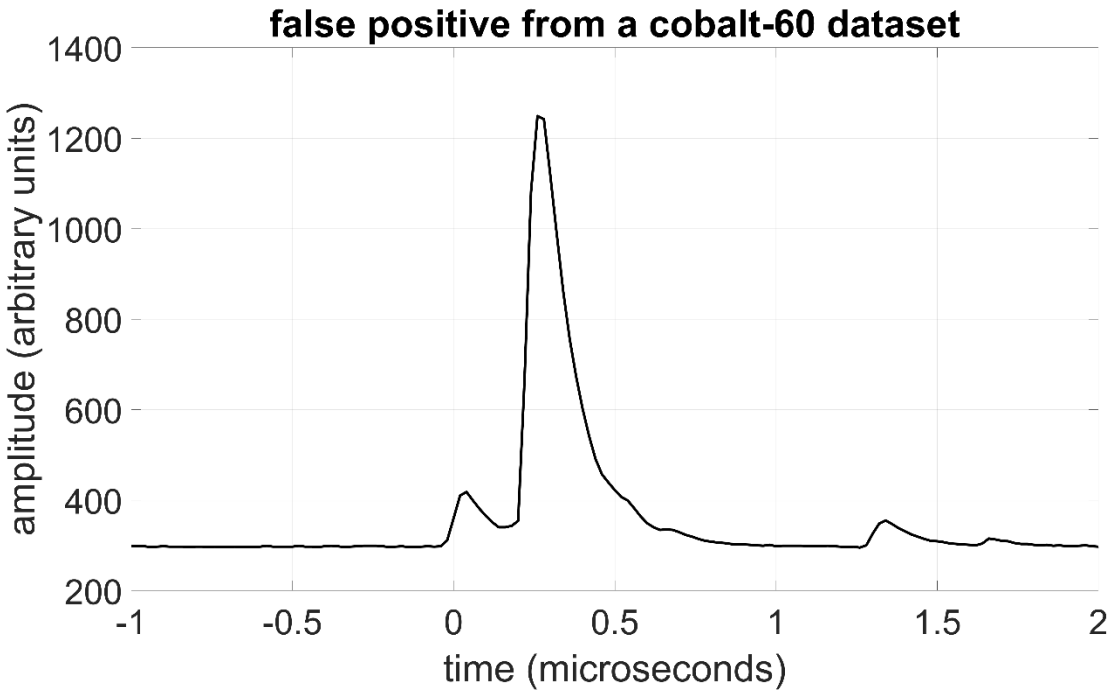

Figure 77: Archetypal pile-up pulse

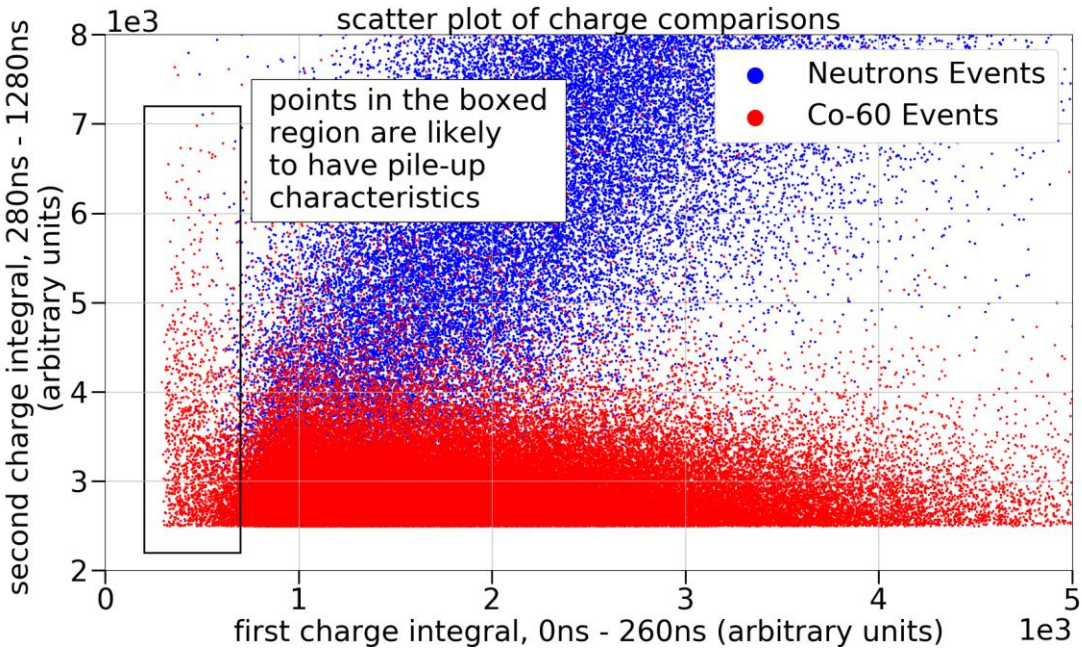

Figure 78: Pile-up noise accumulates in the left-most region of the CC scatter plot

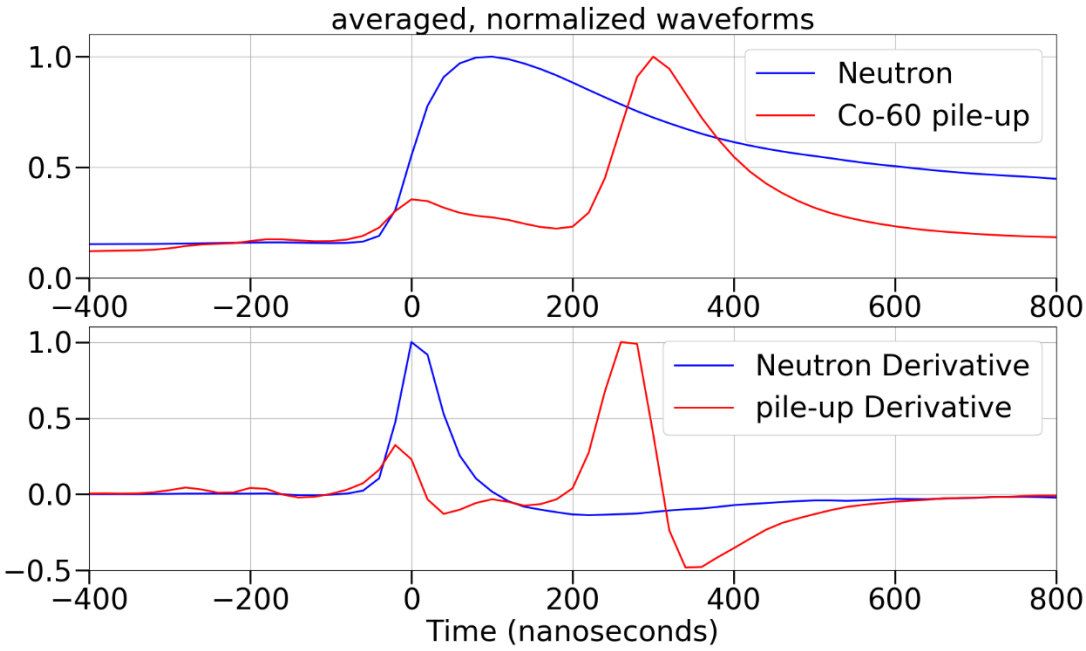

Figure 79: Neutron and pile-up averages, and their derivatives

A “pile-up score” is computed from the derivative. From 0ns to 160ns (samples 0 thru 8) the pile-up derivative is typically less than for a neutron. From 180ns to 300ns (samples 9 thru 15) the pile-up derivative is typically greater than the neutron derivative. And, from 320ns to 540ns (samples 16 thru 27) the pile-up derivative is typically less than the neutron derivative. The pile-up score and integral are computed as:

Equation 10: $pileup\ score\ = -\sum_{n=0}^{8}\frac{dx}{dn} + \sum_{n=9}^{15}\frac{dx}{dn} - \sum_{n=16}^{27}\frac{dx}{dn}$

Equation 11: $integral\ = \sum_{n=0}^{27} x[n]$

These values are computed for large sets of neutrons and cobalt-60 gammas (*Figure 80*). Two classification boundaries are used. They are relational, so there is no threshold value to set. If the pile-up score is negative, the integral must be larger than -8x the pile-up score: integral > -8 x (pile-up). If the pile-up score is positive, the integral must be larger than 16x the pile-up score: integral > 16 x (pile-up).

Figure 81 shows which events are rejected by the pile-up filter. The number of neutrons which are rejected by the pile-up filter is less than 0.2%, but a significant portion of high energy noise is rejected. *Figure 82* shows two ROC curves, one including the pile-up filter and one omitting the pile-up filter. The comparison shows the pile-up filter improves performance modestly (about a 1% increase to neutron ID rate at 10E-7 gamma rejection). One percent isn’t a big improvement to detector performance, but when you consider that 97% of neutrons were already identified, 1% is 1/3 of the remaining unidentified neutron events. A pulse may re-trigger the PSD algorithm after pile-up rejection and be identified as a neutron.

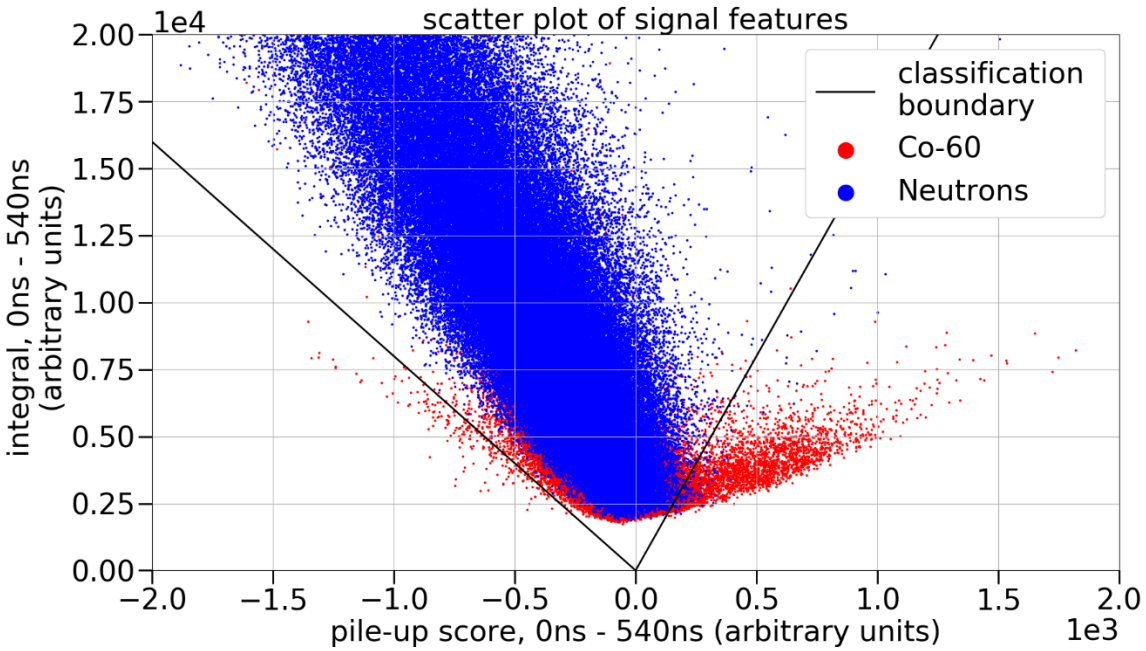

Figure 80: scatter plot of pile-up features

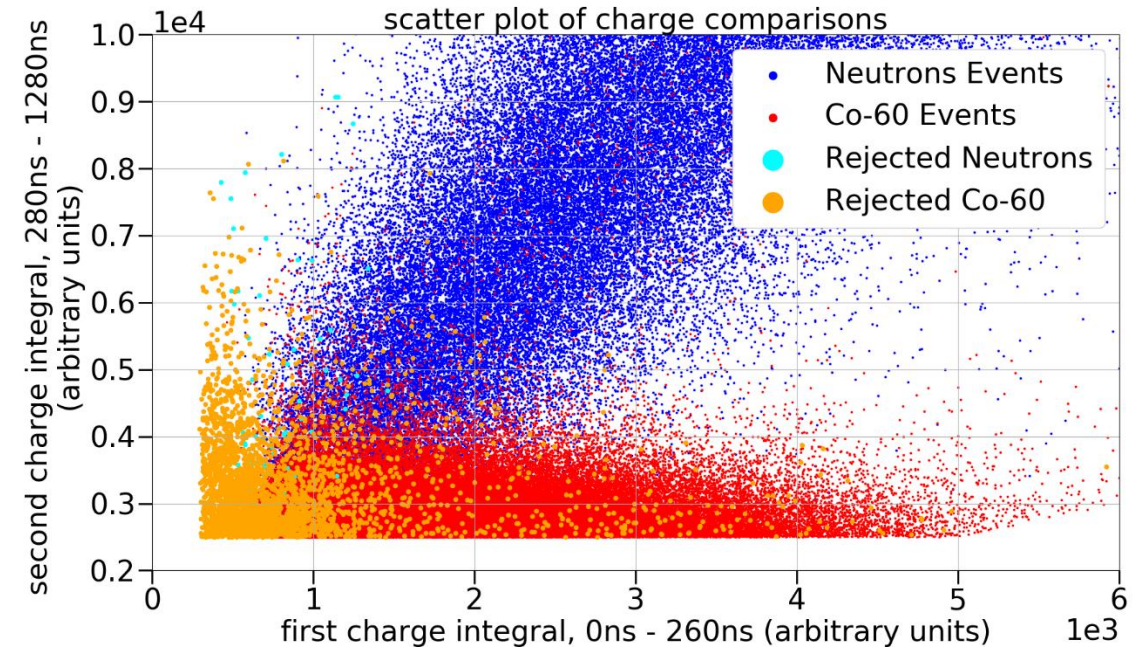

Figure 81: Scatter plot showing the area of pile-up rejection. There are a significant number of background neutrons in the cobalt-60 dataset.

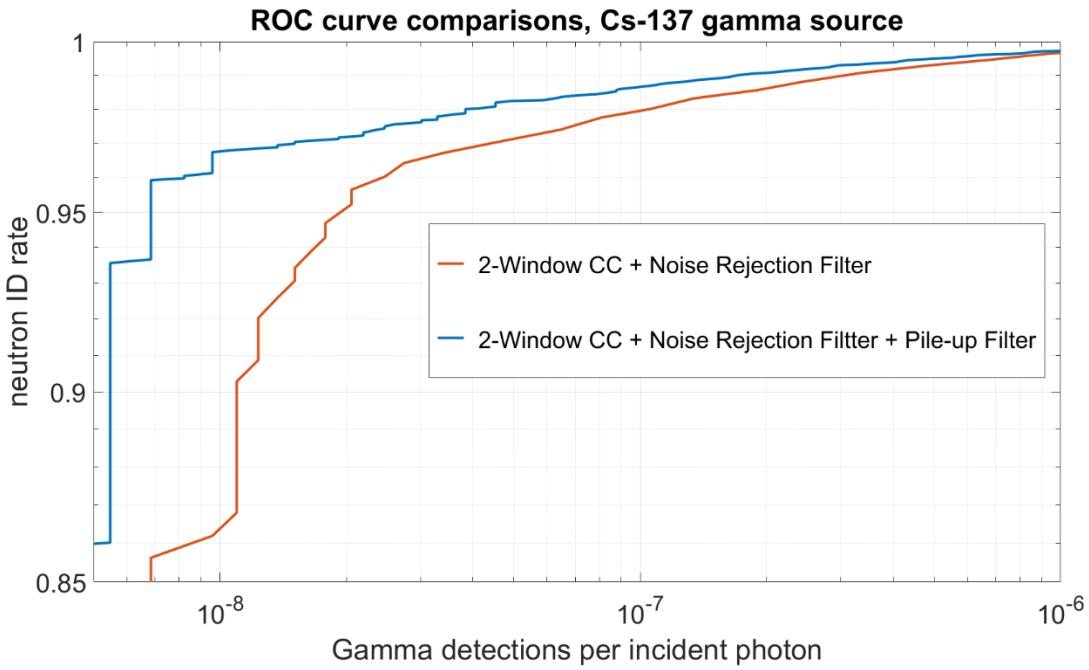

Figure 82: The pile-up filter shows a modest improvement to neutron ID rate

6.7.5. Digital PSD Performance Comparisons

The digital PSD algorithm is vastly superior to energy discrimination, identifying more than twice as many neutrons in some cases. The performance gains are more pronounced for the higher energy gammas (^{60}Co) and for detectors with lower light yield. *Figure 83* and *Figure 84* quantify the improvements using ROC curves for ^{137}Cs and ^{60}Co gamma sources. *Figure 85* shows a close-up of performances for the digital PSD, with delineated thresholds included. The thresholds are given as the number of SiPM pixel discharges falling within the 2nd integral time period (260ns – 1280ns).

A threshold setting of approximately 37 pixel discharges was chosen for performance studies of larger populations of detectors. This ensures better than 10E-7 detections per ^{137}Cs gamma and better than 10E-6 detections per ^{60}Co gamma over the entire detector population.

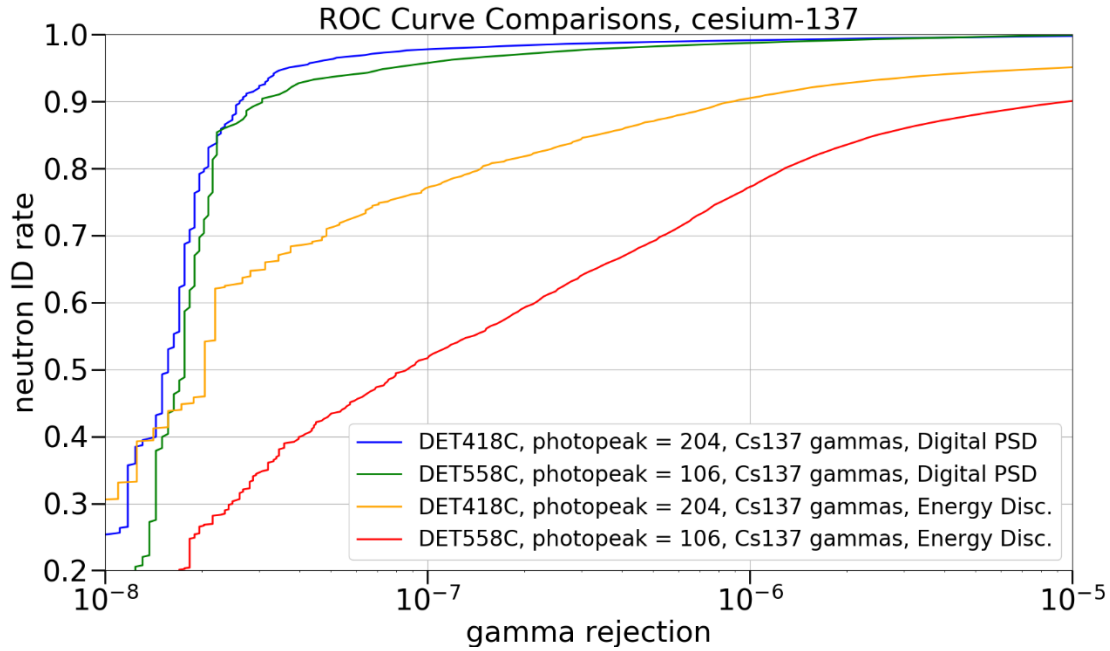

Figure 83: ROC curve comparisons for Cs-137

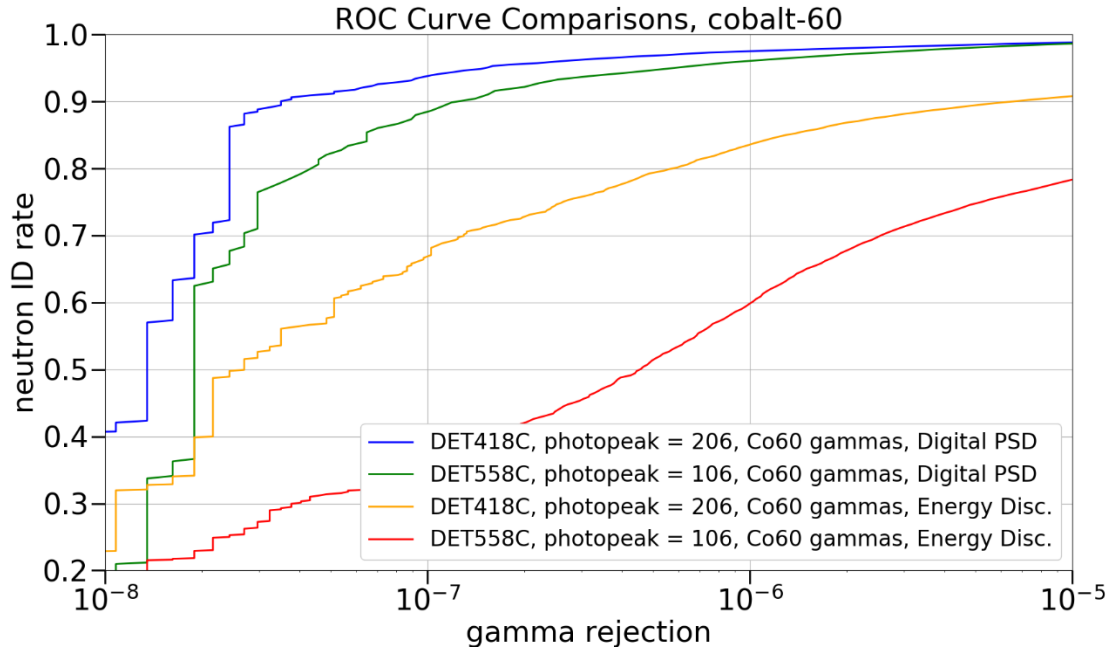

Figure 84: ROC curve comparisons for Co-60

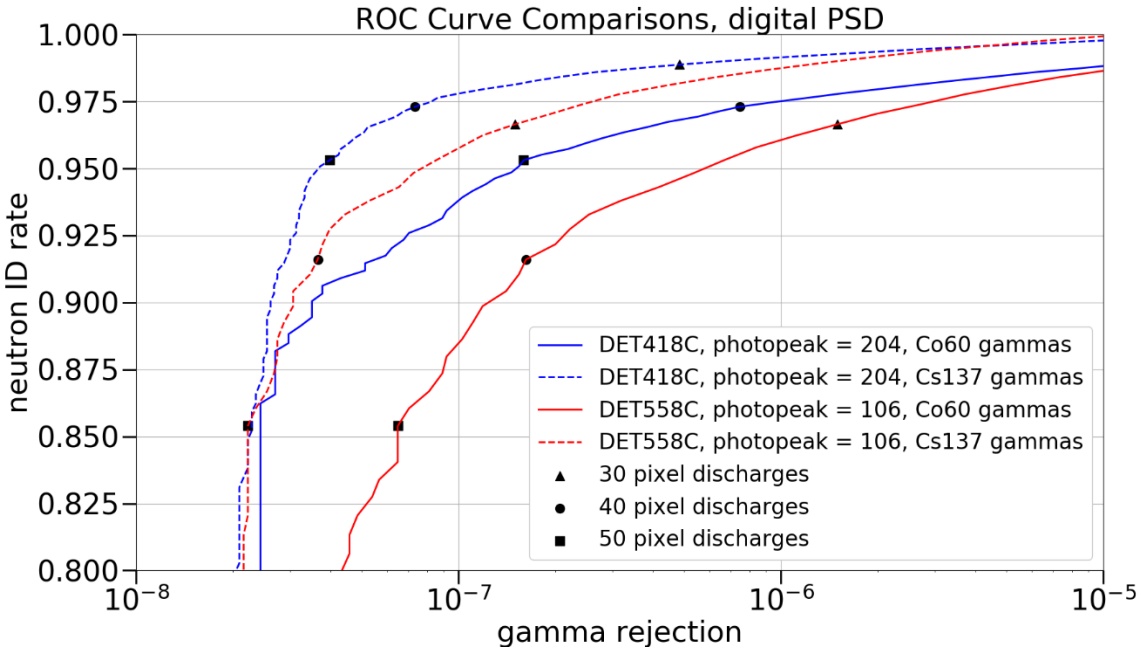

Figure 85: Digital PSD performance with thresholds

6.7.6. Extrapolating ROC curves to estimate performance beyond the neutron background

At very, very small gamma rejection ratios (< 10E-8 detections per photon), the neutron background of the measurement environment begins to foul the gamma dataset. Stray neutrons are everywhere in the environment from natural decay of matter, not just in nuclear facilities. Neutron backgrounds are even higher for gamma data taken while the NCNR reactor source is on. This is seen in ***Figure 86***. Fortunately, performance at very small gamma rejection ratios can be predicted by fitting and extrapolating an exponential decay to the gamma rejection ratio as a function of classification threshold.

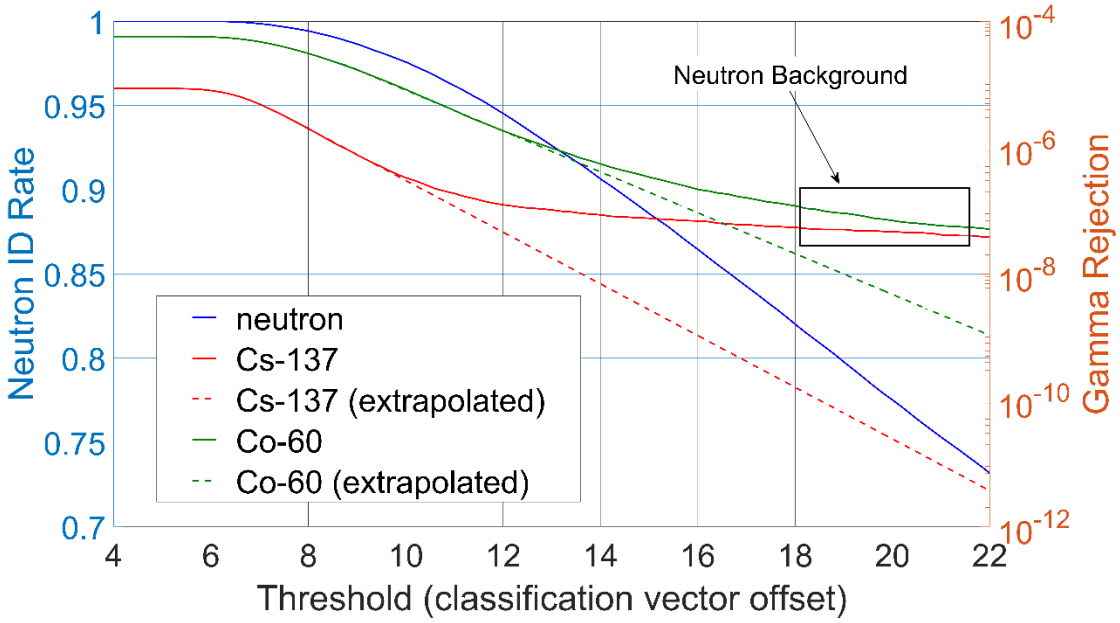

Figure 86: Neutron background is higher when the reactor is on.

The extrapolated gamma rejection is used in the ROC curve to estimate performance at small gamma rejection ratios (*Figure 87*)

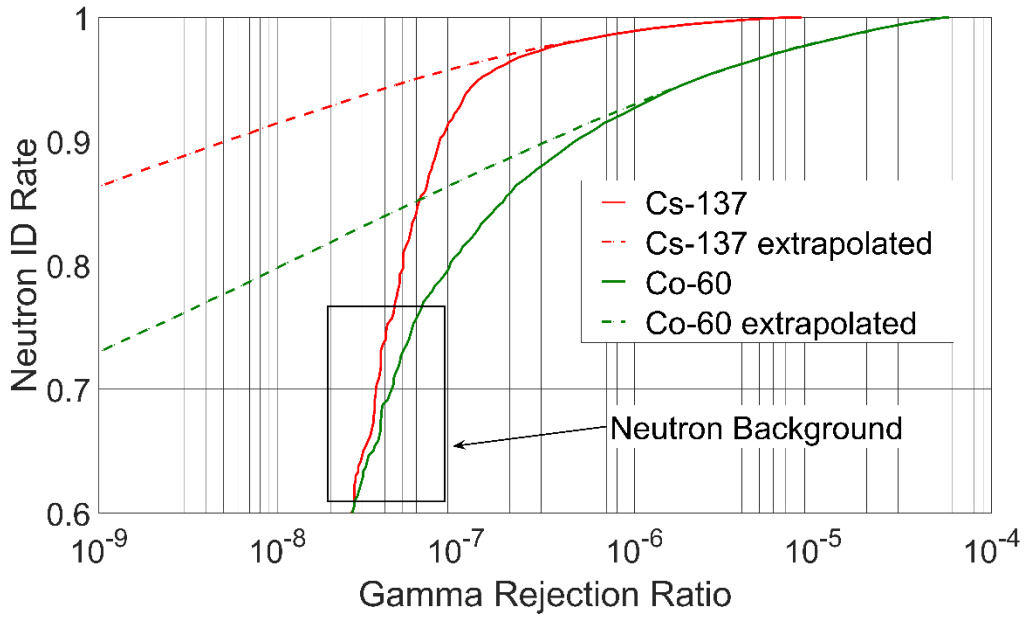

Figure 87: Performance estimates at very low gamma rejection ratios

6.7.7. ROC curves for optimizing SiPM bias voltage

Physical variants of the CANDOR detector were compared using ROC curves and data extrapolations. One question that our research group had was what SiPM bias voltage would give the best detector performance? As mentioned earlier, the photodetection efficiency (PDE) of an SiPM increased with bias voltage. However, the nonlinearities and dark counts increase as well.

To determine the proper operating voltage for the SiPM in our application, we recorded neutron and gamma datasets for a series of bias voltages. ROC curves were computed from these datasets (*Figure 88*). By comparing these curves we determined that for our SensL J-series SiPM, a bias voltage of 28.5 V provides us with the highest neutron sensitivity with the least impact to gamma rejection, although slightly higher bias voltages perform nearly as well. We chose to use an SiPM bias voltage of 29.5V in the CANDOR instrument, so that the electrical gain between channels would be more consistent. Slight variations in breakdown voltage from device to device creates a distribution of electrical gains (*Figure 113*). The variance of this distribution is lower for a higher SiPM bias voltage. Although individual classification thresholds can be set for each detector in the CANDOR_DAQ, more consistent electrical gains better accommodate the analog discriminator solution across many channels.

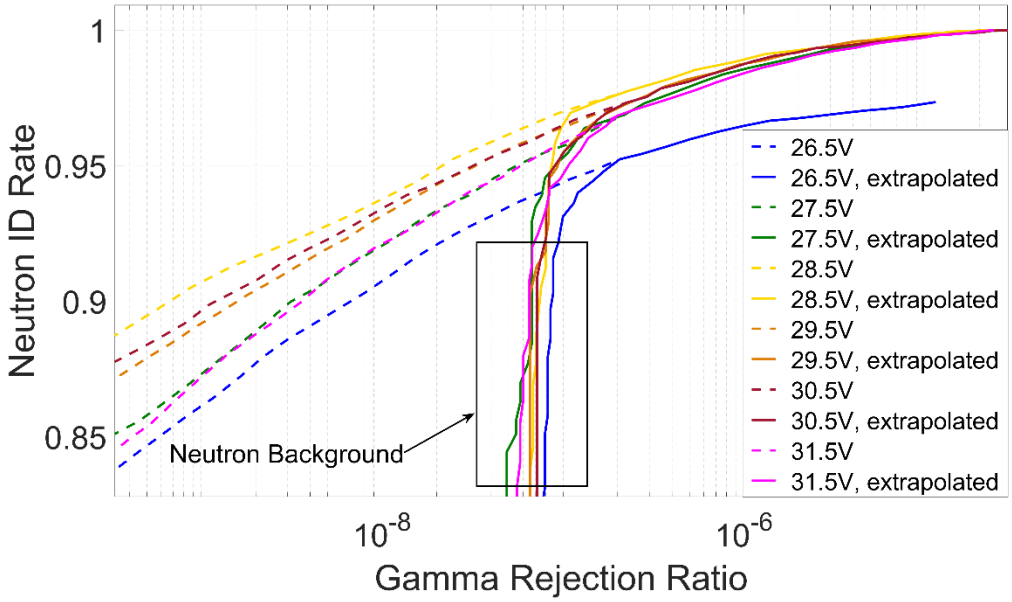

Figure 88: SiPM bias voltage is optimized by comparing ROC curves

6.8. Pulse Processing Speed and Count Rates

6.8.1. Terminology: Double Count Fraction, Dead Time, and Adaptive Cooloff

Neutron scintillation in ZnS(Ag) is very long lasting. Delayed fluorescence can last up to 60μs for larger pulses (*Figure 89*). The decay follows an exponential trend, but it is jagged and irregular. Pulse Shape Discrimination only takes 500ns in the case of the analog discriminator, or 1.5μs in the case of the digital PSD algorithm. Since the entire decay of the pulse is dozens of times longer than the PSD decision period, it is possible for the PSD algorithm to "double count" the same pulse after initial identification. To prevent this from happening, the sensitivity of the discriminator must be reduced or eliminated, or the long decay must be compensated for.

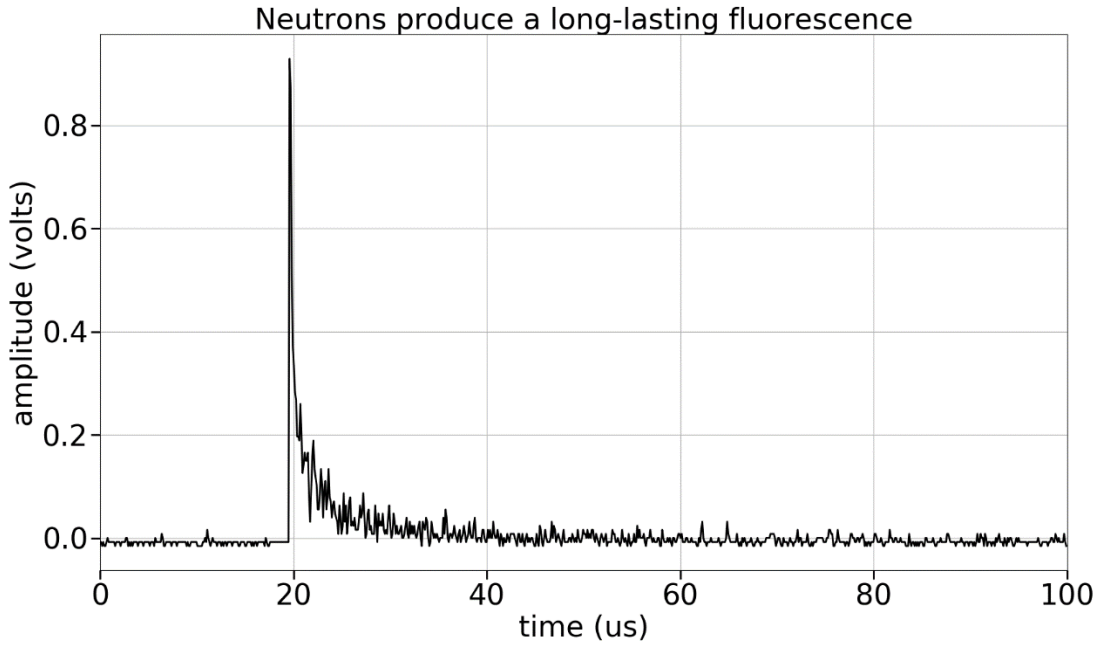

Figure 89: long neutron fluorescence

Unfortunately, since neutron fluorescence lasts for so long, a hold-off time encompassing the entire decay of 60μs would be far too long. The discriminator must be built in a way to compensate for the fluorescent decay of a preceding pulse while continuing to process new pulses. This is the only way to prevent double-counting while at the same time allowing for a high event processing rate. Since neutron pulses have a large range in magnitude, the decay compensation also needs to be proportional to the size of the preceding pulse. The act of compensating for decay fluorescence in a proportional manner will be referred to as “adaptive cooloff”. The amount of time the discriminator is insensitive to new events is commonly known as the “dead time”. Lastly, the fraction of events which are double counted will be referred to as the “double count fraction”.

If double-counting cannot be completely eliminated, it must be reduced below a rate of one double-count per 1000 processed pulses or less. A double count fraction of 0.001 (0.1%) is an acceptable measurement error for neutron scattering data. Double-count fractions are generally some of the most tedious measurements to make, since it requires the individual inspection of thousands of pulse waveforms. Alternative methods for measuring double count rates will be discussed later along with deadtime analysis. Since individual waveform inspection relies on the subjective human eye, statistical methods may offer a better way to assess both the deadtime and the double count fraction of an adaptive cooloff scheme.

6.8.2. Fluorescence decay behavior

The decay shape of a neutron event appears to have some dependence on the size of the pulse. Larger pulses decay more quickly than small pulses, on average (*Figure 90*). The cause of this energy dependence in unknown. One possibility is that SiPM non-linearities may somehow add some non-linear behavior to the waveforms. To test for this possibility, datasets were gathered for two SiPM bias voltages: 29.5V (*Figure 90*) and 27.5V (*Figure 91*). SiPM non-linearities are reduced at lower bias voltages, so if the SiPM were responsible for the distortion, the 27.5V dataset would decay more uniformly with pulse magnitude. Examining the two figures taken at different bias voltages, the decay trends persist with great resemblance, so it appears that the SiPM is not responsible.

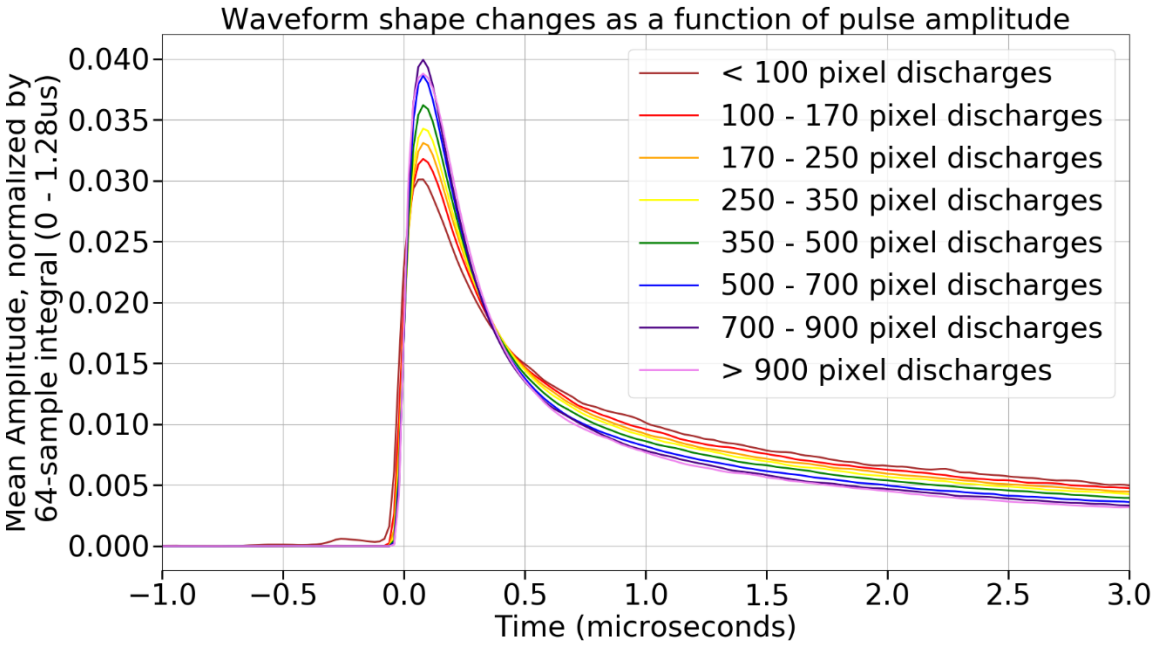

Figure 90: average, normalized waveforms for pulse energies at 29.5V SiPM voltage.

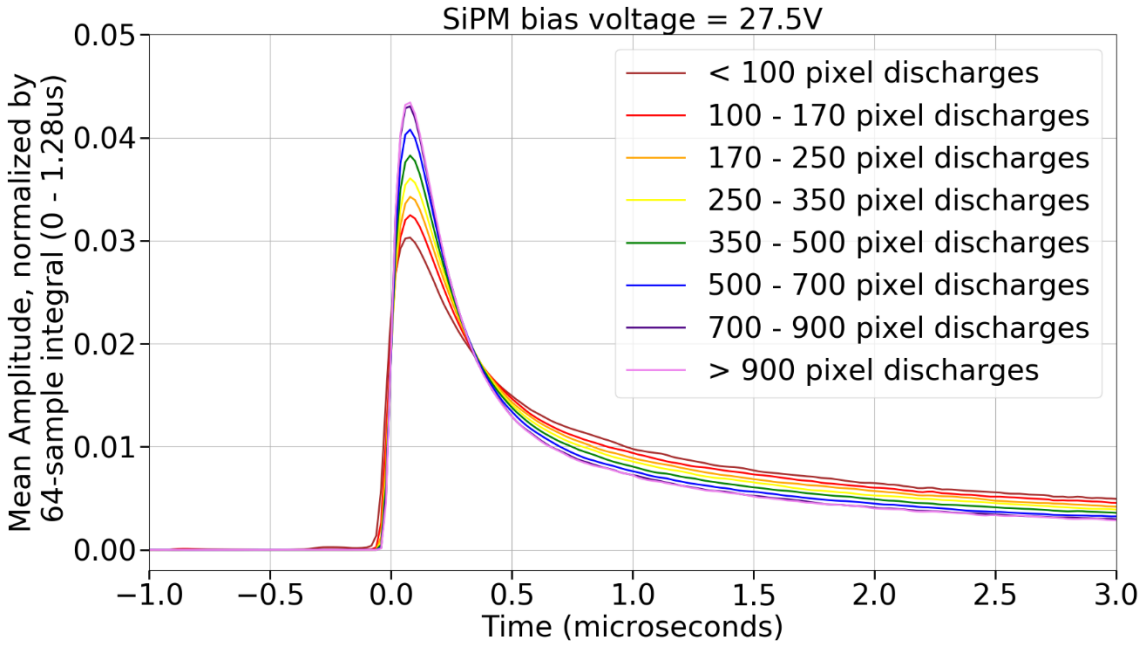

Figure 91: average, normalized waveforms for pulse energies at 27.5V SiPM voltage

Another possibility could be the “nickel-killing” feature of the primer layer of scintillator, which was purposefully added for fast quenching of neutron absorptions adjacent to the WLS fibers. Those absorptions are assumed to be the largest because they originate closest to the WLS fibers. Whetever the cause, an optimized adaptive cooloff scheme will take this energy dependence into consideration.

6.8.3. Digital Adaptive Cooloff Scheme

A two-term exponential decay function was fit for each shape. In discrete time systems such as FPGA processes, an exponential decay is most easily calculated by multiplying by a constant with a value between 0 and 1. The difference equation for this two-term exponential decay profile is given in ***Equation 12***.

Equation 12: $$f[n] = k_1 \alpha f[n-1] + k_2 \beta f[n-1]$$

Where α and β define the exponential decay rate and k_1 and k_2 are the initial conditions. For all of the decay profiles in *Figure 92*, α and β are constant and only the initial conditions are altered for each fit.

The preceding 1.28μs pulse integral is multiplied by constants and k_1 and k_2 to calculate the initial conditions for the *mean decay profile*. The decay profile is proportional in size to the preceding pulse and has a shape resembling other pulses in its energy band. The mean decay profile is subtracted from the raw data streaming in from the FPGA. This subtraction is on top of the DC bias subtraction that is already being

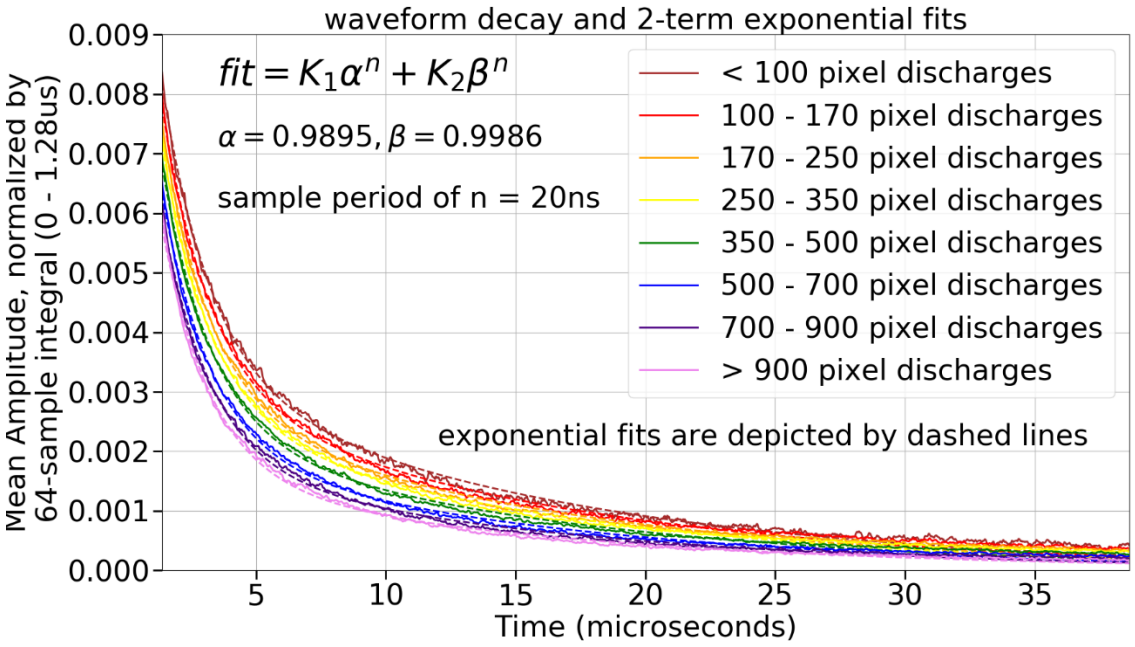

Figure 92: Two-term exponential fits for a series of decay profiles

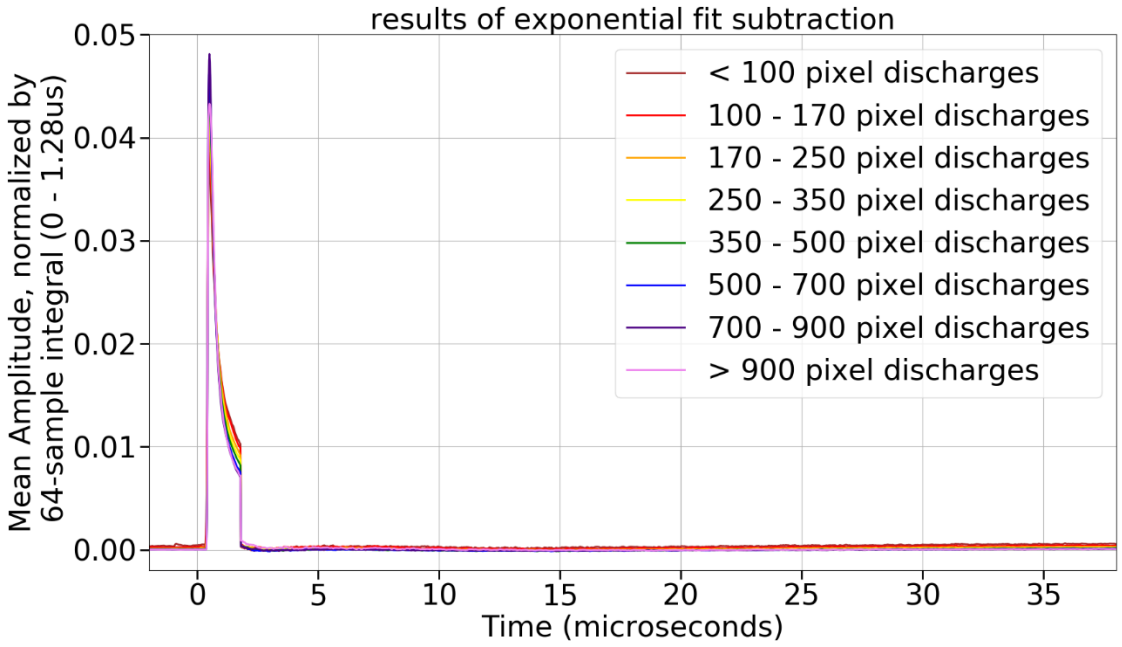

Figure 93: results of mean decay subtraction

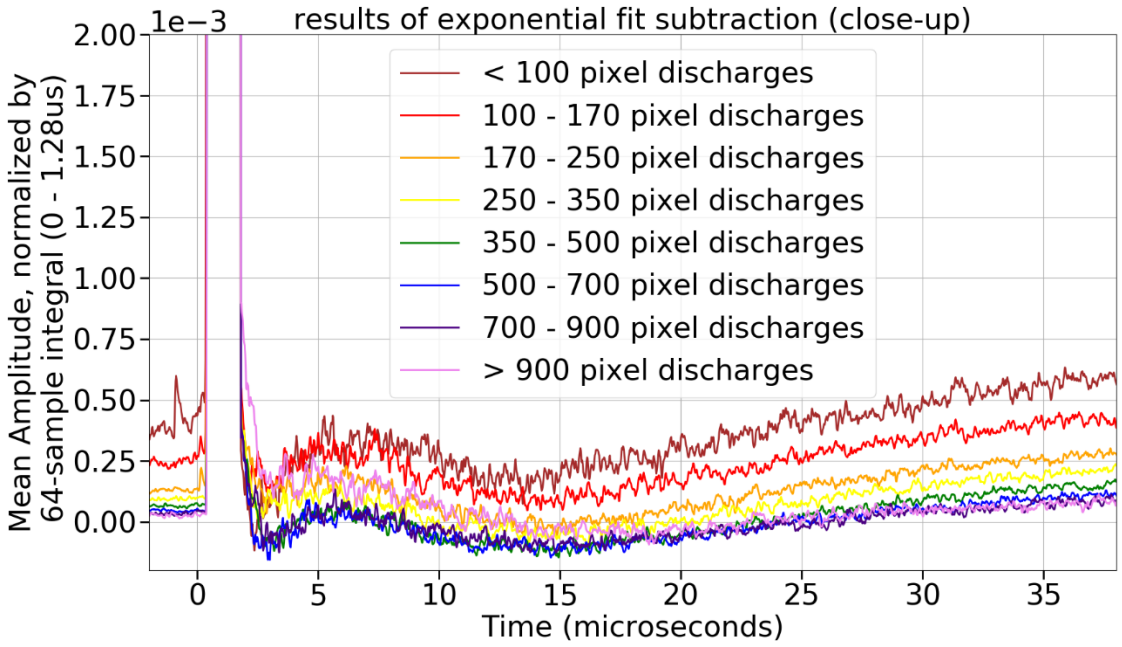

Figure 94: results of mean decay subtraction (close-up)

performed. The results of the mean decay subtraction following neutron identification is shown in *Figure 93* and *Figure 94*.

Mean decay subtraction attempts to compensate for the long decay of the neutron signal. However, it was mentioned earlier that although neutron events follow an exponential decay trend, individual pulses are very jagged and irregular. There is a large variance to the decay profile. The standard deviation of the *16-sample moving average* decay profiles are shown in *Figure 95*. The 16-point moving average is used as opposed to the raw data, because the moving average threshold is the initial trigger for the digital PSD algorithm. The 16-point moving average is also a much smoother signal with a much lower standard deviation than the raw data.

After inspecting *Figure 95*, It makes sense that the standard deviation lowers with pulse energy, because larger pulses with more photons have better counting statistics. As

with the mean, the standard deviation also has a two-term exponential fit following the difference equation in ***Equation 13***.

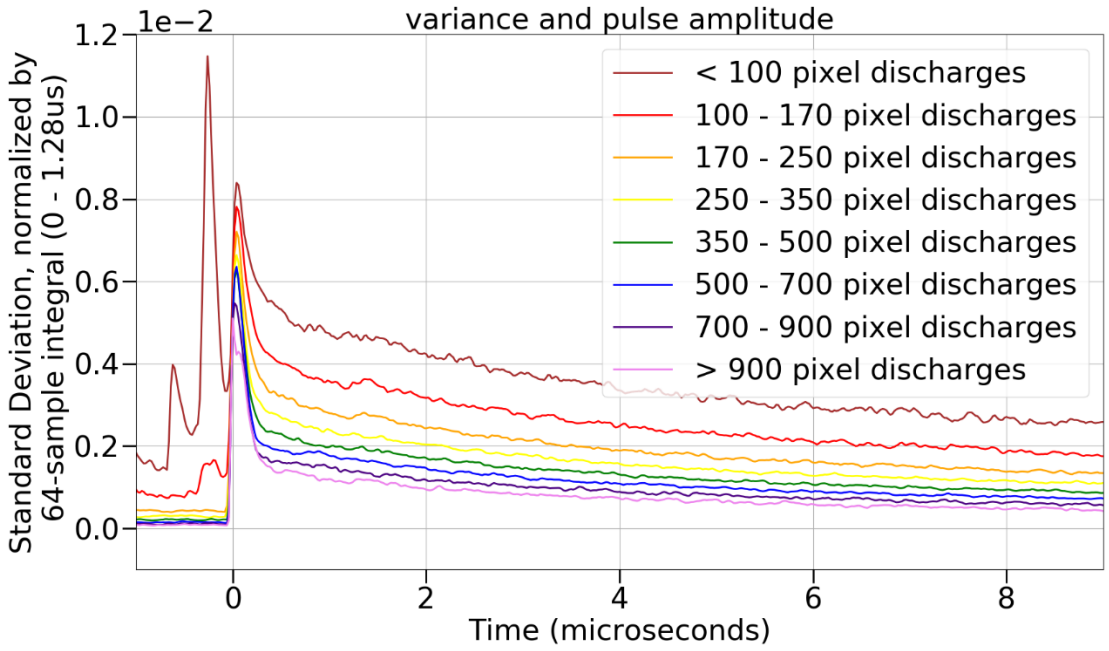

Figure 95: Decay profiles of standard deviation for a series of pulse energies

Equation 13: $$f[n] = k_3\gamma f[n-1] + k_4\tau f[n-1]$$

Where γ and τ define the exponential decay rate and k_3 and k_4 are the initial conditions. The standard deviation fits are shown in *Figure 96*. For all of the decay profiles in *Figure 96*, α and β are constant and only the initial conditions are altered for each fit.

The preceding 1.28μs integral is multiplied by constants and k_3 and k_4 to calculate the initial conditions for the standard deviation. The trigger threshold is *increased* by a multiple of the standard deviation to create the *adaptive cooloff profile*. The adaptive cooloff profile can be increased or reduced by increasing the standard deviation

multiplier. A higher profile will reduce the double count fraction and increase the deadtime. A lower profile will increase the double count fraction and reduce the deadtime.

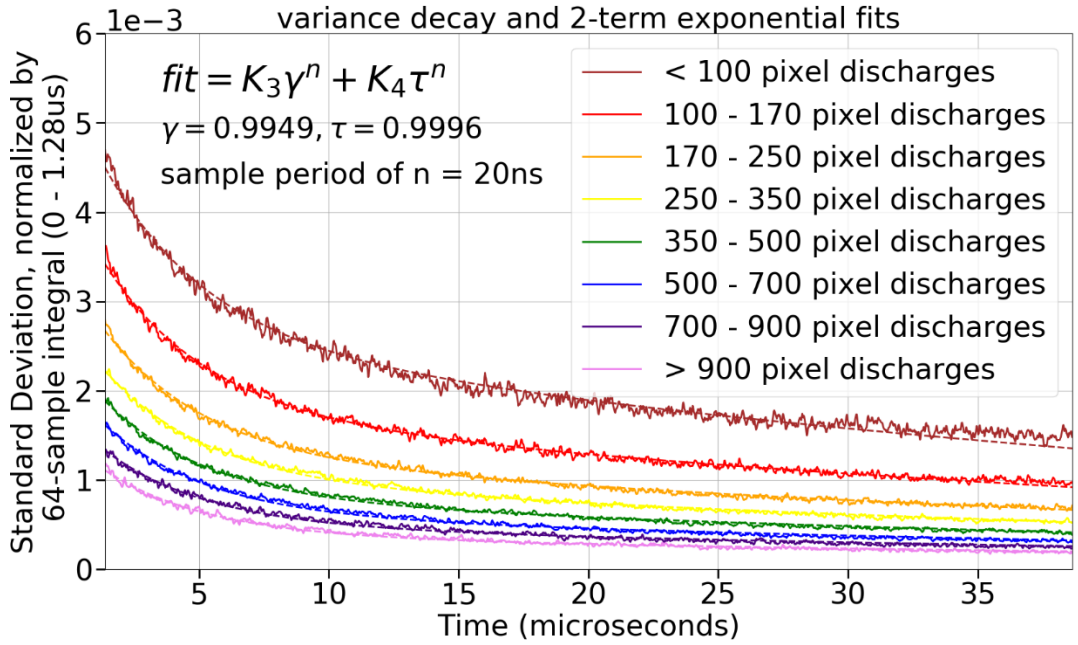

Figure 96: Two-term exponential fits for a series of standard deviation decay profiles

To summarize, the mean and standard deviation of a neutron pulse decay with a two-exponential term trend. The decay profiles are a function of the magnitude of the neutron pulse. The exponential decay rates (α,β,γ,τ) are all constant with respect to pulse energy, but the initial conditions (k_1,k_2,k_3,k_4) change according to the pulse energy. The mean decay profile is subtracted from the incoming raw data. A multiple of the standard deviation called the *adaptive cooloff profile* is added to the trigger threshold. The 16-point moving average must surpass the adaptive cooloff profile in order to trigger the PSD algorithm to examine the next pulse. The mean and standard deviation decay constants are tabulated in *Table 5* and *Table 6*.

Table 5: Mean decay constants

Mean Decay Constants	**alpha = 0.9895**	**beta = 0.9986**
Pulse Size	**K1***	**K2***
< 100 pixel discharges	5.243E-03	3.575E-03
100 - 170 pixel discharges	4.852E-03	3.188E-03
170 - 250 pixel discharges	4.638E-03	2.892E-03
250 - 350 pixel discharges	4.591E-03	2.681E-03
350 - 500 pixel discharges	4.396E-03	2.457E-03
500 - 700 pixel discharges	4.280E-03	2.102E-03
700 - 900 pixel discharges	4.164E-03	1.811E-03
> 900 pixel discharges	4.110E-03	1.565E-03

*decay initial conditions are the product of these constants and the 64-sample pulse integration (0-1.28μs).

Table 6: Standard Deviation decay constants

Std. Dev. Decay Constants	**gamma = 0.9940**	**tau = 0.99965**
Pulse Size	**K3***	**K4***
< 100 pixel discharges	1.591E-03	2.242E-03
100 - 170 pixel discharges	1.351E-03	1.797E-03
170 - 250 pixel discharges	1.325E-03	1.005E-03
250 - 350 pixel discharges	1.188E-03	7.871E-04
350 - 500 pixel discharges	1.092E-03	6.180E-04
500 - 700 pixel discharges	9.839E-04	4.885E-04
700 - 900 pixel discharges	8.830E-04	3.872E-04
> 900 pixel discharges	7.294E-04	3.105E-04

*decay initial conditions are the product of these constants and the 64-sample pulse integration (0-1.28μs).

6.8.4. Example waveforms illustrate the digital adaptive cooloff scheme

Let's look at some examples of how the adaptive cooloff scheme functions on the CANDOR_DAQ. An internal logic analyzer (ILA) was implanted into the Xilinx Kintex 7 FPGA in order to review the internal workings of the adaptive cooloff algorithm. *Figure 97*, *Figure 98*, *Figure 99*, *Figure 100*, *Figure 101* all shows four signals: the raw ADC datastream (blue), the DC bias subtracted and mean-decay subtracted 16-point moving average (green), the trigger threshold (black), and a neutron detection flag (red). *Figure 97* shows normal operation. After a neutron detection, the mean decay is subtracted from the moving average, and the trigger threshold is raised by 5.5 standard deviations. The threshold decays exponentially for 60μs at which point the system returns to normal operation.

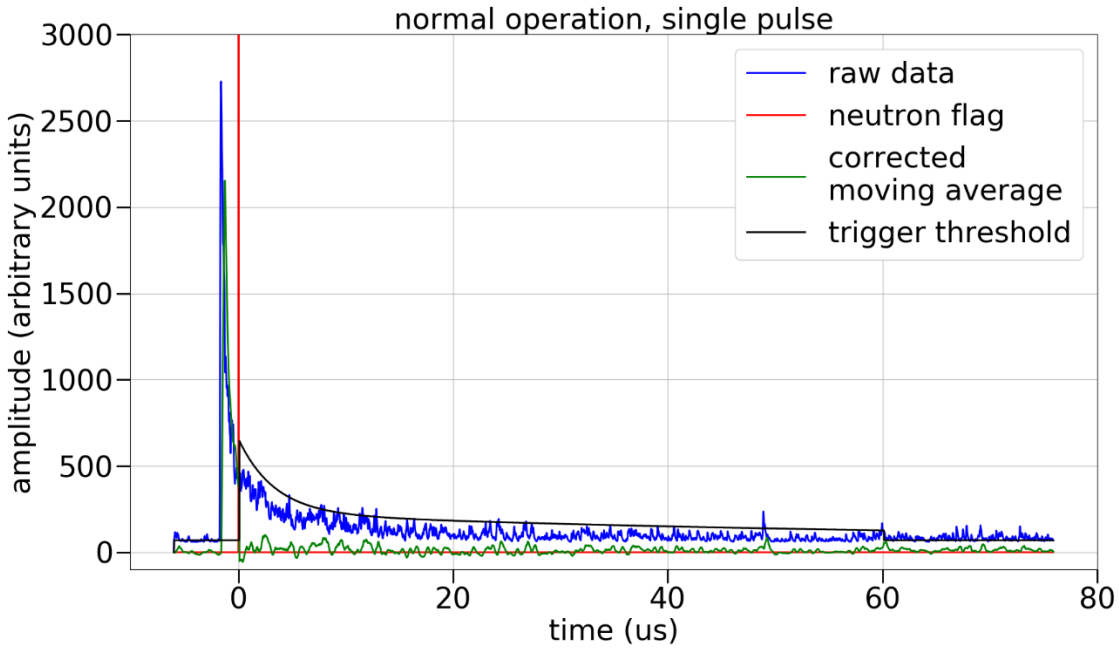

Figure 97: Normal operation, single pulse

Figure 98 shows the adaptive cooloff at a high count rate, where five neutrons arrive in close succession, and the algorithm successfully identifies all five events.

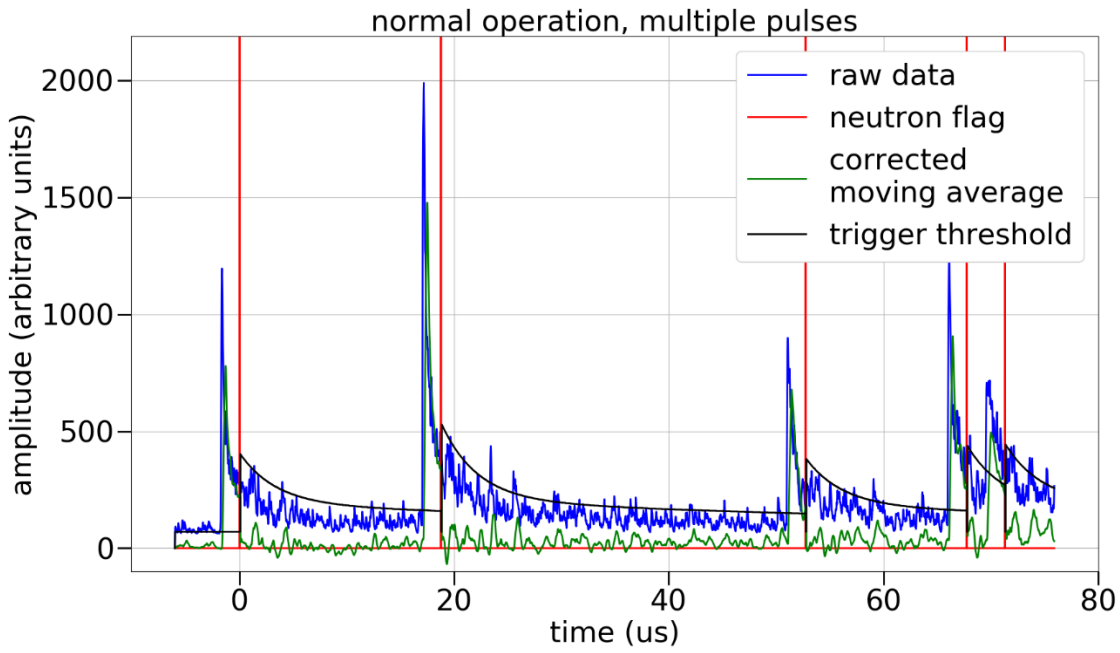

Figure 98: Normal operation, multiple pulses

Figure 99 shows a smaller neutron arriving during the decay of a larger neutron. The adaptive cooloff threshold is set too high to be triggered by the moving average. This is a missed count, and this demonstrates how reduced sensitivity during adaptive cooloff contributes to the deadtime of the detector.

Figure 100 shows the system double counting a neutron at 35µs. Typically, the double count fraction should be limited to 1/1000 or 0.1%. Note that this waveform is from a separate dataset where the adaptive cooloff was only raised by 3 standard deviations. There were no double counts observed from the 5.5 standard deviation adaptive cooloff threshold.

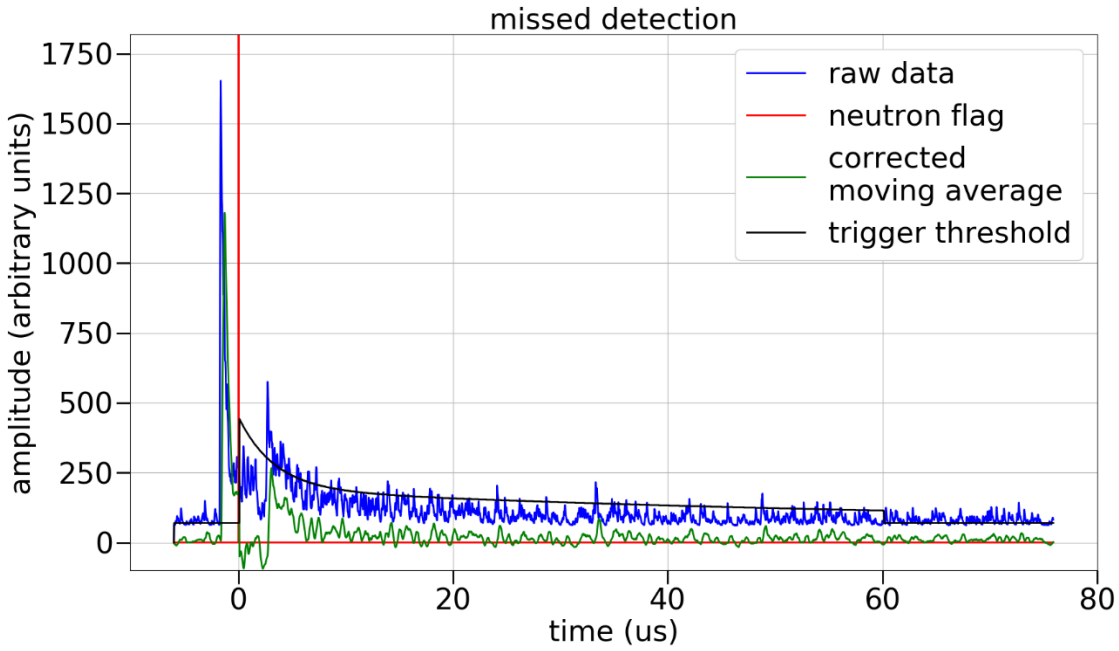

Figure 99: missed detection at ~3us

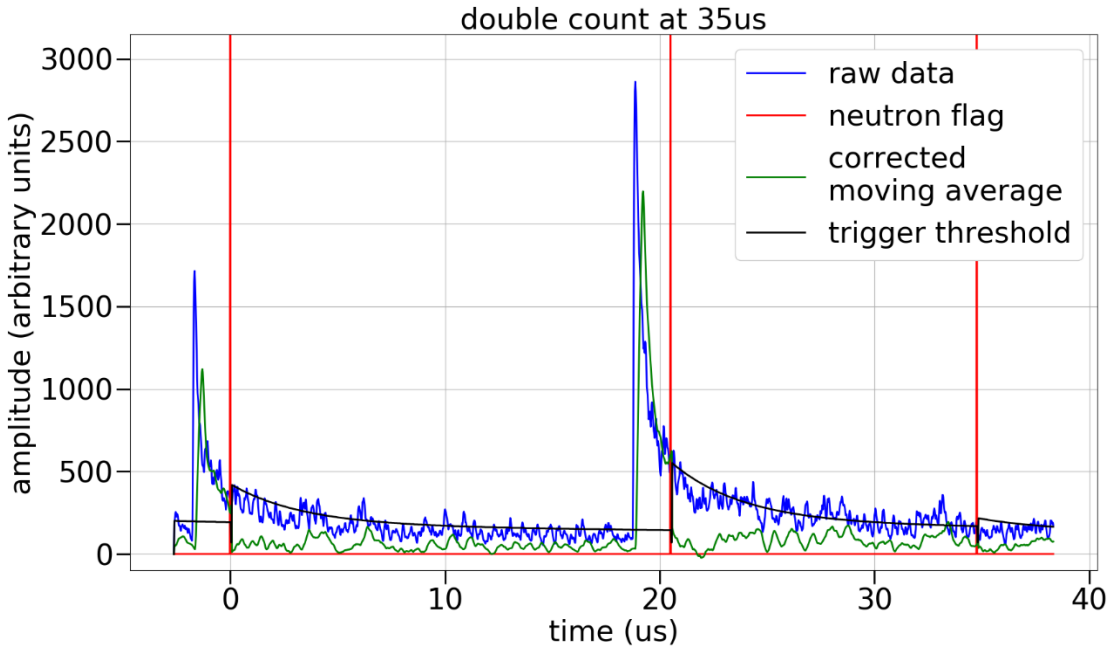

Figure 100: double count at 35us

Figure 101 attempts to show an ambiguous example of a missed neutron arriving near 9µs. This is a small neutron pulse arriving on the tail of a larger neutron. Ir is it just a coincidence? After examining thousands of waveforms, I would say that it is a neutron. But, how keen is my eye at spotting events really? And, if the adaptive cooloff threshold were lowered to accommodate this type of event, how many other spurious events would be falsely identified as well? This is a tough question to answer if the only means of telling is through manual inspection by a subjective eye.

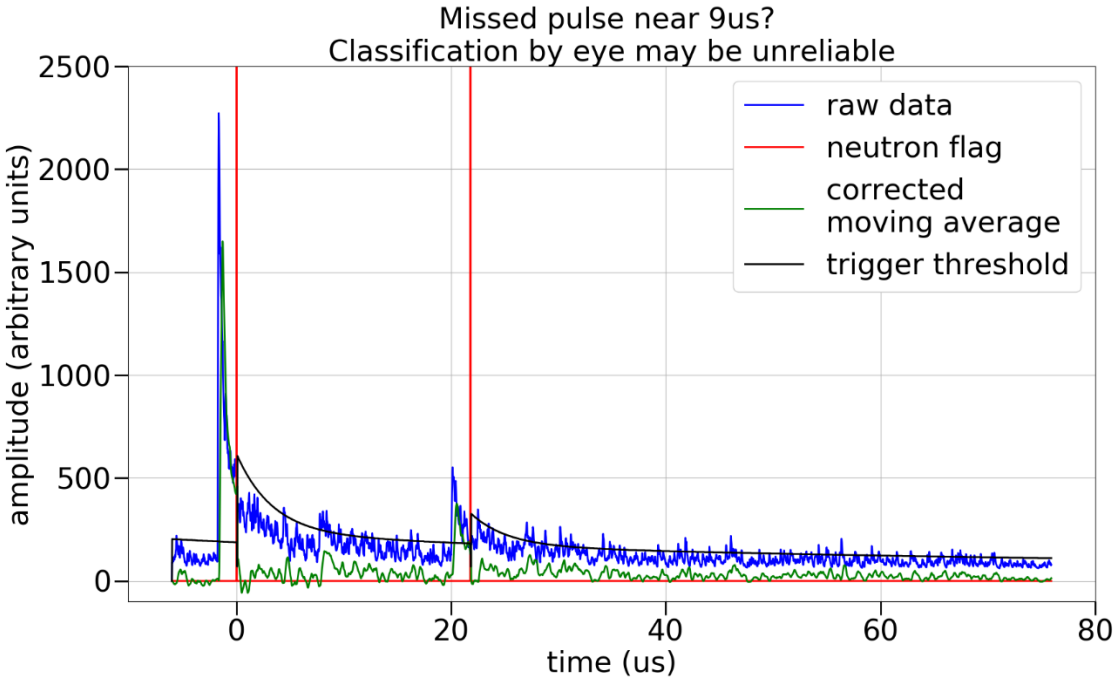

Figure 101: Neutron at 9us? Individual waveform inspection grows unreliable

Figure 102 shows an example with multiple events stack up in close succession. The sdaptive cooloff prediction becomes less accurate. Observe that the corrected moving average hovers above zero beginning after the second event, because the second event was underestimated, and the mean subtraction is inadequate. This could become problematic at high count rates (> 10kHz) where pulse stack-up is more frequent.

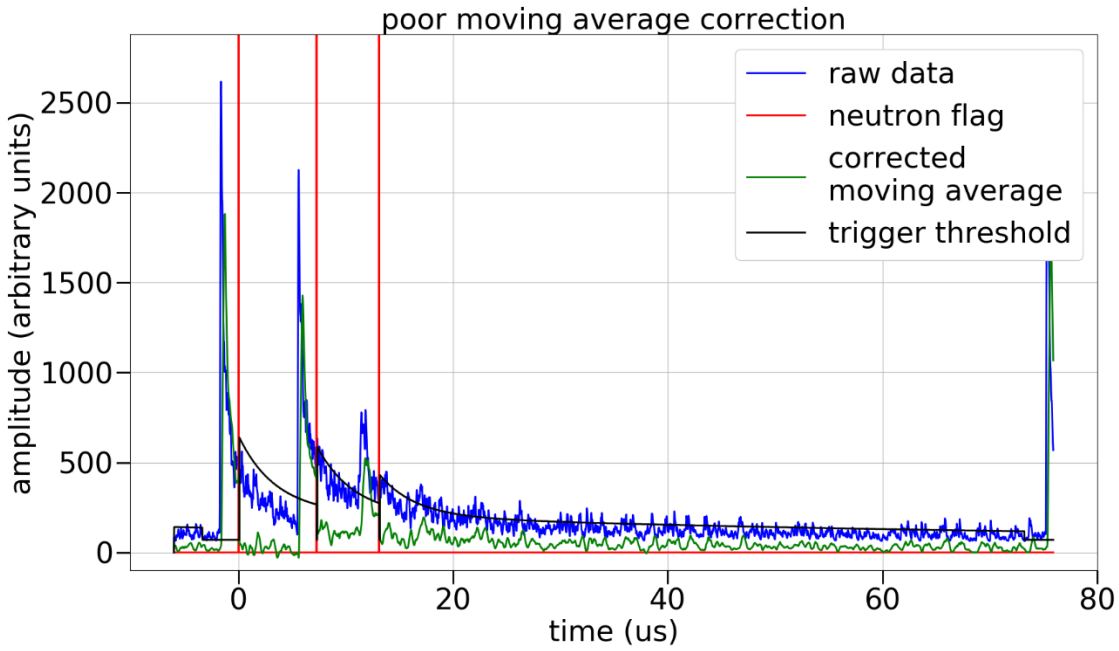

Figure 102: Pulse mean estimation is not always perfect

6.8.5. Analog discriminator adaptive cooloff

Discussed previously, the analog discriminator schematic is shown in *Figure 62*. Its adaptive cooloff scheme works as follows: When U1 switches to indicate neutron detection, it also inhibits the discharge of C12 integration capacitor by the threshold detector. This is to prevent voltage ripples in the tail of a neutron pulse from triggering extra neutron counts. The length of time where this is held off (making discriminator "blind" aka cool-off time) is controlled by the "hold off adj." power supply voltage. The power supply voltage should be adjustable between 7 to 28 volts. The lower the voltage, the shorter the hold-off time.

The concepts of deadtime, double count fraction, and adaptive cooloff have been discussed, and some relevant examples were reviewed. Next, some statistical methods will be introduced which might help determine the deadtime and double count fraction in a more reliable way rather than by manual inspection.

6.8.6. Statistical measurement of deadtime and double count fraction

The analytical expressions and models for deadtime are well established in Poisson processes in radiation detection [164]–[168]. More recent work has been done to model deadtime in non-ideal and non-Poisson situations [169]–[172].

Deadtime measurements are usually done using one of two methods. The first methods is the "two-source" method, where by count rates are measured in the presence of two constant radiation sources separately, and then together. The combined count rate should be a linear superposition of each source, and any deviation is assumed to be a result of deadtime. The second method is the "fast decaying source" method, where a fast-decaying isotope (a half-life ranging from minutes to hours) is placed in the presence of the detector. For a detector system with a deadtime of zero, the count rate should decay exponentially with the source's radioactivity. Any deviation, particularly during high radioactivity periods, is assumed to be the result of deadtime [164], [167], [173]. An third less commonly used method directly analyzes event arrival statistics of a Poisson process [174].

To introduce statistical measurement methods, a high adaptive cooloff threshold is chosen. The adaptive cooloff profile to 5.5 standard deviations. At this level, there were no double counts observed via manual inspection after reviewing 10000 waveforms.

The double count fraction is assumed to be zero (or very close to zero) and only the deadtime needs to be measured.

6.8.7. Deadtime calculations based on superposition of attenuator transmissions

The first method to measure deadtime was tried several times, and yielded anomalous results. The concept is a variation of the "two-source method". It uses the superposition of attenuators with known neutron transmission factors to calculate the actual count rate, and compare with the measured count rate. Let's consider a hypothetical example with an original beam flux of 100kHz on detector, and four attenuators A,B,C, and D each with a transmission factor of 0.1. The concept is illustrated in *Figure 103*.

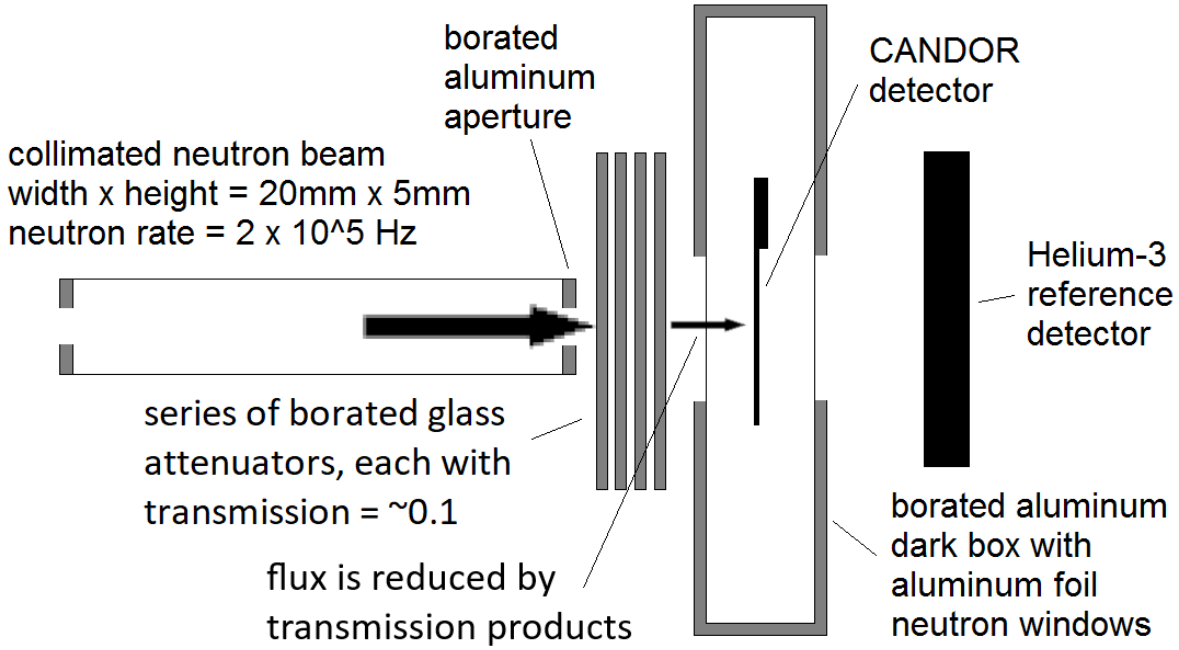

Figure 103: Concept of failed deadtime measurement experiment

Original Beam Rate = 1E+5 Hz

Attenuator A Transmission = 0.1

Attenuator B Transmission = 0.1

Attenuator C Transmission = 0.1

Attenuator D Transmission = 0.1

Beam Rate ABCD = 10 Hz

Beam Rate ABC = 100 Hz

Beam Rate AB = 1000 Hz

Beam Rate A = 10000 Hz

If each attenuator allows 10% of neutrons through, then stacking 2 attenuators would presumably allow passage of 1% of neutrons, 3 attenuators 0.1%, and 4 attenuators 0.01%. Suppose that after measuring the count rate with only attenuator A, the measured count rate was only 9.5 kHz, even though the calculated rate should be 10 kHz. Applying *Equation 14* and *Equation 15* to this example, the deadtime fraction is 0.05, and the deadtime is 5μs. Background count rates are pre-subtracted from the measured and calculated rates.

Equation 14: $Deadtime\ Fraction = 1 - \frac{measured\ rate}{calculated\ rate}$

Equation 15: $Deadtime\ Fraction = (deadtime)\ \times (calculated\ count\ rate)$

Experimentally, the transmission of each attenuator can be characterized at low count rates, where the deadtime percentage is very low even for longer deadtimes. This is accomplished by using the relationship in *Equation 16*:

Equation 16:

$$\frac{n_1}{\alpha_1} = \frac{n_2}{\alpha_2}$$

Where n_1 is the calculated count rate with attenuator configuration α_1 and n_2 is the calculated count rate with attenuator configuration α_2. In the hypothetical example illustrated in *Figure 103*, n_{ABCD} = 10Hz, α_{ABCD} = 0.0001, n_{ABCD} = 100Hz, α_{ABC} = 0.001. To isolate α_D, the following relationship is assumed:

Equation 17

$$\alpha_D = \frac{n_{ABCD}}{n_{ABC}}$$

n, the calculated count rate, is calculated from established relationship for a non-paralyzable detector system in *Equation 18*:

Equation 18

$$n = \frac{m}{1 - m\tau} - b$$

Where *m* is the measured count rate, τ is the deadtime, and *b* is the background count rate. τ is not known, but an estimated value of τ = 3μs ± 2μs is used as an initial guess based on preliminary studies of the detector system. The wide deadtime uncertainty (± 2μs) does not translate to wide uncertainty in the attenuator calculations at low count

rates where the term $m\tau$ is small. In our attenuator characterizations, the highest count rates are below 700Hz and $m\tau < 0.0021$. *Table 7* shows the results of a attenuator characterizations using *Equation 17* and *Equation 18*.

Table 7: attenuation factor measurements

Attenuator	**Attenuation Factor**	**Uncertainty**
A	0.1486	0.0006
C	0.1477	0.0006
F	0.0636	0.0003
G	0.0635	0.0003
H	0.0633	0.0003

After calculating the attenuation factors, the calculated count rate is determined from the relationship in *Equation 16*, and relative to attenuator configuration "AGH" which has a count rate of 99.5Hz and a transmission factor of 5.97E-4 (*Equation 19*).

Equation 19

$$n_1 = \frac{n_{AGH}\alpha_1}{\alpha_{AGH}}$$

Now the deadtime can be calculated from the measured count rates and the calculated count rates derived in *Equation 19*. The deadtime is calculated using *Equation 20* for a non-paralyzable system.

Equation 20

$$\tau = \frac{1}{m} - \frac{1}{n+b}$$

Where *m* is the measured count rate, *n* is the calculated count rate, and *b* is the background count rate. The background count rate used for all calculations is 0.151Hz. The results are shown in *Table 8*.

Table 8: deadtime calculations using attenuator transmission superposition

Attenuators	**Measured Count Rate (Hz)**	**Measured Uncertainty (Hz)**	**Calculated Count Rate (Hz)**	**Calculated Uncertainty (Hz)**	**Deadtime (μs)**	**Deadtime Uncertainty (μs)**
none	106220	141	166580	1334	3.41	0.05
A	23997.4	34.2	24753.9	222.8	1.27	0.37
H	10701.9	14.5	10548.5	96.0	-1.36	0.87
AC	3915.63	6.21	3655.33	36.18	-18.17	2.74
AH	1632.51	2.84	1567.51	15.65	-25.34	6.46
FG	670.01	1.15	672.03	6.77	4.82	15.2
FH	668.37	1.15	670.38	6.75	4.83	15.2
GH	667.61	1.15	669.61	6.74	4.83	15.3
AGH	99.50	0.31	99.51	1.08	15.38	113.6
CGH	98.88	0.31	99.10	1.09	37.54	115.6
FGH	42.65	0.15	42.56	0.47	31.83	267.9

First, notice the deadtime is *not* constant across count rates. Also notice that the calculated deadtime is *negative* at some count rates! This would imply that there is

rampant double counting of pulses. However, manual inspection of waveforms shows no double counts after examining 10000 pulses. The failure is with the experiment concept. The assumption of superposition for attenuators fails when you consider that the attenuators not only absorb neutrons, they also scatter neutrons. The possibility of neutron scattering by the attenuators was neglected. A more accurate experiment diagram, which takes scattering into account is shown in *Figure 104*.

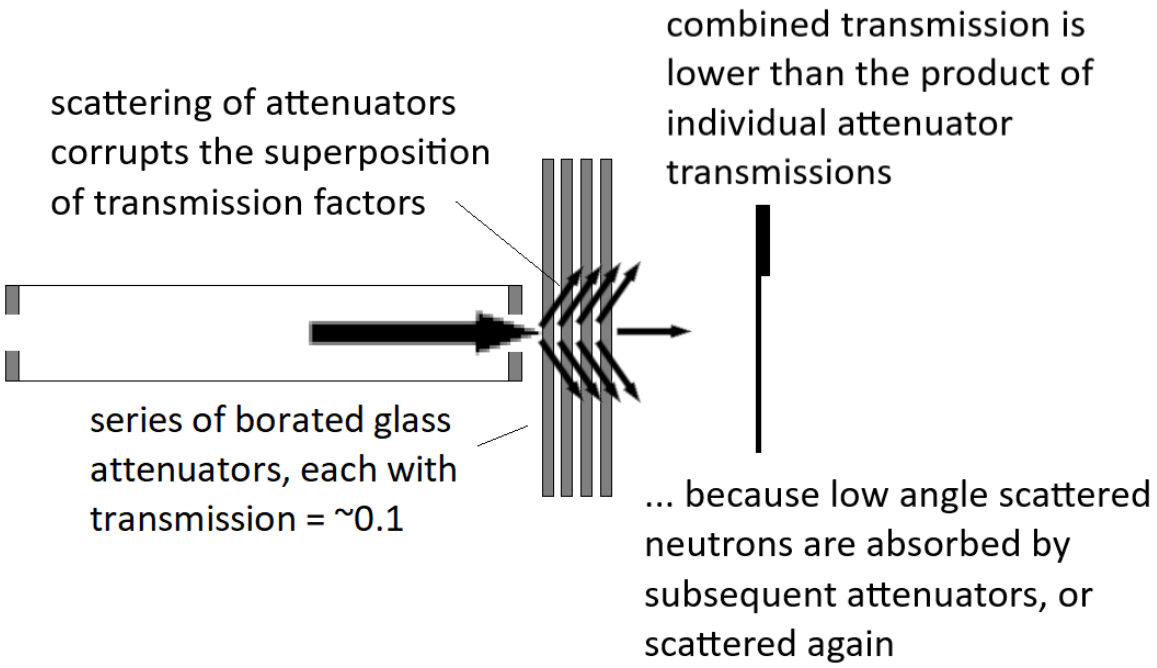

Figure 104: experiment diagram depicting neutron scattering from the attenuators

It appears that the combined transmission through stacked attenuators is actually *lower* than the product of the individual transmission factors ($\alpha_{12} \neq \alpha_1\alpha_2$). This could be because scattered neutrons travel a longer path through the attenuator material after scattering and are more likely to be absorbed. It could also be because neutrons are more likely to be scattered several times while passing through an attenuator stack and the divergence of the beam grows with each attenuator (*Figure 104*). The proper way to

repeat this type of experiment would be to collimate the beam after the attenuator stack to as to eliminate the contribution of scattered neutrons to the measurements. To do this would require a new hardware configuration and attenuators sized for installation inside the 4" x 4" beam port at PHADES. The design must ensure that glass attenuators are fully confined and cannot create debris inside the beam port even if cracked or broken. Given the time constraints and availability of engineering and machining resources, an alternate technique was developed to measure deadtime.

6.8.8. Deadtime calculations based on arrival time statistics

Luckily, the CANDOR_DAQ has timestamping capability. Each event includes the detector address and the time of arrival with a time resolution of 100ns compatible with PTP timing protocols. This allows a comparison of the measured distribution of arrival times with the exponential distribution of arrival times for a random event. For a random process with an average arrival rate of λ and the arrivals occur independently, the probability that an event arrives within a particular period is:

Equation 21: $$P(t_1 < X < t_2) = e^{-\lambda t_1} - e^{-\lambda t_2}$$

where e ≅ 2.71828.

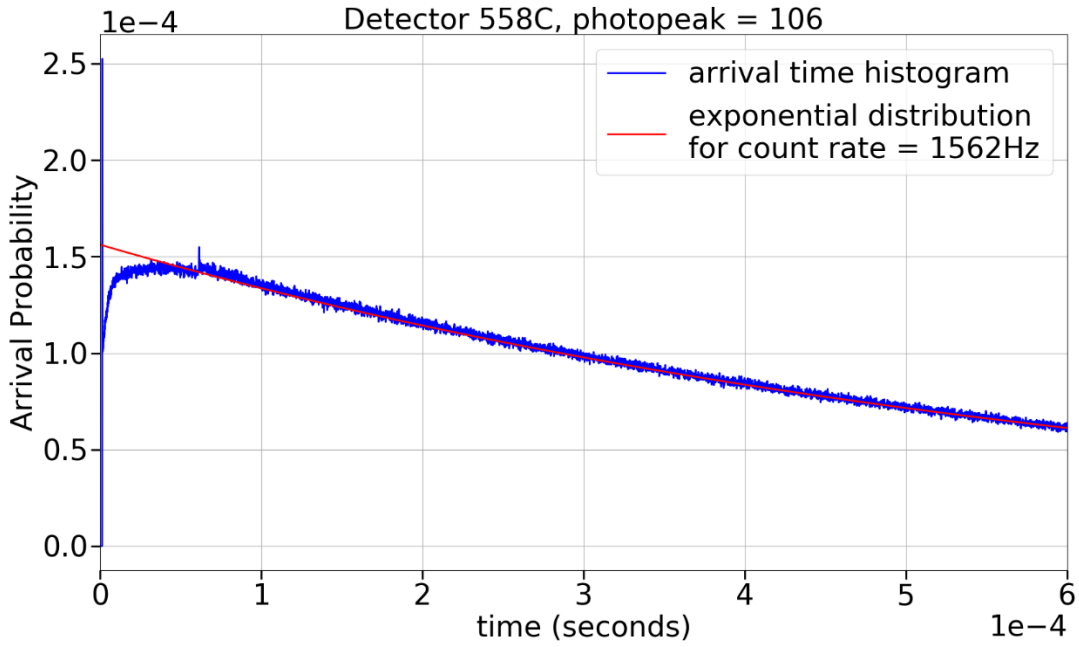

Figure 105: Actual arrival times are compared to the exponential distribution of arrival times for λ = 1666.2 Hz

To compute the arrival times of events, and the count rate, a dataset with a very large number of events (> 10 million) is gathered by the CANDOR_DAQ. The measured count rate for a detector is found from subtracting the first and last event timestamps and dividing by the total number of events. The arrival time for each event is calculated by subtracting the previous event timestamp from the current event timestamp. The arrival times are histogrammed, and a probability density function (PDF) is computed by dividing the arrival time histogram by the total number of events. *Figure 105* and *Figure 106* show the measured PDF and the exponential distribution for the calculated count rate.

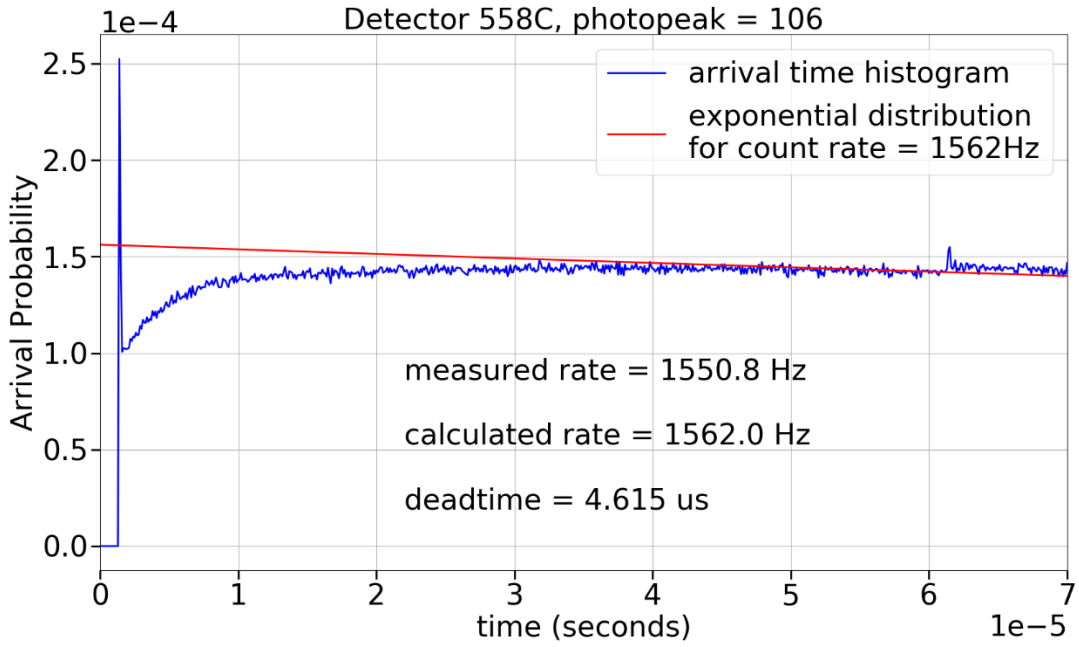

Figure 106: close-up of the measured PDF and exponential distribution

There are some features to discuss in the measured PDF of *Figure 106*. Beginning at t = 0, the probability of detection is zero. This is a firm deadtime for the digital PSD algorithm. After triggering, an event must be integrated for 1.28µs before the neutron is discriminated, plus there is a 100ns period in which the FPGA performs calculations and the adaptive cooloff profile is initialized. At t = 1.4µs, there is brief a spike in sensitivity. This is the first opportunity for the pulse shape discrimination algorithm to re-trigger. There is a possibility that a neutron arriving toward the end of the 1.4µs dead time will be detected separately. After this first opportunity to re-trigger, the sensitivity drops for a period and slowly recovers until the end of the adaptive cooloff period at 61.4µs. There is also a brief spike in sensitivity just after 61.4µs when adaptive cooloff ends. If a neutron arrives toward the end of adaptive cooloff, and this event is too small to breach the raised

adaptive cooloff threshold, but large enough to trigger the normal threshold, then it will trigger the PSD algorithm the moment adaptive cooloff ends.

Calculating the deadtime, τ, and the calculated count rate, r, from the measured PDF and the exponential distribution is a bit of a process.

Equation 22:

$$\tau = \sum_{n=0}^{end\ of\ adaptive\ cooloff} \left(1 - \frac{M[n]}{T[n]}\right) \times timestamp\ resolution$$

Where M[n] is the measured PDF and T[n] is the theoretical exponential distribution. The timestamp resolution is 100ns. After calculating the deadtime, the true count rate is calculated as:

Equation 23:

$$r_{calculated} = \frac{C_{total}}{T_{total} - C_{total}\tau}$$

Where C_{total} is the total number of events in the dataset, and T_{total} is the total collection time found by subtracting the first and last event timestamps. Next, λ, the mean arrival rate, and is calculated from $r_{calculated}$ and the timestamp period of 100ns.

Equation 24: $$\lambda = r_{calculated} \times 100ns$$

The exponential distribution is re-calculated using ***Equation 21*** and the re-calculated value of λ. The whole process involving ***Equation 21***, ***Equation 22***, ***Equation 23***, and ***Equation 24*** is iterated 20 times at which point it has converged to a final value.

The measurement from which the deadtime and true count rate are calculated is a very easy process, if you are working with a reactor source with a nice and steady flow of neutrons: put the detector in a beam with an appropriate count rate and count for an appropriate period of time. This method will not work with a spallation source with brief pulses of high neutron intensity. The caveats with using this method of measuring deadtime are the "appropriate count rate" and the "appropriate period of time".

A basic property of a probability density function that it integrates to one. Think of it like a water bed (if you remember waterbeds 😊); if you lie down on one side of the waterbed, the water will displace and bubble up on the other side of the bed. There is a distortion to the PDF caused by the deadtime. The effect is much more pronounced at higher count rates and is illustrated in *Figure 107*.

The distortion is so high at 28.4kHz that the deadtime is calculated to be negative! An appropriate count rate is a count rate low enough that the distortion seen during the adaptive cooloff period is negligibly small. An appropriate range of count rates was found empirically by performing the deadtime measurements at a progression of count rates (*Table 9*).

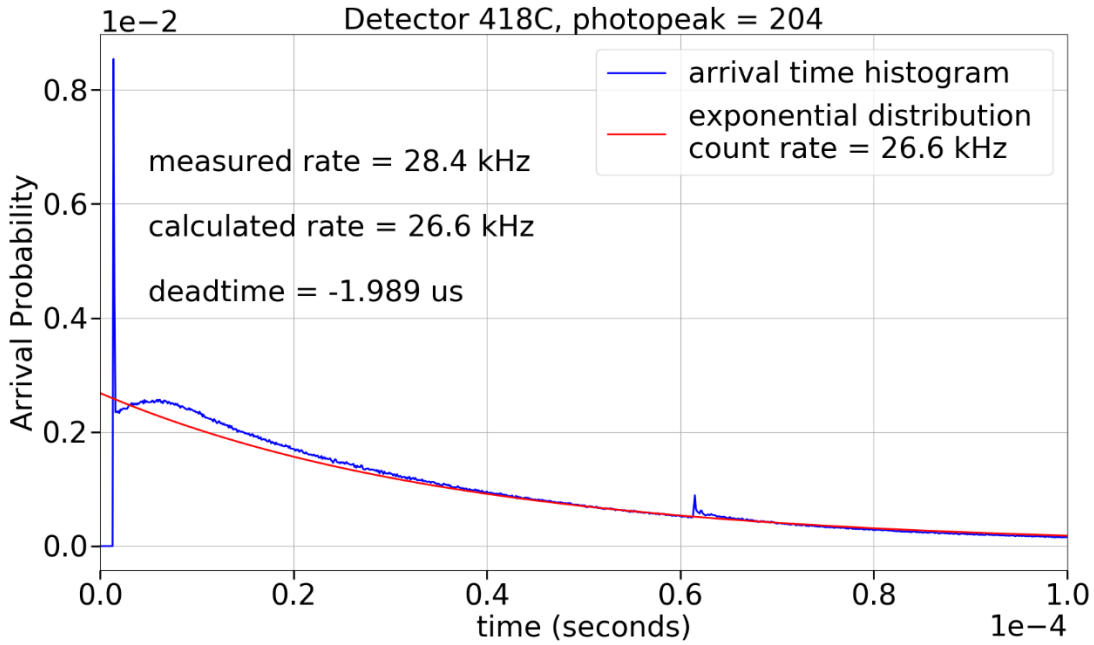

Figure 107: PDF distortion is prevalent at high count rates

Table 9: count rates and deadtime calculations

Detector	detector photopeak	PSD	Adaptive cooloff theshold	rate	deadtime	uncertainty	deadtime percentage
418C	204	digital	5.5 SD	11.532 kHz	negative	N/A	N/A
418C	204	digital	5.5 SD	1.666 kHz	2.2814 µs	0.0008 µs	0.38%
418C	204	digital	5.5 SD	654.0 Hz	2.4754 µs	0.0034 µs	0.16%
418C	204	digital	5.5 SD	231.9 Hz	2.4423 µs	0.0054 µs	0.06%
558C	106	digital	5.5 SD	1.562 kHz	4.6148 µs	0.0011 µs	0.72%
558C	106	digital	5.5 SD	604.4 Hz	4.8693 µs	0.0057 µs	0.29%
558C	106	digital	5.5 SD	216.7 Hz	4.7246 µs	0.0121 µs	0.10%
418C	204	digital	3.25 SD	648.2 Hz	0.8624 µs	0.0012 µs	0.06%
418C	204	digital	3.25 SD	229.1 Hz	0.8119 µs	0.0019 µs	0.02%
558C	106	digital	3.25 SD	607.2 Hz	2.2313 µs	0.0030 µs	0.14%
558C	106	digital	3.25 SD	213.1 Hz	2.5790 µs	0.00363 µs	0.05%

Table 9 shows that the deadtime calculation has converged to a value of 2.475µs ± 0.0034µs for detector 418C at a deadtime percentage of 0.16%, or a deadtime fraction of 0.0016, and that there is about a 10% underestimation of the deadtime calculation for the same detector with a deadtime fraction of 0.0038. Presumably, if the adaptive cooloff period were shorter, the count rate could be increased without significant distortion.

6.8.9. Deadtime calculations for the analog discriminator

The same process was used to examine the PDF and deadtime for the analog discriminator.

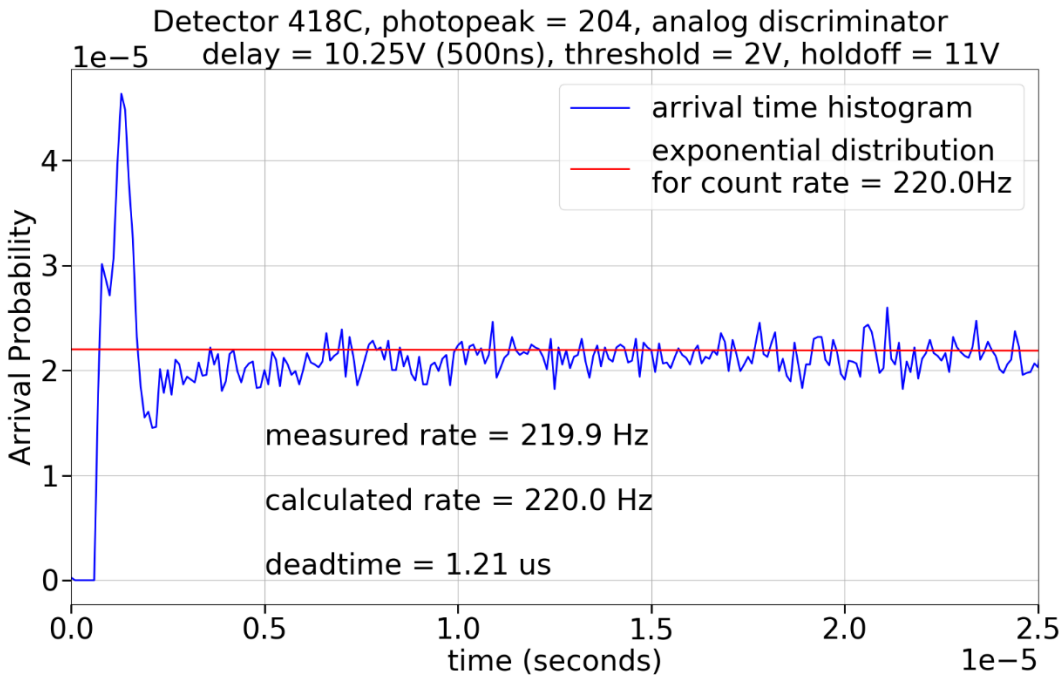

Figure 108: arrival time PDF and exponential distribution for analog discriminator, 220.0Hz

Looking at the arrival time statistics for the analog discriminator, it appears that there is a brief period of complete deadtime (t=0 thru t = 500ns) followed by a period where double counts are prevalent (t=500ns thru t = 1.5μs), and then a longer period where there is reduced sensitivity which eventually recovers to baseline before 20μs. This is an interesting case, because it's clear that there is a mixture of doublecounts as well as missed counts. How many doublecounts are in this mixture? How many missed counts? These questions can't be answered from just this single PDF.

Figure 109 shows a second arrival time PDF for the same detector with the same threshold, delay, and holdoff voltage settings. Only the count rate has increased. The count rate was increased from 220.0Hz to 631.5Hz. Observe that the doublecount and deadtime features have significantly changed. This is because the proportion of doublecounts to missed counts has fallen. At higher count rates, the number of missed counts dominates, whereas before there was a higher proportion of double counts. This makes sense when you consider that the deadtime fraction increases linearly with the count rate, but the doublecount fraction should remain constant regardless of count rate. The double count fraction, in theory, shouldn't be a function of how frequently events arrive, but rather a function of the variability in decay shapes and how high the adaptive cooloff threshold is set. *Doublecount fraction stability* and *linear increase of deadtime fraction* with count rate can be exploited to determine both the doublecount fraction and the deadtime. Let's look at how this is accomplished.

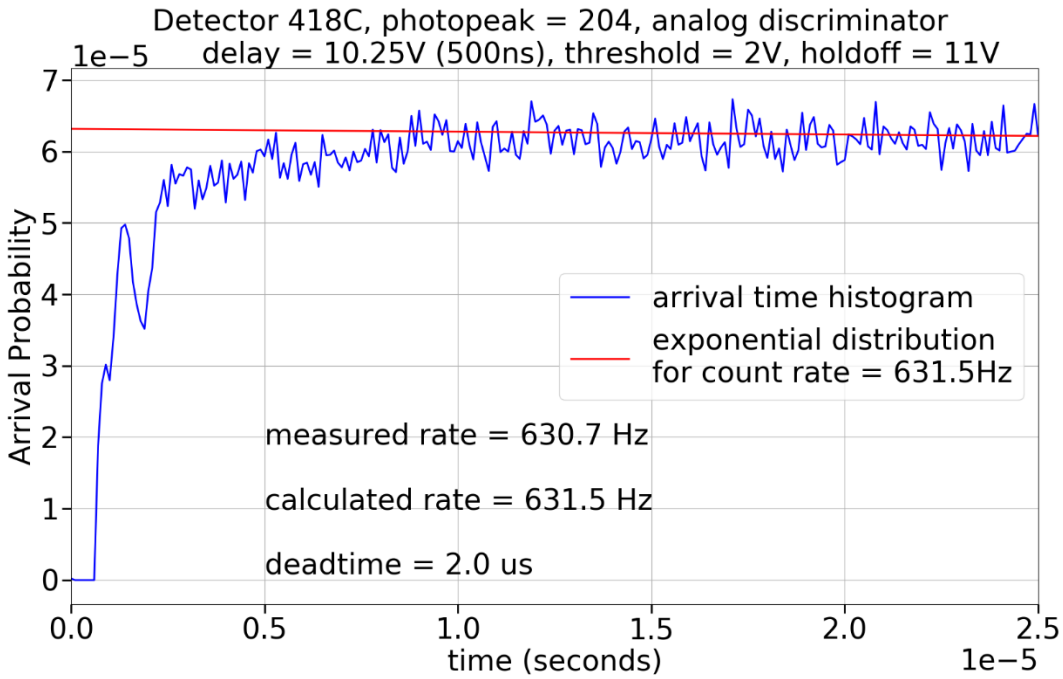

Figure 109: arrival time PDF and exponential distribution for analog discriminator, 631.5Hz

6.8.10. Determining Deadtime and Doublecount Fraction from arrival time PDFs

A solvable system of equations can be derived from ***Equation 25***:

Equation 25:

$$measured\ counts = theoretical\ counts - missed\ counts + doublecounts$$

Where theoretical counts follow the exponential distribution of arrival times for a given count rate. The number of missed counts is expressed as:

Equation 26:

$$missed\ counts = theoretical\ counts \times \tau \times r_c$$

Where τ is the deadtime and r_c is the calculated count rate. The number of missed counts is equal to the theoretical number of counts multiplied by the deadtime fraction. The number of double counts is:

Equation 27:

$$double\ counts = theoretical\ counts\ \times\ d$$

Where d is the doublecount fraction. Consolidating ***Equation 25***, ***Equation 26***, and ***Equation 27*** into ***Equation 28:***

Equation 28:

$$M = T(\ 1\ -\ \tau r_c + d)$$

Where M is the number of measured counts and T is the number of theoretical counts. If measurements are taken at two different count rates, a system of two equations can be generated.

Equation 29:

$$M_1 = T_1(\ 1\ -\ \tau r_1 +\ d)$$

$$M_2 = T_2(\ 1\ -\ \tau r_2 +\ d)$$

The deadtime (τ) and doublecount fraction (d) are assumed to be constant for both measurements. We now have two equations and two unknowns. After performing some algebra:

Equation 30:

$$\tau = \frac{\frac{M_2}{T_2} - \frac{M_1}{T_1}}{r_1 - r_2}$$

$$d = \frac{M_1}{T_1} + \tau r_1 - 1$$

The measured PDF and exponential distribution can be used for M and T respectively, since it is the ratio of these quantities that is important. In that case, T is equal to 1, and M is computed as:

Equation 31:

$$M = 1 - \left(\sum_{n=0}^{end\ of\ adaptive\ cooloff} T[n] - M[n] \right)$$

The deadtime and doublecount fraction were determined for several end cases and tabulated in *Table 10*.

Table 10: results of deadtime and doublecount fraction measurements

Detector	photopeak	Adaptive cooloff theshold	PSD	deadtime	deadtime uncertainty	doublecount fraction	doublecount uncertainty
418C	204	11V	analog	2.465 µs	0.105 µs	2.59E-03	7.51E-05
558C	106	11V	analog	6.474 µs	0.146 µs	1.07E-03	4.31E-05
418C	204	5.5 SD	digital	2.487 µs	0.142 µs	1.11E-05	1.06E-04
558C	106	5.5 SD	digital	4.910 µs	0.130 µs	3.88E-05	8.80E-05
418C	204	3.25 SD	digital	0.902 µs	0.146 µs	1.84E-05	1.08E-04
558C	106	3.25 SD	digital	2.050 µs	0.144 µs	-1.11E-04	1.00E-04

It turns out that the arrival time PDFs actually enable some very powerful calculations to be made. Previously, there was no established way to determine the

doublecount fraction other than the very tedious, subjective, and sometimes unreliable exercise of manual inspection of waveforms. And for deadtime, arrival time analysis is a much easier experiment to set up rather than installing and aligning neutron collimators for a series of attenuator superposition measurements. The procedures described are powerful tools for detector characterization.

Arrival time PDFs also allow a designer to view where in time the adaptive cooloff profile might be too lenient allowing double counts, or too strict with very low sensitivity. This could inform optimizations for the adaptive cooloff profile's shape and length.

6.8.11. Double counting at high count rates

In *Figure 102*, it was shown that when more than two events stack up in close succession, with less than 5μs separating each event, the adaptive cooloff predictions become less accurate, and this could result in a higher doublecount fraction. At lower count rates, the stack-up of three or more events within a 10μs window is negligibly small, but at the maximum operating count rate of 10 kHz with an average arrival period of 100μs, the probability of a second arrival within 5μs is 0.05, and a probability of third arrival within 10μs is 0.0025, or 0.25%. This is still a relatively small percentage, but higher than the 10E-4 and 10E-5 doublecount fractions that were calculated for low count rates.

Anecdotally, I did see a higher doublecount fraction at high count rates. At 3.25 standard deviations and a count rate of 10.8kHz, I observed three doublecounts in set of

~3000 events which would be a doublecount fraction of 10E-3 or 0.1%. I saw no doublcounts at 5.5 standard deviations at 10.8kHz with a similar number of events.

Statistically measuring the doublecount fraction at high count rates requires more attention than the problem deserves. You would have to parse a subset of data with pulses which arrived within 5μs of a preceding pulse, and then examine the doublecount fraction of that subset to see how its doublecount fraction is different from the larger set's. With initial estimates of a 0.1% doublecount percentage at 10.8 kHz, the growth of the doublecount fraction is still much lower than the growth of the deadtime fraction at the operating speeds of the CANDOR instrument (below 10 kHz). If a neutron scattering experiment needs to be precise enough to apply deadtime corrections to collected data, the uncertainty of the deadtime fraction (being as much as 2x different for dimmer and brighter detectors) eclipses the doublecount fraction as a source of imprecision.

6.9. Mixed Field Analysis

There is a less frequently discussed fear that a detection system's performance could degrade in a mixed radiation field, i.e. in a mixture of gammas and neutrons. The worrisome concept is that a gamma could strike the detector during the adaptive cooloff profile and be misidentified as a second neutron. The concept is illustrated in *Figure 110*.

To evaluate if the gamma rejection falters in a mixed field environment, a simple experiment is done to compare count rates with and without a gamma source. An experiment diagram is shown in *Figure 111*. A neutron guard is fashioned from a thin plate of borated aluminum, and attached to the CANDOR detector just outside of the

neutron beam. The guard's purpose is to absorb stray neutrons which might scatter off the gamma source and effect the measurement. With the guard in place, a ^{60}Co source is added for one measurement. The source is removed for the second measurement, keeping the guard in place so that the scattering environment is identical in both cases.

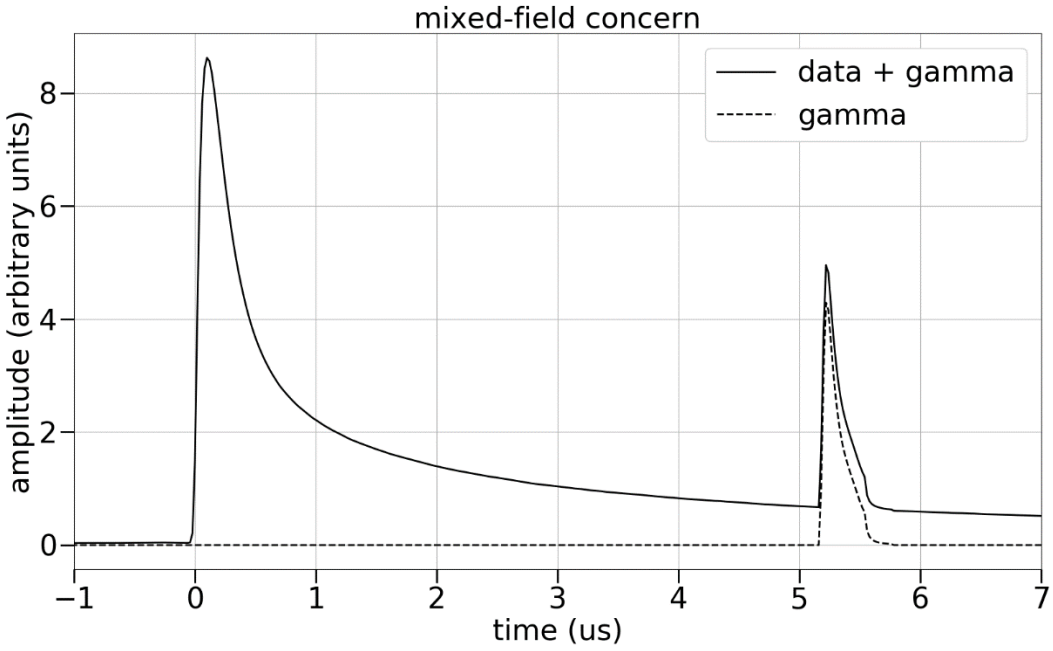

Figure 110: mixed field concern

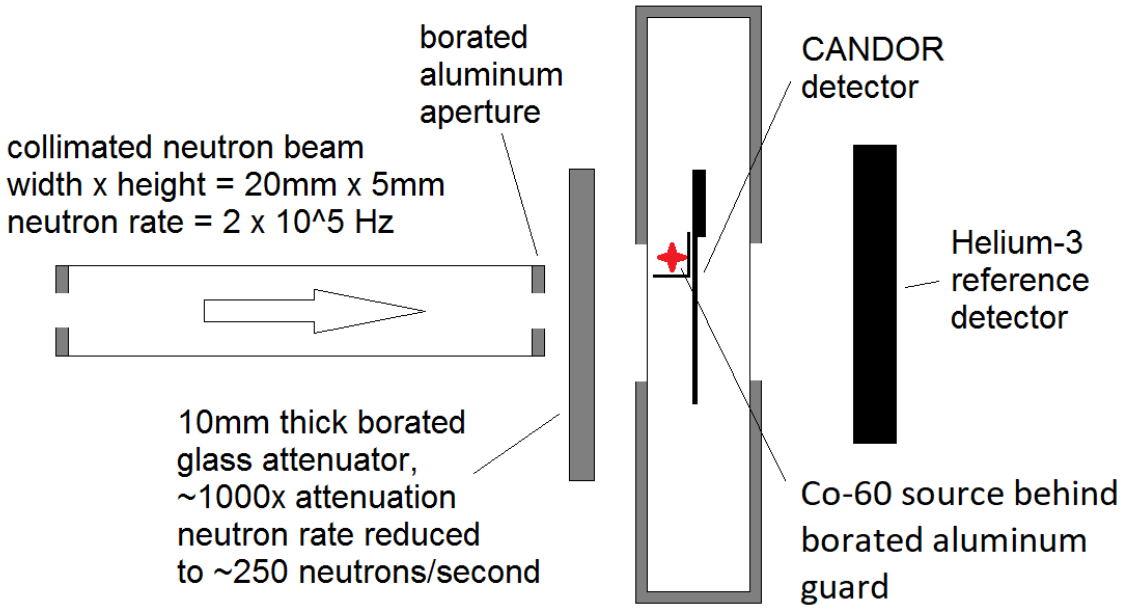

Figure 111: mixed-field experiment diagram

If there is sensitivity to gamma photons during the adaptive cooloff period, the gamma counts will manifest themselves as double counts. Any increase to the doublecount fraction is presumed to be caused by the ^{60}Co gamma source. The gamma rejection ratio during the adaptive cooloff period is calculated in **Equation 32**.

Equation 32:

$$gamma\ rejection_{Adaptive\ Cooloff} = \frac{(d_\gamma - d_0) \times total\ counts}{\gamma_{AC}}$$

Where d_γ is the doublecount fraction with a gamma source, and d_0 is the doublecount fraction with no gamma source, and γ_{AC} is the total number of gammas arriving during the adaptive cooloff period. γ_{AC} is calculated as:

Equation 33:

$$\gamma_{AC} = \gamma_{total} \times R \times T_{AC}$$

Where γ_{total} is the total number of gamma photons, R is the measured count rate, and T_{AC} is the adaptive cooloff period.

Table 11: Calculations for gamma rejection during adaptive cooloff, Equation 32

Variable	d_γ	d_0	total counts	γ_{total}	R (Hz)	T_{AC} (s)	γ_{AC}	gamma rejection adaptive cooloff
Value	-8.03E-06	-5.54E-06	1.94E+07	2.99E+09	2.15E+02	6.14E-05	3.95E+07	**-1.23E-06**
Uncertainty	3.65E-05	3.44E-05	4.41E+03	5.47E+04	4.88E-02	0.00E+00	8.99E+03	**2.47E-05**

Table 12: Calculation for total gammas (*Equation 6*)

time (s)	activity (Bq)	Photon Yield	geometry factor	γ_{total}
9.04E+04	8.27E+04	2.00E+00	2.00E-01	2.99E+09

Table 11 and *Table 12* show the experiment results. The uncertainty in the gamma rejection ratio during adaptive cooloff is 2.57E-5, more than 10 times the calculated value of -1.23E-6. The mixed field measurement is a very difficult measurement to make, because of the very large number of counts required to get adequate counting statistics. Even so the uncertainty is so low as to be unnoticeable in measurements, and the mixed field concern is not an actual problem.

Chapter 7: Performance metrics for a large numbers of detectors

Gamma rejection, deadtime, and mixed-field measurements are very time consuming and costly to perform, so most detectors do not get the full battery of tests that were described previously. However, three key performance metrics are measured for each detector: neutron transmission, photopeak, and detection efficiency relative to a helium-3 reference detector.

7.1. Detector Testing Procedure

The experiment diagram was shown previously in *Figure 51*, and a photograph of a detector magazine is shown in *Figure 112*. This magazine carries 6-triple frames with a total of 18 detector elements. The preamplifier PCB rests above the detectors. The magazine is loaded into a motorized carriage and the lid which connects the preamplifier PCB with the detectors also forms a light tight seal with the carriage box below. The carriage is automated to move laterally, and the detectors are tested one-by-one. A photograph with the collimator, borated glass attenuators, motorized carriage, and some cabling is shown in *Figure 112*. The test station is located at the PHADES experiment suite at the NCNR, and the monochromatic neutron wavelength and energy at PHADES are 4.75Å and 3.63meV.

The test procedure proceeds as follows. First, the detector carriage is moved completely out of the collimated neutron beam. The beam fully illuminates the helium-3 reference detector behind the carriage. A 600-second count is performed and the number

of neutron counts is recorded. Next, the detector carriage moves the first CANDOR detector into the beam (detector position #2 in *Figure 112*). A 600-second count is performed. Event words are recorded for every event during the 600-second exposure INCLUDING the detector addresses, timestamps, and the two charge comparison integrals. The number of counts observed by the helium-3 reference detector (behind the CANDOR detector) is also recorded. The carriage moves through all 18 detectors in the same way collecting 600 seconds worth of data for each detector. After the primary scan is finished, the carriage scans back across the beam much more quickly, only about 8-seconds for each detector. During the quick scan, events words containing full trace data are collected with most of the trace recorded BEFORE the rising edge trigger for purposes of calculating the single pixel discharge i.e. electrical gain.

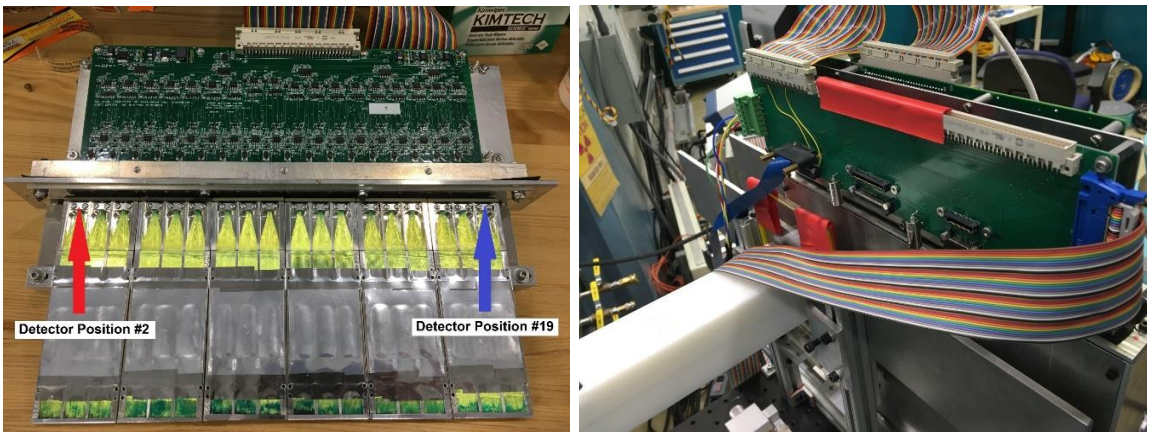

Figure 112: (left) A magazine is loaded with 6-triple frames, or 18 individual detector elements. (right) photograph of the test station.

The following items are calculated from the data collected in the scans:

1. The trace data is used to calculate the single pixel discharge for each detector. This calculation was described earlier. It is worth mentioning that the electrical gain varies between channels by as much as ±10% as seen by the histogram of single pixel discharges in *Figure 113*. Fortunately, electrical gain can be accounted for by setting individual classification thresholds for each detector in the CANDOR_DAQ.

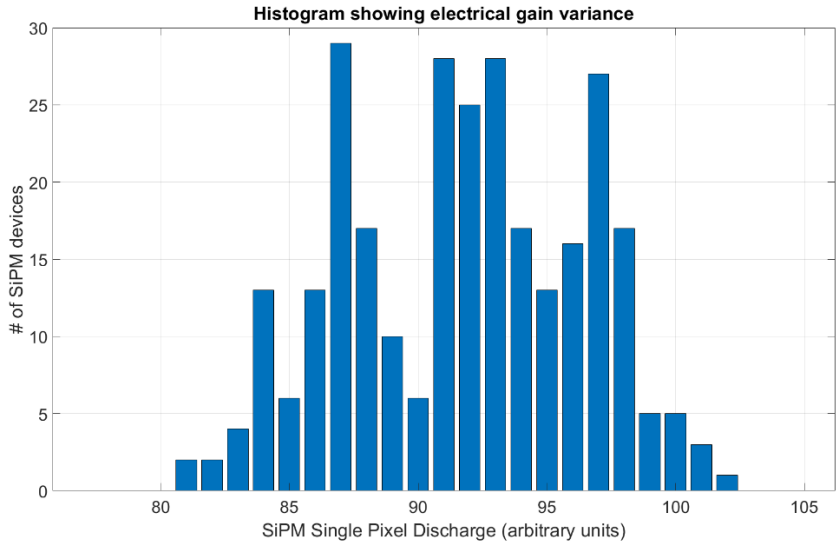

Figure 113: SiPM single pixel discharge varies demonstrating a variance in electrical gain from detector to detector.

2. The photopeak of each detector is calculated using the single pixel discharge and the charge comparison integrals. The pulse energies are histogrammed in units of SiPM pixel discharges, a spline fit is applied, and the location of the spline fit maximum is the photopeak (*Figure 114*).

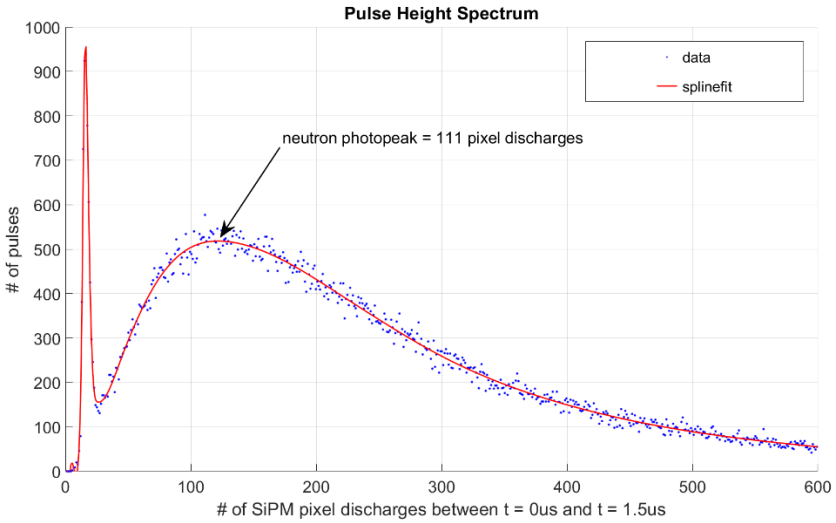

Figure 114: Illustration of photopeak calculation from charge comparison integrals normalized by the single pixel discharge. Figure 115 is repeated from Figure 116.

3. The relative efficiency is calculated from the number of events counted by each detector compared with the number of counts counted by the helium-3 tube at the beginning of the scan (***Equation 34***). The helium-3 reference tube was characterized previously to have an absolute neutron detection efficiency of 93%. The absolute efficiency of each CANDOR detector can be estimated from this. Background corrections are included in these calculations.

Equation 34:

$$Relative\ Efficiency\ = \frac{CANDOR\ counts\ -\ CANDOR\ background}{^{3}He\ counts\ unblocked\ -\ \ ^{3}He\ background}$$

$$Absolute\ Efficiency\ = \frac{Relative\ Efficiency}{0.93}$$

4. The neutron transmission of each detector is calculated by comparing the number of events counted by the helium-3 tube while being blocked by the CANDOR detector to the number of events counted by the helium-3 tube at the beginning of the scan (***Equation 35***). Background corrections are included in these calculations.

Equation 35:

$$Transmission = \frac{^3He\ counts\ blocked - \ ^3He\ background}{^3He\ counts\ unblocked - \ ^3He\ background}$$

7.2. Results

The results for a large number of detectors are analyzed in two scatter plots. Unsurprisingly, *Figure 117* shows that absolute sensitivity increases as a function of the photopeak for the range of detectors tested. There is also a pronounced "shoulder" at a photopeak of 70 SiPM pixel discharges. Below this shoulder, the sensitivity rapidly degrades. This is because a rapidly growing fraction of neutron events yield signals below the detection threshold. The CANDOR instrument will only employ detectors with a photopeak of 100 SiPM pixel discharges or higher, as this will ensure stable and satisfactory performance for a substantial period of service. The estimated time of service for a detector will be discussed in *Chapter 8*.

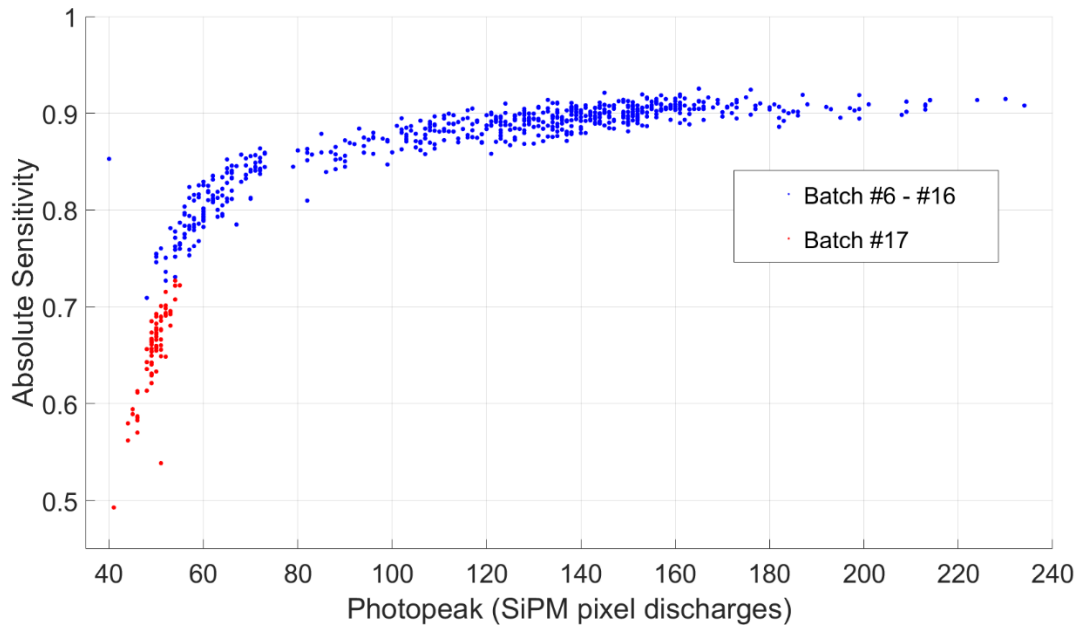

Figure 117: Absolute Sensitivity of the digital PSD system as a function of Photopeak

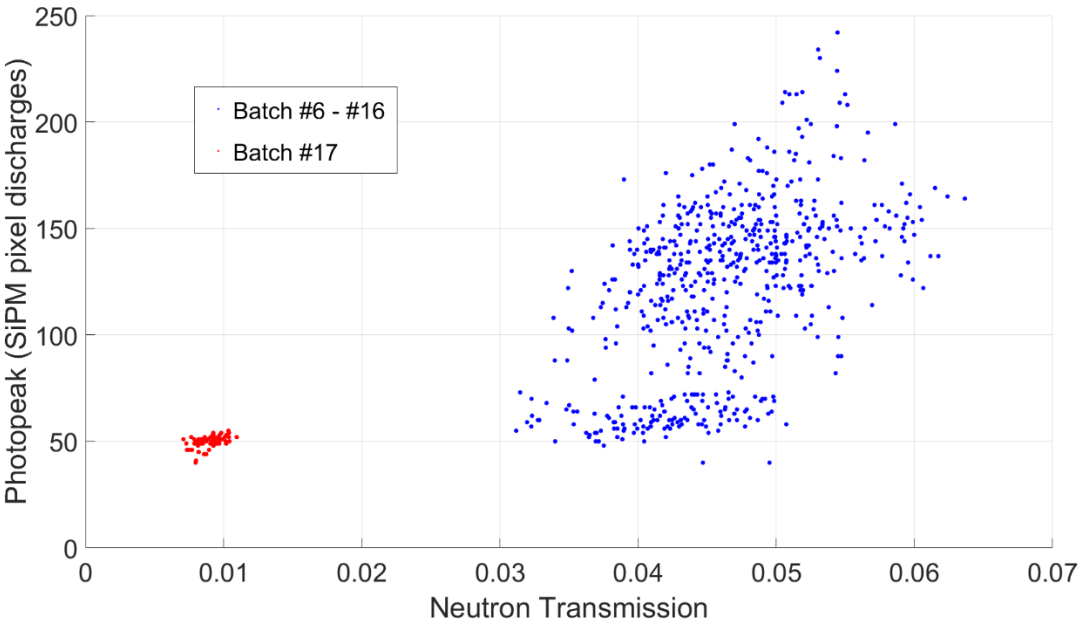

Figure 118: Neutron Transmission and Photopeak

From *Figure 117*, it is also apparent that there are two distributions of detectors: a distribution with SiPM photopeak greater than 80, and a group with photopeak below 80 (blue dots identify batch #6 thru #16, Batch #17 in red is a separate case to discuss). These two distributions are also seen in *Figure 118*.

Table 13 shows the performance metrics for 12 different batches of manufactured detectors. For the most part, detector batches are manufactured to satisfaction, or better. However, batches # 9, #13, and #17 failed to meet the minimum performance criteria entirely. When an entire batch fails, this is not due to craftmanship errors of individual detector frames. Rather, this is the result of the ^{6}LiF:ZnS(Ag) scintillator mixture being fouled in some way as to yield poor photon production, photon transport, or both. For batches #9 and #13, the cause was never discovered. The manufacturer believes that there could have been untracked procedure variations and delays during the manufacturing process. Even the relative humidity of the manufacturing environment is suspected as a contributing factor. Given enough attention to process details, I believe that these manufacturing variations can be eliminated, and these detectors could be made to pass our performance metrics every time. Scintillator variants are not categorically bad. Batch #16 was exceptionally good. Unfortunately as with batches #9 and #13, we do not know the reason why the scintillator was so bright in Batch #16.

In the case of Batch #17, there is a clear mix-up in the scintillator mixture which is not subtle. This batch was highlighted in red in *Figure 117* and *Figure 118*. Batch #7 clearly contains much more ^{6}Li absorber. The stoichiometry of this batch was accidentally altered, perhaps by swapping the ZnS(Ag) and ^{6}LiF mixing weights. This would explain both the very low neutron transmission and the low photopeaks.

Table 13: Manufactured detector batches and their performance metrics

Batch #**	Detectors tested*	Absolute Sensitivity	Std. Dev.	photoPeak	Std. Dev.	Neutron Transmission	Std. Dev.
6	30	0.878	0.010	124.9	13.5	0.0477	0.0027
7	30	0.878	0.029	106.5	18.0	0.0463	0.0030
8	27	0.898	0.009	132.0	16.6	0.0439	0.0036
9*	6*	0.807	0.027	62.7	7.7	0.0450	0.0044
10	12	0.883	0.039	120.3	31.0	0.0483	0.0057
11	75	0.893	0.017	137.8	21.0	0.0554	0.0041
12	150	0.896	0.019	134.7	22.5	0.0424	0.0034
13*	126*	0.814	0.049	62.7	8.7	0.0420	0.0046
14	75	0.893	0.050	126.7	21.9	0.0449	0.0037
15	75	0.889	0.012	135.6	15.7	0.0484	0.0032
16	75	0.900	0.013	175.6	28.4	0.0506	0.0031
17	75	0.647	0.088	49.5	2.8	0.0089	0.0009

*Batches #9, #13 contained 150 and 300 detector elements. All detectors from these batches failed with similar metrics as those presented but were not all tested to save time.

**Batch #1-5 were not included. These detectors are a previous design with WLS fiber loops

Not every detector from a "good" batch passes the performance metrics. In these cases, it was not an issue with the scintillator brightness. Instead, there were craftsmanship errors during the build such as polishing errors. Polishing errors are the most frequent cause of underperforming individual elements from a batch of detectors (*Figure 119*), but there are others malformities such as misalignment of the scintillator with the aluminum frame window, gaps between the frame and end-reflector termination, and reflector delamination.

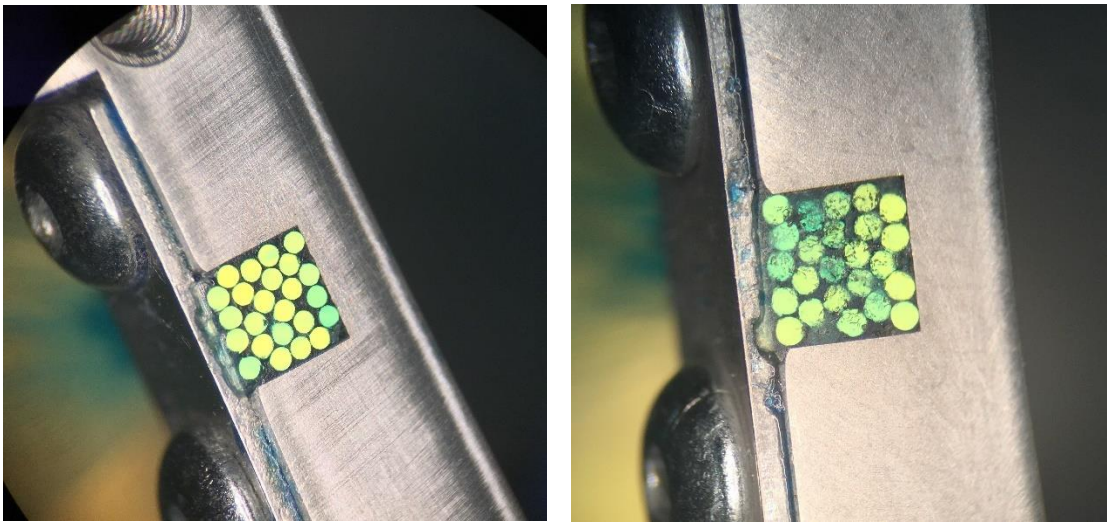

Figure 119: (left) a well polished interface. (right) a poorly polished interface.

Figure 120: (left) abnormal warping likely caused by scintillator/frame misalignment. (right) gap in end reflector termination.

In *Figure 120* (left), poor performance was associated with a detector with an irregular warping of the Vikuiti reflector. This is telling of a misalignment between the scintillator and the scintillator window. In *Figure 120* (right), the Alanod end reflector is poorly formed to the flat surface of the detector end, and so its ability to reflect light back

toward the SiPM is reduced. The manufacturer has since designed a break to repeatably bend the Alanod reflector for a proper fit of the detector end.

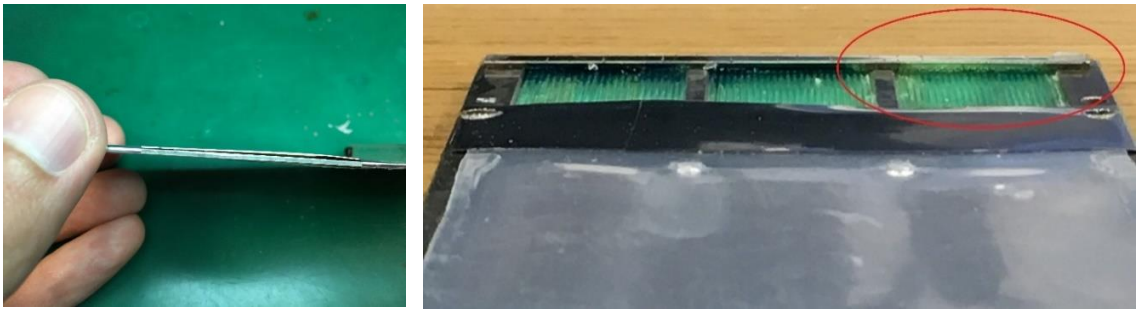

Figure 121: (left) Vikuiti reflector delamination. (right) Missing epoxy is likely the cause for poor polishing and termination.

In *Figure 121* (left), the Alanod reflector has delaminated from the scintillator, reducing its performance. This was caused by improper warping of the Alanod sheet prior to manufacture. Proper storage of the reflective material now ensures the flatness of the reflectors. *Figure 121* (right) highlights the absence of blue-dyed optical epoxy which in turn means that the WLS fibers were not properly secured during polishing.

There are a large number of details involved in the manufacture of CANDOR detectors. Any one oversight can degrade optical performance. There are many opportunities for errors. In the future, detectors of this type should be designed with simpler manufacturing processes in mind.

Chapter 8: Detector Life Cycle

8.1. Performance degradation from high-dose neutron exposure

Over time and neutron exposure, the scintillator material begins to degrade. The photon yield per event drops lower and lower, and fewer events can be reliably identified from the noise background. *Figure 122* shows how the pulse energy spectrum shifts lower after a 1.4E+12 neutron/cm^2 radiation exposure.

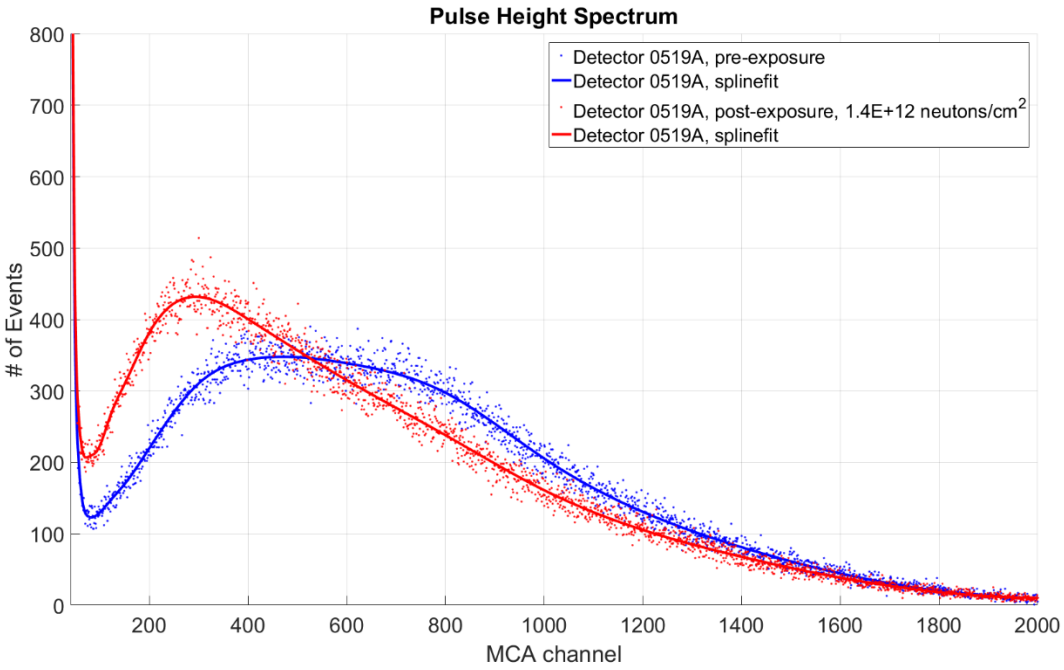

Figure 122: pre and post exposure energy histograms show losses to the average light yield and photopeak. The x-axis is in arbitrary units and not normalized to SiPM pixel discharges.

Keeping in mind that the minimum acceptable detector for use in the CANDOR instrument has a photopeak 100 SiPM pixel discharges and that the performance of a

detector rapidly degrades below a photopeak 70 SiPM pixel discharges (*Figure 117*), a CANDOR detector's photopeak can shift lower by at least 30% and maintain relatively stable performance.

A series of radiation exposures show how the optical performance of the CANDOR detector degrades as a function of radiation exposure. Before significant neutron exposure, a series of nine detector frames were characterized using the performance metrics procedure described in *Chapter 7*. Then, the detectors were exposed to progressively higher doses of neutron radiation. Each detector received a different radiation dose in the progression rather than exposing and re-measuring all of the detectors multiple times. A tenth detector was used as a control and was not exposed to high doses of neutrons. The neutron exposures were done at the NG-6 cold neutron imaging station at the NCNR which can provide some of the highest neutron fluxes in the facility at approximately 2E+9 neutrons per cm^2 per second. The progression of exposures is tabulated in *Table 14*.

After neutron exposure, the detectors were re-tested to see what affect the exposures had on performance. To gauge deterioration, the ratio of the post-exposure photopeak to pre-exposure photopeak was calculated. *Figure 123* shows the progression of photopeak loss as a function of neutron exposure.

Observe that at a total exposure of 10E+12 n/cm^2, the photopeak has degraded by 30% which is the cutoff for guaranteeing stable performance of the CANDOR detector. *Figure 124* shows the photopeak and absolute efficiency before and after neutron exposures. The trends are similar to those in *Figure 117*.

Table 14: Neutron exposures for nine detectors

Detector	Total Neutrons (n/cm^2)	Exposure Time at NG-6 (seconds) (beam flux = $2E+9/cm^2/s$)	Simulated Lifetime Usage (months) (beam flux = $1E+4/cm^2/s$)
DET_0312	3.9E+11	195	15.0462963
DET_0331	9.8E+11	490	37.80864198
DET_0334	3.96E+12	1980	152.7777778
DET_0340	2E+11	100	7.716049383
DET_0342	3.8E+11	190	14.66049383
DET_0343	7.4E+11	370	28.54938272
DET_0347	1.46E+12	730	56.32716049
DET_0348	2.9E+12	1450	111.882716
DET_0529	5.76E+12	2880	222.2222222

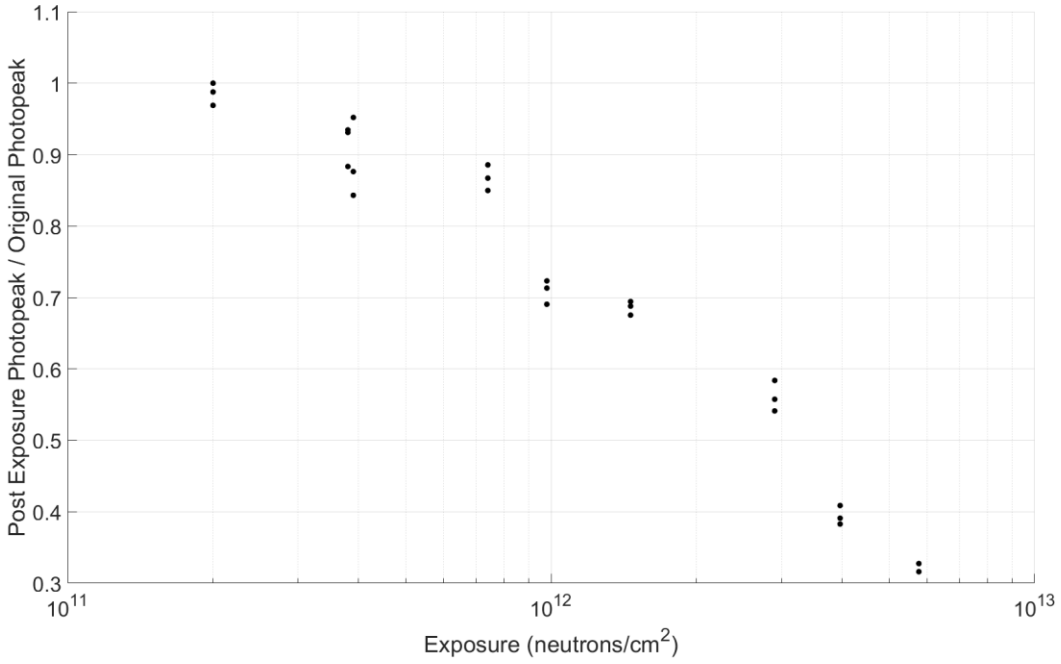

Figure 123: ratio of pre and post exposure photopeaks gauge the degradation of performance, exposure on a log scale

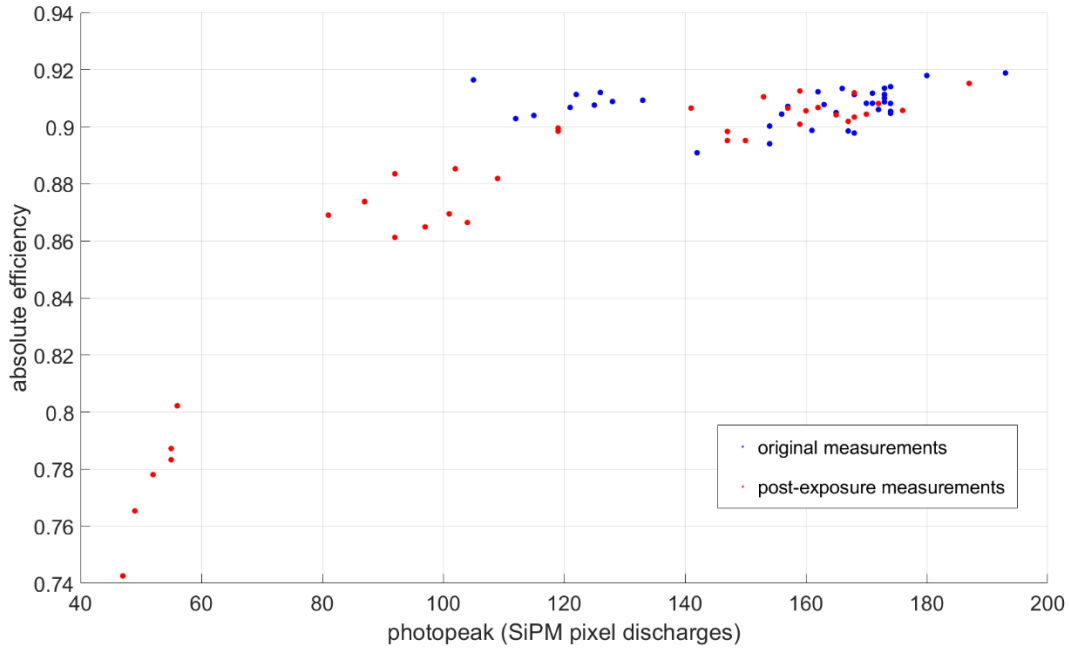

Figure 124: photopeak and absolute efficiency for detectors before and after neutron exposure.

Table 15 charts all of the performance data for each detector element before and after neutron exposure. Notice that the neutron transmission was not affected at all. This is telling that the ^{6}Li neutron absorber isotope is not depleted in any meaningful way. This is to be expected when considering that 10E+12 neutron absorptions is a tiny fraction of the number of ^{6}Li atoms contained in a detector which exceeds 10E+20 (Avogadro's # = 6.022 x 10E+23).

From the lifetime study experiment, it is seen that a total exposure of 10E+12 n/cm^2 is approximately the maximum allowable neutron exposure for guaranteeing reasonably stable performance (a 30% drop in photopeak from 100 to 70). How long will It take a CANDOR detector in normal instrument use to reach the 10E+12 n/cm^2 exposure limit?

Table 15: Chart of performance metrics before and after neutron exposure

Detector SN	Exposure Time (seconds)	neutron Transmission	neutron Transmission (post exposure)	photopeak	photopeak (post exposure)	absolute Sensitivity	absolute Sensitivity (post exposure)
0312A	195	0.0544	0.0541	125	119	0.9076	0.8995
0312B	195	0.0534	0.0530	121	102	0.9068	0.8853
0312C	195	0.0482	0.0500	105	92	0.9164	0.8835
0331A	490	0.0486	0.0473	122	87	0.9113	0.8737
0331B	490	0.0513	0.0503	126	87	0.9120	0.8738
0331C	490	0.0499	0.0501	112	81	0.9029	0.8690
0334A	1980	0.0545	0.0529	133	52	0.9093	0.7781
0334B	1980	0.0526	0.0523	128	49	0.9089	0.7654
0334C	1980	0.0537	0.0517	115	47	0.9039	0.7426
0340A	100	0.0553	0.0552	193	187	0.9189	0.9152
0340B	100	0.0538	0.0527	172	172	0.9060	0.9082
0340C	100	0.0521	0.0520	162	160	0.9123	0.9056
0342A	190	0.0528	0.0533	174	162	0.9140	0.9067
0342B	190	0.0496	0.0517	180	159	0.9180	0.9126
0342C	190	0.0517	0.0505	168	157	0.9113	0.9065
0343A	370	0.0530	0.0512	166	147	0.9134	0.8952
0343B	370	0.0535	0.0530	173	150	0.9135	0.8952
0343C	370	0.0546	0.0532	173	147	0.9113	0.8984
0347A	0	0.0521	0.0522	163	168	0.9078	0.9119
0347B	0	0.0512	0.0523	171	170	0.9082	0.9044
0347C	0	0.0540	0.0537	168	176	0.8978	0.9057
0348A	1450	0.0539	0.0546	174	97	0.9047	0.8649
0348B	1450	0.0524	0.0520	170	92	0.9082	0.8612
0348C	1450	0.0528	0.0534	173	101	0.9087	0.8695
0529A	2880	0.0480	0.0473	174	55	0.9054	0.7833
0529B	2880	0.0457	0.0472	174	55	0.9082	0.7872
0529C	2880	0.0442	0.0433	171	56	0.9118	0.8022
0536A	0	0.0493	0.0492	154	159	0.9003	0.9009
0536B	0	0.0479	0.0477	165	165	0.9050	0.9042
0536C	0	0.0504	0.0503	167	168	0.8985	0.9034
0538A	0	0.0403	0.0415	142	141	0.8909	0.9065
0538B	0	0.0413	0.0419	156	153	0.9044	0.9105
0538C	0	0.0465	0.0474	161	167	0.8987	0.9019
0548A	730	0.0463	0.0453	157	109	0.9071	0.8819
0548B	730	0.0439	0.0439	173	119	0.9101	0.8984
0548C	730	0.0429	0.0448	154	104	0.8940	0.8664

The active area of a CANDOR detector is 3 cm^2, and the counts per second is limited to 10 kHz. The detector lifetime is calculated in *Equation 36*.

Equation 36:

$$Lifetime\ at\ 10kHz\ continuous\ use = \frac{10^{12}\ \mathrm{n}/cm^2}{10^4\ \mathrm{n}/s} \times 3\ cm^2 \ = 3 \times 10^8\ \mathrm{s} \ = \ 9.51\ years$$

A lifetime of 9.51 years is estimated for the poorest allowable detector (photopeak = 100) at the highest allowable neutron flux. In practice, the average neutron flux on a detector is much lower than the 10kHz maximum rate. CANDOR detectors can be expected to remain in service for 20 – 30 years or longer. When considering that only the best detectors were selected for the CANDOR prototype instrument (all detectors have photopeaks > 120 pixel discharges), the service life of these detectors is expected to be even longer.

8.2. Activation Study

What about after the CANDOR detectors have exceeded their useful lifetime, and they are ready to be replaced? What are the radiological hazards associated with handling and disposing detectors which have been made radioactive via many years of neutron exposure? To assess these hazards, CANDOR detector #343 was irradiated in a high flux neutron beam at NG6 (2E+9 neutron/cm^2/s) for 370 seconds. The circular neutron beam has a diameter of 2". The active area of the CANDOR detector was centered in the beam, with the rest of the detector being exposed to air-scattered neutrons. This configuration is somewhat similar to operating conditions in the CANDOR analyzer, where the active

area is exposed to neutrons, but the rest of the detector is expected to have minimal neutron exposure from sporadic neutron scattering inside the analyzer.

Detector #343 rested for 20 hours after neutron exposure before performing gamma spectroscopy analysis. Detector #343 was monitored in a gamma spectroscopy chamber to estimate its radioactivity and to identify any radioisotopes that are present. The analysis of the results (*Table 16*) indicate the following isotopes and activities. *(*Note this list does NOT include activation products that do not emit gammas, e.g. H-3)*

Table 16: Detected radioisotpoes in the CANDOR detector #343, post-exposure

Isotope	Activity (μCi)	Half-life (hours)
Zn-65	2.93E-04	5856.24
Zn-69m	1.46E-03	13.76
Mn-56	5.02E-04	2.58
Cu-64	4.56E-03	12.7
Ga-72	1.87E-04	14.1
Na-24	1.54E-05	14.96

The total exposure of the Detector #343 was 7.2E+11 neutron/cm^2. All of the radioisotopes above have a relatively short half-life (< 24 hours) with the exception of Zn-65 (half-life ~2 years). The activity of Zn-65 was approximately 0.29nCi. This level is acceptably low for handling by radiation workers. Even at 5 years of continuous exposure at 10000 neutrons/second, the gamma radioactivity per triple frame will be below 3nCi.

All of the screws used in detector #343 were made of stainless steel, and it appears that they are not being activated noticeably. Tritium build up from ^{6}Li fission products is not measurable using gamma spectroscopy, but tritium creation is

unavoidable. Special analysis of tritium (^{3}H) build-up must be done as a minimum of 3E+12 tritium atoms will be generated during by each detector during its service life.

As a worst case scenario, if a detector were to accumulate all of its 3E+12 tritium atoms instantaneously, approximately 0.15uCi (5.3E+3 Bq) of radioactivity would be produced by the tritium, with a half-life of 12.3 years. If all 108 detectors in the CANDOR instrument prototype achieved this maximum tritium radioactivity simultaneously, this would total 16uCi or 5.7E+5Bq. Due to its low energy beta decay, tritium is only harmful if ingested, where it can interact with internal tissues of the human body [175].

Annual limit on intake (ALI) is defined in Title 10, Section 20.1003, of the *Code of Federal Regulations* (10 CFR 20.1003). ALI is defined as the derived limit for the amount of radioactive material taken into the body of an adult worker by inhalation or ingestion in a year. ALI is the smaller value of intake of a given radionuclide in a year by the reference man that would result in a committed effective dose equivalent of 5 rems (0.05 Sv) or a committed dose equivalent of 50 rems (0.5 Sv) to any individual organ or tissue [176].

The ALI of hydrogen-3, or tritium, is set at 8E+4 uCi by the NRC [175], [177]. This is 5000 times the maximum anticipated tritium radioactivity for all 108 CANDOR detectors combined. And, most of the tritium radioactivity will remain encapsulated within the LiF:ZnS(Ag) scintillator substrate and will never be ingested by radiation workers. Tritium radioactivity should not be a health risk to workers handling CANDOR detectors.

Chapter 9: Concluding Remarks

9.1. Neutron scattering requirements are met

The CANDOR detector neutron detector largely fulfils the detector requirements for neutron scattering. Table 17 approximates and consolidates the data found *Figure 85* and *Figure 117* for a threshold setting of 37 photons, which is the threshold used for the digital PSD algorithm.

Table 17: Approximate performance at Threshold = 37 pixel discharges

	Low performing, photopeak = 100	High performing, photopeak = 200
Co-60 rejection	4.00E-07	1.00E-06
Cs-137 rejection	5.00E-08	1.00E-07
Neutron ID Rate	93%	98%
Absolute Efficiency	87%	91%

At a detection threshold of 37 photons, two adaptive cooloff thresholds were tested: 5.5 standard deviations and 3.25 standard deviations from the mean. *Table 18* shows that the deadtime for a poor performing detector is about twice that for an excellent detector, regardless of the adaptive cooloff threshold.

Table 18: Deadtime and doublecount fractions at Threshold = 37 pixel discharges

Detector	photopeak	Adaptive cooloff theshold	PSD	deadtime	deadtime uncertainty	doublecount fraction	doublecount uncertainty
418C	204	5.5 SD	digital	2.487 µs	0.142 µs	1.11E-05	1.06E-04
558C	106	5.5 SD	digital	4.910 µs	0.130 µs	3.88E-05	8.80E-05
418C	204	3.25 SD	digital	0.902 µs	0.146 µs	1.84E-05	1.08E-04
558C	106	3.25 SD	digital	2.050 µs	0.144 µs	-1.11E-04	1.00E-04

The deadtime of an excellent detector at a low adaptive cooloff is perhaps unbelievable short (~900ns); shorter than the total integration time of 1.28μs. Perhaps the measurement uncertainties are clouding the measurements, and perhaps the assumptions of constant doublecount fraction and constant deadtime begins to breakdown as lower and lower adaptive cooloff thresholds are sought. However, the arrival time histograms at 3.25 standard deviations appear normal, and it could be possible that the adaptive cooloff algorithm really is that fast.

Regardless, if a conservative adaptive cooloff threshold is used, the detectors in the CANDOR prototype instrument should have deadtimes of approximately 3μs. This is slightly longer than would be desired. At 10 kHz count rate, a 3μs deadtime results in a deadtime percentage of 3%. Ideally, the deadtime would be 1μs or less and the deadtime percentage at 10 kHz would be 1% or less.

The CANDOR detector also meets the requirement of being ultra-thin at less than 2mm thick. And, it uses ^{6}Li as a neutron absorber rather than ^{3}He.

The service lifetime of the CANDOR detector as used in the CANDOR instrument is expected to be a minimum of 10 years in the most strenuous use case and probably more than 20-30 years with normal use.

9.2. techniques well-suited used to gauge performance

Some of the measurement techniques that were used in this research were relatively simple and repeatable procedures, and the measurements yield very detailed results at the same time.

ROC curves were used extensively in Chapter 6, and they are the perfect gauge for binary classification of neutrons in a cold neutron detector. With two detector exposures: neutron and gamma, a ROC curve is computed which details the expected performance over the entire range of useful threshold settings. The procedure is easy enough that multiple detector configurations can be compared. This was done to optimize SiPM bias voltage.

The arrival time statistics are also very easy to obtain, given you have access to a timestamper (as we do with the CANDOR_DAQ) and a reactor neutron source. And again, the detail that you can see across the adaptive cooloff profile can inform whether double counts are present, or where an adaptive cooloff profile needs to be re-shaped, raised, or lowered. The multi-rate method for calculating doublecount fraction and deadtime is also a powerful tool that I have not seen used before. These measurement techniques could help many other researchers better characterize and optimize their devices.

9.3. Noise Rejection & Pile-up Filters

The noise rejection filter and pile-up filter described in Chapter 6.7. are signal processing innovations developed specifically to address the challenges of SiPM thermal noise. SiPMs are a relatively new low-light photodetector with wide ranging applications. They are very attractive in comparison to photomultiplier tubes as they are much smaller,

lower cost, and immune to magnetic fields. They are quickly replacing or superseding photomultiplier tubes in many applications.

However, the signal non-linearities described in Chapter 3.4. are a major detractor from SiPMs. The noise rejection filter is able to quickly reject SiPM thermal noise, minimizing the deadtime required to examine these frequent pulses.

After evaluating the performance improvements offered by the pile-up filter, the neutron detection efficiency improves by only ~1% in our test case. However, this improvement would be much great in situations where the SiPM is operated at higher temperatures (even more frequent thermal noise pulses) and in higher gamma fields. Both of these situations greatly increase the frequency of pile-up events.

The noise and pile-up filter are effective approaches for mitigating SiPM thermal noise using minimal computing resources. It could be that the low signal-to-noise ratio of the CANDOR detector, and the novelty of SiPM devices are both reasons why these types of filters have not been widely researched.

9.4. Future Work

^{6}LiF:ZnS(Ag) scintillator has the potential to be used elsewhere at the NCNR depending on the application. The CANDOR detector is a good template for how to build a 1-dimensional detector that could be lengthened beyond the current 3cm. The detector could be lengthened perhaps as long as 50 cm with similar performance, and in doing so would cover a much larger area with little added complexity.

The CANDOR detector is obviously a 1-dimensional device, but a 2-dimensional position sensitive detector (like a camera) has many more applications. I can't see a reasonable way the CANDOR detector could be reconfigured as a 2D device, but some of the components used for the CANDOR detector could be essential components in future 2D devices. SiPM's are now made into 4x4 or 8x8 grid-arrays (*Figure 125*). These arrays could be used in various ways to construct miniature Anger Cameras, or pixelated devices with optical separation between the individual SiPMs. The SiPMs could be paired with a range of scintillator materials very easily. The CANDOR_DAQ is also a flexible platform that is capable of weighted vector analysis over 32-input channels. This fits very well with SiPM tiled array architectures.

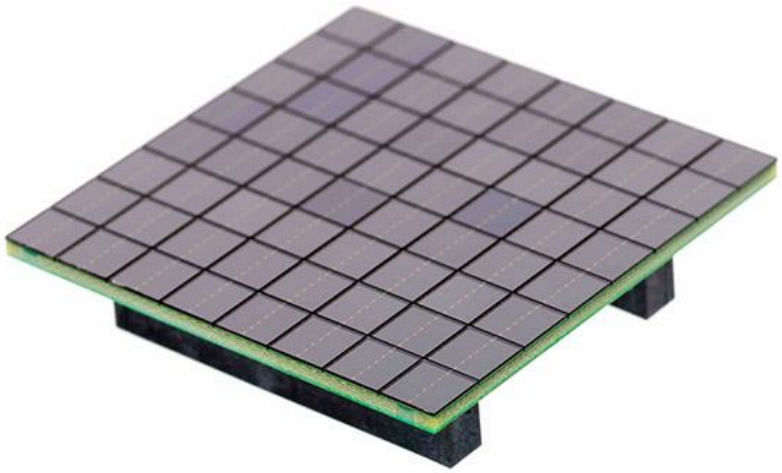

Figure 125: 8x8 SiPM tiled array

Abbreviations

CAD – Computer Aided Design

CANDOR – Chromatic Analyzing Neutron Diffractometer or Reflectometer

DSP – Digital Signal Processing

NCNR – NIST Center for Neutron Research

NIST – National Institute of Standards and Technology

PCA – Printed Circuit Assembly

PCB – Printed Circuit Board

PHADES – Polarized ^{3}He and Detector Experiment Station

PDE – Photo-Detection Efficiency

Phoswich – Phosphor sandwich

PSD – Pulse Shape Discrimination

SiPM – Silicon Photomultiplier

WLS fibers – Wavelength Shifting fibers

Bibliography

[1] "Rosalind Franklin and X-ray diffraction applied to DNA wet fibres." [Online]. Available: https://biology-forums.com/gallery/33_23_06_11_4_13_33.jpeg.

[2] F. Wietfeldt, "Measurements of the Neutron Lifetime," *Atoms*, vol. 6, no. 4, p. 70, Dec. 2018, doi: 10.3390/atoms6040070.

[3] A. Munter, "Neutron scattering lengths and cross sections." https://www.ncnr.nist.gov/resources/n-lengths/ (accessed Jan. 18, 2020).

[4] "Law 1/v," *Nuclear Power*. https://www.nuclear-power.net/nuclear-power/reactor-physics/atomic-nuclear-physics/fundamental-particles/neutron/interactions-neutrons-matter/law-1v/ (accessed Jan. 18, 2020).

[5] J. Donev and et al., "Energy Education - Neutron moderator." University of Calgary, Jul. 21, 2018, Accessed: Nov. 27, 2018. [Online]. Available: https://energyeducation.ca/encyclopedia/Neutron_moderator.

[6] "DOE FUNDAMENTALS HANDBOOK NUCLEAR PHYSICS AND REACTOR THEORY, Volume 1 of 2." Department of Energy, Jan. 1993.

[7] F. D. Brooks and H. Klein, "Neutron spectrometryFhistorical review and present status," *Nucl. Instrum. Methods Phys. Res. A*, vol. 476, p. 11, 2002.

[8] T. C. Doan, "Thermal Neutron Detector Based on Hexagonal Boron Nitride." Texas Tech University, Aug. 2016.

[9] OpenStax, "21.2 Nuclear Equations," in *Chemistry*, 2016.

[10] "Livechart - Table of Nuclides - Nuclear structure and decay data." https://nds.iaea.org/relnsd/vcharthtml/VChartHTML.html (accessed Sep. 10, 2020).

[11] Electricalvoice, "Ionization Chamber | Working," *Electricalvoice*. https://electricalvoice.com/ionization-chamber-working/ (accessed Aug. 26, 2020).

[12] G. Knoll, *Radiation Detection and Measurement*. United States: John Wiley & Sons, Inc., 1979.

[13] D. Sim, *Practical Gaseous Ionization Detection Regions*. 2015.

[14] D. Sim, *Spread of Avalanches in a Geiger-Mueller Tube*. 2012.

[15] S. A. Korff and W. E. Danforth, "Neutron Measurements with Boron-Trifluoride Counters," *Phys Rev*, vol. 55, p. 980, May 1939.

[16] T. Wilpert, "Boron trifuoride detectors," *Neutron News*, vol. 23, no. 4, pp. 14–18, Nov. 2012.

[17] B. Guerard, R. Hall-Wilton, and F. Murtas, "Prospects in MPGDs development for neutron detection," *arXiv:1410.0107*, Oct. 2014.

[18] D. H. Beddingield, N. H. Johnson, and H. O. Menlove, "3He neutron proportional counter performance in high gamma-ray dose environments," *Nucl. Instrum. Methods Phys. Res. A*, vol. 455, pp. 670–682, May 2000.

[19] S. S. Desai and A. M. Shaikh, "On studies of 3He and isobutane mixture as neutron proportional counter gas," *Nucl. Instrum. Methods Phys. Res. A*, vol. 557, pp. 607–614, Dec. 2005.

[20] D. Mazed, S. Mameri, and R. Ciolini, "Design parameters and technology optimization of 3He-filled proportional counters for thermal neutron detection and spectrometry applications," *Radiat. Meas.*, vol. 47, pp. 577–587, 2012.

[21] "Neutron detectors: Alternatives to using Helium-3."
[22] K. Zeitelhack, "Search for alternative techniques to helium-3 detectors for neutron scattering applications," *Neutron News*, vol. 23, no. 4, pp. 10–13, 2012.
[23] R. T. Kouzes, A. T. Lintereur, and E. R. Siciliano, "Progress in alternative neutron detection to address the helium-3 shortage," *Nucl. Instrum. Methods Phys. Res. A*, vol. 784, pp. 172–175, 2015, doi: http://dx.doi.org/10.1016/j.nima.2014.10.046.
[24] D. A. Shea and D. M. Morgan, "The Helium-3 Shortage: Supply, Demand, and Options for Congress," *Congr. Res. Serv.*, vol. R41419, Dec. 2010.
[25] A. P. Simpson and et al., "A REVIEW OF NEUTRON DETECTION TECHNOLOGY ALTERNATIVES TO HELIUM-3 FOR SAFEGUARDS APPLICATIONS," *INMM 52nd Annu. Meet.*, Jul. 2011.
[26] F. Piscitelli, "Novel Boron-10-based detectors for Neutron Scattering Science," *arXiv:1501.05201v1*, Jan. 2015.
[27] F. Piscitelli, G. Mauri, F. Messi, and et. al., "Characterization of the Multi-Blade 10B-based detector at the CRISP reflectometer at ISIS for neutron reflectometry at ESS," *J. Instrum.*, May 2018, [Online]. Available: https://doi.org/10.1088/1748-0221/13/05/P05009.
[28] G. Mauri, F. Messi, M. Anastasopoulos, and et. al., "Neutron reflectometry with the Multi-Blade 10B-based detector," *rspa.royalsocietypublishing.org*, vol. Proc R Soc A, Apr. 2018.
[29] T. Bigault and et al., "10B multi-grid proportional gas counters for large area thermal neutron detectors," *Neutron News*, vol. 23, no. 4, pp. 20–24, Nov. 2012.
[30] Qwerty123uiop, "Photomultiplier Tube and Scintillator." Nov. 30, 2013, Accessed: Jan. 03, 2019. [Online]. Available: http://en.wikipedia.org/wiki/Scintillation_counter.
[31] A. Visser and O. Rolinski, "Basic Photophysics." [Online]. Available: http://photobiology.info/Visser-Rolinski.html.
[32] G. Knoll, *Radiation Detection and Measurement*, 4th ed. United States: John Wiley & Sons, Inc., 2010.
[33] R. Hofstadter, "Alkali Halide Scintillation Counters," *Phys Rev*, vol. 74, no. 100, Jul. 1948, doi: https://doi.org/10.1103/PhysRev.74.100.
[34] S. Derenzo, M. Boswell, M. Weber, and K. Brennan, "Scintillation Properties." Lawrence Berkeley National Laboratory, [Online]. Available: http://scintillator.lbl.gov/.
[35] "The Analysis Pulse-Height Spectrometry." Virginia Commonwealth Universit, [Online]. Available: http://www.people.vcu.edu/~mhcrosthwait/clrs322/Pulseanalysis.htm.
[36] P. Harihar and et al., "Scintillation decays in a trans-stilbene crystal," *Nucl. Instrum. Methods Phys. Res. A*, vol. 336, p. 176, 1993, doi: https://doi.org/10.1016/0168-9002(93)91094-4.
[37] M. Balmer, G. Kellum, and G. Taylor, "Comparative analysis of pulse shape discrimination methods in a 6Li loaded plastic scintillator," *Nucl. Instrum. Methods Phys. Res. A*, vol. 788, pp. 146–153, 2015.

[38] M. Flaska and S. A. Pozzi, “Identification of shielded neutron sources with the liquid scintillator BC-501A using a digital pulse shape discrimination method,” *Nucl. Instrum. Methods Phys. Res. A*, vol. 577, pp. 654–663, 2007.
[39] M. Moszynski and et al., “Study of n-γ discrimination with NE213 and BC501A liquid scintillators of different size,” *Nucl. Instrum. Methods Phys. Res. A*, vol. 350, pp. 226–234, Oct. 1994, doi: https://doi.org/10.1016/0168-9002(94)91169-X.
[40] C. W. E. Eijk, “Inorganic Scintillator Development,” *Nucl. Instrum. Methods Phys. Res. A*, vol. 460, pp. 1–14, 2001.
[41] V. S. Litvin, A. D. Beyaev, and S. M. Ignatov, “V. S. Litvin, A. D. Beyaev and S. M. Ignatov, "ZnS(Ag)/6LiF and LiI(Eu) Scintillaotrs and Silicon Photomultipliers for Thermal Neutron Detetctors with High Space and Time Resolution,” *Bull. Russ. Acad. Sci. Phys.*, vol. 73, pp. 219–221, 2009.
[42] A. Tsunesaburo, M. Masayoshi, and O. Masayuki, “Decay Properties of ZnS(Ag) Phosphors,” *J. Phys. Soc. Jpn.*, vol. 14, no. 12, pp. 1766–1770, 1959.
[43] D. Moses, “Efficient scalable solid-state neutron detector,” *Rev. Sci. Instrum.*, vol. 86, no. 6, p. 065103, Jun. 2015, doi: 10.1063/1.4922530.
[44] K.-C. Huang, R. Dahal, J. J.-Q. Lu, A. Weltz, Y. Danon, and I. B. Bhat, “Scalable large-area solid-state neutron detector with continuous p–n junction and extremely low leakage current,” *Nucl. Instrum. Methods Phys. Res. Sect. Accel. Spectrometers Detect. Assoc. Equip.*, vol. 763, pp. 260–265, Nov. 2014, doi: 10.1016/j.nima.2014.06.047.
[45] C. Petrillo, “Solid state neutron detectors,” p. 11.
[46] A. N. Caruso, “The physics of solid-state neutron detector materials and geometries,” *J. Phys. Condens. Matter*, vol. 22, no. 44, p. 443201, Oct. 2010, doi: 10.1088/0953-8984/22/44/443201.
[47] T. C. Doan, S. Majety, S. Grenadier, J. Li, J. Y. Lin, and H. X. Jiang, “Hexagonal boron nitride thin film thermal neutron detectors with high energy resolution of the reaction products,” *Nucl. Instrum. Methods Phys. Res. Sect. Accel. Spectrometers Detect. Assoc. Equip.*, vol. 783, pp. 121–127, May 2015, doi: 10.1016/j.nima.2015.02.045.
[48] D. G. Chica *et al.*, “Direct thermal neutron detection by the 2D semiconductor 6LiInP2Se6,” *Nature*, vol. 577, no. 7790, pp. 346–349, Jan. 2020, doi: 10.1038/s41586-019-1886-8.
[49] J. L. Wiza, “MICROCHANNEL PLATE DETECTORS,” *Nucl. Instrum. Methods*, vol. 162, pp. 587–601, 1979.
[50] O. H. W. Siegmund, A. S. Tremsin, J. V. Vallerga, and J. Hull, “Cross Strip Anode Imaging Readouts for Microchannel Plate Detectors,” *Univ. Calif. Berkeley*.
[51] G.-Y. Chen and Y.-F. Wang, “Soft X-ray detectors for pulsar navigation,” *IOP Conf Ser. Earth Environ. Sci.*, vol. 69, 2017, doi: 10.1088/1755-1315/69/1/012099.
[52] T. Gys, “Micro-channel plates and vacuum detectors,” *Nucl. Instrum. Methods Phys. Res. Sect. Accel. Spectrometers Detect. Assoc. Equip.*, vol. 787, pp. 254–260, Jul. 2015, doi: 10.1016/j.nima.2014.12.044.
[53] A. S. Tremsin, J. V. Vallerga, J. B. McPhate, O. H. W. Siegmund, and R. Raffanti, “High Resolution Photon Counting With MCP-Timepix Quad Parallel Readout Operating at $> 1~{\rm KHz}$ Frame Rates,” *IEEE Trans. Nucl. Sci.*, vol. 60, no. 2, pp. 578–585, Apr. 2013, doi: 10.1109/TNS.2012.2223714.

[54] K. Watanabe, T. Minniti, W. Kockelmann, R. Dalgliesh, G. Burca, and A. S. Tremsin, “Characterization of a neutron sensitive MCP/Timepix detector for quantitative image analysis at a pulsed neutron source,” *Nucl. Instrum. Methods Phys. Res. Sect. Accel. Spectrometers Detect. Assoc. Equip.*, vol. 861, pp. 55–63, Jul. 2017, doi: 10.1016/j.nima.2017.04.034.
[55] A. S. Tremsin, “High resolution neutron counting detectors with microchannel plates and their applications in neutron radiography, diffraction, and resonance absoption imaging,” *Neutron News*, vol. 23, no. 4, 2012.
[56] A. S. Tremsin *et al.*, “Improved efficiency of high resolution thermal and cold neutron imaging,” *Nucl. Instrum. Methods Phys. Res. Sect. Accel. Spectrometers Detect. Assoc. Equip.*, vol. 628, no. 1, pp. 415–418, Feb. 2011, doi: 10.1016/j.nima.2010.07.014.
[57] J. A. Dura *et al.*, “AND/R: Advanced neutron diffractometer/reflectometer for investigation of thin films and multilayers for the life sciences,” *Rev. Sci. Instrum.*, vol. 77, no. 7, p. 074301, Jul. 2006, doi: 10.1063/1.2219744.
[58] S. Krueger *et al.*, “Investigation of Hybrid Bilayer Membranes with Neutron Reflectometry: Probing the Interactions of Melittin,” *Langmuir*, vol. 17, no. 2, pp. 511–521, Jan. 2001, doi: 10.1021/la001134t.
[59] “ORDELA MODEL 1250N, POSITION-SENSITIVE PROPORTIONAL COUNTER.” 1992.
[60] C. J. Borkowski and M. K. Kopp, “Design and properties of position-sensitive proportional counters using resistance–capacitance position encoding,” *Rev. Sci. Instrum.*, vol. 46, no. 8, pp. 951–962, Aug. 1975, doi: 10.1063/1.1134379.
[61] C. J. Borkowski and M. K. Kopp, “Recent Improvements to RC-Line Encoded Position-Sensitive Proportional Counters,” *J Appl Cryst*, vol. 11, pp. 430–434, 1978.
[62] Oak Ridge Detetctor Laboratory, “ORDELA Model 2651N Position-Sensitive Proportional Counter.” Mar. 27, 1991.
[63] K. Toh and et. al., “Performance evaluation of high-pressure MWPC with individual line readout under Cf-252 neutron irradiation,” *J. Phys. Conf. Ser.*, vol. 528, p. 012045, 2014, doi: doi:10.1088/1742-6596/528/1/012045.
[64] L. Tian, “Prototype of a large neutron detector based on MWPC,” *Sci. China - Phys. Mech. Astron.*, vol. 57, no. 11, pp. 2049–2053, Nov. 2014, doi: doi: 10.1007/s11433-014-5571-5.
[65] B. Lescop and et al., “A new system for in-core wide range neutron monitoring,” *IEEE Symp. Conf. Rec. Nucl. Sci.*, 2004, doi: 10.1109/NSSMIC.2004.1462539.
[66] C. Jammes and et al., “Assessment of the High Temperature Fission Chamber Technology for the French Fast Reactor Program,” *IEEE Trans. Nucl. Sci.*, vol. 59, no. 4, pp. 1351–1359, Aug. 2012, doi: 10.1109/TNS.2012.2205161.
[67] R. A. DuBridge, “CAMPBELL THEOREM - SYSTEM CONCEPTS AND RESULTS,” *IEEE Trans. Nucl. Sci.*, pp. 241–246, Feb. 1967.
[68] T. A. J. JAQUES, H. A. Ballinger, and F. Wade, “NEUTRON DETECTORS FOR REACTOR INSTRUMENTATION,” *Symp. Pap. Nucl. React. Instrumentat*, vol. Measurements Section, pp. 110–116, 1952.
[69] R. Kouzes and et al., “BF3 Neutron Detector Tests.” PACIFIC NORTHWEST NATIONAL LABORATORY, Dec. 09, 2009.

[70] M. Kohli and et. al., “CASCADE - a multi-layer Boron-10 neutron detection system,” *J. Phys. Conf. Ser.*, vol. 746, 2016, doi: doi:10.1088/1742-6596/746/1/012003.
[71] M. Köhli and et. al., “Efficiency and spatial resolution of the CASCADE thermal neutron detector,” *Nucl. Instrum. Methods Phys. Res. A*, vol. 828, pp. 242–249, May 2016, doi: http://dx.doi.org/10.1016/j.nima.2016.05.014.
[72] F. Sauli, “The gas electron multiplier (GEM): Operating principles and applications,” *Nucl. Instrum. Methods Phys. Res. A*, vol. 805, pp. 2–24, 2016, doi: http://dx.doi.org/10.1016/j.nima.2015.07.060.
[73] S. Uno and et. al., “Two-dimensional Neutron Detector with GEM and its Applications,” *Phys. Procedia*, vol. 26, pp. 142–152, 2012, doi: doi: 10.1016/j.phpro.2012.03.019.
[74] A. Osovizky *et al.*, “6LiF:ZnS(Ag) Mixture Optimization for a Highly Efficient Ultrathin Cold Neutron Detector,” 2018.
[75] N. C. Maliszewskyj *et al.*, “An energy analyzing detector for cold neutrons,” 2018.
[76] M. Katagiri *et al.*, “Scintillation materials for neutron imaging detectors,” *Nucl. Instrum. Methods Phys. Res. Sect. Accel. Spectrometers Detect. Assoc. Equip.*, vol. 529, no. 1–3, pp. 274–279, Aug. 2004, doi: 10.1016/j.nima.2004.04.165.
[77] M. Katagiri *et al.*, “High-position-resolution neutron imaging detector with crossed wavelength shifting fiber read-out using two ZnS/6LiF scintillator sheets,” *Nucl. Instrum. Methods Phys. Res. Sect. Accel. Spectrometers Detect. Assoc. Equip.*, vol. 573, no. 1–2, pp. 149–152, Apr. 2007, doi: 10.1016/j.nima.2006.11.011.
[78] C. W. E. van Eijk, “Inorganic Scintillators for Thermal Neutron Detection,” *IEEE Trans. Nucl. Sci.*, vol. 59, no. 5, pp. 2242–2247, Oct. 2012, doi: 10.1109/TNS.2012.2186154.
[79] K. Hirota and et. al., “Development of neutron Anger-camera detector based on flatpanel PMT,” *Phys. B*, pp. 1297–1299, 2006, doi: doi:10.1016/j.physb.2006.06.058.
[80] J. G. Barker, “Development Proposal for Scintillation High-Resolution Detectors for the Very Small-Angle Neutron Scattering (VSANS) Instrument.” Sep. 2011.
[81] “Lithium Glass Scintillators.” Saint-Gobain, 2016 2007.
[82] R. A. Riedel and et. al., “Design and performance of a large area neutron sensitive anger camera,” *Nucl. Instrum. Methods Phys. Res. A*, vol. 794, pp. 224–233, 2015, doi: http://dx.doi.org/10.1016/j.nima.2015.05.026.
[83] M. M. Bourne, C. Mussi, E. C. Miller, S. D. Clarke, S. A. Pozzi, and A. Gueorguiev, “Characterization of the CLYC detector for neutron and photon detection,” *Nucl. Instrum. Methods Phys. Res. Sect. Accel. Spectrometers Detect. Assoc. Equip.*, vol. 736, pp. 124–127, Feb. 2014, doi: 10.1016/j.nima.2013.10.030.
[84] J. Glodo, R. Hawrami, E. van Loef, U. Shirwadkar, and K. S. Shah, “Pulse Shape Discrimination With Selected Elpasolite Crystals,” *IEEE Trans. Nucl. Sci.*, vol. 59, no. 5, pp. 2328–2333, Oct. 2012, doi: 10.1109/TNS.2012.2188646.
[85] W. M. Higgins *et al.*, “Bridgman growth of Cs2LiYCl6:Ce and 6Li-enriched Cs26LiYCl6:Ce crystals for high resolution gamma ray and neutron spectrometers,” *J. Cryst. Growth*, vol. 312, no. 8, pp. 1216–1220, Apr. 2010, doi: 10.1016/j.jcrysgro.2009.09.046.

[86] L. Soundara-Pandian and et al., “Recent results with a combined gamma-ray and neutron imaging detector,” *Proc. SPIE*, vol. 9215, no. 03, pp. 1–8, 2014, doi: 10.1117/12.2066674.
[87] T. Fujiwara and et al., “Study on Ce:LiCAF scintillator for 3He alternative detector,” *Neutron News*, vol. 23, no. 4, pp. 31–34, 2012.
[88] S. Lam, J. Fiala, M. Hackett, and S. Motakef, “A High-Performance CLYC(Ce)-PVT Composite for Neutron and Gamma Detection,” *IEEE Trans. Nucl. Sci.*, vol. 65, no. 1, pp. 609–615, Jan. 2018, doi: 10.1109/TNS.2017.2779783.
[89] Y. Yehuda-Zada *et al.*, “Optimization of 6LiF:ZnS(Ag) Scintillator Light Yield Using GEANT4,” 2018.
[90] “Thermal Neutron Detection – EJ426.” Eljen Technology, [Online]. Available: https://eljentechnology.com/products/neutron-detectors/ej-426.
[91] “J-Series SiPM Sensors, Rev. 6.” SensL / ON Semiconductor, Dec. 2018, [Online]. Available: https://www.onsemi.com/pub/Collateral/MICROJ-SERIES-D.PDF.
[92] “Wavelength Shifting Fibers.” Kuraray Co. Ltd., [Online]. Available: http://kuraraypsf.jp/psf/ws.html.
[93] “Plastic Scintillating Fibers (Materials and Structures).” Kuraray Co. Ltd., [Online]. Available: http://kuraraypsf.jp/psf/index.html.
[94] M. L. Ruch, C. B. Sivels, S. A. Czyz, M. Flaska, and S. A. Pozzi, “Comparison between silicon photomultipliers and photomultiplier tubes for pulse shape discrimination with stilbene,” in *2014 IEEE Nuclear Science Symposium and Medical Imaging Conference (NSS/MIC)*, Seattle, WA, USA, Nov. 2014, pp. 1–3, doi: 10.1109/NSSMIC.2014.7431167.
[95] V. Golovin and V. Saveliev, “Novel type of avalanche photodetector with Geiger mode operation,” *Nucl. Instrum. Methods Phys. Res. Sect. Accel. Spectrometers Detect. Assoc. Equip.*, vol. 518, no. 1–2, pp. 560–564, Feb. 2004, doi: 10.1016/j.nima.2003.11.085.
[96] B. Dolgoshein *et al.*, “Status report on silicon photomultiplier development and its applications,” *Nucl. Instrum. Methods Phys. Res. Sect. Accel. Spectrometers Detect. Assoc. Equip.*, vol. 563, no. 2, pp. 368–376, Jul. 2006, doi: 10.1016/j.nima.2006.02.193.
[97] D. Ginzburg *et al.*, “Optimizing the design of a silicon photomultiplier-based radiation detector,” *Nucl. Instrum. Methods Phys. Res. Sect. Accel. Spectrometers Detect. Assoc. Equip.*, vol. 652, no. 1, pp. 474–478, Oct. 2011, doi: 10.1016/j.nima.2011.01.022.
[98] H. C. Schultz-Coulon, “Silicon Photomultipliers and their application in HEP and Midical Imaging.” University of Heidelberg, Mar. 2014.
[99] D. Badoni, “SiPM, a Short Introduction,” University of Tor Vergata, 2015.
[100] N. Dinu, A. Nagai, and A. Para, “Breakdown voltage and triggering probability of SiPM from IV curves at different temperatures,” *Nucl. Instrum. Methods Phys. Res. Sect. Accel. Spectrometers Detect. Assoc. Equip.*, vol. 845, pp. 64–68, Feb. 2017, doi: 10.1016/j.nima.2016.05.110.
[101] G. Collazuol, “SiPM behavior at low T,” Jun. 2010.

[102] A. L. Lacaita, F. Zappa, S. Bigliardi, and M. Manfredi, “On the Bremsstrahlung Origin of Hot-Carrier-Induced Photons in Silicon Devices,” *IEEE Trans. Electron Devices*, vol. 40, no. 3, pp. 577–582, Mar. 1993.
[103] L. Gallego, J. Rosado, F. Blanco, and F. Arqueros, “Modeling crosstalk in silicon photomultipliers,” *J. Instrum.*, vol. 8, no. 05, pp. P05010–P05010, May 2013, doi: 10.1088/1748-0221/8/05/P05010.
[104] J. Rosado, V. M. Aranda, F. Blanco, and F. Arqueros, “Modeling crosstalk and afterpulsing in silicon photomultipliers,” *Nucl. Instrum. Methods Phys. Res. Sect. Accel. Spectrometers Detect. Assoc. Equip.*, vol. 787, pp. 153–156, Jul. 2015, doi: 10.1016/j.nima.2014.11.080.
[105] J. Rosado and S. Hidalgo, “Characterization and modeling of crosstalk and afterpulsing in Hamamatsu silicon photomultipliers,” *J. Instrum.*, vol. 10, no. 10, pp. P10031–P10031, Oct. 2015, doi: 10.1088/1748-0221/10/10/P10031.
[106] A. Para, “Afterpulsing in Silicon Photomultipliers: Impact on the Photodetectors Characterization,” *ArXiv150301525 Phys.*, Mar. 2015, Accessed: Jan. 15, 2019. [Online]. Available: http://arxiv.org/abs/1503.01525.
[107] “MPPC (Multi-Pixel Photon Counter), S13360 series.” Hamamatsu, Aug. 2016, [Online]. Available: www.hamamatsu.com.
[108] B. Biró *et al.*, “A Comparison of the Effects of Neutron and Gamma Radiation in Silicon Photomultipliers,” *ArXiv180904594 Hep-Ex Physicsnucl-Ex Physicsphysics*, Sep. 2018, Accessed: Jan. 15, 2019. [Online]. Available: http://arxiv.org/abs/1809.04594.
[109] E. Garutti and Y. Musienko, “Radiation damage of SiPMs,” *ArXiv180906361 Hep-Ex Physicsphysics*, Sep. 2018, Accessed: Jan. 15, 2019. [Online]. Available: http://arxiv.org/abs/1809.06361.
[110] M. Andreotti *et al.*, “Study of the radiation damage of Silicon Photo-Multipliers at the GELINA facility,” *J. Instrum.*, vol. 9, no. 04, pp. P04004–P04004, Apr. 2014, doi: 10.1088/1748-0221/9/04/P04004.
[111] A. Osovizky *et al.*, “Selection of silicon photomultipliers for a 6LiF:ZnS(Ag) scintillator based neutron detector,” 2018.
[112] Alanod-Westlake, “MIRO-SILVER®.” https://alanod-westlake.com/wp-content/uploads/2017/11/MIRO_SILVER_PD_8s_FINAL_D_E_11_14.pdf.
[113] 3M, “Vikuiti™ Enhanced Specular Reflector (ESR).” http://multimedia.3m.com/mws/media/193294O/vikuiti-tm-esr-application-guidelines.pdf.
[114] I. Kandarakis *et al.*, “Evaluation of ZnS:Cu phosphor as X-ray to light converter under mammographic conditions,” *Radiat. Meas.*, vol. 39, no. 3, pp. 263–275, Jun. 2005, doi: 10.1016/j.radmeas.2004.02.023.
[115] A. Siddavatam, “A Parveen, Methods of Pulse Shape Discrimination (PSD).pdf.” International Journal of Application or Innovation in Engineering & Management, 2014.
[116] L. Saldana, “Pulse Shape Discrimination Methods.” Jul. 2014.
[117] A. Yamazaki *et al.*, “Neutron–gamma discrimination based on pulse shape discrimination in a Ce:LiCaAlF6 scintillator,” *Nucl. Instrum. Methods Phys. Res. Sect. Accel. Spectrometers Detect. Assoc. Equip.*, vol. 652, no. 1, pp. 435–438, Oct. 2011, doi: 10.1016/j.nima.2011.02.064.

[118] C. S. Sosa, M. Flaska, and S. A. Pozzi, “Comparison of analog and digital pulse-shape-discrimination systems,” *Nucl. Instrum. Methods Phys. Res. Sect. Accel. Spectrometers Detect. Assoc. Equip.*, vol. 826, pp. 72–79, Aug. 2016, doi: 10.1016/j.nima.2016.03.088.
[119] C. L. Wang and R. A. Riedel, “Improved neutron-gamma discrimination for a ^{6}Li-glass neutron detector using digital signal analysis methods,” *Rev. Sci. Instrum.*, vol. 87, no. 1, p. 013301, Jan. 2016, doi: 10.1063/1.4939821.
[120] J.-B. Mosset *et al.*, “A 16-ch module for thermal neutron detection using ZnS:^{6}LiF scintillator with embedded WLS fibers coupled to SiPMs and its dedicated readout electronics,” *Nucl. Instrum. Methods Phys. Res. Sect. Accel. Spectrometers Detect. Assoc. Equip.*, vol. 845, pp. 494–498, Feb. 2017, doi: 10.1016/j.nima.2016.05.002.
[121] A. Stoykov, J. B. Mosset, U. Greuter, and M. Hildebrandt, “A SiPM-based 6LiF:ZnS Scintillation Neutron Detector,” *Nucl. Instrum. Methods Phys. Res. A*, vol. 787, pp. 361–366, 2015.
[122] T. Nakamura *et al.*, “A large-area two-dimensional scintillator detector with a wavelength-shifting fibre readout for a time-of-flight single-crystal neutron diffractometer,” *Nucl. Instrum. Methods Phys. Res. Sect. Accel. Spectrometers Detect. Assoc. Equip.*, vol. 686, pp. 64–70, Sep. 2012, doi: 10.1016/j.nima.2012.05.038.
[123] T. Nakamura *et al.*, “A position-sensitive tubular scintillator-based detector as an alternative to a 3He-gas-based detector for neutron-scattering instruments,” *Nucl. Instrum. Methods Phys. Res. Sect. Accel. Spectrometers Detect. Assoc. Equip.*, vol. 741, pp. 42–46, Mar. 2014, doi: 10.1016/j.nima.2013.12.043.
[124] V. Esmaeili-sani, A. Moussavi-zarandi, N. Akbar-ashrafi, B. Boghrati, and H. Afarideh, “Neutron–gamma discrimination based on bipolar trapezoidal pulse shaping using FPGAs in NE213,” *Nucl. Instrum. Methods Phys. Res. Sect. Accel. Spectrometers Detect. Assoc. Equip.*, vol. 694, pp. 113–118, Dec. 2012, doi: 10.1016/j.nima.2012.08.025.
[125] M. Nakhostin, “A new digital method for high precision neutron-gamma discrimination with liquid scintillation detectors,” *J. Instrum.*, vol. 8, no. 05, pp. P05023–P05023, May 2013, doi: 10.1088/1748-0221/8/05/P05023.
[126] J.-B. Mosset, A. Stoykov, U. Greuter, M. Hildebrandt, and N. Schlumpf, “Digital signal processing for a thermal neutron detector using ZnS(Ag):6LiF scintillating layers read out with WLS fibers and SiPMs,” *Nucl. Instrum. Methods Phys. Res. Sect. Accel. Spectrometers Detect. Assoc. Equip.*, vol. 824, pp. 319–321, Jul. 2016, doi: 10.1016/j.nima.2015.11.062.
[127] E. Gatti and F. de Martini, “A new linear method of discrimination between elementary particles in scintillation counters,” *Nucl. Electron.*, vol. 2, pp. 265–276, 1962.
[128] S. Korolczuk, M. Linczuk, R. Romaniuk, and I. Zychor, “Development of a digital method for neutron/gamma-ray discrimination based on matched filtering,” *J. Instrum.*, vol. 11, no. 09, pp. C09013–C09013, Sep. 2016, doi: 10.1088/1748-0221/11/09/C09013.

[129] G. Ranucci *et al.*, “A sampling board optimized for pulse shape discrimination in liquid scintillator applications,” *IEEE Trans. Nucl. Sci.*, vol. 51, no. 4, pp. 1784–1790, Aug. 2004, doi: 10.1109/TNS.2004.832607.
[130] J. Kamleitner, S. Coda, S. Gnesin, and Ph. Marmillod, “Comparative analysis of digital pulse processing methods at high count rates,” *Nucl. Instrum. Methods Phys. Res. Sect. Accel. Spectrometers Detect. Assoc. Equip.*, vol. 736, pp. 88–98, Feb. 2014, doi: 10.1016/j.nima.2013.10.023.
[131] D. Takaku, T. Oishi, and M. Baba, “Development of Neutron-Gamma Discrimination Technique using Pattern-Recognition Method with Digital Signal Processing,” *Prog. Nucl. Sci. Technol.*, vol. 1, no. 0, pp. 210–213, Feb. 2011, doi: 10.15669/pnst.1.210.
[132] R. M. Preston, J. E. Eberhardt, and J. R. Tickner, “Neutron generator burst timing measured using a pulse shape discrimination plastic scintillator with silicon photomultiplier readout,” *J. Instrum.*, vol. 8, no. 12, pp. P12005–P12005, Dec. 2013, doi: 10.1088/1748-0221/8/12/P12005.
[133] B. D’Mellow, M. D. Aspinall, R. O. Mackin, M. J. Joyce, and A. J. Peyton, “Digital discrimination of neutrons and -rays in liquid scintillators using pulse gradient analysis,” *Nucl. Instrum. Methods Phys. Res. Sect. Accel. Spectrometers Detect. Assoc. Equip.*, vol. 578, no. 1, pp. 191–197, Jul. 2007, doi: 10.1016/j.nima.2007.04.174.
[134] M. He, “He, Pulse Shape Discrimination of n-γ Based on Pulse Shape Model and Adaptive Kalman Filter.pdf.” Chendu University of Technology.
[135] G. Liu, “An investigation of the digital discrimination of neutrons and γ rays with organic scintillation detectors using an artificial neural network,” *Nucl. Instrum. Methods Phys. Res. A*, vol. 207, 2009.
[136] C. Liao and H. Yang, “Pulse shape discrimination using EJ-299-33 plastic scintillator coupled with a Silicon Photomultiplier array,” *Nucl. Instrum. Methods Phys. Res. Sect. Accel. Spectrometers Detect. Assoc. Equip.*, vol. 789, pp. 150–157, Jul. 2015, doi: 10.1016/j.nima.2015.04.016.
[137] D. Lee and A. Yamamoto, “wavelet analysis: theory and applications.pdf.” Hewlitt Packard, 1994.
[138] C. Torrence and G. P. Compo, “A Practical Guide to Wavelet Analysis,” *Bull. Am. Meteorol. Soc.*, vol. 79, no. 1, pp. 61–78, Jan. 1998, doi: 10.1175/1520-0477(1998)079<0061:APGTWA>2.0.CO;2.
[139] *Understanding Wavelets: Parts 1 - 4*. Matlab.
[140] S. Yousefi, L. Lucchese, and M. D. Aspinall, “Digital discrimination of neutrons and gamma-rays in liquid scintillators using wavelets,” *Nucl. Instrum. Methods Phys. Res. Sect. Accel. Spectrometers Detect. Assoc. Equip.*, vol. 598, no. 2, pp. 551–555, Jan. 2009, doi: 10.1016/j.nima.2008.09.028.
[141] D. I. Shippen, M. J. Joyce, and M. D. Aspinall, “A Wavelet Packet Transform Inspired Method of Neutron-Gamma Discrimination,” *IEEE Trans. Nucl. Sci.*, vol. 57, no. 5, pp. 2617–2624, Oct. 2010, doi: 10.1109/TNS.2010.2044190.
[142] W. G. J. Langeveld, M. J. King, J. Kwong, and D. T. Wakeford, “Pulse Shape Discrimination Algorithms, Figures of Merit, and Gamma-Rejection for Liquid and Solid Scintillators,” *IEEE Trans. Nucl. Sci.*, vol. 64, no. 7, pp. 1801–1809, Jul. 2017, doi: 10.1109/TNS.2017.2681654.

[143] H. Singh and R. Mehra, “Discrete Wavelet Transform Method for High Flux $n-\gamma $ Discrimination With Liquid Scintillators,” *IEEE Trans. Nucl. Sci.*, vol. 64, no. 7, pp. 1927–1933, Jul. 2017, doi: 10.1109/TNS.2017.2708602.
[144] S. Yousefi, L. Lucchese, and S. Yousefi, “A new technique for simultaneous beta and gamma spectroscopy based on wavelet analysis of pulse shapes,” in *2008 IEEE Nuclear Science Symposium Conference Record*, Dresden, Germany, Oct. 2008, pp. 1733–1740, doi: 10.1109/NSSMIC.2008.4774736.
[145] S. Yousefi, L. Lucchese, and M. D. Aspinall, “A novel wavelet-based method for neutron/gamma discrimination in liquid scintillators,” in *2008 IEEE Nuclear Science Symposium Conference Record*, Dresden, Germany, Oct. 2008, pp. 2387–2391, doi: 10.1109/NSSMIC.2008.4774836.
[146] Y. Yang and et. al., “Xie, The Digital discrimination of neutron and γ ray using organic scintillation detector based on wavelet transform modulus maximum.pdf,” *Chin. Phys. C*, vol. 38, no. 3, Apr. 2013.
[147] D. Wisniewski *et al.*, “Digital Pulse Shape Discrimination Methods for Phoswich Detectors,” in *IEEE Nuclear Science Symposium Conference Record, 2005.*, Wyndham El Conquistador Resort, Puerto Rico, 2005, vol. 5, pp. 2979–2983, doi: 10.1109/NSSMIC.2005.1596957.
[148] E. Ronchi *et al.*, “An artificial neural network based neutron–gamma discrimination and pile-up rejection framework for the BC-501 liquid scintillation detector,” *Nucl. Instrum. Methods Phys. Res. Sect. Accel. Spectrometers Detect. Assoc. Equip.*, vol. 610, no. 2, pp. 534–539, Nov. 2009, doi: 10.1016/j.nima.2009.08.064.
[149] J. Griffiths, S. Kleinegesse, D. Saunders, R. Taylor, and A. Vacheret, “Pulse Shape Discrimination and Exploration of Scintillation Signals Using Convolutional Neural Networks,” *ArXiv180706853 Phys.*, Jul. 2018, Accessed: Mar. 07, 2019. [Online]. Available: http://arxiv.org/abs/1807.06853.
[150] C. Fu, A. Di Fulvio, S. D. Clarke, D. Wentzloff, S. A. Pozzi, and H. S. Kim, “Artificial neural network algorithms for pulse shape discrimination and recovery of piled-up pulses in organic scintillators,” *Ann. Nucl. Energy*, vol. 120, pp. 410–421, Oct. 2018, doi: 10.1016/j.anucene.2018.05.054.
[151] C.-X. Zhang and et. al., “Zhang, Discrimination of neutrons and γ-rays in liquid scintillator based on Elman neural network.pdf,” *Chin. Phys. C*, vol. 40, no. 8, 2016.
[152] M. D. Aspinall *et al.*, “Verification of the digital discrimination of neutrons and rays using pulse gradient analysis by digital measurement of time of flight,” *Nucl. Instrum. Methods Phys. Res. Sect. Accel. Spectrometers Detect. Assoc. Equip.*, vol. 583, no. 2–3, pp. 432–438, Dec. 2007, doi: 10.1016/j.nima.2007.09.041.
[153] I. T. Jollife, *Principal Component Analysis*, 2nd ed. Springer, 2002.
[154] A. Hyvärinen, J. Karhunen, and E. Oja, *Independent Component Analysis*, 1st ed. Wiley, 2001.
[155] R. O. Duda, P. Hart, and D. H. Stork, *Pattern Classification*, 2nd ed. Wiley Interscience, 2000.
[156] I. Steinwart and A. Christmann, *Support Vector Machines*. Springer, 2008.
[157] X. Yu *et al.*, “Neutron–gamma discrimination based on the support vector machine method,” *Nucl. Instrum. Methods Phys. Res. Sect. Accel. Spectrometers*

Detect. Assoc. Equip., vol. 777, pp. 80–84, Mar. 2015, doi: 10.1016/j.nima.2014.12.087.
[158] C. M. Bishop, *Neural networks for pattern recognition*. Clarendon Press, 1995.
[159] F. Belli, B. Esposito, D. Marocco, M. Riva, Y. Kaschuck, and G. Bonheure, "A method for digital processing of pile-up events in organic scintillators," *Nucl. Instrum. Methods Phys. Res. Sect. Accel. Spectrometers Detect. Assoc. Equip.*, vol. 595, no. 2, pp. 512–519, Oct. 2008, doi: 10.1016/j.nima.2008.06.045.
[160] J.-B. Mosset, A. Stoykov, V. Davydov, M. Hildebrandt, H. Van Swygenhoven, and W. Wagner, "Upgrade of the POLDI diffractometer with a ZnS(Ag)/6LiF scintillation detector read out with WLS fibers coupled to SiPMs," *J. Phys. Conf. Ser.*, vol. 528, p. 012041, Jul. 2014, doi: 10.1088/1742-6596/528/1/012041.
[161] M. L. Crow, J. P. Hodges, and R. G. Cooper, "Shifting scintillator prototype large pixel wavelength-shifting fiber detector for the POWGEN3 powder diffractometer," *Nucl. Instrum. Methods Phys. Res. Sect. Accel. Spectrometers Detect. Assoc. Equip.*, vol. 529, no. 1–3, pp. 287–292, Aug. 2004, doi: 10.1016/j.nima.2004.04.167.
[162] A. Stoykov, J.-B. Mosset, and M. Hildebrandt, "Trigger Efficiency of a ZnS: ^{6}LiF Scintillation Neutron Detector Readout With a SiPM," *IEEE Trans. Nucl. Sci.*, vol. 63, no. 4, pp. 2271–2277, Aug. 2016, doi: 10.1109/TNS.2016.2590441.
[163] R. M. Preston, J. E. Eberhardt, and J. R. Tickner, "Neutron-Gamma Pulse Shape Discrimination Using Organic Scintillators With Silicon Photomultiplier Readout," *IEEE Trans. Nucl. Sci.*, vol. 61, no. 4, pp. 2410–2418, Aug. 2014, doi: 10.1109/TNS.2014.2335208.
[164] G. Knoll, *Radiation Detection and Measurement*, 4th ed. United States: John Wiley & Sons, Inc., 2010.
[165] Jorg Muller, "Counting Statistics of a Poisson Process with Deadime," Report BIPM-111, Oct. 1970.
[166] Jorg Muller, "On the interval-distributions for recurrent events with a non-extended dead time," BIPM-105, Nov. 1967.
[167] S. Usman and A. Patil, "Radiation detector deadtime and pile up: A review of the status of science," *Nucl. Eng. Technol.*, vol. 50, no. 7, pp. 1006–1016, Oct. 2018, doi: 10.1016/j.net.2018.06.014.
[168] L. Takacs, "On probability problems in the theory of counters," *Ann Math Stat.*, vol. 29, no. 4, pp. 1257–1263, 1958.
[169] B. Denecke and S. de Jonge, "An Analyzer for Pulse-interval Times to Study High-order Effects in the Processing of Nuclear Detector Signals," *Appl Dadiat Isot*, vol. 49, no. 9–11, pp. 1099–1105, 1998.
[170] V. Bécares and J. Blázquez, "Detector Dead Time Determination and Optimal Counting Rate for a Detector Near a Spallation Source or a Subcritical Multiplying System," *Sci. Technol. Nucl. Install.*, vol. 2012, pp. 1–7, 2012, doi: 10.1155/2012/240693.
[171] S. H. Lee, R. P. Gardner, and M. Jab, "Determination of Dead Times in the Recently Introduced Hybrid G-M Counter Dead Time Model," p. 5, 2004.
[172] V. Kornilov, "Effects of dead time and after-pulses in photon detector on measured statistics of stochastic radiation," *J. Opt. Soc. Am. A*, vol. 31, no. 1, p. 7, Jan. 2014, doi: 10.1364/JOSAA.31.000007.

[173] A. Patil, “Dead time and count loss determination for radiation detection systems in high count rate applications,” p. 79.
[174] M. Arkani and G. Raisali, “Measurement of dead time by time interval distribution method,” *Nucl. Instrum. Methods Phys. Res. Sect. Accel. Spectrometers Detect. Assoc. Equip.*, vol. 774, pp. 151–158, Feb. 2015, doi: 10.1016/j.nima.2014.11.069.
[175] Commission canadienne de sûreté nucléaire, *Health effects, dosimetry and radiological protection of tritium: part of the Tritium Studies Project.* Ottawa: Commission canadienne se sûreté nucléaire, 2010.
[176] “NRC: Glossary -- Annual limit on intake (ALI).” https://www.nrc.gov/reading-rm/basic-ref/glossary/annual-limit-on-intake-ali.html (accessed Aug. 26, 2020).
[177] “NRC: 10 CFR Part 20 - Appendix B - Radionuclide Table - Hydrogen-3.” https://www.nrc.gov/reading-rm/doc-collections/cfr/part020/appb/hydrogen-3.html (accessed Aug. 26, 2020).